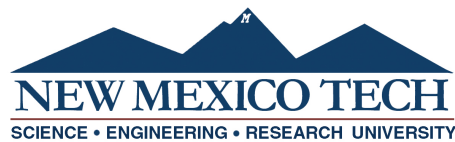


# IRREGULAR REFLECTIONS OF UNSTEADY SHOCK WAVES

by

Kyle Oakley Winter

Submitted in Partial Fulfillment  
of the Requirements for the Degree of  
Doctor of Philosophy in Mechanical Engineering  
with Dissertation in Intelligent Energetic Systems



New Mexico Institute of Mining and Technology  
Socorro, New Mexico  
May, 2021

## ABSTRACT

The majority of prior research in the field of shock wave reflections has focused on pseudo-steady reflections which are fundamentally different from the most common case of explosively-driven unsteady shock waves. The present work combines prior pseudo-steady reflection theory with new models, methodologies, and scaling to better predict and understand unsteady shock waves and their reflections from solid surfaces. Analytical models developed here allow the prediction of shock wave reflection type and characteristics, including pressure and impulse, for explosively-driven shock waves. The models include an update for estimation of the pressure pulse duration of free air shocks, a methodology for calculating duration of reflected shocks, and a new scaling approach for the Friedlander decay coefficient  $\alpha$ . Using these new models, methodologies, and scaling the overpressure, decay coefficient, and impulse from a shock wave reflection can be analytically predicted for any charge size, height of burst, or distance from the charge.

Experiments were performed using gram-scale charges of pentaerythritol tetranitrate (PETN) and kilogram-scale charges of PBXN-110 to generate data for comparison to the developed models. The experiments used refractive imaging techniques to visualize and quantify the shock wave propagation and reflection characteristics. Pressure gages were used to measure overpressures, pulse duration, and explosive impulse. Using the shock Mach number determined from the imaging systems and the height of burst, the type of shock reflection was predicted using the developed analytical model and shown to agree with the measurements to within the expected uncertainty. Using the reflection type, Mach number and height of burst the overpressure of the shock wave reflection was estimated through the analytical models and shown to agree with the experimental results. The analytical process was then used to determine the peak pressure and impulse over a wide range of heights of burst and distances from the charge to visualize the effect of charge height on impulse.

A methodology for calculating reflected pulse duration was proposed and shown to match the experimental data better than previous models. The methodology updated previous approaches where a release wave is propagated outward through the post-shock field. The new approach places the origin of this release wave at the point of zero overpressure on the fireball surface rather than the explosive center. The pressure decay process was predicted using this new methodology and the decay coefficient evolution with distance was explored. The decay coefficient was found to vary for non-reflected and reflected shock waves and to vary with explosive composition. By comparing the decay coefficient between the gram and kilogram charges a novel scaling approach for Friedlander decay

coefficient was proposed to account for differences between explosive type. The scaling uses the heat of reaction of the explosive material as a scaling parameter to collapse data between PETN and PBXN-110.

**Keywords:** Explosively-driven Shock Reflections, Regular Reflections, Irregular Reflection, Impulse, Overpressure, Pulse Duration, Pressure Decay Coefficient, Friedlander, Refractive Imaging, Shadowgraph, Schlieren, Background Oriented Schlieren, BOS, PETN, PBXN-110

## ACKNOWLEDGMENTS

I would like to thank Dr. Micheal Hargather for his countless hours of teaching, guidance, and leadership during my time at New Mexico Tech. Dr. Hargather has made me a stronger researcher and better overall person. I also want to specifically thank him for all the time he has put into helping me develop my writing and communication skills.

I would like to thank Dr. Suhithi Peiris, Dr. Chi Mai and Dr. Christopher "Kit" Neel of the Air Force Research Laboratory and Dr. Lindsey Thornhill of IS4S for funding this work. I would also to thank the staff of the Advanced Warhead Experimentation Facility (AWEF) at Eglin Air Force Base and IS4S for their assistance and expertise.

I would also like to thank the Defense Threat Reduction Agency for funding portions of the gram-scale tests series under grant HDTRA1-18-0022.

I want to thank all of my current and former lab mates in the Shock and Gas Dynamics Laboratory for your help, encouragement and friendship over the last 5 years. I could not have asked for a better group to work alongside everyday.

I also want to thank my friends and family for supporting me in my decision to go back to school and earn my PhD. I especially want to thank my parents for their constant encouragement and belief in me.

Finally, and most importantly, I want to thank my amazing wife. I could not have made through grad school without her. I want to thank her for always being supportive of this crazy dream and for her endless understanding.

# CONTENTS

	<b>Page</b>
<b>LIST OF TABLES</b>	<b>vii</b>
<b>LIST OF FIGURES</b>	<b>viii</b>
<b>CHAPTER 1. INTRODUCTION</b>	<b>1</b>
1.1 Research Motivation . . . . .	1
1.2 Literature Review . . . . .	1
1.2.1 Overview and History of Shock Wave Reflections . . . . .	1
1.2.2 Shock Reflection Types . . . . .	2
1.2.3 Transition Between Shock Reflections . . . . .	4
1.2.4 Galilean Frame of Reference Transformation . . . . .	6
1.2.5 Multiple Reflections and Complex Geometries . . . . .	7
1.2.6 Refractive Imaging Techniques . . . . .	8
1.2.7 Shock Wave Propagation in Air . . . . .	14
1.3 Objectives of the Present Research . . . . .	16
<b>CHAPTER 2. ANALYTICAL APPROACH TO SHOCK WAVE REFLECTIONS</b>	<b>17</b>
2.1 Determining Mach number and Reflection Angle . . . . .	17
2.2 Regular Reflection . . . . .	19
2.2.1 Numerical Solution . . . . .	20
2.2.2 Shock Polar Analysis . . . . .	21
2.3 Mach Reflection . . . . .	22
2.3.1 Numerical Solution . . . . .	25
2.3.2 Shock Polar Analysis . . . . .	26
2.4 Formation Conditions of Regular and Mach Reflections . . . . .	28
2.5 Pressure Across a Shock Reflection . . . . .	32
2.6 Unsteady Shock Reflection . . . . .	33

<b>CHAPTER 3. EXPERIMENTAL METHODS OF GRAM-SCALE TEST SERIES</b>	<b>34</b>
3.1 Explosive Pellet . . . . .	37
3.2 Reflection Structure . . . . .	39
3.3 Refractive Imaging Systems . . . . .	42
3.3.1 One-meter-diameter Shadowgraph System . . . . .	42
3.3.2 30 Centimeter Schlieren System . . . . .	44
<b>CHAPTER 4. RESULTS AND DISCUSSION OF THE NON-REFLECTED GRAM-SCALE TEST SERIES</b>	<b>45</b>
4.1 Discussion of Uniformity of Explosive Charges . . . . .	45
4.2 Calculating Mach Radius Curve for 1g PETN . . . . .	50
4.3 Experimental Peak Pressure and Impulse . . . . .	58
4.4 Analytical Peak Pressure and Impulse . . . . .	64
4.4.1 Analytical Peak Pressure . . . . .	66
4.4.2 Analytical Pulse Duration . . . . .	68
4.4.3 Analytical Model of Pulse Duration Release Wave . . . . .	73
4.4.4 CTH Simulation of the Pulse Duration Release Wave . . . . .	85
4.4.5 Decay Coefficient . . . . .	97
4.4.6 Analytical Impulse . . . . .	99
<b>CHAPTER 5. RESULTS AND DISCUSSION OF THE REFLECTED GRAM-SCALE TEST SERIES</b>	<b>105</b>
5.1 Shock Reflection Transition . . . . .	105
5.1.1 Analytical Shock Reflection Transition . . . . .	105
5.1.2 Refractive Imaging of Shock Reflection Transitions . . . . .	108
5.1.3 Mach Stem Growth Effect on Visualization of Mach Reflection	118
5.2 Experimental Peak Pressure and Impulse . . . . .	123
5.2.1 Fitting Experimental Pressure Data . . . . .	123
5.2.2 Uncertainty In Pressure Data . . . . .	133
5.3 Analytical Peak Pressure and Impulse . . . . .	141
5.3.1 Analytical Peak Pressure . . . . .	144
5.3.2 Analytical Pulse Duration . . . . .	147
5.3.3 Decay Coefficient . . . . .	156
5.3.4 Analytical Impulse . . . . .	158
5.3.5 Surface Plots of Peak Pressure, Pulse Duration and Impulse	162

<b>CHAPTER 6. EXPERIMENTAL METHODS OF KILOGRAM-SCALE TEST SERIES</b>	<b>165</b>
6.1 Refractive Imaging Systems . . . . .	167
6.2 Camera Synchronizing . . . . .	170
6.3 Camera Calibration Techniques . . . . .	174
6.4 BOS Processing . . . . .	174
<b>CHAPTER 7. RESULTS AND DISCUSSION OF KILOGRAM-SCALE TEST SERIES</b>	<b>177</b>
7.1 Shock Reflection Transition . . . . .	177
7.2 Experimental Peak Pressure and Impulse . . . . .	180
7.2.1 Frequency Filtering Pressure Data . . . . .	180
7.2.2 Fitting and Uncertainty of Experimental Pressure Data . . . . .	183
7.3 Analytical Peak Pressure and Impulse . . . . .	188
7.3.1 Analytical Peak Pressure . . . . .	188
7.3.2 Analytical Pulse Duration . . . . .	193
7.3.3 Decay Coefficient . . . . .	198
7.3.4 Analytical Impulse . . . . .	204
<b>CHAPTER 8. CONCLUSIONS AND RECOMMENDATIONS FOR FUTURE RESEARCH</b>	<b>207</b>
8.1 Summary and Conclusions . . . . .	207
8.2 Recommendations for Future Research . . . . .	209
<b>REFERENCES</b>	<b>211</b>
<b>APPENDIX A. SPHERE PRESSING DIE DESIGN</b>	<b>220</b>
<b>APPENDIX B. REFLECTION PLATE DESIGN</b>	<b>229</b>
<b>APPENDIX C. MIRROR BASE DESIGN</b>	<b>235</b>

## LIST OF TABLES

Table	Page
3.1 Summary of the gram-scale reflection tests series. . . . .	35
3.2 Summary of the no reflection tests series. . . . .	36
4.1 Resulting coefficients from different Dewey Curve fits. All coefficients were determined using units of meters and seconds. . . . .	58
4.2 Summary of the data collected for each no reflection test. . . . .	62
5.1 Summary of the reflection tests series. . . . .	108
6.1 Details of the explosive charge used in each test. The rounded charge weight denotes which of the three weight ranges the charge falls in: 0.45 kg (1 lb.), 1.36 kg (3 lb.), or 2.72 kg (6 lb.). . . . .	167
6.2 The difference, in $\mu\text{s}$ , between the time the camera receives a trigger signal and when it opens its digital shutter for the frame 0 for five individual tests. . . . .	171
6.3 The difference, in frames, between the time the camera receives a trigger signal and when any light is seen from the explosive. All cameras were recording at 50,000 fps so the time between each frame is 20 $\mu\text{s}$ . . . . .	171
7.1 List of the power law fit terms from the scaled and un-scaled gram, kilogram and combined tests. The $\alpha$ scaling factor for the scaled gram and kilogram tests is shown. . . . .	202

## LIST OF FIGURES

Figure	Page
Figure 1.1 Wave diagram of the 4 types of reflections for an oblique shock wave traveling from left to right interacting with a solid reflecting surface. a) Regular reflection which has two waves. b) Mach reflection which can be identified by a single Mach stem. c) Transitional Mach reflection which has a "kink" in the reflected shock. d) Double Mach reflection which has two Mach stems. The incident (I) and reflected (R) shocks in each reflection is indicated .	2
Figure 1.2 Schematic representation of (a) regular and (b) singular Mach reflections. In a regular reflection, the initial (I) and reflected (R) shock meet at the reflecting surface, resulting in a new zero deflection of the flow. Single Mach reflections include a third shock wave, the Mach stem (m), which connects the reflecting surface to the intersection of the initial and reflected shock waves. Here the shock is assumed to be steady and the flow propagates toward the shock from right to left. . . . .	3
Figure 1.3 a) Transitional Mach reflection where the initial shock wave is connected to the Mach stem but the reflected shock is connected to the Mach stem via a smaller shock referred to as the kink. b) Double Mach reflection where a second Mach stem connects the second triple point to the end of the first slip stream. The shock wave is in the steady frame of reference with flow propagating from right to left. . . . .	4
Figure 1.4 Diagram of Galilean transformation of regular reflection from the (a) laboratory to the (b) pseudo-steady frame of reference.	8
Figure 1.5 Diagram of typical lens schlieren system with light ray paths shown. . . . .	9
Figure 1.6 (a) Schlieren image of a lighter utilizing a vertical knife edge. (b) Retro-reflective shadowgraph of a candle. . . . .	10
Figure 1.7 a) Diagram of Z type schlieren system made with two parabolic mirrors. b) Diagram of coincident schlieren system using only one spherical mirror . . . . .	11
Figure 1.8 Diagram of rod mirror retro-reflective shadowgraph system with light ray paths shown. . . . .	12
Figure 1.9 Diagram of typical BOS system with light ray paths shown.	13

Figure 2.1	Diagram defining the wedge angle, $\theta_w$ , for a explosive detonated at some height of burst (HOB) from a reflecting surface. Trigonometry is used to calculate the wedge angle for a given HOB and shock wave radius (r) at any given time t. . . . .	18
Figure 2.2	Labeled diagram for a regular reflection. With I indicating the incident shock, and R the reflected shock. The number of the state is listed in the oval. The deflection, $\delta$ , and wave angle, $\phi$ , is listed for each shock. The boundary condition of equivalent deflection angle is listed at the bottom of the figure. . . . .	19
Figure 2.3	Shock polar diagram of the regular reflection of a Mach 3 flow with a $60^\circ$ wave angle. . . . .	21
Figure 2.4	Labeled diagram of a single Mach reflection. With I indicating the incident shock, R the reflected shock, m the Mach stem, and S the slip line. The number of the state is listed in the oval. The deflection, $\delta$ , and wave angle, $\phi$ , is listed for each shock. The boundary conditions are listed at the bottom of the figure. The Mach stem is shown to have two distinct angles, $\phi_3$ at the triple point and perpendicular to the reflection plane at the reflection plane. In the diagram there is a sharp transition between the two angles but in experiments this has been shown to be a smooth transition between the two angles. . . . .	23
Figure 2.5	Shock polar diagram of the reflection of a Mach 3 flow with a $45^\circ$ wave angle. The formation conditions of the Mach reflection are indicated. . . . .	27
Figure 2.6	Shock polar diagram of the sonic condition which is the transition criteria for pseudo-steady shock waves. This diagram show the reflection of a shock wave in a Mach 2 flow with an angle of $42.7^\circ$ between the flow and the shock. . . . .	29
Figure 2.7	Domain diagram showing which pseudo-steady shock wave reflection will occur given a wedge angle and Mach Number. . . . .	30
Figure 2.8	Labeled diagram of a transitional-Mach reflection. With I indicating the incident shock, R the reflected shock, m the Mach stem, s the slip line and the new feature of the kink, K. The number of the state is listed in the oval. The deflection, $\delta$ , and wave angle, $\phi$ , is listed for each shock. . . . .	31
Figure 2.9	Labeled diagram of a double Mach reflection. With I indicating the incident shock, R the reflected shock, m the Mach stem, and s the slip line. The number of the state is listed in the oval. The deflection, $\delta$ , and wave angle, $\phi$ , are listed for each shock. $\theta$ is used to denote the angle between shock waves. The ' is on features, such as Mach stem, to denote the second feature and the ' is used on values to indicate it is taken in reference to the second triple point. . . . .	32

Figure 3.1	Diagram of mirrors and reflection plate setup for the reflection gram scale test series. . . . .	35
Figure 3.2	Model of charge and reflection plate setup for the gram scale test series. The rigid test section plate has tapped holes for pressure transducers. The extension plates are positioned to allow the shock wave to expand without introducing rarefaction waves. A gantry made of 80/20 aluminum framing is used to suspend the explosive charge. . . . .	36
Figure 3.3	Cutaway diagram of pellet pressing die. . . . .	38
Figure 3.4	Cutaway diagram of explosive pellet being extracted from die. . . . .	39
Figure 3.5	Model of the shock wave reflection structure. The rigid test section plate has tapped holes for pressure transducers. The extension plates are positioned to allow the shock wave to expand without introducing rarefaction waves. A gantry made of 80/20 is used to suspend the explosive charge. . . . .	40
Figure 3.6	Light ray diagram of the double pass focused shadowgraph system that will be used in the gram scale test series. . . . .	42
Figure 3.7	Photograph of the 1-m-diameter flat mirror with the coordinate system used to define it shown. Note that the mirror has a hole in the center of it, which prevents imaging at that location. . .	43
Figure 3.8	Schematic of the 30-cm-diameter parabolic mirror and mirror support. . . . .	44
Figure 4.1	A PETN pellet with an RP-3 detonator glued to it with cyanoacrylate. A US penny is included for scale. . . . .	46
Figure 4.2	A PETN pellet with an RP-3 detonator attached to it with electrical tape. The pellet is suspended over the test section. The yellow tube above the charge is a polymer straw used to provide a consistent charge height. A ruler with cm graduations, used to determine the exact charge height, is shown to the left of the charge. . . . .	48
Figure 4.3	Refractive image from the 30-cm Z-schlieren system from Test R4 at $t = 30 \mu s$ where $t = 0$ is first light. . . . .	49
Figure 4.4	Refractive image from the 30-cm Z-schlieren system from Test R1 at $t = 132 \mu s$ where $t = 0$ is first light. . . . .	50
Figure 4.5	Unscaled shock wave time radius . . . . .	51
Figure 4.6	The scaled shock wave time and radius data with the Dewey curve fit found by fitting all coefficients. . . . .	54
Figure 4.7	Scaled shock wave Radius Mach number for the coefficients $A = 0.00773$ , $B = 2.15$ , $C = -2.06$ , and $D = 0.747$ using units of meters and seconds. . . . .	54

Figure 4.8	The scaled shock wave time and radius data with the fit Dewey curve fit found by fitting $A$ , $C$ , and $D$ coefficient. . . . .	55
Figure 4.9	Scaled shock wave Radius Mach number from the coefficients $A = 0.0228$ , $B = 1$ , $C = -0.463$ and $D = 0.576$ using units of meters and seconds. . . . .	55
Figure 4.10	The scaled shock wave time and radius data with the dimensionless Dewey curve fit found by fitting all coefficients with a characteristic length scale of $L_c = 0.005$ m. . . . .	56
Figure 4.11	The scaled shock wave time and radius data with the fit Dewey curve fit found by fitting $A$ , $C$ , and $D$ coefficient with a characteristic length scale of $L_c = 0.005$ m. . . . .	57
Figure 4.12	The scaled shock wave time and radius data with the fit Dewey curve fit found by fitting $C$ , and $D$ coefficient with a characteristic length scale of $L_c = 0.005$ m. . . . .	57
Figure 4.13	Flow chart outlining the calculation of Friedlander parameters. . . . .	59
Figure 4.14	Representative un-modified pressure trace from test N1 which is a no shock reflection test. . . . .	60
Figure 4.15	The pressure trace from N1 cropped from the time of arrival to when the pressure returned to zero. The cropped pressure trace was then fit to the Friedlander equation . . . . .	60
Figure 4.16	Representative high noise pressure trace from test N2 pressure probe 13, which was 0.457 m from the charge, that was cropped and fit to the Friedlander equation. . . . .	61
Figure 4.17	Ratio of pressure across the shock wave as a function of radius for the fit experimental data. . . . .	62
Figure 4.18	Pulse duration of the shock pressure as a function of radius for the fit experimental data. . . . .	63
Figure 4.19	The decay coefficient $\alpha$ as a function of radius for the fit experimental data. . . . .	63
Figure 4.20	Flow chart outlining the calculation of analytical impulse. . . . .	65
Figure 4.21	The Mach number and pressure ratio across the shock as a function of radius. . . . .	66
Figure 4.22	Comparison between peak pressure found from the pressure traces and Friedlander curve fit versus the shock radius versus time and one-dimensional gas dynamics. . . . .	67
Figure 4.23	The Mach number and post shock temperature as a function of radius. . . . .	69
Figure 4.24	The Mach number and post shock speed of sound as a function of radius. . . . .	69

Figure 4.25 The wave velocities of the shock wave and relaxation wave as function of radius . . . . .	70
Figure 4.26 x-t diagram of the position of the shock and relaxation wave as a function of radius. The area between the curves is highlighted since the vertical distance is the pulse duration. . . . .	71
Figure 4.27 x-t diagram of the position of the shock and relaxation wave as a function of radius and the resulting numerical value of the pulse duration. . . . .	72
Figure 4.28 Comparison of the experimental and analytical values for pulse duration. . . . .	72
Figure 4.29 Simple 1D wave diagram of the detonation and expansion of a high explosive. The rarefaction fan generated at shock wave breakout is divided into 10 wavelet. . . . .	74
Figure 4.30 Streak shadowgraph image from test N5. The zero radius point is at the center of the charge and the streak image was generated from a horizontal line. . . . .	76
Figure 4.31 The solution for the pressure and particle velocity for the first wavelet at the center line and interface. . . . .	77
Figure 4.32 The solution for the pressure and particle velocity for the fifth wavelet at the center line and interface. . . . .	78
Figure 4.33 Diagram of the impact of a sandwich plate problem geometry. . . . .	80
Figure 4.34 The solution for the pressure and particle velocity for the first wavelet at the center line and interface using the modified centerline assumption. . . . .	80
Figure 4.35 The solution for the pressure and particle velocity for the fifth wavelet at the center line and interface using the modified centerline assumption. . . . .	81
Figure 4.36 The first 20 $\mu s$ of a scale wave diagram of the expansion of a PETN pellet with a radius of 5.5 mm. . . . .	82
Figure 4.37 The first 100 $\mu s$ of a scale wave diagram of the expansion of a PETN pellet with a radius of 5.5 mm. . . . .	83
Figure 4.38 The first 600 $\mu s$ of a scale wave diagram of the expansion of a PETN pellet with a radius of 5.5 mm. . . . .	83
Figure 4.39 A scale wave diagram of the expansion of a PETN pellet with a radius of 5.5 mm. . . . .	84
Figure 4.40 Plot of particle velocity as a function radius for a 1D rectangular simulation of the PETN pellet. The dashed line denotes the boundary between the PETN or PETN detonation products and air. . . . .	86

Figure 4.41 Plot of density as a function of time and distance for a 1D rectangular simulation of the PETN pellet. Four points of interest are labeled. Point 1 is the air shock. Point two is the point of maximum expansion of the air-detonation products interface. Point 3 indicates the region where the density and pressure of the detonation products drops to effectively zero. Point 4 is after the detonation products have rebounded against the $x = 0$ boundary. .	87
Figure 4.42 Plot of pressure as a function of time and distance for a 1D rectangular simulation of the PETN pellet. Four points of interest are labeled. Point 1 is the air shock. Point two is the approximate location of the air-detonation products interface. The product interface cannot support a pressure differential which is why there is no discontinuity. Point 3 indicates the region where the density and pressure of the detonation products drops to effectively zero. Point 4 is after the detonation products have rebounded against the $x = 0$ boundary. . . . .	88
Figure 4.43 Plot of density at 2.5 ms for a 1D rectangular simulation of the PETN pellet. . . . .	89
Figure 4.44 Plot of density as a function of time and radius for a 1D spherical simulation of the PETN pellet. . . . .	90
Figure 4.45 Plot of density as a function of time and radius for a 1D spherical simulation of the PETN pellet. . . . .	91
Figure 4.46 Plot of pressure as a function of time and radius for a 1D spherical simulation of the PETN pellet. . . . .	91
Figure 4.47 Plot of density as a function of time and radius for a 1D spherical simulation of the PETN pellet. The figure has been cropped to 10 <i>cm</i> and 200 $\mu$ s. . . . .	92
Figure 4.48 Plot of pressure as a function of time and radius for a 1D spherical simulation of the PETN pellet. The figure has been cropped to 10 <i>cm</i> and 200 $\mu$ s. . . . .	92
Figure 4.49 a is the experimental streak image. b is the synthetic streak image with a Canny edge detection overlaid. c is the edges of the synthetic streak image overlaid onto the experimental streak image. . . . .	94
Figure 4.50 Composite image generated from the density and pressure data from the spherical simulation. A color legend for the pressure and density is shown. . . . .	95
Figure 4.51 Comparison of the experimental pulse duration and the analytical pulse duration were the release wave has been started at either the point of zero over pressure or the point of maximum product expansion. . . . .	96

Figure 4.52 Predicted $\alpha$ values as function of scaled distance (Z) reproduced from multiple literature sources. . . . .	97
Figure 4.53 The decay coefficient $\alpha$ as a function of radius for the fit experimental data and the resulting numerical power law fit of the data. . . . .	98
Figure 4.54 The decay coefficient $\alpha$ and the resulting numerical power law fit of the data. Additionally the $\alpha$ curve from multiple literature sources. . . . .	98
Figure 4.55 Shock impulse as a function of radius for experimental data and analytical. The Kinney and Graham empirical equation for impulse per unit area is shown. . . . .	99
Figure 4.56 Shock impulse as a function of radius for experimental data and analytical. The Kinney and Graham empirical equation for impulse per unit area is shown. Data scaled to 1kg . . . . .	100
Figure 4.57 The value of part of the Friedlander impulse equation that contains the $\alpha$ variable as a function of $\alpha$ . . . . .	101
Figure 4.58 The value of part of the Friedlander impulse equation that contains the $\alpha$ variable as a function of radius. . . . .	102
Figure 5.1 The Mach number and effective wedge angle path of the shock wave from 1 g of PETN detonated 0.1 m above a reflecting surface. The initial reflection point is shown as a green dot and the final point shown is highlighted with a magenta dot. An arrow was added to indicate the progression of the reflection. . . . .	106
Figure 5.2 The Mach number and effective wedge angle path of the shock wave from test R1 overlaid on the shock reflection type domain map. . . . .	106
Figure 5.3 The Mach number and effective wedge angle path of the shock wave from test R1 overlaid on the shock reflection type domain map. The location of the frames from the 30 cm schlieren system are shown as blue circles. The first frame following the predicted transition from a regular reflection to irregular reflection is shown as a solid blue dot. . . . .	107
Figure 5.4 Frames from a test with an unusable shock reflection transition. Oblique shocks disrupt the primary shock immediately prior to the reflection transition. This figure will be broken into two rows to make it more easily seen. . . . .	109
Figure 5.5 Frames, with time stamp added, from test R1 to show the shock reflection transition. . . . .	111
Figure 5.6 Select frames from Figure 5.5 enlarged to show the lower right edge of the primary shock lifting off of the reflection surface. . . . .	112

Figure 5.7	The Mach number and effective wedge angle path of the shock wave from R1 overlaid on the shock reflection type domain map. The predicted reflection transition is shown in solid blue and the observed transition is shown in solid green. . . . .	112
Figure 5.8	Frames from R8 showing the transition of regular to irregular reflection. . . . .	114
Figure 5.9	An enlarged view from Figure 5.10 to show how the leading edge of the shock is being defined in the refractive images. . . . .	115
Figure 5.10	Frames from R8 showing the transition of the primary shock to a Mach stem. . . . .	115
Figure 5.11	The Mach number and effective wedge angle path of the shock wave from R8 overlaid on the shock reflection type domain map. The predicted reflection transition is shown in solid blue and the observed transition is shown in solid green. . . . .	116
Figure 5.12	Frames from R11 showing the transition of the primary shock to a Mach stem. . . . .	116
Figure 5.13	The Mach number and effective wedge angle path of the shock wave from R11 overlaid on the shock reflection type domain map. The predicted reflection transition is shown in solid blue and the observed transition is shown in solid green. . . . .	117
Figure 5.14	The triple point trajectory $\chi$ as a function of time for tests R1, R8, R11. . . . .	118
Figure 5.15	The Mach stem height as a function of time for tests R1, R8, R11. . . . .	119
Figure 5.16	The final frame of the regular reflections from Tests R1, R8, and R11. The bottom pixels of the primary and reflected shocks are highlighted and a fit line shown. . . . .	122
Figure 5.17	Flow chart outlining the calculation of the Friedlander parameters for a reflected shock. . . . .	124
Figure 5.18	Raw pressure trace from the pressure probe at $X=-5.1$ cm from Test R1. . . . .	125
Figure 5.19	Raw pressure trace from the pressure probe at $X=-15.2$ cm from Test R1 . . . . .	126
Figure 5.20	Two step fitting to the pressure trace from the pressure probe at $X=-7.6$ cm from Test R1. The left plot is the linear fit to the semi-log data to find the pulse duration. The right plot is the Friedlander fit to determine the remaining two variables. . . . .	127
Figure 5.21	Peak pressure values for the 8 charge diameter HOB tests. .	128
Figure 5.22	Peak pressure values for the 9 charge diameter HOB tests. .	128
Figure 5.23	Peak pressure values for the 11 charge diameter HOB tests. .	129
Figure 5.24	Peak pressure values for the 14 charge diameter HOB tests. .	129

Figure 5.25	Pulse duration values for the 8 charge diameter HOB tests. .	130
Figure 5.26	Pulse duration values for the 9 charge diameter HOB tests. .	130
Figure 5.27	Pulse duration values for the 11 charge diameter HOB tests.	131
Figure 5.28	Pulse duration values for the 14 charge diameter HOB tests.	131
Figure 5.29	Decay coefficient, $\alpha$ , for all tests. . . . .	132
Figure 5.30	Uncertainty as a function of radius for the decay coefficient, $\alpha$ .	133
Figure 5.31	Uncertainty as a function of radius for the peak pressure for 8 charge diameters. . . . .	134
Figure 5.32	Uncertainty as a function of radius for the peak pressure for 9 charge diameters. . . . .	134
Figure 5.33	Uncertainty as a function of radius for the peak pressure for 11 charge diameters. . . . .	135
Figure 5.34	Uncertainty as a function of radius for the peak pressure for 14 charge diameters. . . . .	135
Figure 5.35	Uncertainty as a function of radius for the pulse duration for 8 charge diameters. . . . .	136
Figure 5.36	Uncertainty as a function of radius for the pulse duration for 9 charge diameters. . . . .	136
Figure 5.37	Uncertainty as a function of radius for the pulse duration for 11 charge diameters. . . . .	137
Figure 5.38	Uncertainty as a function of radius for the pulse duration for 14 charge diameters. . . . .	137
Figure 5.39	Experimental values and uncertainty of impulse as a func- tion of radius for the 8 charge diameter tests. . . . .	139
Figure 5.40	Experimental values and uncertainty of impulse as a func- tion of radius for the 9 charge diameter tests. . . . .	139
Figure 5.41	Experimental values and uncertainty of impulse as a func- tion of radius for the 11 charge diameter tests. . . . .	140
Figure 5.42	Experimental values and uncertainty of impulse as a func- tion of radius for the 14 charge diameter tests. . . . .	140
Figure 5.43	Flow chart outlining the calculation of analytical impulse for a reflected shock. The subprocess used to calculate pulse dura- tion is shown in the following figure. . . . .	142
Figure 5.44	Flow chart outlining the calculation of analytical pulse du- ration for a reflected shock. . . . .	143
Figure 5.45	Comparison between the analytical and experimental val- ues for peak pressure for the 8 charge diameter tests. . . . .	145
Figure 5.46	Comparison between the analytical and experimental val- ues for peak pressure for the 9 charge diameter tests. . . . .	145

Figure 5.47 Comparison between the analytical and experimental values for peak pressure for the 11 charge diameter tests. . . . .	146
Figure 5.48 Comparison between the analytical and experimental values for peak pressure for the 14 charge diameter tests. . . . .	146
Figure 5.49 Schematic of how the radius of the reflection shock is defined.	147
Figure 5.50 a) plot of the temperature ratio across primary shock. b) Plot of the temperature ratio across the reflected shock. c) Plot of the temperature ratio across the primary and reflected shock. . . . .	149
Figure 5.51 Plot of the speed of sound after the reflected shock. . . . .	149
Figure 5.52 Comparison between the analytical pulse duration, for both a non-reflected and reflected shock, and experimental pulse duration. a) is the 8 charge diameter tests. b) is the 9 charge diameter tests. c) is the 11 charge diameter tests. d) is the 14 charge diameter tests. . . . .	151
Figure 5.53 Comparison between the analytical pulse duration, for both a non-reflected and reflected shock, and experimental pulse duration. a) is the 8 charge diameter tests. b) is the 9 charge diameter tests. c) is the 11 charge diameter tests. d) is the 14 charge diameter tests. . . . .	153
Figure 5.54 Comparison between the analytical non-reflected pulse duration and the experimental pulse duration for all the shock reflection tests. . . . .	154
Figure 5.55 Comparison between the analytical non-reflected pulse duration and the experimental pulse duration for all tests, both shock reflection and the non-reflected tests. . . . .	155
Figure 5.56 The experimental decay coefficient, $\alpha$ , for the reflection tests and power law fit to the data. . . . .	156
Figure 5.57 The experimental decay coefficient, $\alpha$ , for all tests and the power law fit to both the reflected and non-reflected data . . . . .	157
Figure 5.58 The experimental impulse with one standard deviation and the analytical impulse for the 8 charge diameter tests shown as a function of total radius from the charge. The transition from regular reflection to irregular reflection is shown as the vertical dotted line. . . . .	159
Figure 5.59 The experimental impulse with one standard deviation and the analytical impulse for the 9 charge diameter tests shown as a function of total radius from the charge. The transition from regular reflection to irregular reflection is shown as the vertical dotted line. . . . .	160

Figure 5.60	The experimental impulse with one standard deviation and the analytical impulse for the 11 charge diameter tests shown as a function of total radius from the charge. The transition from regular reflection to irregular reflection is shown as the vertical dotted line. . . . .	160
Figure 5.61	The experimental impulse with one standard deviation and the analytical impulse for the 14 charge diameter tests shown as a function of total radius from the charge. The transition from regular reflection to irregular reflection is shown as the vertical dotted line. . . . .	161
Figure 5.62	Surface plot of peak pressure as function of height of burst and X distance from the charge. The transition from regular to irregular reflection is shown as the black line. . . . .	162
Figure 5.63	Surface plot of pulse duration as function of height of burst and X distance from the charge. The areas inside of the product gasses are not shown. . . . .	163
Figure 5.64	Surface plot of impulse per unit area as function of height of burst and X distance from the charge. . . . .	163
Figure 6.1	Diagram of the pressure probe locations for the kilogram-scale test series. A pressure gauge was located at the intersection of each ring and radial line. . . . .	166
Figure 6.2	Photograph of part of the setup for the large scale tests. In the center of the image is the reflection platform in which the starburst pattern of the pressure gauges can be seen. The speckle boards used as a background for BOS are positioned behind the reflection platform. The non-speckled space is where the retro-reflective shadowgraph screen is placed prior to the test. . . . .	168
Figure 6.3	Photograph of part of the setup for the large scale tests. A 1.36 kg (3 lb.) sphere charge is hanging from the gantry. Behind the charge is the retro-reflective shadowgraph screen. . . . .	169
Figure 6.4	The frame at which first light was observed for cylinder test C1. Frame 0 is defined by the camera as the first frame after it receives the trigger signal. The images have been image processed to improve visibility of the charge. a) Frame 0 for camera 1, the shadowgraph camera. b) Frame 0 for camera 2. c) Frame -1 for camera 3. d) Frame -2 for camera 4. e) Frame 0 for camera 5. . . . .	173
Figure 6.5	(a) Reference image before detonation. (b) Hot image 3.34 ms after detonation. (c) BOS image created by image subtracting (a) and (b). (d) Reference image recorded 1 frame (0.017 ms) before hot image. (e) Hot image, identical to (b), 3.34 ms after detonation. (f) Sequential BOS image created by image subtracting (d) and (e). All images are from test S6. . . . .	176

Figure 7.1	Radius-time plot for 1 kg of PBXN-110. The data from the 0.45 kg and 1.36 kg is shown along with the Dewey Curve fit. . . .	178
Figure 7.2	Shadowgraph of a regular shock wave reflection from test S3 0.87 ms after detonation. The location of regular reflection is indicated by the arrow. The charge used was 1.36 kg of PBXN-110. . . .	179
Figure 7.3	Pressure trace from probe A4 from tests S3 which was a 1.36 kg (3 lb) charge at a height of burst of 1.16 m (46 inches). . . .	180
Figure 7.4	Left, frequency analysis of the pressure trace from test S3 probe A4 before and after filtering. Right, the pressure trace before and after frequency filtering. . . . .	181
Figure 7.5	The frequency filtered pressure trace from test S3 probe A4 fit to the Friedlander equation via the two step process. . . . .	182
Figure 7.6	The unfiltered pressure trace from test S3 probe A4 fit to the Friedlander equation via the two step process. . . . .	182
Figure 7.7	Peak pressure values for the 4 spherical test configurations. 'B' are the base line tests, 'E' are the elevated tests, 'L' are the light tests and 'H' are the heavy tests. . . . .	184
Figure 7.8	Pulse duration values for the 4 spherical test configurations. 'B' are the base line tests, 'E' are the elevated tests, 'L' are the light tests and 'H' are the heavy tests. . . . .	185
Figure 7.9	Decay coefficient, $\alpha$ , for all spherical tests. 'B' are the base line tests, 'E' are the elevated tests, 'L' are the light tests and 'H' are the heavy tests. . . . .	186
Figure 7.10	Experimental impulse for all spherical tests and the uncertainty found by propagating the uncertainties of peak pressure, pulse duration and decay coefficient. 'B' are the base line tests, 'E' are the elevated tests, 'L' are the light tests and 'H' are the heavy tests. . . . .	187
Figure 7.11	Analytical peak pressure and the Friedlander experimental peak pressure for each test configuration. 'B' are the base line tests, 'E' are the elevated tests, 'L' are the light tests and 'H' are the heavy tests. . . . .	189
Figure 7.12	Pressure trace from the A1 pressure probe from the S2 test which is a baseline configuration. The Friedlander fit and resulting peak pressure is shown along with the analytical peak pressure. . . .	190
Figure 7.13	R is the pressure trace from the A3 pressure probe from the S2 test which is a baseline configuration. The reflection at this location was analytically predicted to be a regular reflection. I is the pressure trace from the A6 pressure probe from the S2 test which is a baseline configuration. The reflection at this location was analytically predicted to be an irregular reflection. The Friedlander fit and resulting peak pressure is shown along with the analytical peak pressure. . . . .	191

Figure 7.14 Analytical peak pressure and the unfitted experimental peak pressure for each test configuration. 'B' are the base line tests, 'E' are the elevated tests, 'L' are the light tests and 'H' are the heavy tests. . . . .	192
Figure 7.15 Streak image from test S4 which was a 1.3 kg (3 lb.) charge. The radial direction is parallel to the reflection plane. . . . .	194
Figure 7.16 Comparison of the experimental, experimental uncertainty, and analytical pulse duration for the 'B' test configuration. . . . .	194
Figure 7.17 Comparison of the experimental, experimental uncertainty, and analytical pulse duration for the 'E' test configuration. . . . .	195
Figure 7.18 Streak image from test S6 which was a 0.45 kg (1 lb.) charge. The radial direction is parallel to the reflection plane. . . . .	196
Figure 7.19 Comparison of the experimental, experimental uncertainty, and analytical pulse duration for the 'L' test configuration. . . . .	197
Figure 7.20 Plot of the decay coefficient $\alpha$ for all the kilogram scale sphere tests as a function of scaled radius. The power fit to the data is shown with the resulting parameters. . . . .	198
Figure 7.21 Comparison of the reflected decay coefficient $\alpha$ between the gram and kilogram scale test series. Only the radius has been scaled using Sachs scaling. The power fits are also shown. . . . .	199
Figure 7.22 Comparison of the scaled reflected decay coefficient $\alpha$ between the gram and kilogram scale test series. Both the $\alpha$ term and radius have been scaled. The power law fits are also shown. . . . .	201
Figure 7.23 The combined gram and kilogram scaled data of the reflected decay coefficient $\alpha$ and resulting power law fit. Both the $\alpha$ term and radius have been scaled. . . . .	201
Figure 7.24 The combined gram and kilogram scaled data of the reflected decay coefficient $\alpha$ and resulting power law fit with two $\alpha$ curve from literature shown. Both the $\alpha$ term and radius have been scaled. . . . .	202
Figure 7.25 Comparison between the experimental and analytical impulse for the 'B' test configuration. The impulse is undefined below the maximum product expansion. . . . .	204
Figure 7.26 Comparison between the experimental and analytical impulse for the 'E' test configuration. . . . .	205
Figure 7.27 Comparison between the Friedlander experimental and analytical impulse for the 'L' test configuration. . . . .	206
Figure 7.28 Comparison between the experimental and analytical impulse for the 'L' test configuration. The peak pressure term is the unfitted peak pressure. . . . .	206

This thesis is accepted on behalf of the faculty of the Institute by the following committee:

Michael J. Hargather

---

Academic and Research Advisor

Michael J. Hargather

---

Jamie Kimberley

---

Seokbin Lim

---

William Stone

---

I release this document to the New Mexico Institute of Mining and Technology.

Kyle Oakley Winter

January, 2021

---

# CHAPTER 1

## INTRODUCTION

### 1.1 Research Motivation

Frequently in explosive applications, an explosive charge is detonated at some height above the ground or a reflecting surface, resulting in a shock wave reflection from a surface. The manner in which the shock wave reflects from the surface affects the overpressure and impulse generated on the reflecting surface. Ernst Mach first described irregular reflections and identified that they generate higher overpressures than regular reflections [1]. Since then, experimental and numerical studies have focused on defining shock wave reflections in supersonic wind tunnels and for planar shock waves. Prior work has developed a physical basis for the transition between regular and irregular reflections for steady and pseudo-steady shock wave applications. The majority of prior research on shock wave reflections, however, has not explored the common case of unsteady, i.e. explosively-driven, shock wave reflections. Applying current shock wave reflection theory to unsteady shock waves and experimentally validating the analytical theory are the primary goals of this research.

### 1.2 Literature Review

#### 1.2.1 Overview and History of Shock Wave Reflections

In 1878, Ernst Mach used spark gaps to generate two shock waves simultaneously over a soot covered plate and, for the first time, recorded an irregular shock wave reflection [1]. Through his study of how shock waves disturb soot covered plates, he established that these irregular reflections generated higher pressures than regular reflections and provided an early description of the transition parameters between regular and irregular reflections [1]. In 1943 von Neumann proposed the main structural elements for both regular reflections and Mach reflections: zero net deflection across the regular reflection, and a slipstream separating two flow fields behind the Mach reflection [2]. He also suggested transition criteria between regular and irregular reflections [3]. This theoretical work was expanded by Kawamura and Saito in 1956 by plotting the possible states for the shock waves in a reflection as a function of total deflection angle and pressure

[4]. This technique, known as shock polar analysis, simplifies the analysis of the formation of shock wave reflections [3]. These early advancements developed the most important tools and ideas used in the current study of shock wave reflections. Detailed reviews of the development of shock wave reflection theory can be found in works published by Griffith [3], Pack [5], and Ben Dor [6].

The present work focuses on four kinds of shock wave reflections: regular, single Mach, transitional Mach, and double Mach reflections. The basic shock diagrams of each type of reflection are shown in Figure 1.1. In Figure 1.1 the incident and reflected shocks are shown as straight for simplicity but are curved for explosively driven shocks. The regular reflection, Figure 1.1a, can be identified as two oblique shocks, the incident and reflected shocks, that meet at the reflection surface. The single Mach reflection, Figure 1.1b, is comprised of 3 shocks: the incident and reflected shocks, and the shock that connects the two shocks to the surface, a Mach stem. The slip line that originates at the point where the three shocks meet, the triple point, may be visible in refractive images and is not required for identification. The transitional Mach reflection, Figure 1.1c, is very similar to a Mach reflection except that a portion of the reflected shock has straightened out into what is referred to as the kink. A transitional Mach reflection can be identified by the sharp transition from the kink to the reflected shock. The double Mach reflection, Figure 1.1d, can be identified by a second Mach stem originating at the kink and pointing towards the reflection surface. The second Mach stem terminates at the slip line originating from the first triple point. The termination point of the second Mach stem may occur at the reflection surface.

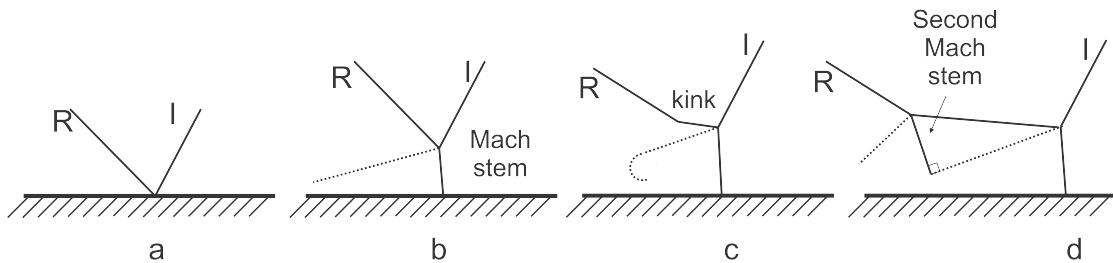


Figure 1.1: Wave diagram of the 4 types of reflections for an oblique shock wave traveling from left to right interacting with a solid reflecting surface. a) Regular reflection which has two waves. b) Mach reflection which can be identified by a single Mach stem. c) Transitional Mach reflection which has a "kink" in the reflected shock. d) Double Mach reflection which has two Mach stems. The incident (I) and reflected (R) shocks in each reflection is indicated

### 1.2.2 Shock Reflection Types

The regular shock wave reflection was named based on its similar behavior to reflections of acoustic waves. Like an acoustic wave, the shock wave impacts a

reflecting surface at some angle. The shock wave is then reflected from the point of impact at a similar angle. For this and other reasons, prior to the contributions of Mach and Sommer, it was believed that shock waves were just stronger acoustic waves [1, 7]. Through his study of shock wave traces, Mach was able to determine the general shape of regular reflections (RR) [1]. The boundary conditions used to define regular reflections proposed by von Neumann, completed the modern understanding of regular reflections [8]. Figure 1.2a schematically shows a regular reflection. In a steady frame of reference, like a wind tunnel, the incident shock (I) deflects the flow towards the reflecting surface with the exact angle of the deflection dictated by the flow Mach number and angle of the shock relative to the flow. The reflected shock (R) then deflects the flow back to parallel with the initial flow. The exact angle of the reflected shock can be determined using shock polar analysis or by solving the two-dimensional compressible flow equations [4, 9].

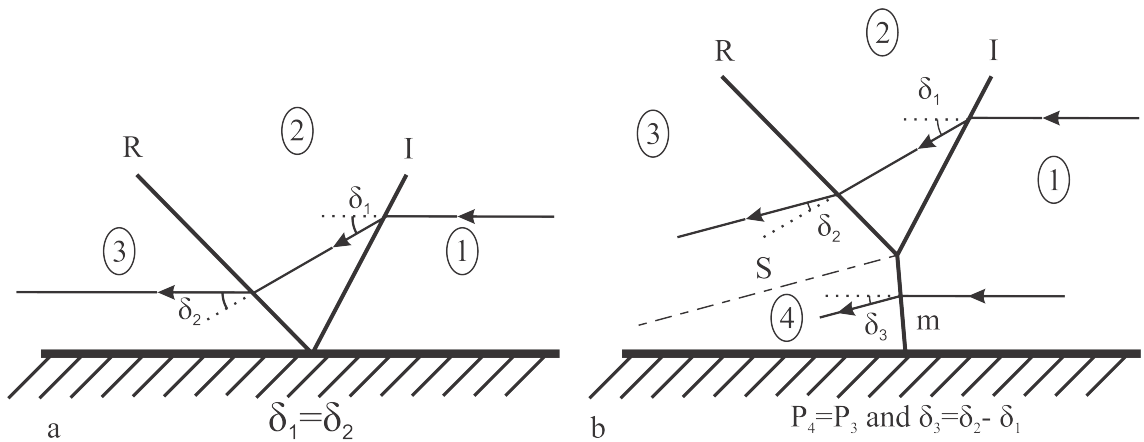


Figure 1.2: Schematic representation of (a) regular and (b) singular Mach reflections. In a regular reflection, the initial (I) and reflected (R) shock meet at the reflecting surface, resulting in a new zero deflection of the flow. Single Mach reflections include a third shock wave, the Mach stem (m), which connects the reflecting surface to the intersection of the initial and reflected shock waves. Here the shock is assumed to be steady and the flow propagates toward the shock from right to left.

The term irregular reflection (IR) is used to describe all shock wave reflections other than the regular reflection. The simplest irregular reflection, referred to as a Mach reflection or single Mach reflection since at least 1944 [10], is comprised of a initial shock and reflected shock connected to the reflecting plane via a third shock, the Mach stem (m), and a slip line (S) separating the flow processed by the reflected shock and Mach stem. This structure was first predicted by von Neumann in 1943 and first recorded with schlieren and shadowgraph photography in 1945 [8, 11]. The Mach reflection was believed to be the only other reflection type until the recording of a transitional-Mach reflection (TMR) by Smith in

1945 [11]. A transitional-Mach reflection, shown in Figure 1.3a, is differentiated from a Mach reflection by two key features: a kink (k) in the reflected shock and a slip line (S) that points towards reflection surface and curls into a recirculation zone [6]. In 1952 the double Mach reflection (DMR) was first described by White [12]. The double Mach reflection, which is shown in Figure 1.3b, is distinguished by its second Mach stem which intersects with the first slip line. These three shock wave reflections, Mach, transitional-Mach, and double Mach reflections, along with the weak shock reflections, discussed later, comprise the main divisions of irregular reflections that have been observed. A review in 1979 compiled experimental data to map irregular reflections type as a function of Mach number and angle for pseudo-steady planar shock waves [13].

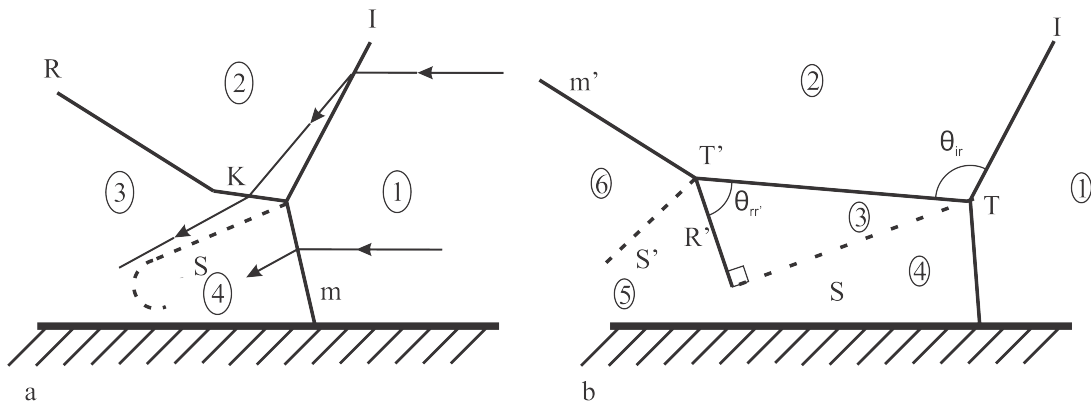


Figure 1.3: a) Transitional Mach reflection where the initial shock wave is connected to the Mach stem but the reflected shock is connected to the Mach stem via a smaller shock referred to as the kink. b) Double Mach reflection where a second Mach stem connects the second triple point to the end of the first slip stream. The shock wave is in the steady frame of reference with flow propagating from right to left.

### 1.2.3 Transition Between Shock Reflections

In the early 1940's von Neumann proposed two transition criteria from regular to irregular reflections based on pressure matching or maximum deflection [2, 8, 14]. The criterion he proposed for strong shocks, what is today called the mechanical equilibrium criterion, stated that the reflection type will transition when the pressure behind a regular reflection is equal to the pressure of a normal shock in same flow [3, 6]. This criterion only occurs for shock reflections with a initial Mach number greater than 2.2 so a second criterion was proposed for weak shocks. The transition point for low Mach numbers, later named the detachment criterion, was proposed to be the point of maximum deflection after which the

shock wave would become detached [3, 6]. Early investigations by Bleakney and Taub in 1949 used schlieren and shadowgraphy to study the transition conditions and found discrepancies at low Mach numbers. This study found that at low Mach numbers regular reflections persisted beyond what was expected by von Neumann's transition criteria and what they believed to be Mach reflections occurred in conditions not allowed by three shock theory [15]. This apparent deviation from two and three shock theory was given the name "the von Neumann paradox" [16].

Since the discovery of the von Neumann paradox in 1949, substantial research was devoted to finding an accurate transition criteria between regular and irregular reflections. The first breakthrough was in 1990 when Colella and Henderson used high resolution numerical simulations to show a new reflection type, which they named the von Neumann reflection, that could be easily mistaken for a Mach reflection [17]. In this new reflection type the initial shock and Mach stem were not two distinct shock waves but blurred together at the apparent triple point. The reflected shock of the von Neumann reflection did not meet at the apparent triple point but was connected by a series of compression waves. The next advancement in solving the paradox was in 1999 when Vasilev et. al. used numerical simulations to demonstrate a four-shock structure reflection, first proposed in 1947 [18, 19]. This reflection was experimentally demonstrated in 2005 and named the Guderley reflection after the scientist that originally predicted it [20]. Vasilev's 1999 paper also suggested a third region of weak reflection between von Neumann and Guderley reflection, which is referred to as Vasilev reflection. The discovery of the three additional types of shock reflections: the von Neumann reflection, Guderley reflection, and Vasilev reflection, showed that the von Neumann paradox, rather than being a problem within three shock theory's description of Mach reflections, was a separate domain of irregular reflections, now known as weak-shock wave reflections [6].

Variations of the transition criteria between reflections types have been continuously studied since discrepancies were discovered between von Neumann's criteria and experimental results in 1949 [15]. Over time, the two-stage transition criteria proposed by von Neumann was replaced with only applying the detachment criteria. Under which, the transition to irregular reflections occurs at the point of maximum deflection of a regular reflection [21]. Further experimental shock tube investigations showed the detachment criteria to not accurately predict the regular to irregular transition at low Mach numbers [15]. This led to further examination and the suggestion by Henderson and Lozzi in 1975 that the criteria was non-physical [22]. At the transition point predicted by the detachment criteria, there is a pressure difference between a regular and Mach reflection. They argued that if this criteria were physical, then upon transitioning, a compression or rarefaction wave would be propagated through the flow, which was not found in experimental data [4]. This led Henderson and Lozzi to suggest the mechanical equilibrium was the correct transition criteria [22]. Their conclusion was accepted for steady cases but not for pseudo-steady [3]. A modification to the detachment criteria was the sonic criterion, which stated that transition occurred when the velocity behind the reflections exceeded the speed of sound.

The transition angle between the sonic and detachment criteria was within a few degrees, which was below the uncertainty of most experiments [23]. Lock and Dewey were able to remove this limitation by precisely measuring the speed of sound behind the shock wave, and were able to show that in low Mach number pseudo-steady cases, the regular to irregular transition occurred at the sonic condition [24].

In 1979 the mechanical equilibrium and sonic conditions were combined into the length scale criterion [25]. This theory was based on the fact that a regular reflection does not have a finite length scale, the initial and reflected shock can extend indefinitely while being self similar, whereas the Mach stem of a Mach reflection has a finite length that is dependent on the physical system causing the reflection. Because the Mach stem has a fixed height for a Mach reflection to form, a signal must be transmitted between the point defining the length scale and the reflection. For a pseudo-steady reflection, this can only occur when the Mach number behind the shock is at or below the speed of sound. For reflections in steady flow, the length scale signal can be transmitted at all Mach numbers so a Mach reflection will occur whenever possible. Thus using the length scale criterion, regular to Mach reflection transition in pseudo-steady flows will form according to the sonic condition, whereas in steady flows, reflections will transition according to the mechanical equilibrium condition[6].

The length scale criterion was able to accurately describe transition between regular and Mach reflection but was unable to describe the transition between, or growth of, transitional-Mach and double Mach reflections. It was observed in the mid 1990's that complex irregular reflections, specifically transitional-Mach and double Mach reflections, can have a delay in formation, resulting in misidentification of the final reflection type for experiments in shock tubes with short test sections [26, 27]. The misidentification of reflection type resulted in the theoretical transition point for transitional-Mach and double Mach reflections not matching experimental results. The resolution was found in work initiated 20 years prior by treating the reflection process as the combination of two sub processes: the shock-reflection process and the flow-deflection process [28, 29]. The new process, referred to as the "Shock-Diffraction Process", examines the flow around the reflection as well as the flow down-stream from the reflection to determine the exact reflection type that will form and is the current state of the art for determining which shock wave type will occur in a strong shock wave reflection [6].

#### **1.2.4 Galilean Frame of Reference Transformation**

In the steady frame of reference, the deflection of flow can be simply predicted as it moves through the shocks in a regular reflection. In the case of a moving planar shock wave, the path of the gas through the shock reflection is difficult to calculate. To simplify the calculations, the frame of reference is shifted from a laboratory (Lagrangian) frame of reference, where the shock is moving

into stagnant gas, to a fixed shock frame (Eulerian) of reference, where the shock wave is fixed and the gas moves into the shock. The reference frame transformation, which is shown in Figure 1.4, was proposed by von Neumann and is referred to as a Galilean transformation [6, 8, 30].

Figure 1.4 show two equivalent regular shock wave reflections. In Figure 1.4a, the laboratory reference frame, a normal shock wave that is propagating horizontally encounters a "wedge" up which the normal shock wave travels creating a reflected shock wave. In Figure 1.4b, the pseudo-steady frame of reference, the flow is parallel with the wedge/reflecting surface. For a regular reflection in the laboratory frame of reference, the direction of the flow relative to the initial shock is given by:

$$\phi_1 = 90^\circ - \theta_W \quad (1.1)$$

where  $\phi_1$  is the angle between the direction of flow and the initial shock and  $\theta_W$  is the wedge angle. The effective Mach number of the shock wave in the laboratory frame of reference is given by:

$$M_S = M_1 \sin(\phi_1) \quad (1.2)$$

where  $M_S$  is the initial Mach number of the shock wave before the transformation and after the transformation  $M_1$  is the Mach number of the flow before the shock, in region 1. For irregular reflections, the flow relative to the initial shock is given by:

$$\phi_1 = 90^\circ - (\theta_W + \chi) \quad (1.3)$$

$$\phi_3 = 90^\circ - \chi \quad (1.4)$$

where  $\chi$  is the trajectory of the triple point, which is the junction of the initial, reflecting, and Mach stem shock waves, and  $\phi_3$  is the wave angle of the Mach stem.

For a planar shock moving over constant angled surfaces, the transformed frame of reference is referred to as pseudo-steady, because the flow immediately around the intersection can be treated as steady [31]. For many other geometries such as a planar shock over a changing angle or a curved shock over a constant angle, this coordinate transformation simplifies analysis but does not result in a pseudo-steady flow. In these cases no frame of reference can be used to describe the flow as steady or pseudosteady, thus they are referred to as unsteady [32].

### 1.2.5 Multiple Reflections and Complex Geometries

The majority of shock wave reflection studies have focused on a planar shock wave over a single wedge, but recently significant work has studied the reflection

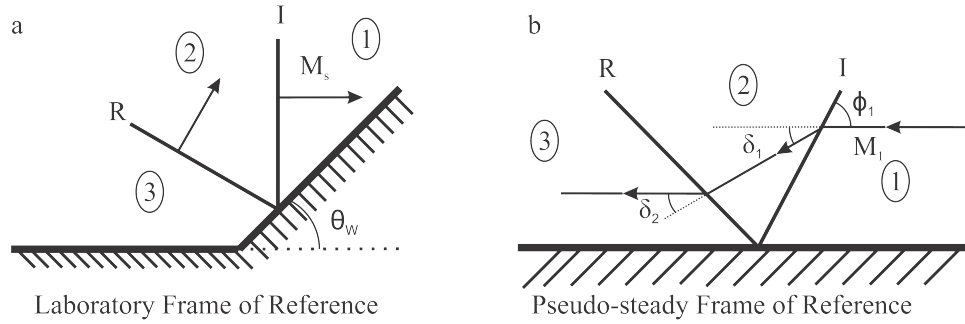


Figure 1.4: Diagram of Galilean transformation of regular reflection from the (a) laboratory to the (b) pseudo-steady frame of reference.

of planar shock waves over increasingly complex geometries. The first study of this kind was of the reflection of a shock wave over a cylinder in 1969 [33]. The continually varying angle of the cylinder resulted in an unsteady reflection process and an interesting progression of reflections types. Later work simplified this problem by focusing on the reflection of a planar shock over a double-wedge system [34]. This allowed for an analytical model for regular and Mach reflections to be developed for the double-wedge system [35]. This model used the transition criteria for a shock over a single wedge to predict the reflection structure that would form at the point of inflection and in the far field away from the inflection point. It was also shown that a pressure spike or dip would occur at the inflection point, depending on whether the second wedge had a larger or smaller angle respectively [23]. Increasing the complexity of the system by inclusion of complex irregular reflection, more complex geometries, or both, generates ever-more complex reflections which require more complex models to describe [36, 37, 38]. As of present, no single theory has been able to fully describe these systems.

When a shock wave impinges on another shock wave, it generates a reflection similar to if a rigid reflecting surface was placed at the symmetry plane between the shock waves. This phenomenon was how Mach first visualized irregular reflections over his soot covered plates[1]. Reflections of equivalent shock waves were first shown to be equivalent to a reflecting surface in 1959[39]. How this redistributes the energy of explosive blasts has been studied in large scale experiments and computational simulations[40, 41]. Recent computational studies have investigated using shock-shock reflections as a way to focus explosive effects [42, 43, 44].

### 1.2.6 Refractive Imaging Techniques

Refractive imaging systems are used to image differences in the refractive index of a material located within a test section. Schlieren and shadowgraph are two common refractive imaging techniques and were first described in the 17th

century by Robert Hooke. Schlieren was rediscovered in the 1900s by August Toepler and has since been used widely for high-speed wind tunnel testing and laboratory investigations of explosives [45].

A traditional lens-type schlieren imaging system, shown schematically in Figure 1.5, uses a simple parabolic lens to collimate light from a point source. The parallel light passes through the test section and enters a second lens, which focuses the light to a point. A knife edge is placed at the focal point and a camera is placed behind the knife edge. When a refractive object enters the test section, it bends the collimated light causing more or less interaction with the knife edge. The camera records the refractive index gradient as a gradient of bright to dark areas in the image. A schlieren image of a lighter is shown in Figure 1.6. The figure demonstrates the sensitivity and resolution with which a schlieren system can capture a refractive object. This system is also capable of quantitatively measuring the refractive-index distributions within the test section yielding the density of the flow with some limiting assumptions [46]. The diameter of the test section is limited to the diameter of optics used. Lens schlieren systems are generally limited to 15 cm diameter due to cost of the lenses [47].

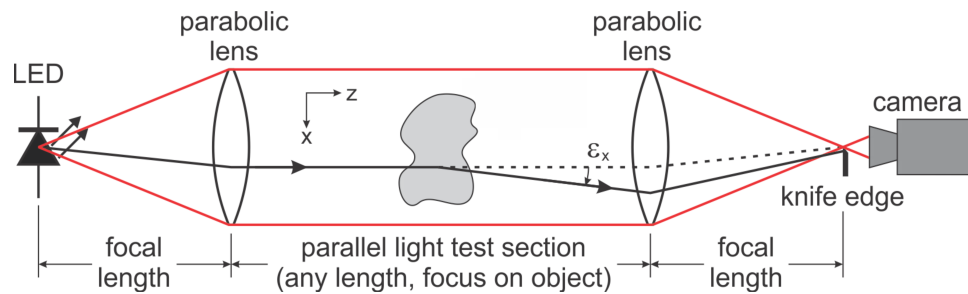


Figure 1.5: Diagram of typical lens schlieren system with light ray paths shown.

A practical method to assemble a larger scale schlieren imaging system is to use mirrors. In a Z-type schlieren system, which is shown schematically in Figure 1.7a, parabolic mirrors replace the lenses for collimating the point source illumination and refocusing the light [45]. A similar system can be produced with only a single spherical mirror using a double pass arrangement, which is shown in Figure 1.7b. In this system the point light is passed through a beam splitter and onto the mirror. The light is then returned to the beam splitter where it is directed on a different path to a camera. The double-pass, diverging nature of the system makes quantitative measurements difficult or impossible but these systems have been shown to be very sensitive and useful for visualizing shock waves [48].

Shadowgraph systems are capable of imaging much larger areas than schlieren because no collimating optics are required, but shadowgraphy lacks the sensitivity and ability for quantitative density measurements that are possible with schlieren [47]. The difference between the two visualization approaches can be observed in Figure 1.6: schlieren visualizes refractive index gradients and thus has a smooth variation from light to dark areas, whereas shadowgraph visualizes

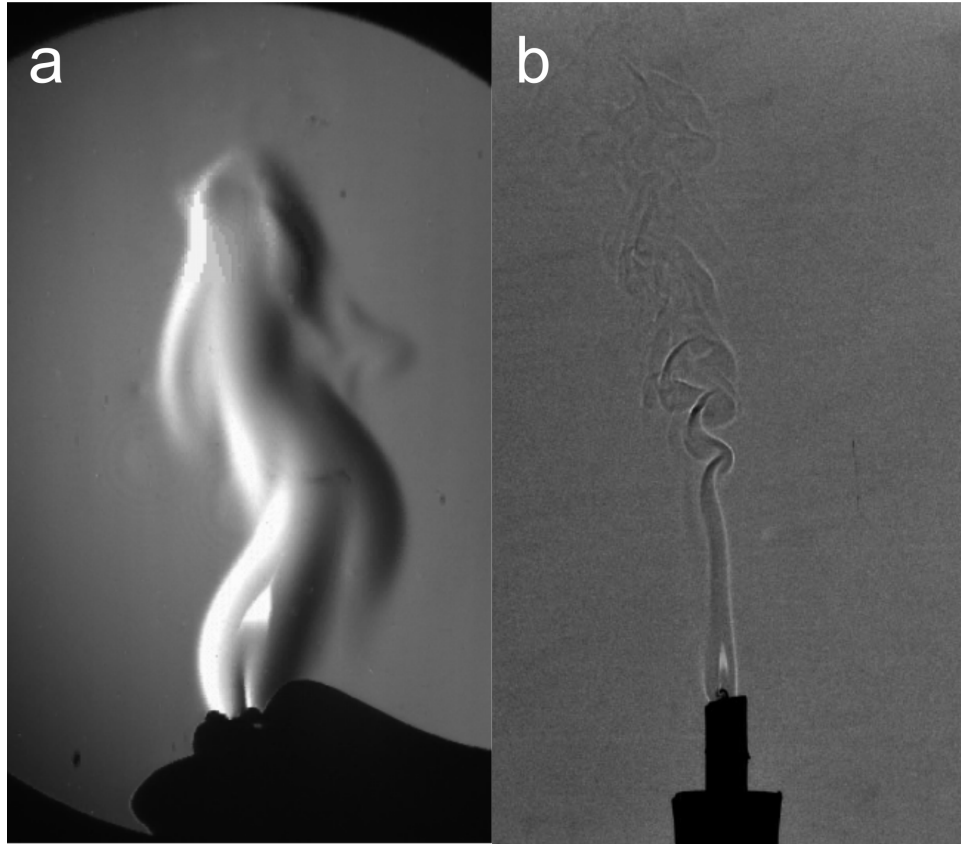


Figure 1.6: (a) Schlieren image of a lighter utilizing a vertical knife edge. (b) Retro-reflective shadowgraph of a candle.

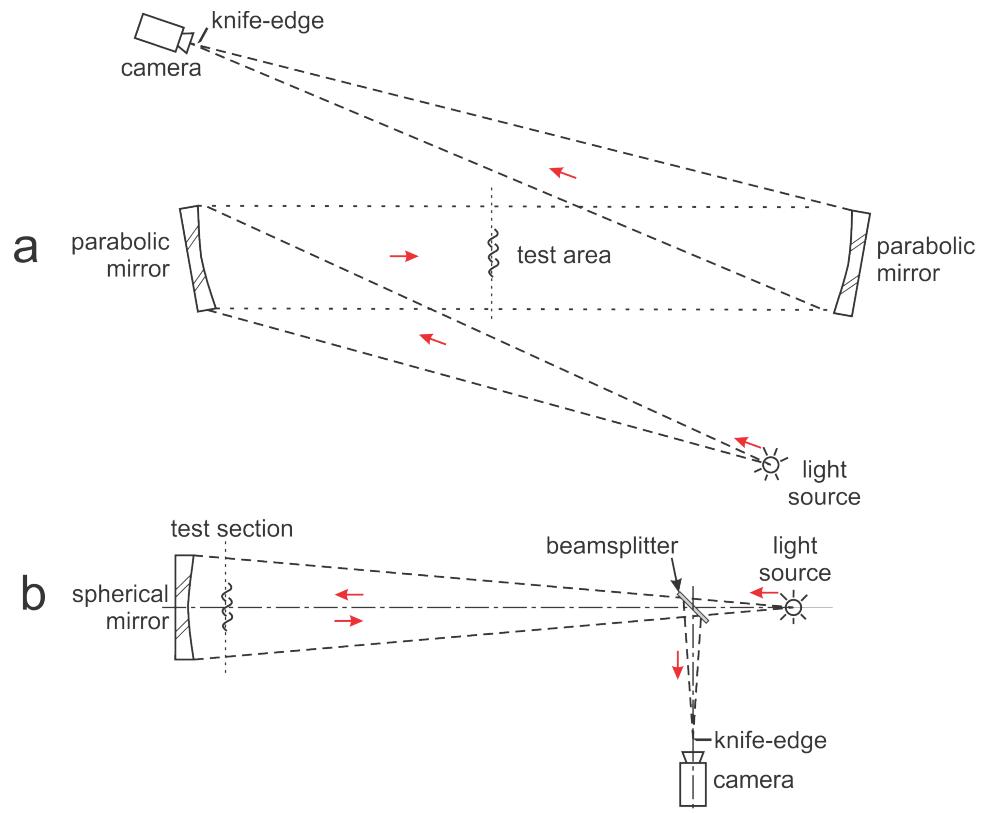


Figure 1.7: a) Diagram of Z type schlieren system made with two parabolic mirrors. b) Diagram of coincident schlieren system using only one spherical mirror

the second derivative of refractive index field and thus has sharp variations from light to dark at edges of the candle plume.

The modern retro-reflective shadowgraph system used for high speed imaging was developed in 1958 by H. E. Edgerton [49]. The system consists of a high intensity light source that is projected onto a retro-reflective screen. When a refractive object is placed between the light and screen, it distorts the path of the light rays, casting a shadow of the object on the screen. This effect is shown in Figure 1.8. A camera placed near the light source is then able to record the image on the screen. The first documented use of this system was the imaging of the shock wave from a "dynamite cap" [49]. This technique has been revived in recent works to be used again for explosive testing [50, 51]. The main advantage of the system is that it can be economically scaled up to a 2.5m by 2.5m test section. The larger test section allows for the study of refractive objects too large to be imaged with a traditional schlieren system, such as explosively driven fragments and firearms [47]. Increasing the size of the test section beyond this becomes technically challenging due to the need for a point light source in excess of 1 kilowatt and a retroreflective screen to provide the background. Larger systems have been demonstrated up to about 5 m by 5 m [52], but this can be challenging to illuminate with microsecond exposures. In general, the components of the retroreflective shadowgraph system can be easily damaged by explosive fragments. This fragility and the limited test section size, limit the explosive articles that can be imaged within a shadowgraph system without damaging components.

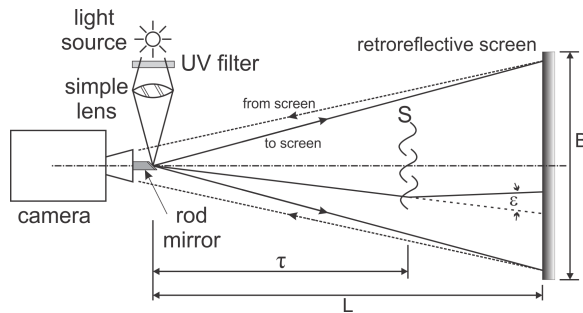


Figure 1.8: Diagram of rod mirror retro-reflective shadowgraph system with light ray paths shown.

Background oriented schlieren (BOS) is a modern refractive imaging technique that visualizes refractive objects via their distortion of a distant background [53]. BOS typically has a lower resolution and sensitivity than schlieren or shadowgraph but has no limitation on the area it can image. The phenomenon that BOS utilizes was first noticed by Schardin in 1942, but it was not until 60 years later that the digital imaging and image processing technology ideal for the modern technique was commonly available [47, 54]. The modern BOS technique was simultaneously developed by Dalziel et al. [55] and Meier [56] in 1998-1999 and was recently reviewed by Raffel [53].

An advantage of BOS systems is their simplicity in setup. The two require-

ments for a BOS system are a camera at a fixed location and a background opposite the camera. BOS systems typically utilize a speckled background to provide the high contrast and spatial frequency needed. The speckle pattern is typically applied with dye or paint or projected with a laser system [53]. It was shown by Raffel et al. [57], Kindler et al. [58], and Hargather et al. [59] that many naturally occurring landscapes contain sufficient spatial frequency to be used as a background for BOS images. The camera is used to record a reference image of the background. A refractive object is then placed in the field of view of the camera, as is shown in Figure 1.9, and the camera records a second image. The density variation within the field of view will cause the apparent location of features in the background to shift. The location of the object is an important factor in the sensitivity of the BOS system. The sensitivity of the system is defined as the minimum angle  $\epsilon$ , in Figure 1.9, or the smallest density gradient the camera is able to detect [59, 60]. The exact sensitivity can be calculated using:

$$\epsilon = d / (L - \tau) \quad (1.5)$$

in which  $\epsilon$  is the sensitivity or smallest angle of refraction the system can detect,  $d$  is the apparent feature shift,  $L$  is the distance from the background to camera and  $\tau$  is the distance from the refractive object to the camera [46, 61]. The sensitivity of a BOS system can be generally improved by minimizing the ratio  $\tau/L$  while keeping the object and background in clear focus [46]. In practice it has been found that a  $\tau/L = 0.5$  gives the optimum sensitivity and performance [60].

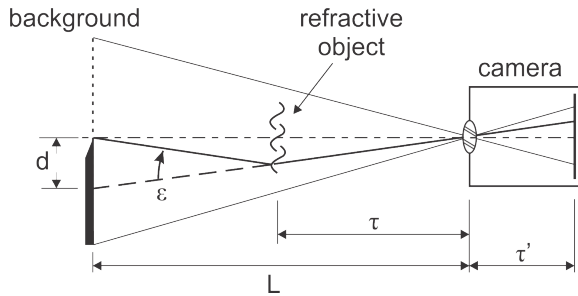


Figure 1.9: Diagram of typical BOS system with light ray paths shown.

There are multiple methods that can be used to detect and quantify the background shift between the two images and generate BOS images. The first method used to process BOS images uses cross correlation algorithms to detect and quantify the movement of background patterns between images. This processing is similar to the algorithms used in particle image velocimetry (PIV) or digital image correlation (DIC) softwares, and many commercial softwares can be used directly to perform BOS analysis [62]. This method produces BOS images that show the shape and structure of the refractive object as well as quantify the direction and magnitude of the pixel displacement and is optically equivalent to a schlieren image [58]. The cross correlation method does have inherent drawbacks such as a reduction in resolution and high computational time.

Another method for BOS processing is image subtraction. Image subtraction compares the pixel intensities between the two images to detect refractive disturbances [59]. This method has higher resolution and lower computational time than the cross correlation method because it is performed on a pixel-by-pixel basis, but it is unable to determine the magnitude or direction of the pixel displacement. BOS image subtraction was first used to study explosive shock waves in 2008 by Sommersel et al. [63]. The BOS image subtraction process was then improved for shock wave detection by Mizukaki et al. [64], and Hargather et al. [59]. This technique has been used to study explosive shock waves from charges ranging from  $10^{-3}$  kg to  $10^3$  kg [59].

### 1.2.7 Shock Wave Propagation in Air

The scaled time-radius curve of a shock wave propagating through air is a fundamental property of an explosive material, an idea first proposed in 1915 by Hopkinson [65]. Thirty years later in 1944, this idea was expanded by Sachs to include effects of atmospheric conditions [66]. The Sachs' scaling equations are defined as:

$$R_s = \frac{R}{S} \quad (1.6)$$

$$t_s = \frac{ct}{S} \quad (1.7)$$

$$S = \left(\frac{W}{W_0}\right)^{\frac{1}{3}} \left(\frac{101.325}{P_{atm}}\right)^{\frac{1}{3}} \quad (1.8)$$

$$c = \left(\frac{T}{288.16}\right)^{\frac{1}{2}} \quad (1.9)$$

where  $T$  is the atmospheric temperature in Kelvin,  $P_{atm}$  is atmospheric pressure in kPa,  $W$  is the mass of an explosive article and  $W_0$  is the reference mass. These are used to determine scaling factors  $S$  and  $c$  [67]. These scaling factors can be used to estimate an explosive's effects, such as the shock radius  $R_s$  and time  $t_s$ , across different explosive weights. Sachs' scaling has been shown to hold over a wide range of explosive masses ranging from  $10^{-6}$  kg to  $10^6$  kg [67]. This scaling also allows the influence of atmospheric conditions to be removed so tests can be reported at standard temperature and pressure (STP,  $P_{atm} = 1 \text{ atm}$ ,  $T = 298 \text{ K}$ ).

Historically the shock wave time-radius curve has been reported graphically or as a large table. In 1971 Dewey proposed using the least squares method to fit the radius of a shock wave to a parametric equation [68]. This empirically derived equation was written so that the shock wave would have a defined initial radius  $A$  and its velocity would decay to a defined velocity  $B$  at infinite time  $t$ :

$$R_s = A + Ba_0t_s + C\ln(1 + a_0t_s) + D\sqrt{\ln(1 + a_0t_s)} \quad (1.10)$$

with additional  $C$ ,  $D$ , and ambient sound speed  $a_0$  [69]. In practice the coefficient  $B$  is typically set to 1 to force the wave speed to decay to the local sound speed. The parameters  $A$ ,  $C$ ,  $D$  are determined by fitting the shock radius time data to the equation using a non-linear regression [67]. When reporting these parameters, it is important to also report the range over which they were determined. This is done to prevent extrapolating the data into areas where it may not be valid, as with this multi-parameter curve fit, non-physical results are easily found outside the range of data. An advantage of this method is that the Dewey equation can be differentiated, with respect to time:

$$\frac{dR_s}{dt_s} = Ba_0 + \frac{Ca_0}{1 + a_0t_s} + \frac{Da_0}{2(1 + a_0t_s)\sqrt{\ln(1 + a_0t_s)}} \quad (1.11)$$

which yields velocity as a function of time. This equation can be used to plot Mach number as a function of radius by parametrically varying time in the two equations. Mach number  $M$  is given by:

$$M = v/a_0 \quad (1.12)$$

where  $v$  is velocity.

The Mach number of a shock wave can be used to calculate the pressure ratio across the shock wave, which is given by:

$$\frac{P_b}{P_a} = \frac{2\gamma(M^2 - 1)}{\gamma + 1} \quad (1.13)$$

where  $\gamma$  is the ratio of the specific heats for the gas in which the shock is propagating,  $P_a$  is the absolute pressure before the shock,  $P_b$  is the absolute pressure after the shock wave, and  $M$  is the Mach number of the shock wave [70].

Immediately after the shock, the pressure begins to decay back to atmospheric pressure. The integral of pressure from the peak pressure at the shock to when the overpressure reaches zero is impulse.

The pressure across an expanding or explosively-driven shock wave is frequently measured experimentally using piezoelectric gauges. The peak overpressure value is often taken as the highest value in the pressure trace. Due to the limited response time of pressure transducers, this value is often greater than the true peak pressure [70]. This results in a signal that oscillates around the true value and in a larger uncertainty in the peak pressure value than the error reported by the manufacturer for a given pressure transducer. One method to improve the accuracy of the pressure trace from a shock wave is to use regression analysis to fit the pressure trace to the Friedlander Equation:

$$P(t) = P_s e^{\frac{-\alpha t}{t_d}} \left(1 - \frac{t}{t_d}\right) \quad (1.14)$$

where  $P(t)$  is the pressure at time  $t$ ,  $P_s$  is the peak pressure,  $t_d$  is the time at which the pressure first crosses the horizontal axis and  $\alpha$  is a curve fitting parameter [71]. This equation can be integrated from the time of arrival to the pulse width with respect to time to give impulse per unit area [70].

$$I/A = \int_0^{t_d} P(t) dt = P_s t_d \left[ \frac{1}{\alpha} - \frac{1 - e^{-\alpha}}{\alpha^2} \right] \quad (1.15)$$

### 1.3 Objectives of the Present Research

The literature review shows a lack of research on shock wave reflections of unsteady, explosively-driven shock waves. The majority of previous research has focused on pseudo-steady cases where a planar shock wave impinges on a single wedge. The present research seeks to apply modern shock wave diffraction theory to unsteady, explosively-driven shock wave cases to accurately predict the reflection type, overpressure, and impulse as a function of charge height and Mach number. An analytical approach will be developed and applied to predict the state of a shock wave reflection as it transitions from regular reflection to irregular reflection for the case of a spherical explosively-driven shock wave. The analytical methodology will be applied to understand explosively-driven shock waves impinging on a flat plate from various heights of burst. This will be compared with experimental results from gram-scale explosive tests.

The secondary goal of this work is to predict the impulse from unsteady explosively-driven shock wave reflections. An hybrid analytical, computational, and experimental approach will be developed and applied to predict the pulse duration and decay coefficient of a shock wave reflection. The peak overpressure, found through the analytical reflection methodology, will be combined with the pulse duration and a decay term within the Friedlander equation to predict impulse. This will be compared with experimental results from gram-scale explosive tests.

The final goal of this work is to evaluate how the developed methodologies work for different explosive materials and explosive masses. The methodologies will be compared with experimental results from kilogram-scale explosive tests. An assessment of the scaling between gram and kilogram tests will be conducted.

## CHAPTER 2

### ANALYTICAL APPROACH TO SHOCK WAVE REFLECTIONS

The analytical approach to shock wave reflections developed here uses information from the experimental setup to define the shock reflection type that will occur. The analytical approach uses two parameters to fully define a shock wave reflection in air: the Mach number of the shock wave and the angle between the shock wave and the reflection surface. Both of these parameters can be determined at any point in an experimental setup for a well characterized explosive and known geometry. From these two values the reflection type, Mach number of the reflected waves, pressure ratio across the shock waves and Mach number behind the reflection can be determined. This process can be repeated throughout the length of a shock wave path to identify points of transition and inflection of different characteristics.

#### 2.1 Determining Mach number and Reflection Angle

The first step in applying the analytical process at a reflection location is to establish the Mach number and the effective wedge angle at the location. For a characterized explosive the Mach number at any time can be determined using Equation 1.11 or for any radius by using both Equations 1.10 and 1.11. An explosive can be characterized by measuring the shock wave radius as a function of time and fitting that data to the Dewey curve fit, given in Equation 1.10. This characteristic profile can be scaled for different explosive weights and atmospheric conditions using Equations 1.6 through 1.9. For a spherical shock wave, the effective wedge angle,  $\theta_W$ , can be calculated using the shock wave radius, height of burst, horizontal distance and simple geometry as shown schematically in Figure 2.1.

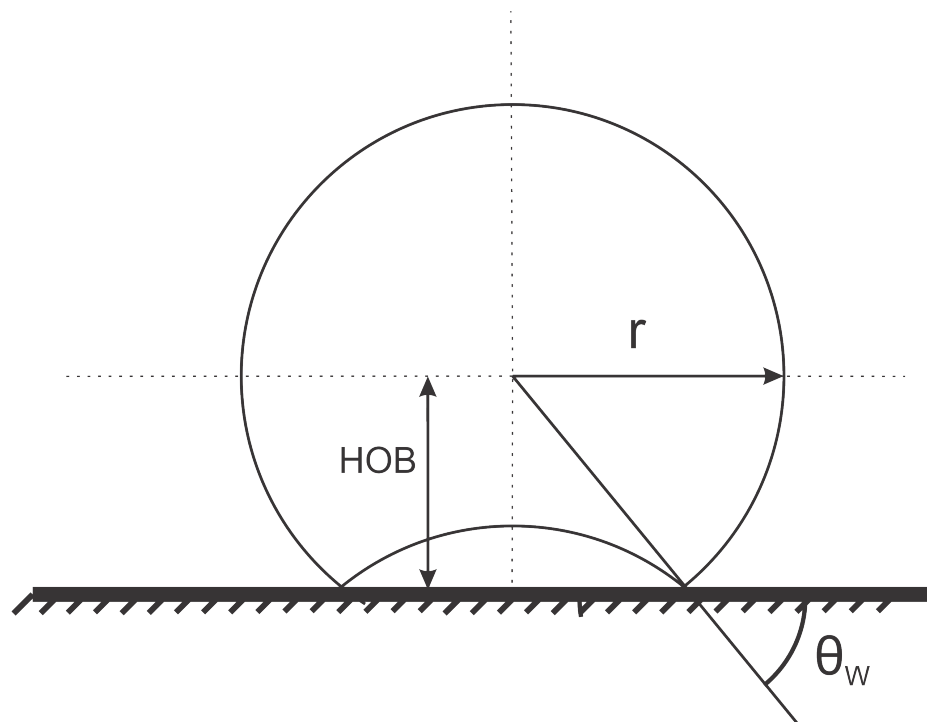


Figure 2.1: Diagram defining the wedge angle,  $\theta_w$ , for an explosive detonated at some height of burst (HOB) from a reflecting surface. Trigonometry is used to calculate the wedge angle for a given HOB and shock wave radius ( $r$ ) at any given time  $t$ .

## 2.2 Regular Reflection

The simplest application of the analytical method is to solve for a regular shock wave reflection. For clarity on the discussion of this analytical approach, a numerical example is solved here to accompany the theoretical discussion. The example uses a shock wave with a Mach number of 3.46 and effective wedge angle of  $30^\circ$ .

The first step is to perform a Galilean coordinate transformation to describe the shock as pseudo-steady. For a regular reflection the Galilean transformation is given by Equations 1.1 and 1.2 which describes the Mach number and wave angle of flow moving into the shock, state 1 in Figure 2.2. The Mach number of the flow after the Galilean transformation,  $M_1$ , is 3.00 with a wave angle,  $\phi_1$ , of  $60^\circ$ .

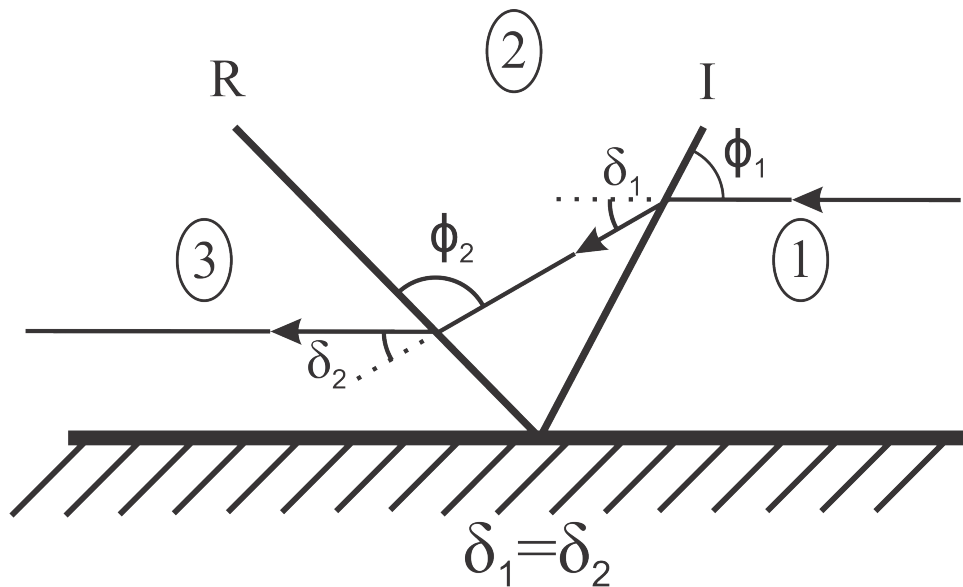


Figure 2.2: Labeled diagram for a regular reflection. With I indicating the incident shock, and R the reflected shock. The number of the state is listed in the oval. The deflection,  $\delta$ , and wave angle,  $\phi$ , is listed for each shock. The boundary condition of equivalent deflection angle is listed at the bottom of the figure.

After the transformation the details of the regular reflection can be found by applying boundary conditions which can be done numerically or graphically. The defining boundary condition for a regular reflection is no net deflection across the reflection, i.e.  $\delta_1 = \delta_2$ .

### 2.2.1 Numerical Solution

This boundary condition can be solved numerically by determining the deflection caused by the first shock and then determining the wave angle of the second shock required to generate the same deflection. The deflection of the flow by an oblique shock wave is given by:

$$\cot(\delta) = \left( \frac{(\gamma + 1)M_a^2}{2(M_a^2 \sin^2 \phi - 1)} - 1 \right) \tan \phi \quad (2.1)$$

where  $\delta$  is the deflection of the flow,  $\gamma$  is the ratio of specific heats,  $M_a$  is the Mach number of the flow before the shock and  $\phi$  is the wave angle between the flow and the shock [72]. Using the above flow conditions of  $M_1 = 3.00$  and  $\phi_1 = 60.^\circ$  the deflection across the incident shock wave,  $\delta_1$ , is  $12.8^\circ$ . The Mach number of the flow changes across the shock wave, given by:

$$M_b^2 = \frac{(\gamma + 1)^2 M_a^4 \sin^2 \phi - 4(M_a^2 \sin^2 \phi - 1)(\gamma M_a^2 \sin^2 \phi + 1)}{[2\gamma M_a^2 \sin^2 \phi - (\gamma - 1)][(\gamma - 1)M_a^2 \sin^2 \phi + 2]} \quad (2.2)$$

where  $M_b$  is the Mach number after the oblique shock [72]. Using the flow conditions, the Mach number after the incident shock,  $M_2$ , is 2.37. The wave angle of the reflected shock,  $\phi_2$ , can then be solved by applying Equation 2.1 to the reflected shock and varying  $\phi_2$  until the deflection caused by the reflected shock,  $\delta_2$ , is equal to the deflection caused by the incident shock,  $\delta_1$ . Solving for the given shock reflection problem, the reflected shock has a wave angle  $\phi_2 = 36.2^\circ$ .

The pressure ratio across the reflection can be determined by applying standard compressible flow equations. The pressure ratio across an oblique shock is given by:

$$\frac{P_b}{P_a} = \frac{2\gamma M_a^2 \sin^2 \phi - (\gamma - 1)}{\gamma + 1} \quad (2.3)$$

where  $P_b$  is the absolute static pressure behind the oblique shock and  $P_a$  is the absolute pressure before the shock [72]. Applying this equation to the example incident shock gives a pressure ratio of 2.46, and across the reflected shock a value of 2.12. The pressure ratio across the entire reflection process is:

$$\frac{P_3}{P_1} = \frac{P_2}{P_1} \frac{P_3}{P_2} \quad (2.4)$$

where  $P_1$  is the pressure in front of the incident shock,  $P_2$  is the pressure behind of the incident shock,  $P_3$  is the pressure after the reflection. Applying Equation 2.4 gives the pressure ratio across the regular reflection of 5.22.

## 2.2.2 Shock Polar Analysis

Shock polar analysis is a graphical method that plots the locus of the shock wave reflection on axes of deflection angle and the logarithm of the pressure ratio. This method starts by defining the flow Mach number,  $M_1$ , and then plotting all solutions to Equations 2.1 and 2.3 for that Mach number. Using the regular reflection example, the locus of an oblique shock in a Mach 3 flow is shown as the solid line in Figure 2.3. Next the wave angle of the shock and Equation 2.2 is used to determine the Mach number of the flow behind the first shock and the deflection angle  $\delta$  for the flow through this oblique shock wave, this is shown as the red dot in Figure 2.3. Using the second Mach number,  $M_2$ , and Equations 2.1 and 2.3 all possible reflected shocks are plotted as a function of net pressure and net deflection. This locus of points can be translated and reflected within the shock polar diagram to graphically solve for the reflection [25]. In this case, the reflected shock polar is first mirrored horizontally, because the reflected wave is propagating in the opposite direction from the incident wave. The shock polar is then translated to the location on the first shock polar representing the actual incident shock wave. This is shown as the dotted line in Figure 2.3 for the example problem.

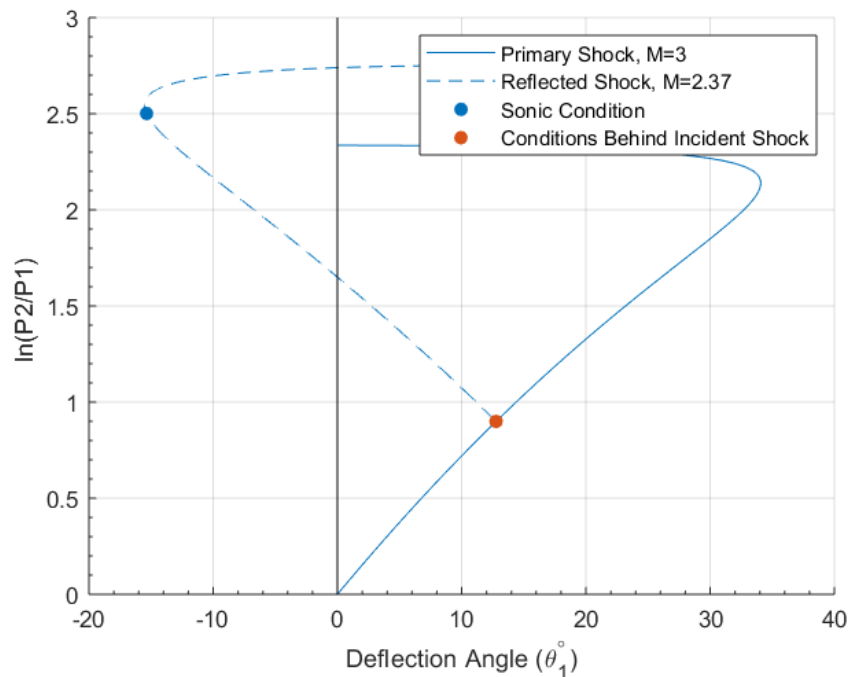


Figure 2.3: Shock polar diagram of the regular reflection of a Mach 3 flow with a  $60^\circ$  wave angle.

The boundary condition for a regular reflection is no net deflection across the reflection which occurs where the reflected shock locus crosses the Y-axis. In

Figure 2.3 there are two points where the reflected shock locus crosses the Y-axis, at approximately  $\ln(P_2/P_1)$  of 1.5, which relates to the weak shock solution, and at approximately 2.75, which is the strong shock solution. Here the weak shock wave solution is taken as the resulting shock because the strong shock wave is unlikely to form [25]. The pressure ratio across the reflection can be determined directly from the shock polar diagram but to determine other details of the reflection requires using the above analytical equations.

### 2.3 Mach Reflection

A single Mach reflection can also be solved either numerically or graphically but the numerical solution must be solved simultaneously. To solve using either method, first the Galilean coordinate transformation is used to shift the reflection from unsteady to fixed frame of reference. For an irregular reflection, the triple point is used as the fixed point so the transformation is given by Equations 1.2 through 1.4. The main boundary conditions for a Mach reflection is that the pressure is equal across the slip line, shown as  $s$  in Figure 2.4:

$$P_4 = P_3 \quad (2.5)$$

where  $P_4$  is the pressure after the Mach stem, and  $P_3$  is the pressure after the reflected shock. By taking these pressures as a ratio to the pressure before the shock, reduces the number of variables required to solve the reflection by eliminating the pre-shock pressure. The modified boundary condition is given by:

$$\frac{P_4}{P_1} = \frac{P_3}{P_1} \quad (2.6)$$

where  $P_1$  is the pressure before the reflected shock. The other two boundary conditions for a Mach reflection are that the Mach stem is perpendicular to the reflection surface at the reflection surface and at the triple point the flow is parallel on either side of the slip line. These boundary conditions can be expressed as:

$$\delta_3 = \delta_1 - \delta_2 \quad (2.7)$$

$$\left. \frac{dx}{dy} \right|_{m_G} = 0 \quad (2.8)$$

where  $\delta_1$  is the deflection caused by the incident shock,  $\delta_2$  is the deflection caused by the reflected shock,  $\delta_3$  is the deflection caused by the Mach stem and  $\left. \frac{dx}{dy} \right|_{m_G}$  is the slope of the Mach stem evaluated at the ground level.

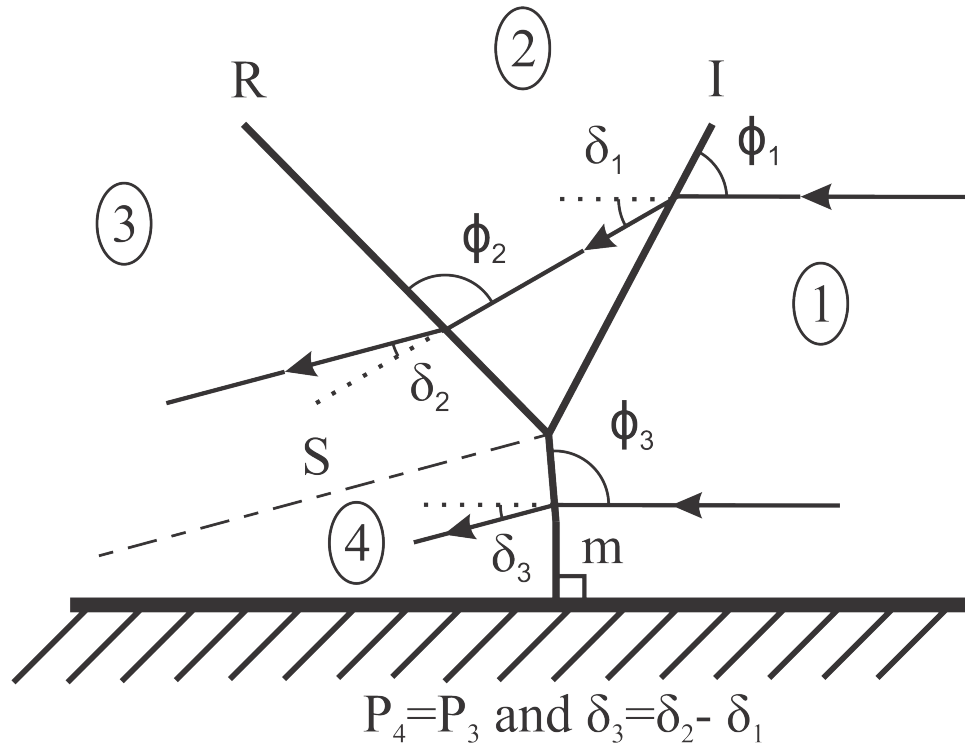


Figure 2.4: Labeled diagram of a single Mach reflection. With I indicating the incident shock, R the reflected shock, m the Mach stem, and S the slip line. The number of the state is listed in the oval. The deflection,  $\delta$ , and wave angle,  $\phi$ , is listed for each shock. The boundary conditions are listed at the bottom of the figure. The Mach stem is shown to have two distinct angles,  $\phi_3$  at the triple point and perpendicular to the reflection plane at the reflection plane. In the diagram there is a sharp transition between the two angles but in experiments this has been shown to be a smooth transition between the two angles.

The reason the equations defining a Mach reflection must be solved simultaneously is it that the triple point trajectory,  $\chi$ , is a function of Mach number and angle but is not solved for explicitly. A method to simplify this analysis is to use published tables or graphs to determine  $\chi$  for a given Mach number and wedge angle.

To help clarify this discussion the triple point trajectory,  $\chi$ , is determined using multiple methods for a moving shock in air with a Mach number of 4.24 impacting a reflecting surface with an effective wedge angle of  $41^\circ$ . Using the graph of triple point trajectories in [6] the triple point trajectory is determined to be  $4^\circ$ . After the Galilean transformation this gives a Mach number of the flow of 3 and a wave angle,  $\phi_1$ , of  $45^\circ$ . The pressure ratio across the Mach stem can then be solved for directly which is 10.3. Simultaneously solving the governing equations for the example gives a  $\chi$  of 4.15 and a pressure behind the Mach stem of 10.2. This example shows that there is less than a 1% difference between using the published values for  $\chi$  and directly calculating them.

### 2.3.1 Numerical Solution

The remaining equations required to define the reflection numerically are the oblique shock equations, Equations 2.1 through 2.3, applied to the Mach stem, incident shock and reflected shock. These nine equations, three for each shock wave, equations can be expressed as:

$$M_2 = f(\gamma, M_1, \phi_1) \quad (2.9)$$

$$\delta_1 = f(\gamma, M_1, \phi_1) \quad (2.10)$$

$$\frac{P_2}{P_1} = f(\gamma, M_1, \phi_1) \quad (2.11)$$

$$M_3 = f(\gamma, M_2, \phi_2) \quad (2.12)$$

$$\delta_2 = f(\gamma, M_2, \phi_2) \quad (2.13)$$

$$\frac{P_3}{P_2} = f(\gamma, M_2, \phi_2) \quad (2.14)$$

$$M_4 = f(\gamma, M_1, \phi_3) \quad (2.15)$$

$$\delta_3 = f(\gamma, M_1, \phi_3) \quad (2.16)$$

$$\frac{P_4}{P_1} = f(\gamma, M_1, \phi_3) \quad (2.17)$$

where  $M_i$  is the Mach number in state  $i$ ,  $P_i$  the absolute pressure in state  $i$ ,  $\delta_1$  and  $\phi_1$  is the deflection and wave angle of the incident shock,  $\delta_2$  and  $\phi_2$ , is the deflection and wave angle of the reflected shock, and  $\delta_3$  and  $\phi_3$  are the deflection and wave angle of the Mach stem.

Fourteen equations fully define a single Mach reflection: Equations 1.2 and 1.4 for the Galilean coordinate transformation, Equations 2.6 and 1.4 provide the boundary conditions and Equations 2.9 through 2.17 detail each feature of the reflection. While these 14 equations fully define the Mach reflection, the Mach number after the reflected shock and Mach stem are not required to solve the system. Removing these two equations, leaves 12 equations with 15 variables which can be solved simultaneously by providing input values of  $\gamma$ , the Mach number of the shock,  $M_s$ , and the effective wedge angle,  $\theta_w$ .

### 2.3.2 Shock Polar Analysis

Shock polar analysis can be used to solve the Mach reflection system of equations graphically. The shock polar graph for a Mach reflection is performed identical to a regular reflection. To help clarify this discussion a numerical example is solved for a Mach shock reflection in a Mach 3 flow with a  $45^\circ$  wave angle. In Figure 2.5, the locus of shocks in a Mach 3 flow is plotted as the solid line. The Mach number, pressure ratio and deflection after an oblique shock with a wave angle of  $45^\circ$  is calculated and shown as the red dot in Figure 2.5. The locus of all shocks in that flow is plotted as the dotted line. Examination of Figure 2.5 shows that at no point does the reflected shock cross the Y-axis, which indicates a regular reflection is not possible. There is one point where the reflected shock crosses the strong shock portion of the incident shock. At this intersection the pressure behind the reflected shock is equal to a strong shock with the same net deflection. At this point the two boundary conditions, no pressure difference across the slip line and Equation 2.7, are satisfied. From this point the wave angle of the reflected shock and Mach stem at the triple point can be determined. This analysis shows that, at the triple point, the Mach stem is not a normal shock but a strong oblique shock. Because the Mach stem must be perpendicular to the flow at the reflection surface this causes the Mach stem to have some curvature. The pressure ratio behind the triple point can be determined directly from the shock polar diagrams as this intersection on the strong shock branch of the initial shock wave. The pressure across the Mach stem is very close to the pressure across a normal shock. For this reason the pressure across the Mach stem is approximated as the pressure across a normal shock.

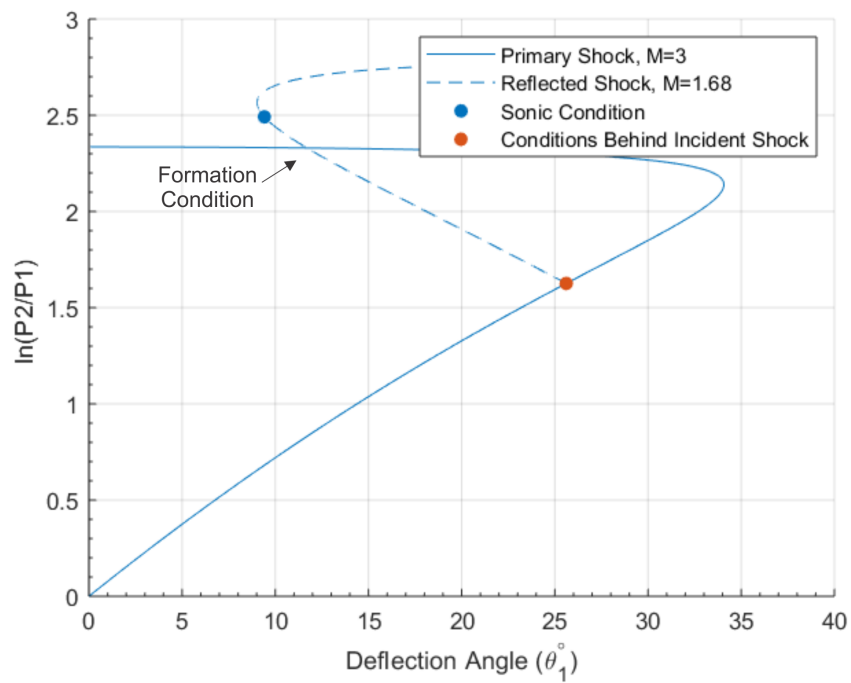


Figure 2.5: Shock polar diagram of the reflection of a Mach 3 flow with a  $45^\circ$  wave angle. The formation conditions of the Mach reflection are indicated.

## 2.4 Formation Conditions of Regular and Mach Reflections

In the above analysis either a regular or irregular reflection was possible for the given Mach number and wedge angle but there is a range of Mach number and wedge angle combinations where both reflection types are mathematically possible. In shock diffraction theory the transition point between the formation of a regular and Mach reflection is given by the length scale criterion [6]. For a reflection in a steady flow the length scale criterion dictates that a Mach reflection will occur whenever possible. For a reflection in pseudo-steady or unsteady flow the length scale criterion states that a Mach reflection can only occur if the flow behind the reflection is sub-sonic relative to the reflection point [6]. This condition, which is referred to as the sonic condition, is equivalent to the flow behind the reflected shock, state 3, of a regular reflection being subsonic after the Galilean transformation.

The sonic condition can be determined either analytically or with shock polar analysis. Both methods rely on iteratively solving for the same condition which is a regular reflection with a Mach number of unity behind the reflection. The analytical method, using the method laid out in Section 2.2, iteratively solves the reflection until sonic flow behind the reflected shock is determined to the desired level of accuracy. This transition condition can be found in shock polar analysis by plotting, on the reflected shock locus, the point where the flow behind the reflected shock is sonic, this point is shown as the blue dot in Figures 2.3, 2.5, and 2.6. The transition condition can be determined by locating the conditions when the sonic point meets the Y axis, which defines a regular reflection that has sonic flow behind the reflection, which is shown in Figure 2.6.

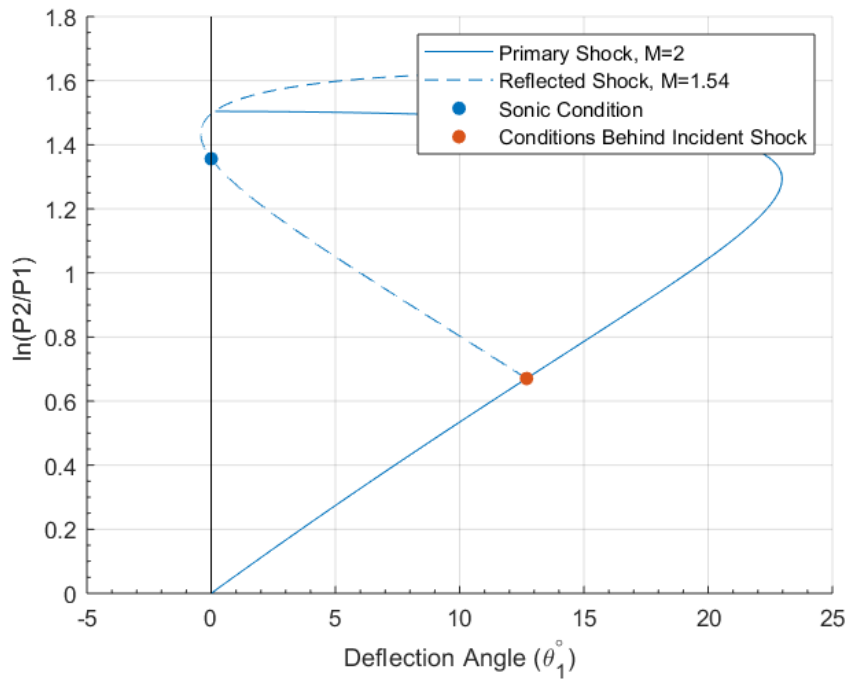


Figure 2.6: Shock polar diagram of the sonic condition which is the transition criteria for pseudo-steady shock waves. This diagram shows the reflection of a shock wave in a Mach 2 flow with an angle of  $42.7^\circ$  between the flow and the shock.

The sonic condition, the transition line between a regular and irregular shock reflection, should be a continuous function of Mach number and wedge angle. Based on this assumption the angle corresponding to the sonic condition was calculated for a range of Mach numbers between 1 and 6 and is shown as the dashed line in Figure 2.7.

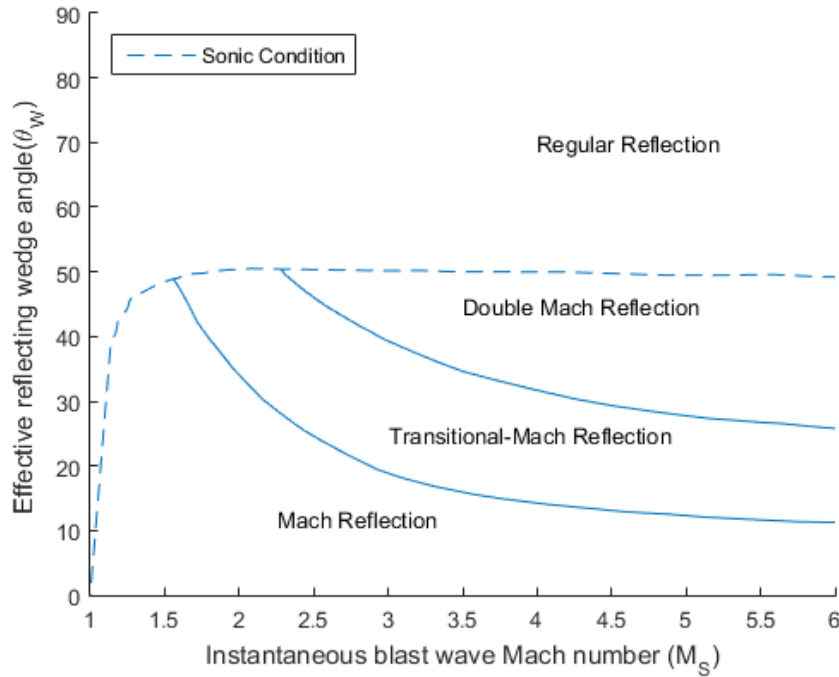


Figure 2.7: Domain diagram showing which pseudo-steady shock wave reflection will occur for a given wedge angle and Mach Number. The sonic condition was calculated analytically using the method in Section 2.2 but the transition conditions to transitional-Mach reflection and double Mach reflection are taken from [6].

Similar to the transition between a regular and Mach reflection, the transition condition between different types of irregular reflections is given by sonic flow in different sections of the reflection. As the Mach number of the flow before a Mach reflection is increased, the Mach number behind the reflected shock, state 3 in Figure 2.4, also increases. Once the flow in state 3 is equal to Mach 1, in the reference frame attached to the triple point, the Mach reflection transitions into a transitional-Mach reflection. The transition point between a transitional-Mach and Mach reflection is plotted in Figure 2.7.

The transitional-Mach reflection is similar to a Mach reflection with the addition of the feature referred to as the kink. The kink, labeled  $k$  in Figure 2.8, is a straight shock wave section attached to the triple point, which through a sudden change of angle becomes the main curved reflected shock. The analytical flow

description of a transitional-Mach reflection is identical to a Mach reflection with the added boundary condition that the flow in state 3, shown in Figure 2.8, is Mach 1 in a reference frame attached to the kink. Stated differently, in the reference frame attached to the triple point the transition point between the flat and curved section of the reflected shock moves away from the triple point with a velocity equal to the Mach number of the flow in state 3 minus Mach 1.

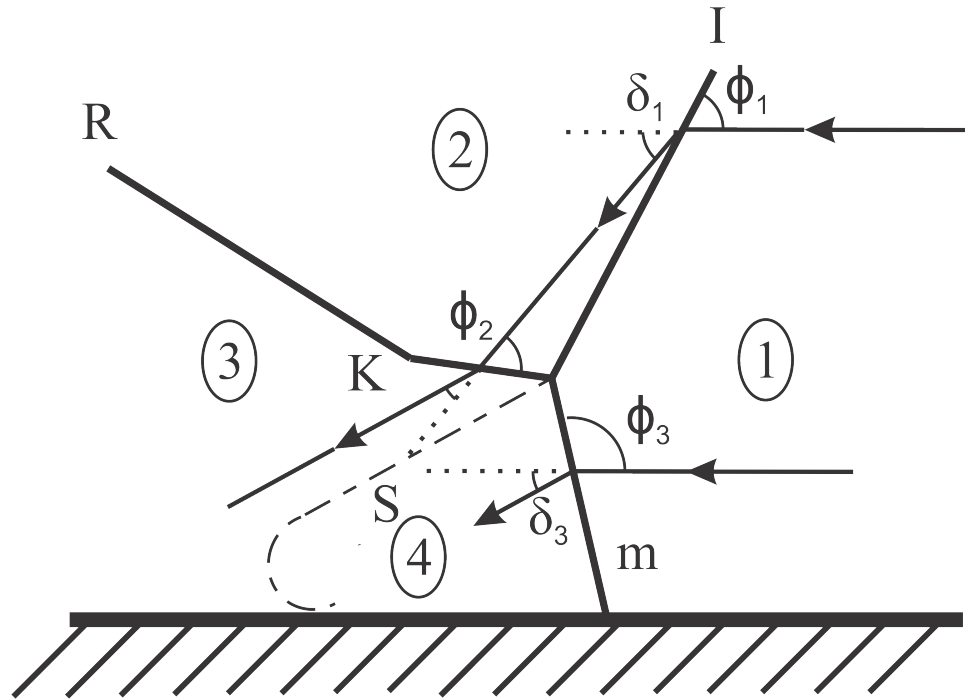


Figure 2.8: Labeled diagram of a transitional-Mach reflection. With I indicating the incident shock, R the reflected shock, m the Mach stem, s the slip line and the new feature of the kink, K. The number of the state is listed in the oval. The deflection,  $\delta$ , and wave angle,  $\phi$ , is listed for each shock.

The transition condition between a transitional-Mach reflection and double Mach reflection is solved for based on flow conditions within the double Mach reflection. A double Mach reflection will occur if the flow in state 3, shown in Figure 2.9, is greater than Mach 1 in a reference frame attached to the second triple point,  $T'$ . The transition point between a transitional-Mach and double Mach reflection is plotted in Figure 2.7.

The double Mach reflection is similar to a transitional-Mach reflection except that a shock wave now extends down from what was previously referred to as the kink, now referred to as the second triple point, and the first slip stream now ends at this new shock. A full analytical solution does not currently exist for the double Mach reflection and can only be solved by solving the full Navier-Stokes equations [6]. Two simplified analytical models have been developed but are outside the scope of this work. The proposed experiments are not expected

to produce a reflection at a high enough Mach number to cause a double Mach reflection so they are only covered here for completeness.

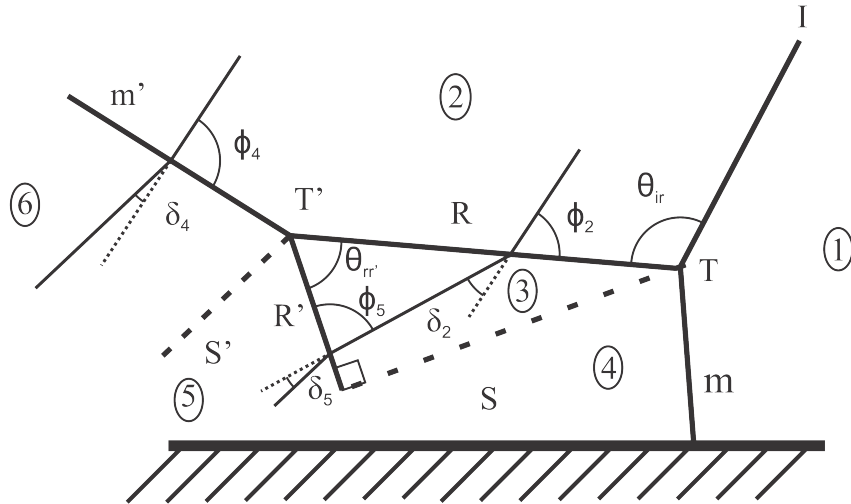


Figure 2.9: Labeled diagram of a double Mach reflection. With I indicating the incident shock, R the reflected shock, m the Mach stem, and s the slip line. The number of the state is listed in the oval. The deflection,  $\delta$ , and wave angle,  $\phi$ , are listed for each shock.  $\theta$  is used to denote the angle between shock waves. The ' is on features, such as Mach stem, to denote the second feature and the ' is used on values to indicate it is taken in reference to the second triple point.

## 2.5 Pressure Across a Shock Reflection

To determine the overpressure across a reflection the type of reflection must first be determined by shock diffraction theory. Then, depending on the type of reflection, the flow conditions of the reflection can be solved and the pressure ratio across the reflection determined numerically, or simplifications can be made so the pressure ratio can be determined without solving for each detail of the reflection.

The analytical solution for regular reflections is trivial so simplification is unnecessary. Double and transitional-Mach reflections are complicated enough that a true analytical solution is impractical but through simplification a pressure across the reflection can be estimated. The pressure across a Mach reflection can be determined by either simultaneously solving all the governing equations or through simplification.

In the above discussion it was shown that the boundary conditions necessitate that the Mach stem has a slight curve. To study the effect Mach stem curvature has on overpressure, the test case of a Mach 2 shock wave over a  $30^\circ$  wedge

is examined. These conditions were compared to experimental results from [6] to determine the trajectory of the first triple point, which was estimated to be approximately  $8^\circ$ . This value was used with Equations 1.2 and 1.3 to determine the wave angles for the incident shock,  $\phi_1 = 54^\circ$ , and the Mach stem,  $\phi_3 = 82^\circ$ . This result shows that at the triple point the Mach stem has an angle relative to the flow of  $82^\circ$  while the lower boundary condition, given by Equation 2.8, dictates that the foot of the Mach stem must be perpendicular to the flow. Prior experimental observations show that the Mach stem is expected to smoothly vary between these two conditions [11]. Given the small angle difference, the Mach stem has minimal curvature and the pressure ratio across the Mach stem varies by only 2% along its length. This difference is expected to increase as the Mach stem grows and the curvature becomes more pronounced.

Do to the growth of the Mach stem over time, the Mach stem has a higher Mach number than the incident shock wave. The Mach number of the Mach stem is given by

$$M_m = M_s \frac{\cos(\chi)}{\cos(\theta_1 + \chi)} \quad (2.18)$$

where  $M_m$  is the Mach number of the Mach stem [73].

The pressure ratio across a Mach reflection can be estimated using triple point trajectory,  $\chi$ , and the assumption of a perpendicular Mach stem.  $\chi$  is a function of the Mach number of the shock and the effective wedge angle. The value of  $\chi$  can either be calculated using the system of equations in Section 2.3.1 or found in published tables and plots, such as [6]. These three parameters can then be used with Equation 2.18 to determine the Mach number of the Mach stem in a laboratory frame of reference. Since the Mach stem can be assumed to be a normal shock Equation 1.13 can be used to determine the pressure ratio across the Mach stem which is equivalent to the pressure ratio across the Mach or transitional-Mach reflection.

## 2.6 Unsteady Shock Reflection

As a spherical shock wave expands from an elevated point source its Mach number and reflection angle continuously change. The process by which the unsteady shock wave reflection changes over time can be predicted by discretizing the reflection path and applying shock diffraction theory to each step and evaluating the finite changes between steps [73]. Large changes between steps or increasing effective wedge angle can result in complex and interesting reflections that are outside the scope of this work. Further information on these complex cases can be found in [73] and [35]. In the current work, all reflections started at high Mach number and high effective wedge angle and both continuously decreased. When discretized each step on the reflection paths should resemble the pseudo-steady case with the same Mach number and wedge angle.

## CHAPTER 3

### EXPERIMENTAL METHODS OF GRAM-SCALE TEST SERIES

To investigate the reflection of explosively driven shock waves experiments were conducted at the Energetic Materials Research and Testing Center (EMRTC) at the New Mexico Institute of Mining and Technology. The test series studied the reflection of the shock waves generated from gram-scale charges. The primary test series was designed to allow the shock wave reflection type to be tracked as the shock wave expanded using refractive imaging and reflected pressure recorded as a one-dimensional function of distance. A secondary test series was designed as a control, to study shock wave expansion using refractive imaging and overpressure without reflections.

The reflection test series conducted at EMRTC consisted of the detonation of gram-scale charges over an instrumented reflection plate with the resulting shock wave and reflection visualized with focused shadowgraph and schlieren. The refractive imaging mirrors and the reflection system are shown to scale in Figure 3.1. The explosive charge was suspended above a steel reflection plate which had an array of pressure probes flush-mounted at set distances along the plate. The reflection plate was placed within the shadowgraph and schlieren systems to visualize the reflection type as it passes over the pressure gauges. Table 3.1 list the details of each test.

Table 3.1: Summary of the gram-scale reflection tests series.

Test ID	Pellet Mass (g)	Charge Height (m)	Ambient Temperature (C)	Ambient Pressure (kpa)
R1	0.9680	0.100	10.6	84.77
R2	0.9655	0.103	11.6	84.76
R3	0.9739	0.085	11.4	84.74
R4	0.9650	0.085	11.8	84.68
R5	0.9647	0.088	12.0	84.62
R6	0.9606	0.123	12.3	84.58
R7	0.9718	0.123	12.4	84.52
R8	0.9751	0.122	12.6	84.50
R9	0.9476	0.155	12.9	84.45
R10	0.9513	0.154	13.2	84.42
R11	0.9754	0.154	13.4	84.39
R12	0.9720	0.155	13.9	84.35
R13	0.9663	0.091	14.4	84.27
R14	0.9523	0.088	14.5	84.27
R15	0.9658	0.089	14.6	84.22

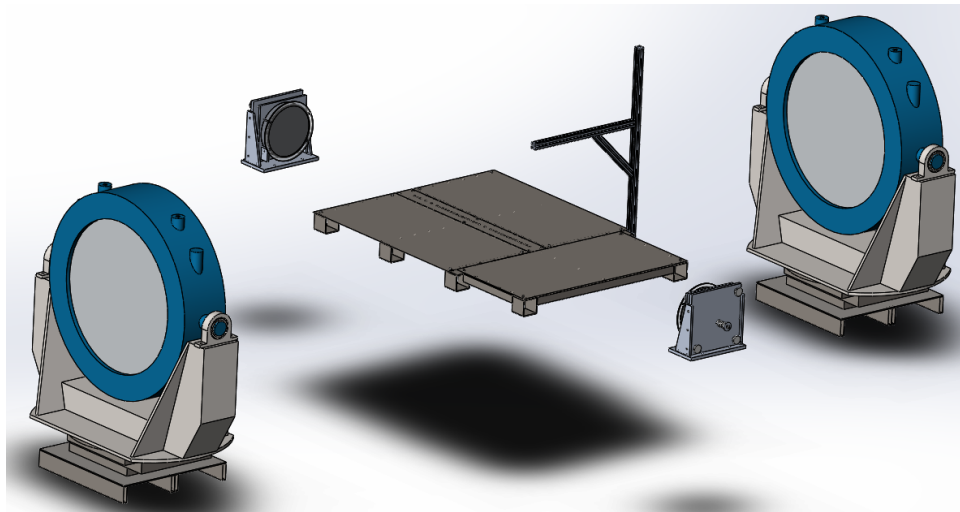


Figure 3.1: Diagram of mirrors and reflection plate setup for the reflection gram scale test series.

The no reflection test series consisted of the detonation of gram-scale charges in line with an instrumented reflection plate with the shock wave visualized with shadowgraph. The charge placement, pressure plate system and wave cutoff are shown to scale in Figure 3.2. The explosive charge was suspended in line with the steel reflection plate which had an array of pressure probes flush-mounted at set distances along the plate. To minimize distortions and reflections of the shock wave, a cutoff wedge was placed between the charge and pressure plate to ensure the shock wave propagated normally across the pressure plate. The reflection plate was placed within the shadowgraph system to visualize the reflection type as it passes over the pressure gauges. Table 3.2 list the details of each test.

Table 3.2: Summary of the no reflection tests series.

Test ID	Pellet Mass (g)	Charge Distance to First Probe (m)	Ambient Temperature (C)	Ambient Pressure (kpa)
N1	0.9732	0.15	17	84.27
N2	0.9740	0.127	13.9	85.21
N3	0.9739	0.127	14.3	85.21
N4	0.9650	0.127	14.6	85.21
N5	0.9647	0.127	15	85.19

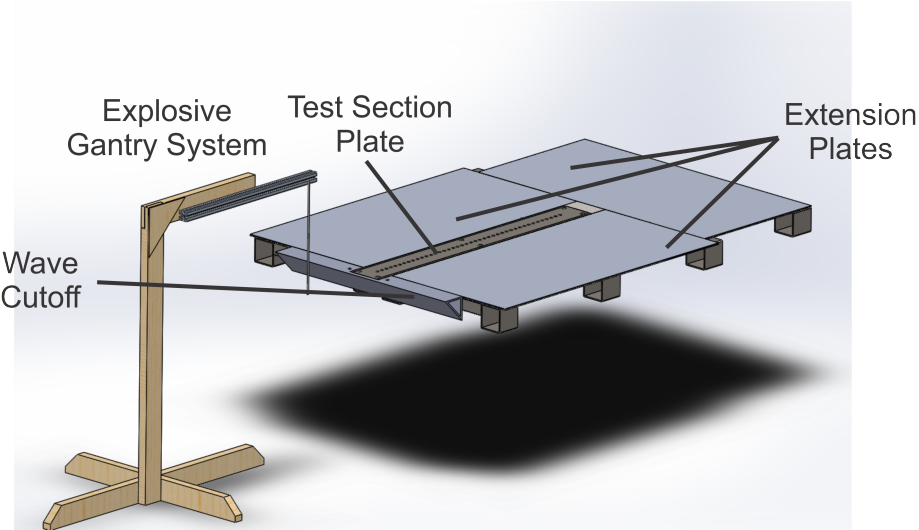


Figure 3.2: Model of charge and reflection plate setup for the gram scale test series. The rigid test section plate has tapped holes for pressure transducers. The extension plates are positioned to allow the shock wave to expand without introducing rarefaction waves. A gantry made of 80/20 aluminum framing is used to suspend the explosive charge.

### 3.1 Explosive Pellet

The explosive charges used in the small scale test series were nominally 1-gram spheres of pentaerythritol tetranitrate (PETN) [74] which were center initiated. The charges were formed by uniaxial pressing of loose PETN powder with no binder. The pressing dies were machined from 4140 steel and the pressing surfaces polished to a mirror finish. The importance of the surface finish of the pressing surfaces of the dies cannot be overstated. Failure to achieve a proper surface finish, even with ample mold release agent, resulted in the pellets tearing in half during extraction. Engineering drawings of the dies designed are included in Appendix A. To allow for the charges to be center-initiated, an insert was included in the dies which is approximately the size of an RP-3 detonator, which has a diameter of 3.3 mm (0.130 inches)[75]. The insert, which is shown in Figure 3.3, has a slight taper allowing the detonator to be easily inserted without excessive movement after insertion. To press the pellets, the entire die assembly was coated in a light layer of calcium stearate mold release agent. Then one gram of PETN powder was placed into the lower anvil with the extractor pin, detonator insert and alignment sleeve in place. The top anvil was then put in place. The assembly was then pressed in a hydraulic press.

To consistently press the pellets, the maximum compression was controlled by limiting the travel of the top anvil. When the top anvil is flush with the manual stop then additional force will not move the top anvil or increase the compression. This will produce a 1 gram pellet with a density of  $1.7 \text{ g/cm}^3$ . A limitation of this pressing system was the low contrast camera used to remotely observe the pressing operations. As a result it was difficult to determine when the top anvil and manual stop were flush. To ensure pressing reached the mechanical stop, each pellet was pressed to a higher pressure than required to achieve a density of  $1.7 \text{ g/cm}^3$ , which for PETN requires 140 MPa (20000 psi) [76]. To measure the force applied to the die an industrial scale with a max load of 4535 kg (10,000 lb) and resolution of 0.5 kg (1 lb.) was placed between the die and lower base of the press. The scale, Model FSK-A manufactured by A and A Scales LLC, was calibrated by the manufacturer and found to have a precision of 0.02% and creep of 0.02% over 30 minutes. Each pellet was pressed to a force over 27 kN (6000 lb) which corresponded to a pressure in the die of 280 MPa (40000 psi), which is double the required pressure. The die was held under pressure for 3 minutes to allow the powder to consolidate. Once pressure had been relieved from the system, the top anvil and alignment sleeve were removed. To remove the pellet from the die, an extractor plate, shown in Figure 3.4a, was placed under the bottom anvil and extractor pin. This assembly was placed back in the hydraulic press. When placed under load, the extractor plate applied pressure to the extracting pins pushing the pellet upward while an extractor collar maintains downward force on the anvil; this is shown in Figure 3.4b. This allowed the pellet to be extracted from the die even if it had become stuck during pressing.

Final assembly of the explosive charge consisted of inserting an RP-3 detonator into the charge cavity. The RP-3 is an exploding-bridge wire (EBW) detonator

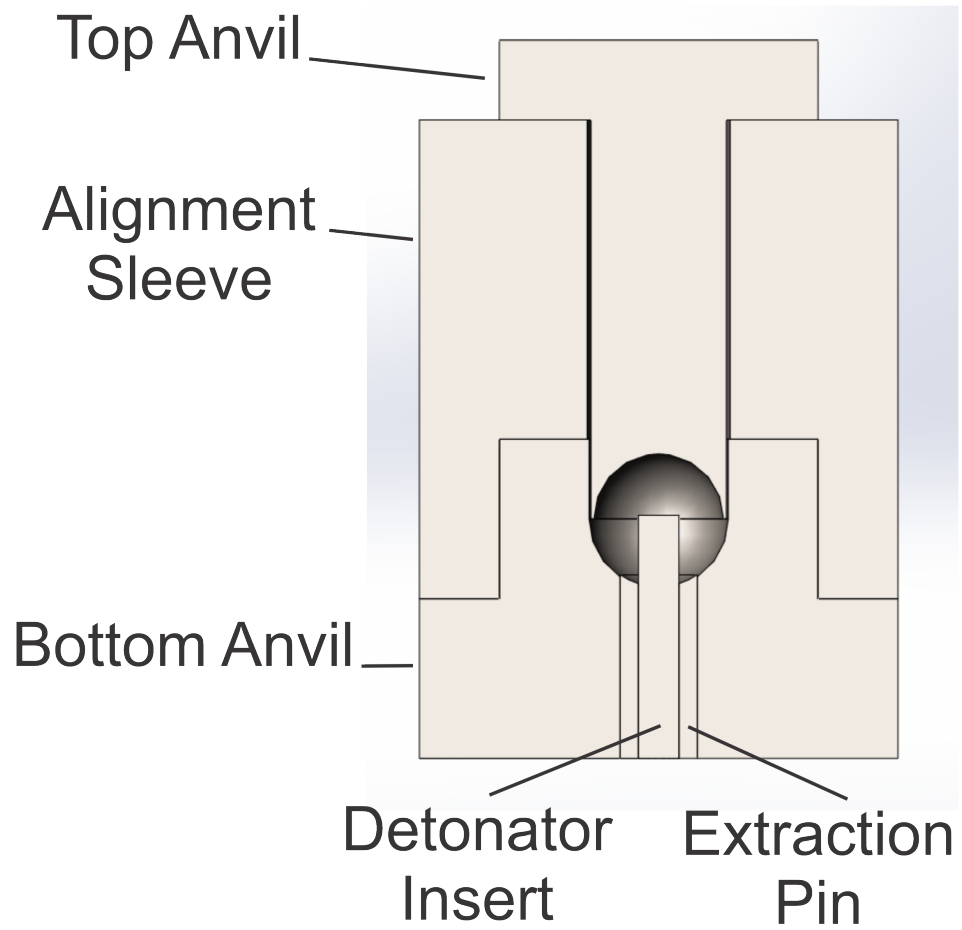


Figure 3.3: Cutaway diagram of pellet pressing die.

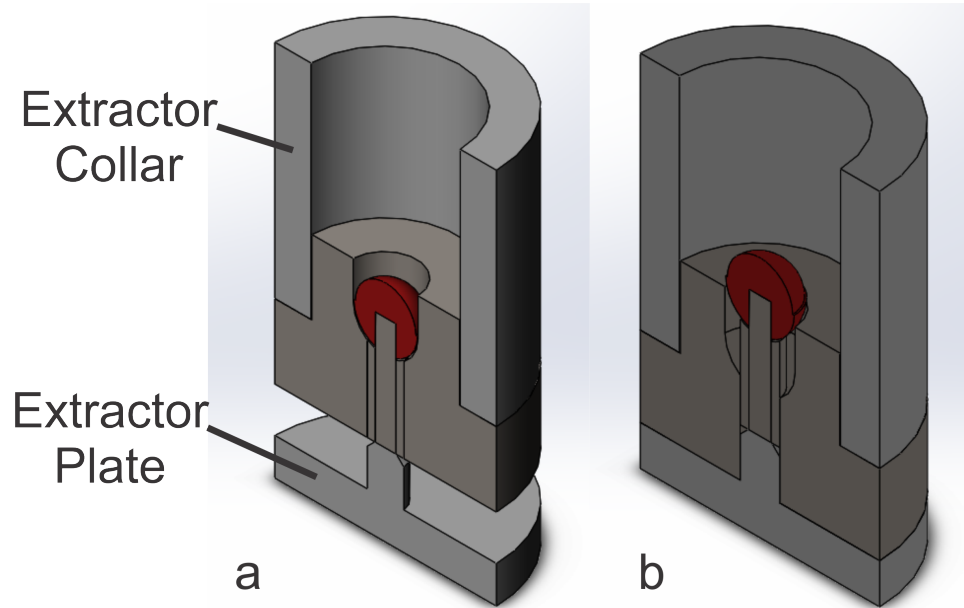


Figure 3.4: Cutaway diagram of explosive pellet being extracted from die.

with less than 30 mg of PETN [75]. Full details of the RP-3 are included in Appendix A. The detonator was affixed to the charge with either cyanoacrylate glue paired with a commercially available curing accelerant or electrical tape. Other methods of affixing the detonator to the pellet were attempted but either failed to cure or did not bind to the pellet strongly enough.

### 3.2 Reflection Structure

The explosive charge was suspended either above or in line with the rigid reflection plate with flush mounted pressure transducers. The reflection structure was fabricated from mild steel and 80/20-brand aluminum beams and fixtures, which is shown in Figure 3.5. The engineering drawings for the reflection plate are included in Appendix B. The reflection structure is comprised of four main pieces: the test section plate, the extension plates, wave cutoff and an explosive support structure. The test section plate was made from a 152 mm (6 inch) wide, 1.2 m (4 feet) long and 6.25 mm (0.25 inch) thick plate of mild steel. Down the length of the plate, 42 holes were drilled and tapped on 25.4 mm (1 inch) centers to accept pressure gauges. 16 gauges were used in each test with the unused holes filled with flush-mounted set screws to prevent unwanted shock wave reflections from the voids. For the reflection tests, the gauges were placed in the center of the test section. For the no reflection tests, the gauges were placed at the end of the

test section closest to the shock cut off. The pressure data was then recorded with a Hi-Techniques Synergy Data Acquisition system at a sample rate of 2 million samples per second.

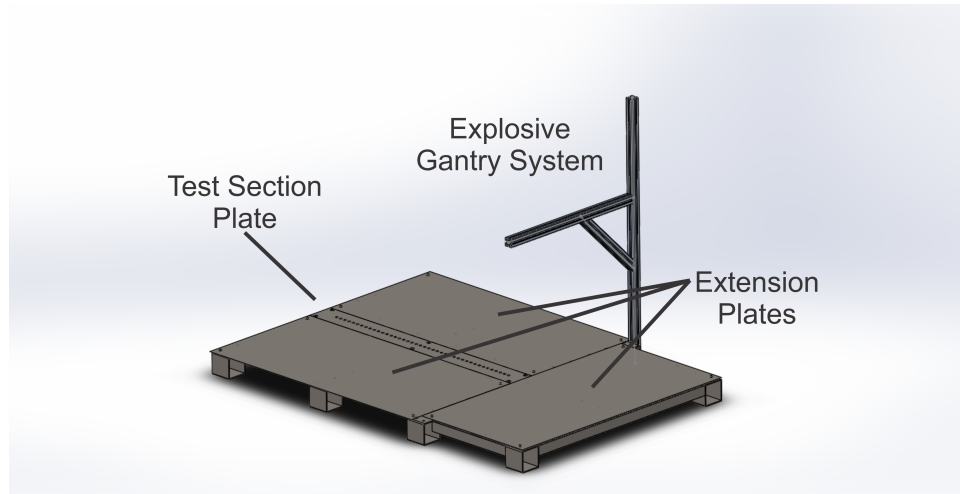


Figure 3.5: Model of the shock wave reflection structure. The rigid test section plate has tapped holes for pressure transducers. The extension plates are positioned to allow the shock wave to expand without introducing rarefaction waves. A gantry made of 80/20 is used to suspend the explosive charge.

The extension plates allow the shock wave to expand past the width of the test section plate without generating unwanted additional waves. As the shock wave grows it will quickly expand past the sides of the test section plate. Without a continuous surface for the shock wave to expand into, unwanted rarefactions will be introduced behind the primary shock wave. To prevent these extra waves, large extension plates were flush-mounted with the test section plate. Each extension plate is made of 0.5 mm (18 gauge) steel sheet that is 600 mm by 1200 mm (2 feet by 4 feet). These plates are configured to ensure that the primary shock from the charge can propagate the full length of the test section before rarefaction waves enter the test section. The extension plate and test section plates are elevated by a steel tube support structure. The support structure maintains the alignment of the different plates while allowing pressure probes to extend below the plates.

In the no reflection tests, the wave cutoff minimizes the reflections and distortions of the shock wave as it begins to propagate over the test section. The cutoff was welded from two pieces of mild steel, a flat and 'L' beam. The front edge of the cutoff, which directly interacted with the shock, was ground to an edge to minimize the reflection generated. A channel was cut into the top surface to accept the test section plate and minimize the distance from the charge to the first pressure probe.

A gantry system suspend the explosive charge at a variable height over the test section plate or at variable distances from the front of the wave cutoff. The

gantry was assembled out of wood for a frame and 80/20-brand beams and fasteners. The lead wires from the detonator were routed along the gantry and secured at the end of the beam. The exact distance between the charge and reflection surface was controlled by lengthening or shortening the amount of wire between the detonator and gantry. Between the end of the gantry and the explosive charge, the lead wires were routed through extra long plastic drinking straws cut to the exact distance needed. The straws increase the rigidity of the lead wires without introducing material which would cause excessive shock distortions or reflections.

A potential source of experimental error in this setup is the deflection of the reflection plate by the shock wave. If the deflection of the reflection plate is substantial then the flow direction around the shock can be changed enough to introduce additional experimental error [77]. Since the focus of this research is flow through the shock wave, to have a detrimental effect, the deflection would have to be caused by the momentum transfer from the shock wave impact and not the impulse resulting from the pressure differential after the reflection. Hugoniot matching was used to calculate the velocity of the steel reflection plate as a result of the shock wave impact [74]. Hugoniot matching is the process of either graphically or numerically finding the intersection of two shock Hugoniot curves for two adjacent materials, for example [78, 79, 80, 81, 82, 83]. The intersection of the curves predicts the equilibrium state after a shock wave has passed from one material to the other. An upper limit for this test series will be a Mach 10 shock wave impacting the reflection plate at 45 degrees, so this will be used to calculate the worst case for deflection. The conditions immediately behind the shock wave were calculated using standard temperature and pressure (STP) conditions for the initial state of the air and normal shock wave relationship equations. Hugoniot matching was then used to impact the shocked air state into steel, using bulk sound speeds and slope values from [74]. The resulting particle velocity after the impact was found to be negligible relative to the velocity of the shock wave. As a result, deflection of the plate will be assumed to have negligible effect on error and all plates will be assumed to be rigid.

### 3.3 Refractive Imaging Systems

#### 3.3.1 One-meter-diameter Shadowgraph System

The first diagnostic for this test series was a 1-m-diameter, double-pass focused shadowgraph system. The focused shadowgraph system, is shown schematically in Figure 3.6, and has four main components: sending optics, receiving optics, a 1-m-diameter parabolic mirror and a 1-m-diameter flat mirror. The sending optics of the system were comprised of a light source and a beam splitter, which is placed at the focal length of the parabolic mirror. The light from the source is focused onto the beam splitter which directs the light towards the parabolic mirror. The parabolic mirror collimates the light and reflects it towards the flat mirror. The area between the parabolic and flat mirror is the test section of the system. The flat mirror returns the collimated light to the parabolic mirror which focuses the light back onto the beam splitter. The light passes through the beam splitter and enters the high speed camera where it is recorded. The system is referred to as double pass because the light passes through the test section twice. This imaging system is essentially the same as the z-type schlieren system combined with the double-pass system to create a parallel light test section with only one parabolic mirror.

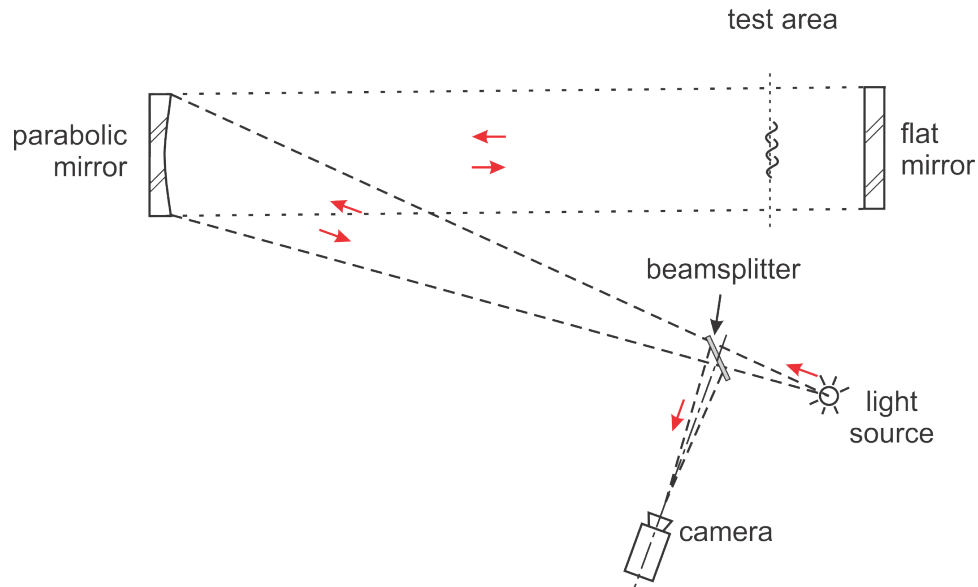


Figure 3.6: Light ray diagram of the double pass focused shadowgraph system that will be used in the gram scale test series.

The 1-m-diameter mirrors were supported with a translation and rotation system that allowed fine and coarse adjustments. A photograph of the mirror system is shown in Figure 3.7. The mirror can be precisely rotated about the Y (tilt) and Z (pan) axis by two adjustment knobs. The fine adjustment controls

can be detached which then allows for gross rotation by hand. The mirrors can be precisely translated in the X and Y by use of two small adjustment knobs. To allow coarse translations of the mirror, each mirror system rests on a platform which allows moving the system using a pallet jack. These adjustments assist in alignment of the shadowgraph system. The engineering drawings for the platform are included in Appendix C.

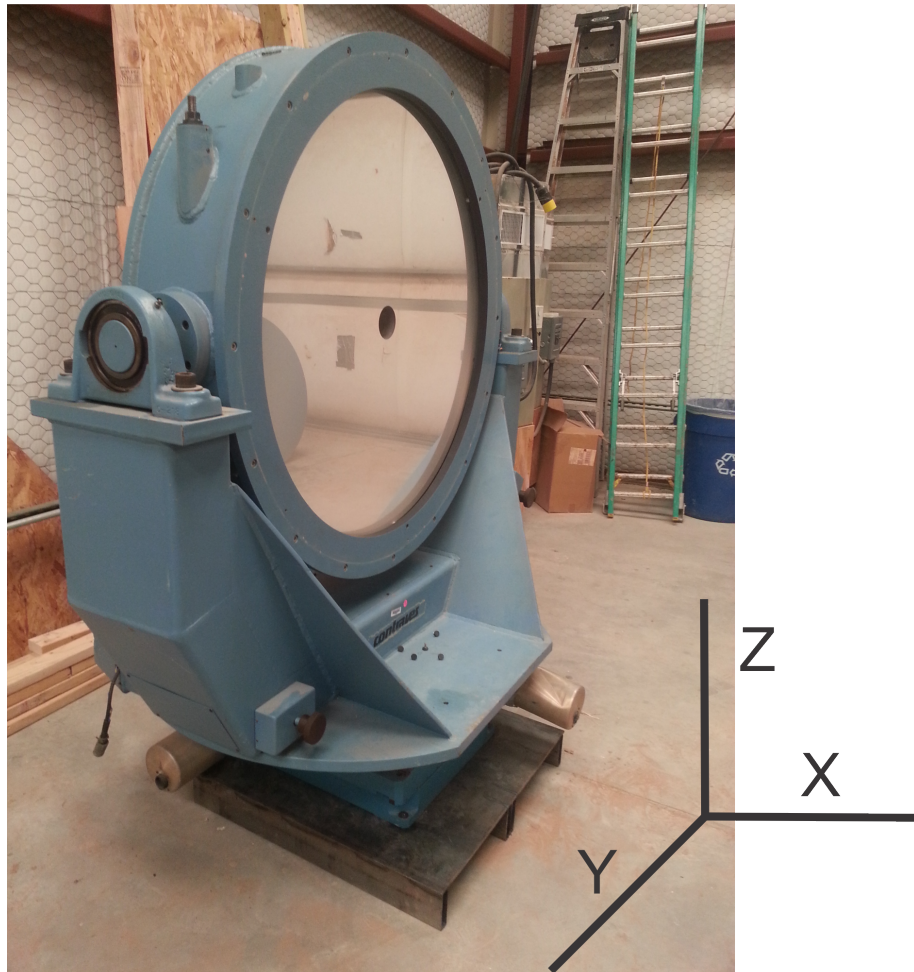


Figure 3.7: Photograph of the 1-m-diameter flat mirror with the coordinate system used to define it shown. Note that the mirror has a hole in the center of it, which prevents imaging at that location.

### 3.3.2 30 Centimeter Schlieren System

The second refractive system used for the test series was a 30-cm-diameter mirror schlieren system. The system is shown schematically in Figure 1.7a. The system had 4 major components: a light source, two parabolic mirrors, and receiving optics. The light source was a 400 W Si-Lux 640 laser illumination system which was synchronized with the camera to pulse only when the digital shutter was open. The laser was operated with a 10 ns pulse width. The laser light was transmitted through a liquid light guide resulting in a source that was temporally coherent but not spatially coherent. The light was collimated by the first 30-cm-diameter (12 inch) parabolic mirror. The mirrors were mounted on support structure which allowed fine tilt adjustment, Figure 3.8. The collimated light then passed through the test section to reach the second mirror. The second mirror was identical to the the first and focused the collimated light into the receiving optics. Between the lights focal point and the focusing mirror was a neutral density filter to protect the camera sensor from overexposure due to the intense focused light. At the focal point was placed a standard schlieren knife edge. After the focal point was a Shimadzu Hyper Vision HPV high speed camera.

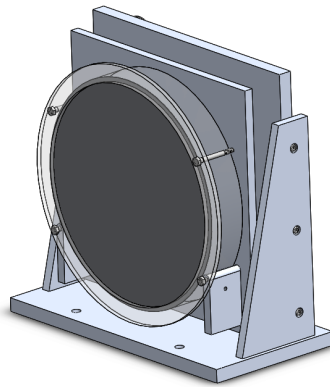


Figure 3.8: Schematic of the 30-cm-diameter parabolic mirror and mirror support.

## CHAPTER 4

### RESULTS AND DISCUSSION OF THE NON-REFLECTED GRAM-SCALE TEST SERIES

#### 4.1 Discussion of Uniformity of Explosive Charges

The PETN pellets used for this work were not all perfectly uniform. There were three sources of inconsistency between the pellets: pellet density, minor pellet damage, and pellet mounting. The variation in pellet density is a result of slight differences in the mass added to the pressing dies prior to pressing. Imperfections in the pressing dies and other problems in pressing led to a number of pellets suffering small chips fracturing off during extraction from the pressing dies. The method used to attach the detonator to the pellet varied over the course of the present work, starting with a cyanoacrylate and accelerant combination and setting on standard electrical style tape.

Each PETN pellet was formed by pressing approximately 1 g of loose PETN powder. The loose PETN powder was measured out to  $1.0025 \text{ g} \pm 0.0025 \text{ g}$  with a mean mass of 1.0027 g. The loose powder was then added to the dies and pressed. The pellet was then extracted and the mass of the pellet measured again. The final pellets had a mass of  $0.968 \pm 0.02 \text{ g}$ . The actual volume of the pellets were not measured, but assuming the pellets achieved a consistent volume, the variance in final mass results in a uncertainty in the density of 2 %.

The reason the volume of the pellet could not be directly measured was the pellet's irregular shape, which is shown in Figure 4.1. The pellet's shape was made by combining two spheres of different radii. This shape was a design choice in the pressing dies. To avoid pinch points in the explosive pressing the dies were designed to have one fit in the other, this is shown in Figure 3.3. A very thin leading edge of the upper die would be very delicate and prone to rolling inward during high loads, which would make it very likely the pellet would split in half during extraction. To increase the durability of the upper die leading edge it was designed to have a lip, this would result in a pellet with a step as is shown in Figure 4.1. Since the pellets were not perfect spheres their volume could not be easily measured. The pellet volume was calculated using the aid of CAD and the engineering drawing shown in Appendix A. The critical dimensions of the finished dies were measured to ensure they were within the tolerances shown in Appendix A.

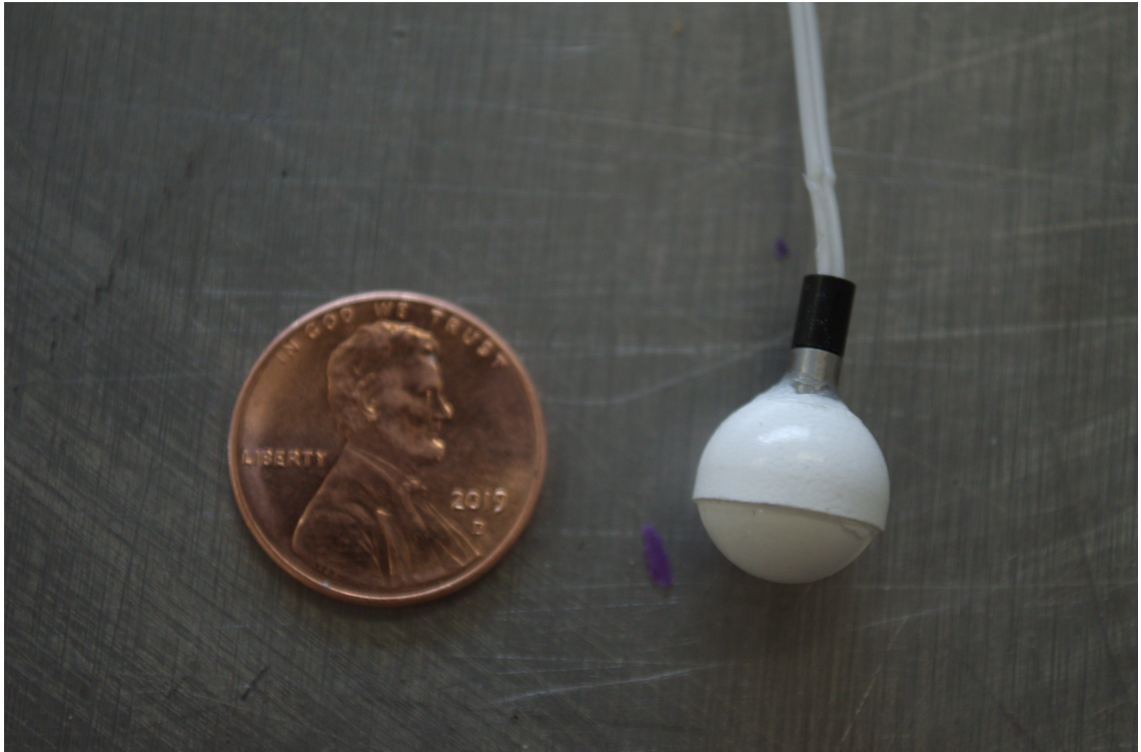


Figure 4.1: A PETN pellet with an RP-3 detonator glued to it with cyanoacrylate. A US penny is included for scale.

Detonation velocity,  $D$ , is a function explosive density,  $\rho$ , as given by: [74]

$$D_1 = D_2 + b(\rho_1 - \rho_2) \quad (4.1)$$

Where  $b$  is equal to 3 for a change in density within the range of 10-15 % [74]. Using the theoretical maximum density for PETN as  $\rho_1$  and the estimated minimum press density of the pellets as  $\rho_2$  gives a change in density of 9%. This is slightly outside the ideal range of 10-15 % but will give a reasonable approximation. This equation shows that a 2 % change in density will result in approximately 2% change in detonation velocity. The effect of the change in mass for the charge can be accounted for with Sach's scaling but the effect of changing density and resulting detonation velocity is difficult to account for in the far field. This change in detonation velocity may be a factor in the variation between pellets in Figure 4.5.

An additional problem that occurred during pressing is sections of the pellet fracturing off during pellet extraction. Pellets where the chipped portions occurred in the upper hemisphere of the pellet were noted and used. The upper hemisphere is defined as the hemisphere where the detonator was inserted. Pellets with chipped sections in the bottom hemisphere, opposite the detonator were not used. The most common type of damage was chipping of the corners of the detonator pin cavity. The damaged sections of the pellets may have led to inconsistencies in the shock wave. For this reason, only pellets with damage to the upper hemisphere, not facing the pressure probes, were used in the study. Post-test analysis of images was not able to directly attributed any shock distortions to damaged areas.

The amount of mold release agent on the surface of the pellet may have also caused variation between tests. To prevent pellet fracture ample mold release was applied to the dies. In all tests, non-reacting material is ejected in front of the primary shock. Since the material is non-reacting it is not believed to be PETN. The mold release agent is the only other material in or on the pellets so it is believed the ejecta must be mold release.

The largest difference between the pellets is how each pellet was adhered to the detonator. The first series of pellets were adhered with a combination of cyanoacrylate glue and an glue curing accelerant, one of these pellets is shown in Figure 4.1. According to the glue curing accelerant's Safety Data Sheet, the curing accelerant is dimethyl-P-toluidine dissolved in naphtha solvent [84]. The curing accelerant caused the glue to heat to the point that it caused blistering to human skin in a number of seconds. The peak temperature of this reaction was not measured but this temperature was estimated as being well below the autoignition temperature for PETN [85, 74]. While it was not expected that this temperature would cause the explosive to auto-detonate, the decision was made to find another method to attach the detonators to the pellets. For the majority of the pellets, electrical tape was used to secure the detonator to the pellet. A suspended pellet attached with electrical tape is shown in Figure 4.2.



Figure 4.2: A PETN pellet with an RP-3 detonator attached to it with electrical tape. The pellet is suspended over the test section. The yellow tube above the charge is a polymer straw used to provide a consistent charge height. A ruler with cm graduations, used to determine the exact charge height, is shown to the left of the charge.

A major source of noise in the refractive image data was caused by fragments that propagated faster than the primary shock wave. An example of this fragment noise is shown in Figure 4.3. The majority of these fragments and other shock distortions were observed in the upper half of the explosion. For this reason, it is believed that the detonator and detonator adhesive are the main source of these fragments and distortions. There were substantially more fragments from pellets attached with electrical tape than those using cyanoacrylate. The disturbed areas of the shock were omitted and only smooth areas of the shock were analyzed.

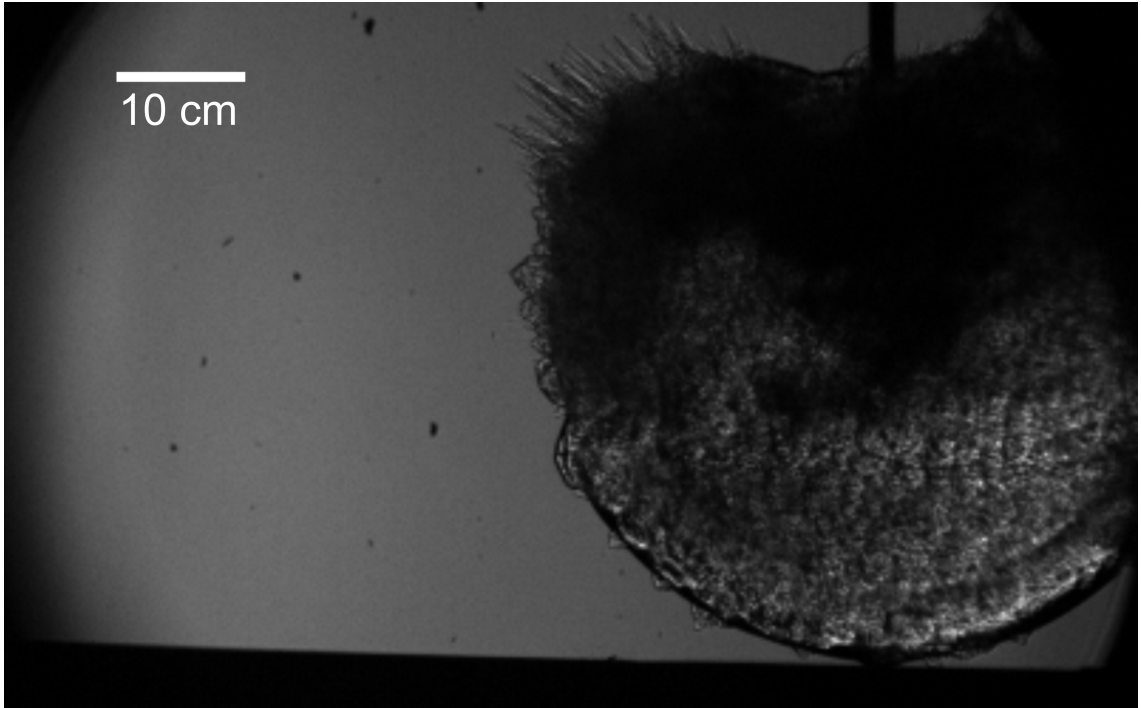


Figure 4.3: Refractive image from the 30-cm Z-schlieren system from Test R4 at  $t = 30 \mu s$  where  $t = 0$  is first light.

## 4.2 Calculating Mach Radius Curve for 1g PETN

The detonation of 1 g spheres of PETN was imaged with multiple refractive imaging systems to visualize the explosively driven shock wave. A representative image from the 30 cm system is shown in Figure 4.4. The location of the shock wave in each refractive image was determined with an automated detection algorithm detailed in [86, 87]. Only undisturbed areas of the shock wave were tracked. Areas of the shock with oblique shocks from fragments, like the upper left portion of Figure 4.4, were disregarded for this analysis. The step in the outside of the pellets also caused a discontinuity in the shock wave in the very near field. The area immediately around this shock discontinuity was also omitted. For purposes of studying the open-air growth of the shock wave, the Mach stem was also considered a discontinuity and was disregarded for this analysis. The measured shock radii were converted from pixels to meters using a calibration value found using an image of a calibration object of known size. A ball bearing with a diameter of 5.08 cm (2 inches) was used as a calibration object. The explosive test and calibration object were imaged in the area of parallel light within the refractive systems so a geometric correction is not needed. Figure 4.5 shows the found shock wave radii as a function of time. The radii and times were then scaled to 1 g at standard temperature and pressure using Sach's scaling (Equations 1.6-1.9).

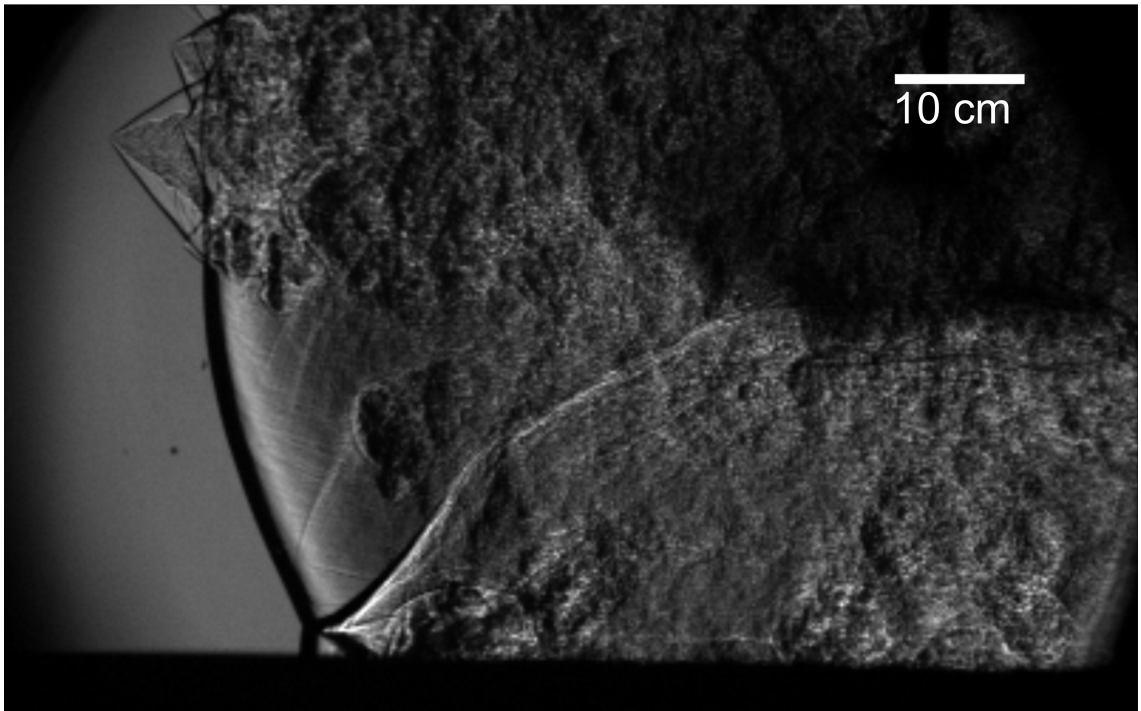


Figure 4.4: Refractive image from the 30-cm Z-schlieren system from Test R1 at  $t = 132 \mu\text{s}$  where  $t = 0$  is first light.

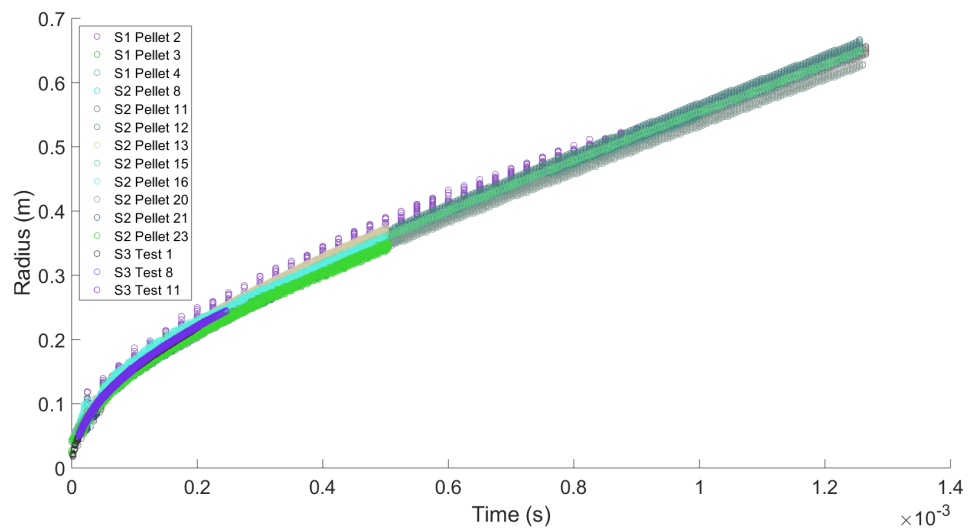


Figure 4.5: Unsealed shock wave time radius

Figure 4.5 is composed of over 75 thousand data points. A common tool to simplify the handling of the time-radius data is to fit the data to the Dewey equation, Equation 1.10, repeated here for convenience:

$$R_s = A + Ba_0t_s + C\ln(1 + a_0t_s) + D\sqrt{\ln(1 + a_0t_s)} \quad (4.2)$$

This reduces the time-radius data to 4 fitting parameters,  $A$ ,  $B$ ,  $C$ , and  $D$ , which can be easily stored, handled and disseminated. The parameter  $a_0$  is the speed of sound in the ambient medium, here taken as the speed of sound in air at 298 Kelvin. The Dewey equation has been widely used in literature for many different scales of explosive charges [60, 67, 68, 69, 86, 87, 88, 89, 90]. The functional form of the Dewey equation was proposed to have the limits of: a fixed radius at  $t = 0$  and as  $t \rightarrow \infty$  the shock propagation decays to a constant velocity [68]. Examining the limit at  $t = 0$  of Equation 1.10 results in:

$$R_s \Big|_{t=0} = A \quad (4.3)$$

So the  $A$  term should equal the initial radius of the shock at time zero, if explosive breakout is taken as  $t = 0$  then  $A$  should be equal to the initial charge radius. This limit was mentioned in the original proposal of the equation [68]. Later uses of the equation in literature have not fixed the  $A$  parameter but allowed it to be fit [60, 69, 86, 87, 88, 90]. In some cases, the resulting  $A$  term is near the initial radius [90] while in other cases the  $A$  term is negative [69, 88].

The second limit of the Dewey equation, decaying to a constant velocity, comes by evaluating the derivative of the Dewey equation which is given in Equation 1.11, and repeated here for convenience:

$$\frac{dR_s}{dt_s} = Ba_0 + \frac{Ca_0}{1 + a_0t_s} + \frac{Da_0}{2(1 + a_0t_s)\sqrt{\ln(1 + a_0t_s)}} \quad (4.4)$$

When evaluated as  $t \rightarrow \infty$  the result is:

$$\frac{dR_s}{dt_s} \Big|_{t \rightarrow \infty} = Ba_0 \quad (4.5)$$

$Ba_0$  is a velocity for which dividing by  $a_0$  gives Mach number. This is the Mach number of the shock as time goes to infinity. Since the shock must decay to a sound wave,  $B$  should equal 1. Many authors have found this limit to be useful and have fixed  $B = 1$  and fit only the remaining 3 parameters [60, 67, 86, 87, 88, 89]. In [68] it was found that by allowing all 4 parameters to be fit resulted in  $B$  being approximately equal to 1. If the found coefficients will be used to predict properties past the range of the data, forcing the  $B$  coefficient to 1 may help ensure the extrapolated data expands at a realistic rate. If all analysis will be within the bounds of the data, the fit that produces the best fit is optimal.

A close look at the Dewey equation reveals that the equation is a dimensional equation and would appear to involve taking the natural logarithm of dimensional quantities. Because the argument of the natural logarithm must be dimensionless, there is an implied normalizing length scale in these function arguments. It can be assumed that this length scale is implicitly chosen to have a value of unity in whatever units are being used (e.g. 1 m). The parameters  $A$ ,  $C$ , and  $D$  all have dimensions of length and  $B$  is dimensionless.

Equation 1.10 could be recast in a dimensionless form by a characteristic length  $L_c$ . The dimensionless equation is then:

$$R^* = \frac{R}{L_c} = A + B \frac{a_0 t_s}{L_c} + C \ln\left(1 + \frac{a_0 t_s}{L_c}\right) + D \sqrt{\ln\left(1 + \frac{a_0 t_s}{L_c}\right)} \quad (4.6)$$

where  $R^*$  is a non-dimensional radius. The resulting coefficients in the modified equation are all dimensionless. The derivative form of Dewey equation, Equation 1.11 can be made dimensionless using the same approach and is given by:

$$\frac{\frac{dR^*}{dt_s}}{\frac{a_0}{L_c}} = M = B + \frac{C}{1 + \frac{a_0 t_s}{L_c}} + \frac{D}{2\left(1 + \frac{a_0 t_s}{L_c}\right) \sqrt{\ln\left(1 + \frac{a_0 t_s}{L_c}\right)}} \quad (4.7)$$

The choice of the characteristic length scale is important and affects the value of the resulting parameters. Figure 4.6 shows the time-radius data from the gram scale charges fit to all 4 parameters and Figure 4.8 shows the data fit to the  $A$ ,  $C$ , and  $D$  parameters. In both cases the fit parameter values are identical between fitting to the traditional Dewey equation, Equation 1.10, and the dimensionless Dewey equation, Equation 4.6 with a characteristic length scale of  $L_c = 1$  m. Figures 4.7 and 4.9 show the Mach number radius curves for the fits to all the parameters and the  $A$ ,  $C$  and  $D$  parameters respectively.

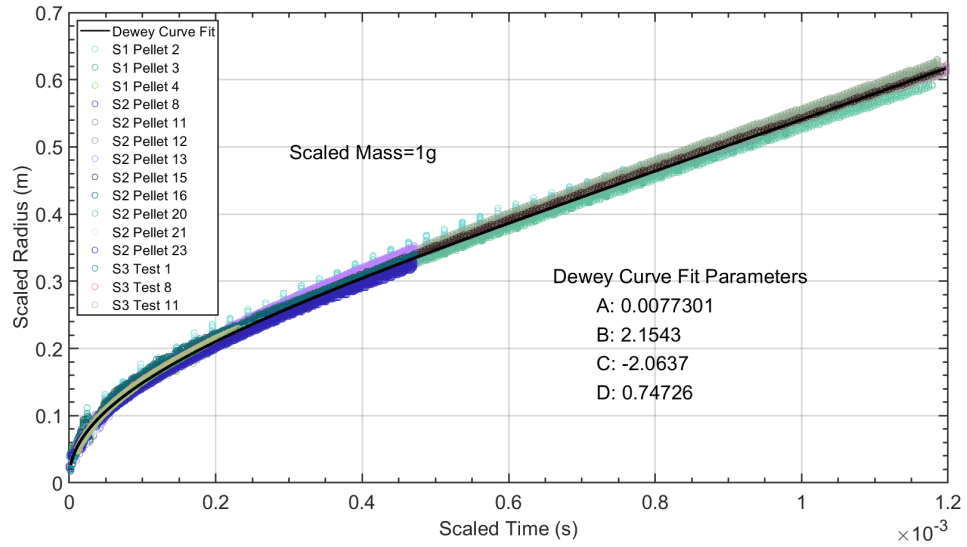


Figure 4.6: The scaled shock wave time and radius data with the Dewey curve fit found by fitting all coefficients.

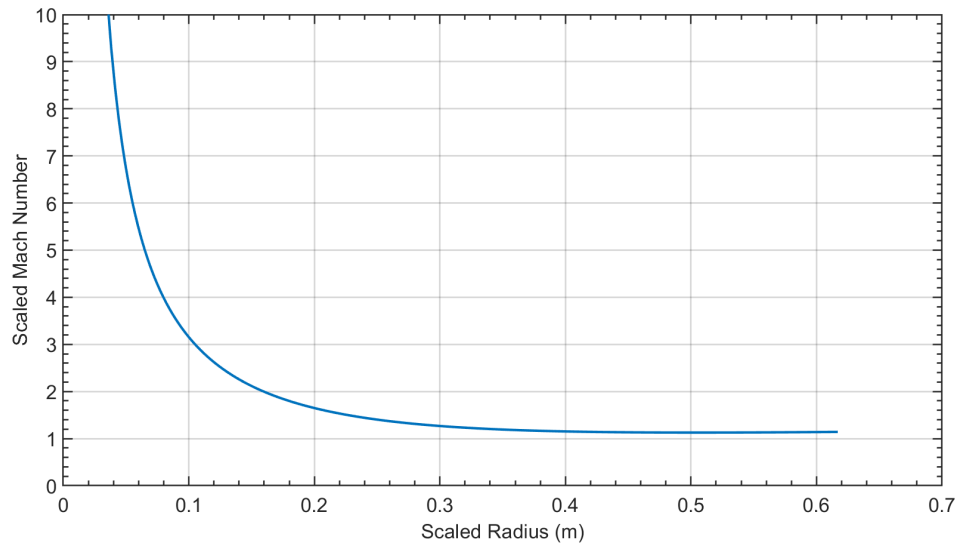


Figure 4.7: Scaled shock wave Radius Mach number for the coefficients  $A = 0.00773$ ,  $B = 2.15$ ,  $C = -2.06$ , and  $D = 0.747$  using units of meters and seconds.

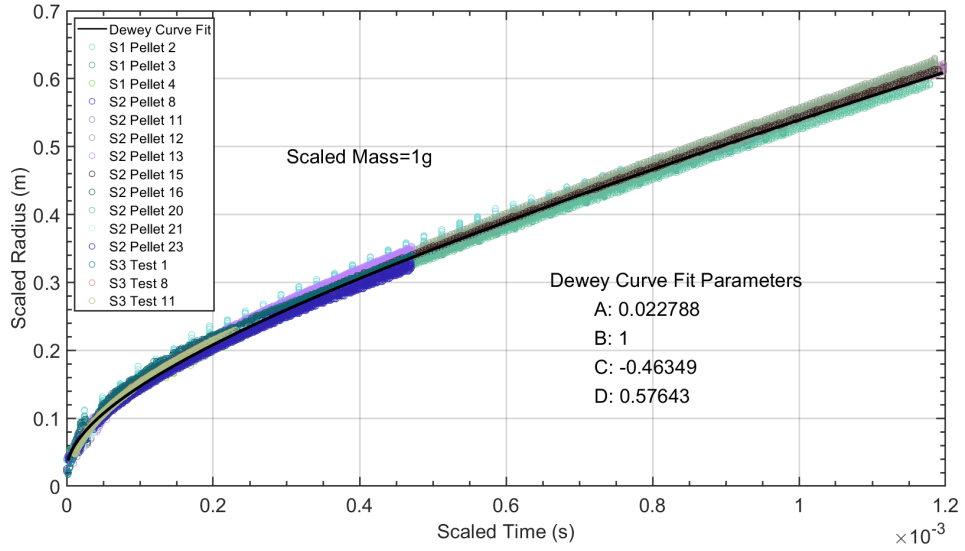


Figure 4.8: The scaled shock wave time and radius data with the fit Dewey curve fit found by fitting  $A$ ,  $C$ , and  $D$  coefficient.

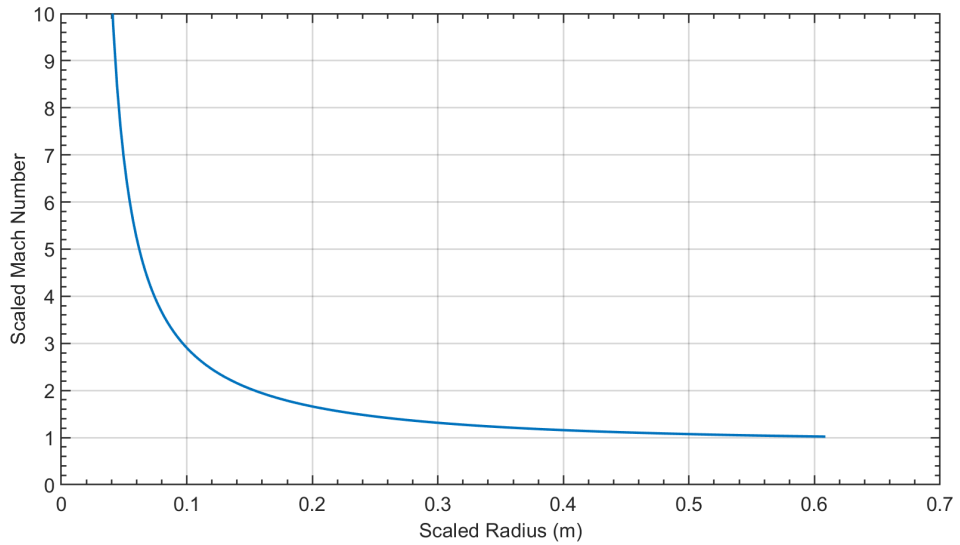


Figure 4.9: Scaled shock wave Radius Mach number from the coefficients  $A = 0.0228$ ,  $B = 1$ ,  $C = -0.463$  and  $D = 0.576$  using units of meters and seconds.

In Figure 4.10 the gram scale data was fit to all the parameters of the dimensionless Dewey equation using a characteristic length scale of  $L_c = 0.005$  m, which is the charge radius. In Figure 4.11 the data was fit to the  $A$ ,  $C$  and  $D$  parameters of the dimensionless Dewey equation and shows that constraining the  $B$  term to unity is useful at any length scale. In the dimensionless form of the Dewey equation the  $A$  term should be the non-dimensional charge radius. By setting the characteristic length scale equal to the charge radius the theoretical value of  $A$  should be unity. Figure 4.12 shows that by fixing the  $A$  and  $B$  terms to unity and fitting the  $C$  and  $D$  terms gives a good fit. Comparing the difference between the fit parameters, listed in Table 4.1, show the importance of the choice of length scale in the use of the new dimensionless Dewey equation.

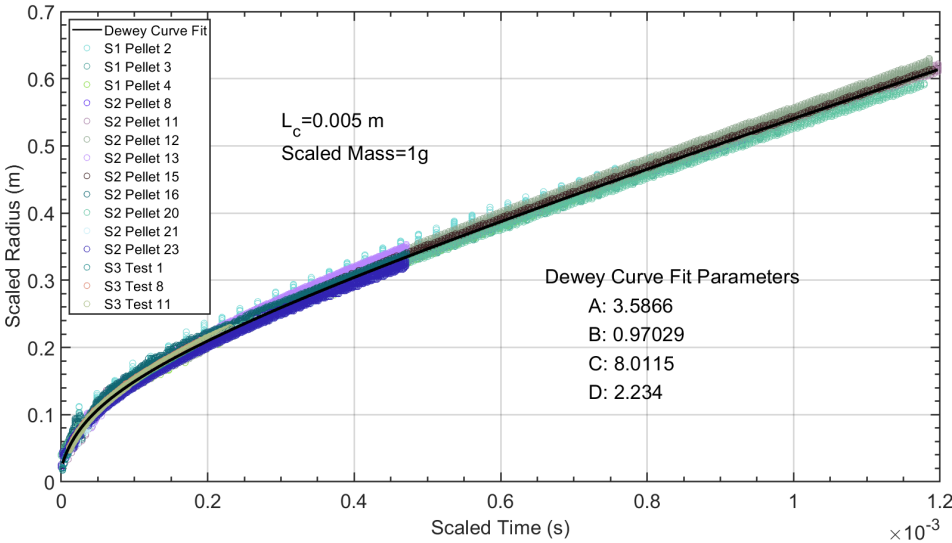


Figure 4.10: The scaled shock wave time and radius data with the dimensionless Dewey curve fit found by fitting all coefficients with a characteristic length scale of  $L_c = 0.005$  m.

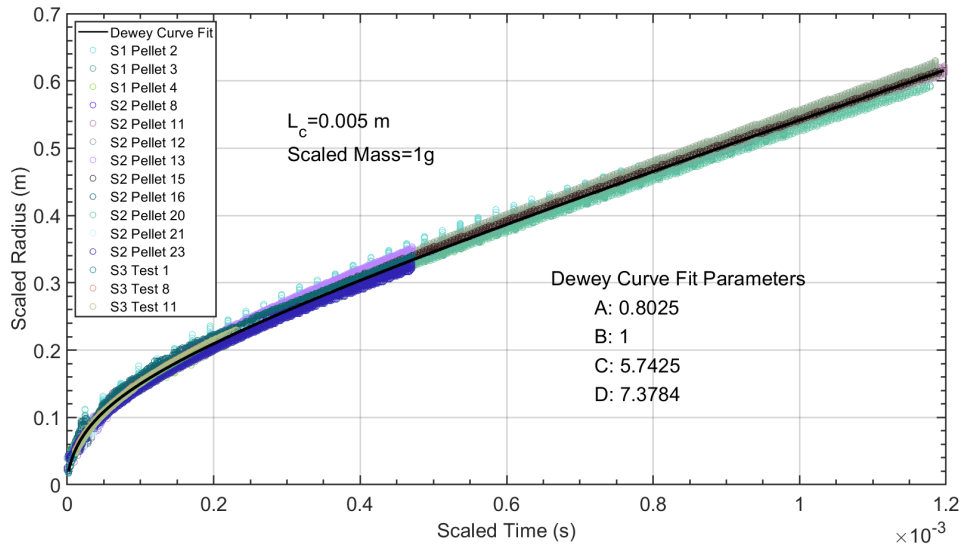


Figure 4.11: The scaled shock wave time and radius data with the fit Dewey curve fit found by fitting  $A$ ,  $C$ , and  $D$  coefficient with a characteristic length scale of  $L_c = 0.005$  m.

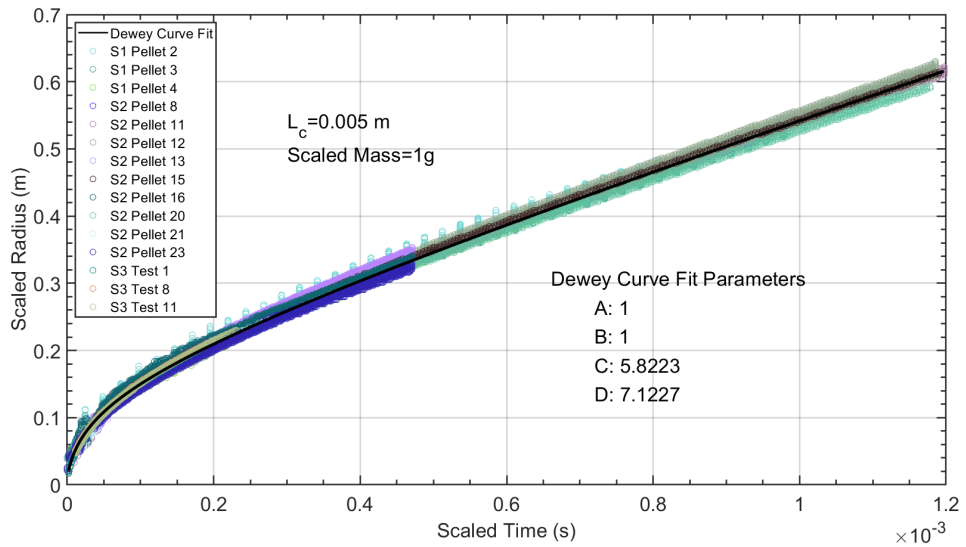


Figure 4.12: The scaled shock wave time and radius data with the fit Dewey curve fit found by fitting  $C$ , and  $D$  coefficient with a characteristic length scale of  $L_c = 0.005$  m.

Table 4.1: Resulting coefficients from different Dewey Curve fits. All coefficients were determined using units of meters and seconds.

$L_c$ (m)	Fixed Terms	$A$	$B$	$C$	$D$	$R^2$ of fit
1	None	0.00773	2.15	-2.06	0.747	0.9976
1	$B$	0.0228	1	-0.463	0.576	0.9970
0.005	None	3.5866	.970	8.01	2.23	0.9976
0.005	$B$	0.803	1	5.74	7.38	0.9976
0.005	$A, B$	1	1	5.82	7.12	0.9976

The dimensionless Dewey equation is a useful tool for curve fitting to handle data but attempting to extract physical interpretations from its parameters is limited. For certain combinations of speed of sound  $a_0$  and characteristic length scale  $L_c$ , which sets the units of time and radius, the  $A$  term is the initial charge radius and the  $B$  term is the Mach number as the shock approaches infinite radius. The  $C$  and  $D$  terms do not provide any physical insights. Future work with this equation should further explore the length scale parameter using data from testing at multiple scales. Additional work could consider improving the functional form of the equation to enhance physical interpretation of the remaining curve fit parameters.

The fit coefficients and resulting  $R^2$  from the five fitting methods are listed in Table 4.1. All the curve fitting approaches provided acceptable agreement with the data. Setting the characteristic length scale equal to the charge radius allowed the  $A$  term to be fixed at unity, but using  $L_c = 1$  m returns the fit parameters for the dimensional form of the Dewey equation that have been reported in the literature. To simplify comparison with literature, the length scale equal to  $L_c = 1$  m will be used in the remainder of this work. None of the analysis of the current work will be done past the bounds of the experimental data, so the curve fit to all coefficients will be used in the analysis with coefficients of  $A = 0.00773$ ,  $B = 2.15$ ,  $C = -2.06$ , and  $D = 0.747$ .

### 4.3 Experimental Peak Pressure and Impulse

Two of the main physical properties of a shock wave that are of interest in this work are the peak pressure and impulse. For a single location, both properties can be measured from a pressure-time history from a pressure transducer. A representative pressure trace from the explosion of 0.9732 g of PETN at a distance of 0.1754 m without a reflected shock is shown in Figure 4.14. The peak pressure is defined as the maximum pressure generated by the shock wave. The shock impulse is defined as the integral of pressure starting at the time of arrival of the shock and ending when the pressure trace returns to zero for the first time. These data can be used as recorded, with values taken directly from the pressure trace, but the limited response time of the pressure transducer, pressure gauge

momentum and other real effects results in an unphysical non-uniform ringing in the data that results in inaccuracies. One method to smooth out the ringing is to fit the data to the Friedlander equation, Equation 1.14, which is repeated here for reference:

$$P(t) = P_s e^{-\frac{\alpha t}{t_d}} \left(1 - \frac{t}{t_d}\right) \quad (4.8)$$

Figure 4.13 is a flow diagram outlining process used to fit the pressure data to the Friedlander equation. The first step was to crop the data from the time of arrival to approximately the first time the pressure trace returns to zero, the cropped data is shown in Figure 4.15. Note that the Friedlander equation form requires that the shock wave peak pressure occurs at a time of  $t=0$ , so the cropped pressure data is plotted versus time from shock wave arrival. A non-linear regression analysis is then used to fit the Friedlander equation to the cropped data. The found fit and resulting parameters are shown in Figure 4.15. The analysis results in three fitting parameters,  $P_s$  which is the peak pressure,  $t_d$  the pulse duration, and  $\alpha$  which is a wave shape parameter. The impulse can be found by integrating the Friedlander equation from time of zero to the pulse duration.

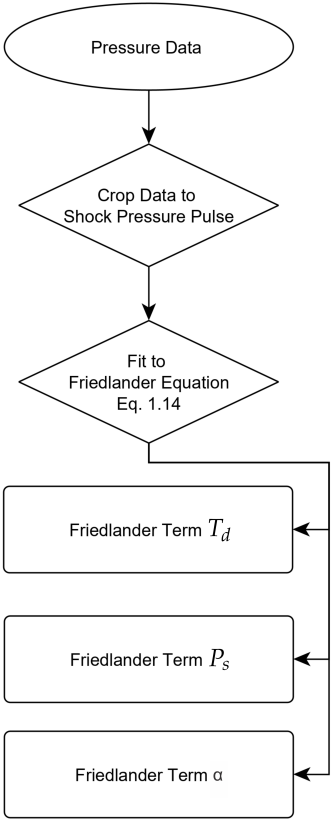


Figure 4.13: Flow chart outlining the calculation of Friedlander parameters.

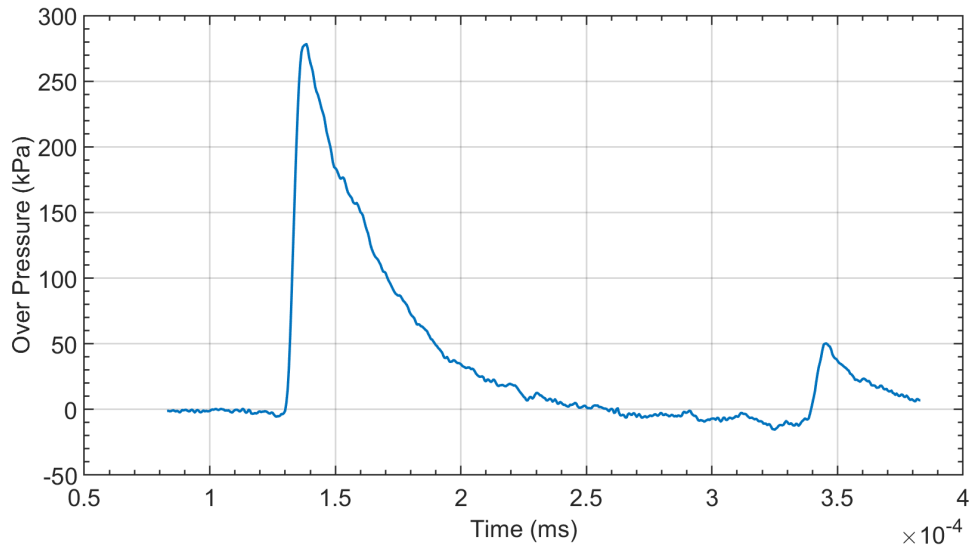


Figure 4.14: Representative un-modified pressure trace from test N1 which is a no shock reflection test.

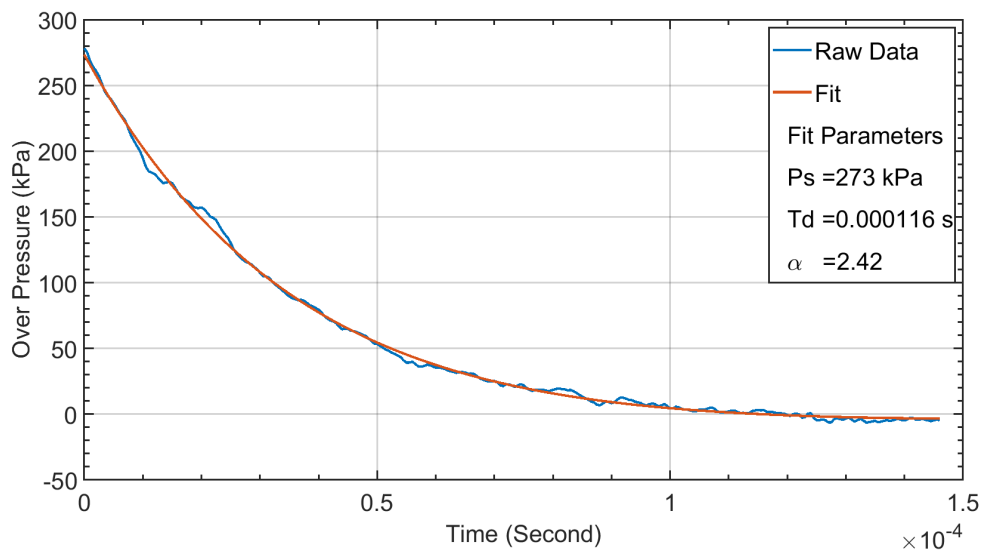


Figure 4.15: The pressure trace from N1 cropped from the time of arrival to when the pressure returned to zero. The cropped pressure trace was then fit to the Friedlander equation

The length of the data fit to the Friedlander equation was found to have a major impact on how well the fit matched the data. The starting point used to crop the pressure trace was the time of arrival of the shock for all cases. A simple algorithm was then used to find the first time the pressure reached zero over pressure, which was used as the end point of the crop. This point will be referred to as the estimated pulse duration. This method worked well for most of the pressure traces. In some cases, however, the fit gave highly unrealistic values, such as values of  $t_d$  that were negative or on the order of seconds. In other less extreme cases the fit was just visibly outside the range of the pressure data. There was found to be multiple sources of error that led to the poor fit, including noise in the pressure data and secondary shock waves.

This problem was fixed by manually adjusting the estimated pulse duration to the first crossing. Figure 4.16 shows a pressure trace with large oscillations within the pressure decay. When the data was cropped to the estimated pulse duration and fitted, the resulting  $t_d$  was an order of magnitude too high. By extending the range of data fit by 40% the fit was greatly improved. The length of data used to fit and resulting fit is shown in Figure 4.16. Similarly, most of the pressure trace data was extended by some amount past the estimated pulse duration prior to fitting, with a 40% extension being the most common. Further automation of the extension to the estimated pulse duration resulted in a large number of unphysical fits so the extension to the estimated pulse duration was determined manually. The manual adjustment was required because variations in the 3 parameters of the Friedlander equation can result in very different curve shapes with minimal difference in  $R^2$  or other metrics of curve fit "goodness".

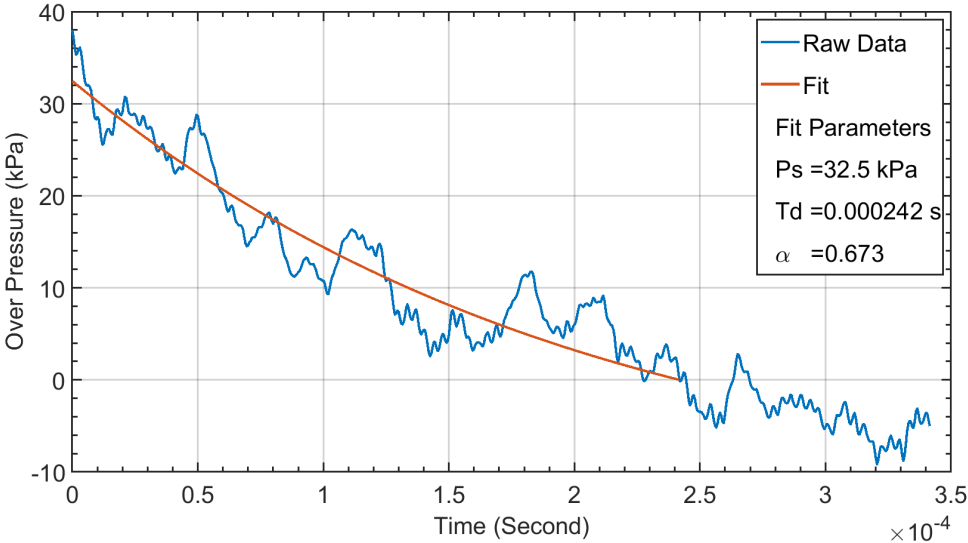


Figure 4.16: Representative high noise pressure trace from test N2 pressure probe 13, which was 0.457 m from the charge, that was cropped and fit to the Friedlander equation.

Table 4.2: Summary of the data collected for each no reflection test.

Test ID	Usable Pressure Traces	1 m Z shadowgraph (kfps)
N1	7	250
N2	12	200
N3	10	200
N4	9	200
N5	9	500

Using this methodology the pressure trace data from all tests was fit to the Friedlander equation. The found Friedlander parameters for all tests are shown as a function of radius in Figures 4.17 - 4.19. Table 4.2 lists the number of usable pressure traces from each test. Figure 4.17 shows the found peak pressure term normalized by the atmospheric pressure as a function of radius. Figure 4.18 shows the found pulse duration as a function of radius. Figure 4.19 shows the Friedlander  $\alpha$  term as a function of radius.

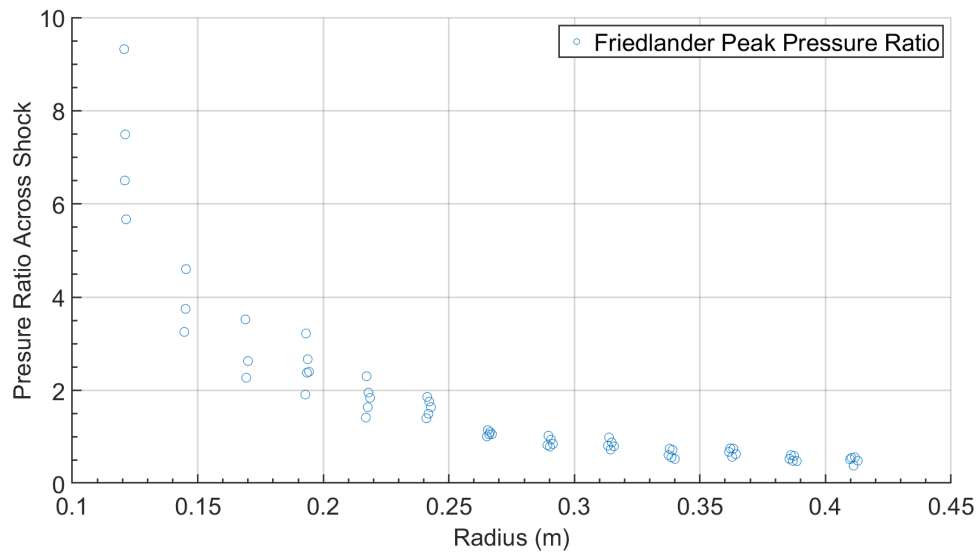


Figure 4.17: Ratio of pressure across the shock wave as a function of radius for the fit experimental data.

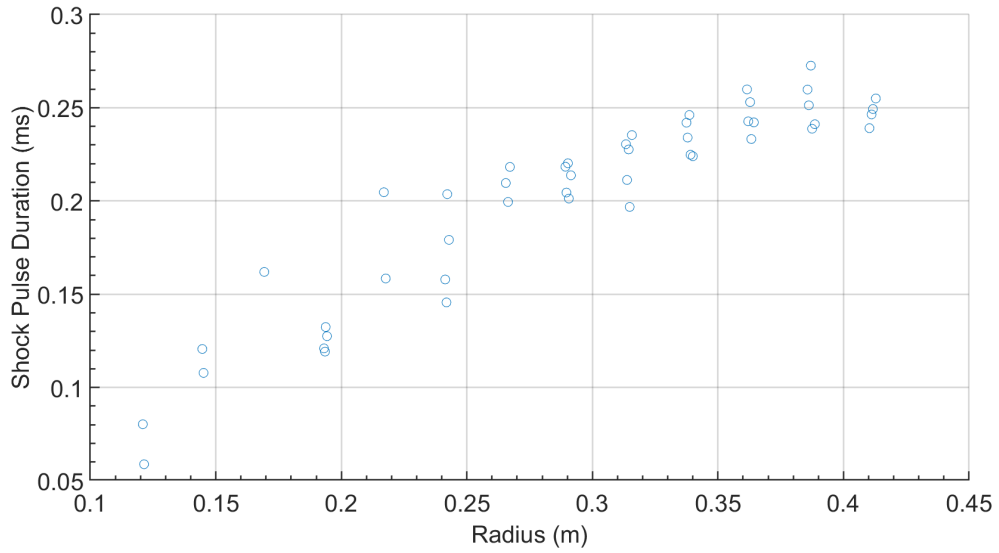


Figure 4.18: Pulse duration of the shock pressure as a function of radius for the fit experimental data.

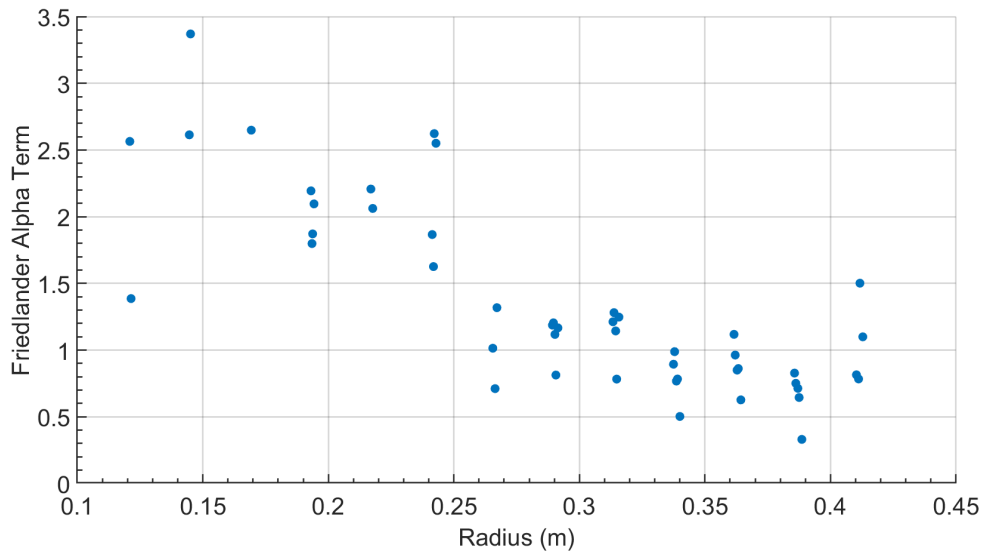


Figure 4.19: The decay coefficient  $\alpha$  as a function of radius for the fit experimental data.

#### 4.4 Analytical Peak Pressure and Impulse

Figure 4.20 is a flow chart to summarize the process that will be detailed in the following section to analytically calculate the peak pressure and impulse. Inputs such as data and assumptions are shown in ovals. Calculations and fits are shown in diamonds. There are three terms that are used to calculate impulse: peak pressure, pulse duration and decay coefficient. The sub-process for each term is grouped and outlined.



Figure 4.20: Flow chart outlining the calculation of analytical impulse.

### 4.4.1 Analytical Peak Pressure

The peak pressure and impulse can also be determined from the Mach number radius curve. The peak pressure from a shock wave can be calculated using classic compressible flow equations [91]. The ratio of peak pressure over atmospheric pressure is given as a function of Mach number in Equation 1.13. Using the Dewey coefficients found in Figure 4.6 the Mach number as well as the resulting over pressure ratios is shown as a function of radius in Figure 4.21. This analytical model shown in Figure 4.21 is representative of the experimental setup where the shock wave passes over the test section without generating a reflection. Both the analytical over pressure ratio and experimental Friedlander data are shown in Figure 4.22. The analytical curve falls within the experimental data but is below the mean of the data.

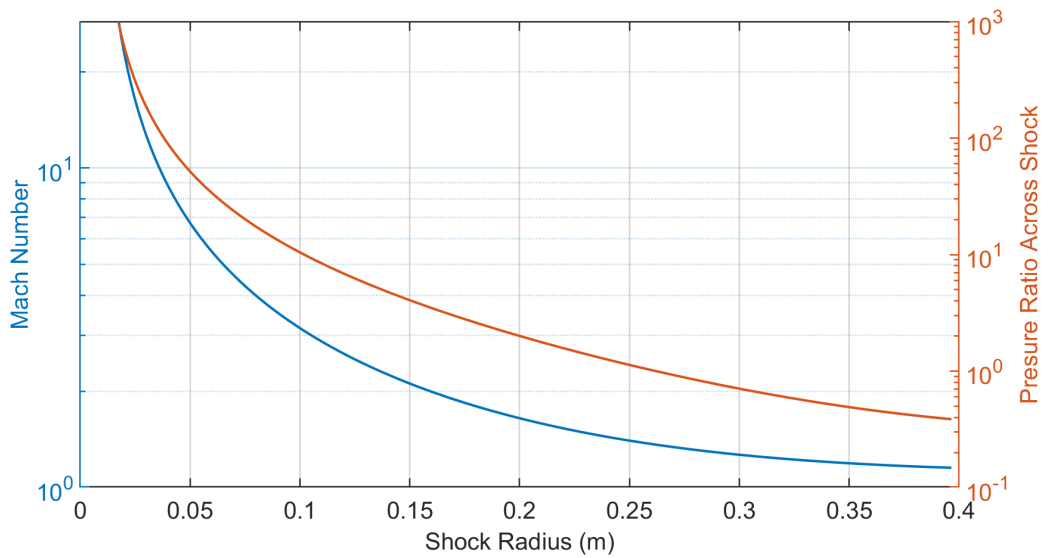


Figure 4.21: The Mach number and pressure ratio across the shock as a function of radius.

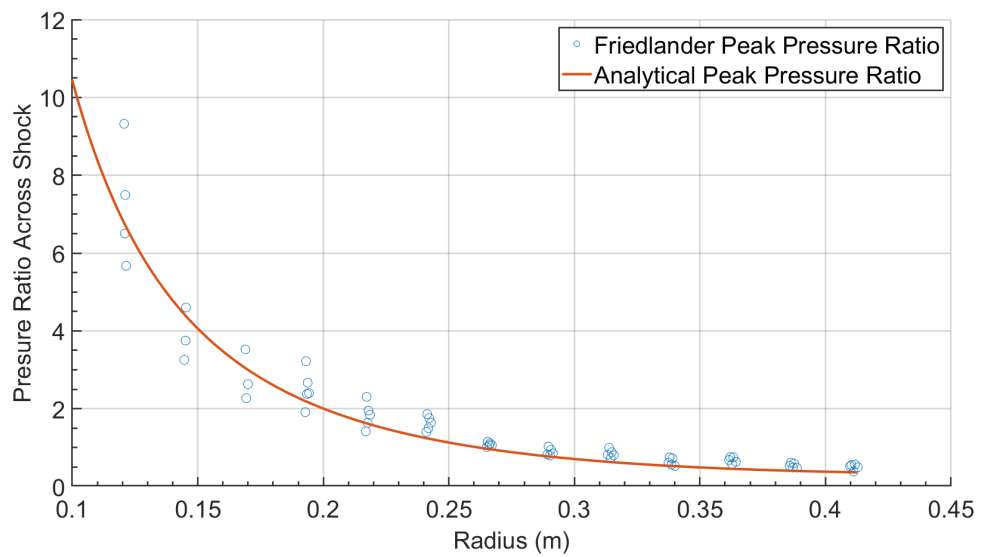


Figure 4.22: Comparison between peak pressure found from the pressure traces and Friedlander curve fit versus the shock radius versus time and one-dimensional gas dynamics.

#### 4.4.2 Analytical Pulse Duration

The current model for pulse duration is based on the idea that pulse duration is the time difference between the arrival of the shock and when the pressure returns to one atmosphere, or zero overpressure [70, 89, 92]. Zero overpressure is characteristic of a sound wave, so it would be expected that the point of zero overpressure propagates at the local speed of sound [70, 74]. This propagating point at zero overpressure is referred to as the "release wave" and tracking this point from the interface forward is a method to determine the pulse duration.

The previous method for estimating pulse duration [70, 89, 92] is investigated here in more depth to ground the estimate in more physical wave behavior. The duration estimation approach tracks the propagation and arrival of a release wave propagating through the shock field. The shock wave time of arrival for any point can be calculated using the standard Dewey equation, Equation 1.10. The release wave will move at the local speed of sound, which is given by

$$a = \sqrt{\gamma R_{spec} T} \quad (4.9)$$

where  $R_{spec}$  is the specific gas constant, and  $T$  is the local temperature [72]. Assuming an ideal gas, where  $\gamma$  and  $R_{spec}$  are constant then the temperature is the only term that will vary as a function of Mach number and radius. The temperature ratio across a shock wave is a function of Mach number and is given by

$$\frac{T_2}{T_1} = \frac{(1 + \frac{\gamma-1}{2} M^2)(\frac{2\gamma}{\gamma-1} M^2 - 1)}{M^2(\frac{2\gamma}{\gamma-1} + \frac{\gamma-1}{2})} \quad (4.10)$$

where  $T_1$  is the temperature before the shock wave,  $T_2$  is the temperature after the shock wave, and  $M$  is the Mach number of the shock wave. Using Equation 4.10 and the Mach number radius curve, the temperature immediately following the shock wave is shown in Figure 4.23. By assuming that the temperature is constant from the time the shock passes until the arrival of the release wave, the local speed of sound at every point in the shock field can be calculated using the post-shock temperature and Equation 4.9. The local speed of sound as a function of radius and Mach number is shown in Figure 4.24. Using the speed of sound as the wave speed for the relaxation wave, the relative wave velocity for the shock and release waves are shown in Figure 4.25.

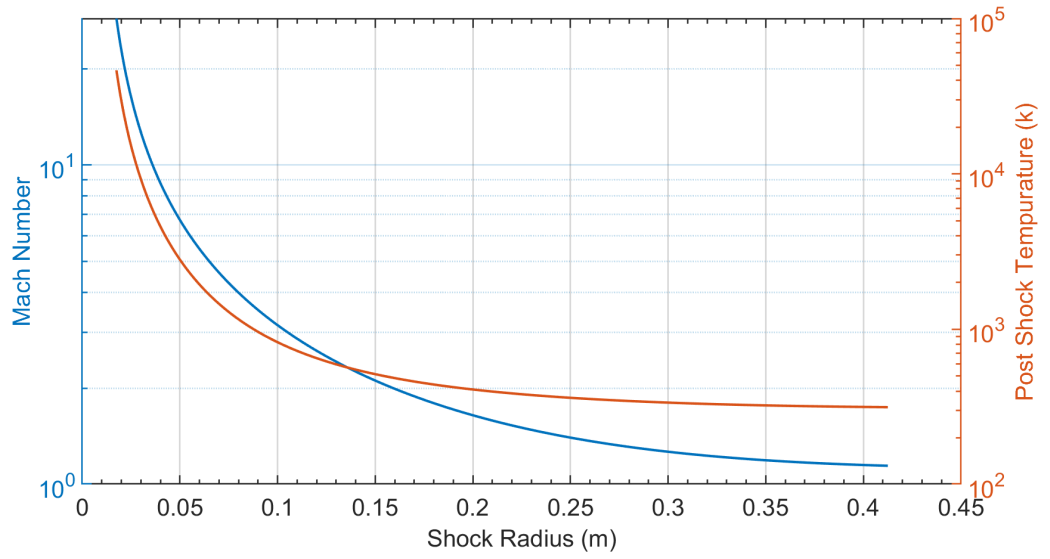


Figure 4.23: The Mach number and post shock temperature as a function of radius.

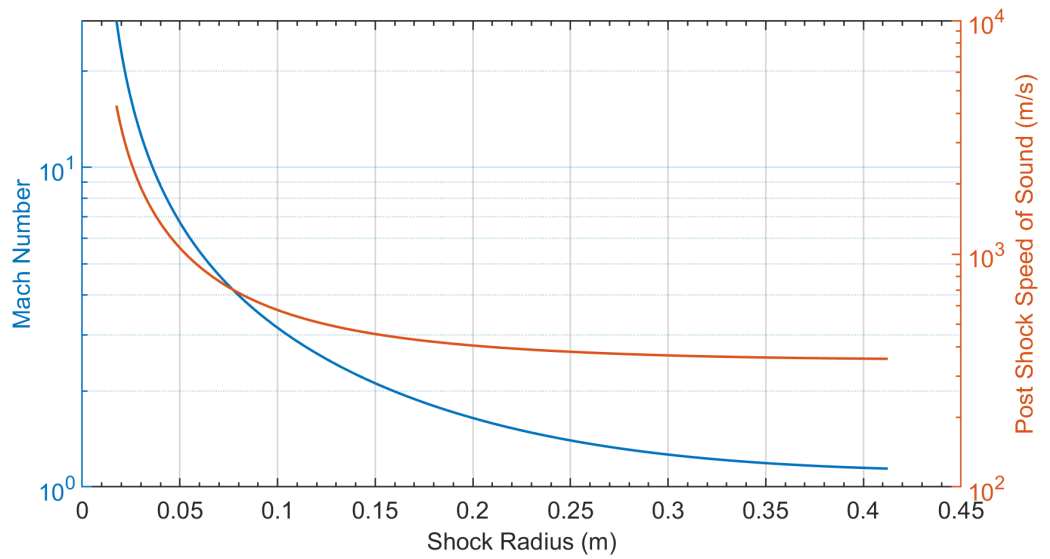


Figure 4.24: The Mach number and post shock speed of sound as a function of radius.

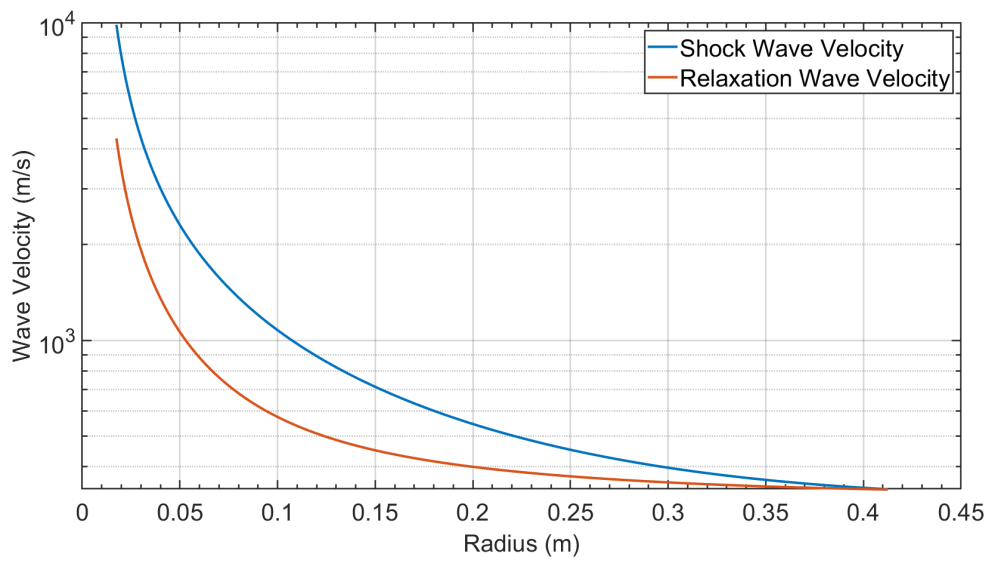


Figure 4.25: The wave velocities of the shock wave and relaxation wave as function of radius

The relative wave speeds can be used to determine the position of the two waves which gives the pulse duration. Figure 4.26 is an  $x-t$  diagram of the shock and release wave positions. The vertical distance between the two lines, colored purple, is the pulse duration. At early times the pulse duration is minimal and increases at greater radii. Figure 4.27 shows the numerical value of the pulse duration as a function of radius as well  $x-t$  diagram of the two waves. Figure 4.28 shows the analytical model of pulse duration and the experimental Friedlander values for pulse duration. The analytical model matches the trend of the experimental data but falls below the mean of the experimental data. This method also predicts that as the shock approaches 0 radius it asymptotically approaches a pulse duration of 0.

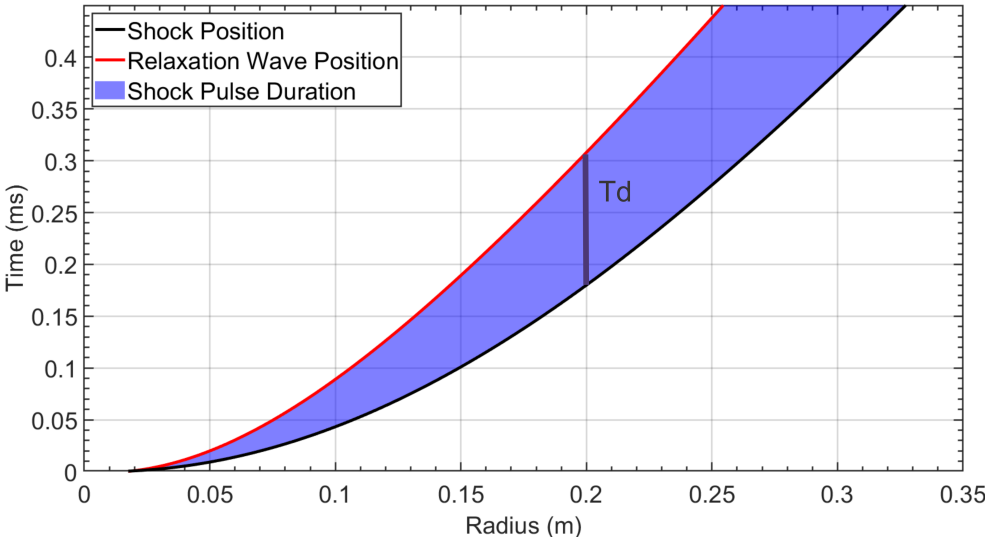


Figure 4.26:  $x-t$  diagram of the position of the shock and relaxation wave as a function of radius. The area between the curves is highlighted since the vertical distance is the pulse duration.

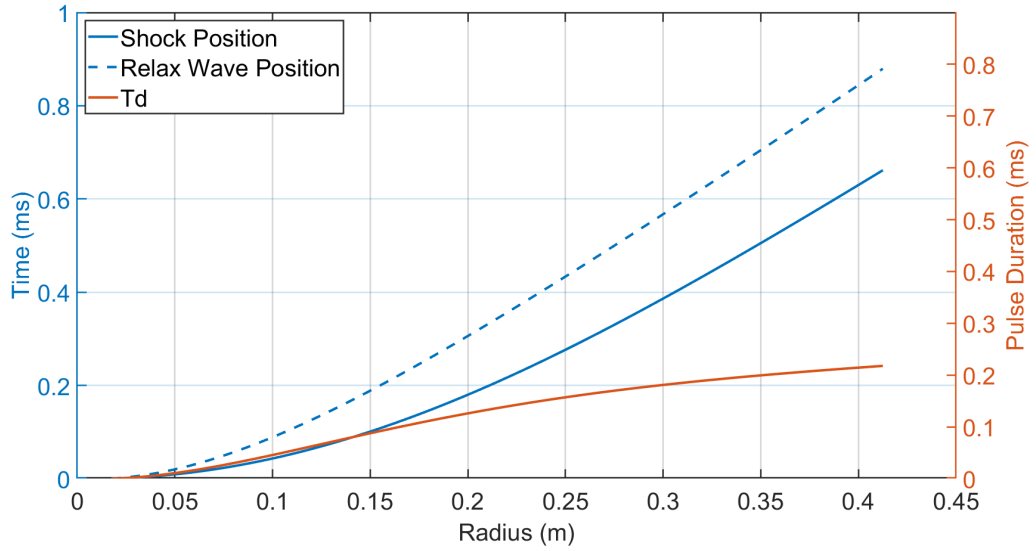


Figure 4.27:  $x$ - $t$  diagram of the position of the shock and relaxation wave as a function of radius and the resulting numerical value of the pulse duration.

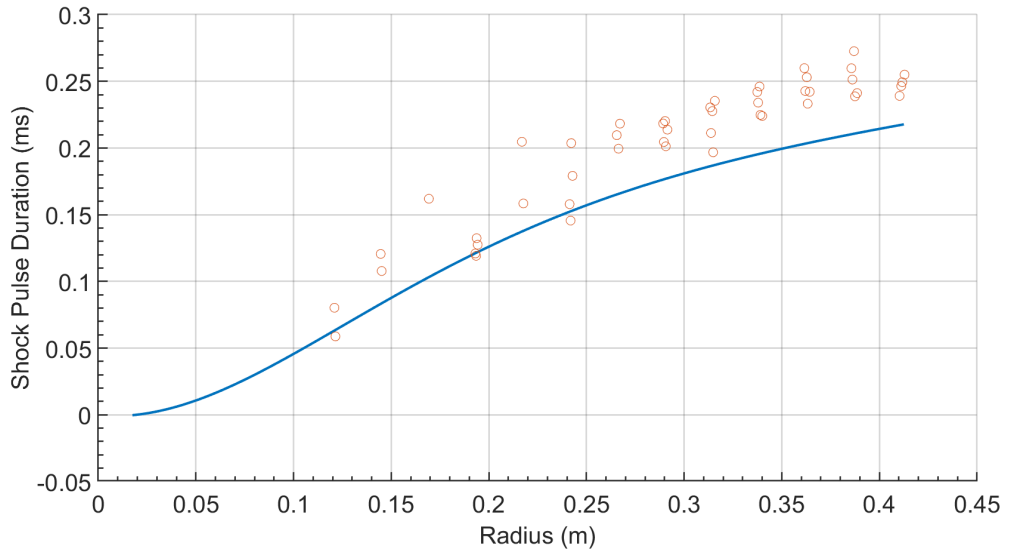


Figure 4.28: Comparison of the experimental and analytical values for pulse duration.

### 4.4.3 Analytical Model of Pulse Duration Release Wave

One cause for the discrepancy between the analytical and experimental pulse duration is the assumption that the release wave begins to propagate outwards from the surface of the pellet at shock wave break out. Figure 4.29 shows a simplified 1D cartesian wave diagram of the explosive pellet. For simplicity all velocities are shown as constant in Figure 4.29 so the diagram is a schematic representation and has been expanded temporally to better show details. To give an approximate time scale for the events in the diagram, the rarefaction fan is expected to reach the zero radius line on the order of microseconds. The first wavelet, or head, of the rarefaction fan is expected to reach the air-detonation product interface at a time on the order of  $10\mu s$  and the tail of the rarefaction fan reaches the interface on the order of  $100\mu s$ . State 0 is unreacted PETN and A1 is ambient air. Time  $t = 0$  is detonator initiation at the pellet center. State 1 is the Chapman-Jouguet (CJ) state for PETN which assumes the detonation shock is not under or over driven. When the shock wave reaches the surface of the pellet an air shock is sent into the ambient air. The gas interface between the shocked air and detonation products cannot support a pressure or particle velocity difference. A rarefaction fan moves from the interface into the detonation products to accelerate the gas to balance pressure and velocity across the interface. In the diagram the rarefaction fan is broken into 10 wavelets for later use with method of characteristics analysis. No other waves are generated at the shock wave breakout. This supports the idea that the shock wave breakout is not the origin of the release wave.

The origin of the release wave should be when the pressure at the detonation product interface reaches atmospheric pressure. Zero over pressure is the defining feature for pulse duration so tracking this point from the interface forward is a possible way to determine the pulse duration. In Figure 4.29 the rarefaction fan moves from the interface at shock wave breakout into the detonation products and reflects from the center line as a rarefaction fan. Since the detonation products have a higher impedance than the shocked air, when the rarefaction fan reaches the interface it is transmitted into the shocked air as a rarefaction fan. During the interaction between the rarefaction fan and the interface the release wave will be generated. Determining this point during the interaction that the absolute pressure reaches one atmosphere, zero over pressure, is difficult. A point that should occur near the same time as the zero over pressure point but can be more easily determined is the point of maximum detonation product expansion.

Neither the point of zero over pressure or maximum expansion can be accurately determined from the experimental focused shadowgraph images. Figure 4.30 is a streak image from a no-reflection test N5, imaged with the the 30 cm focused shadowgraph. In Figure 4.30 identifying the gas cloud in the early time, less than  $100\mu s$ , is difficult due to the high level of turbulence behind the shock wave. Due to the noise from the turbulence it is not possible to accurately determine the time and radius at which the gas cloud is at maximum expansion. It is also not possible to calculate pressure from focused shadowgraph images

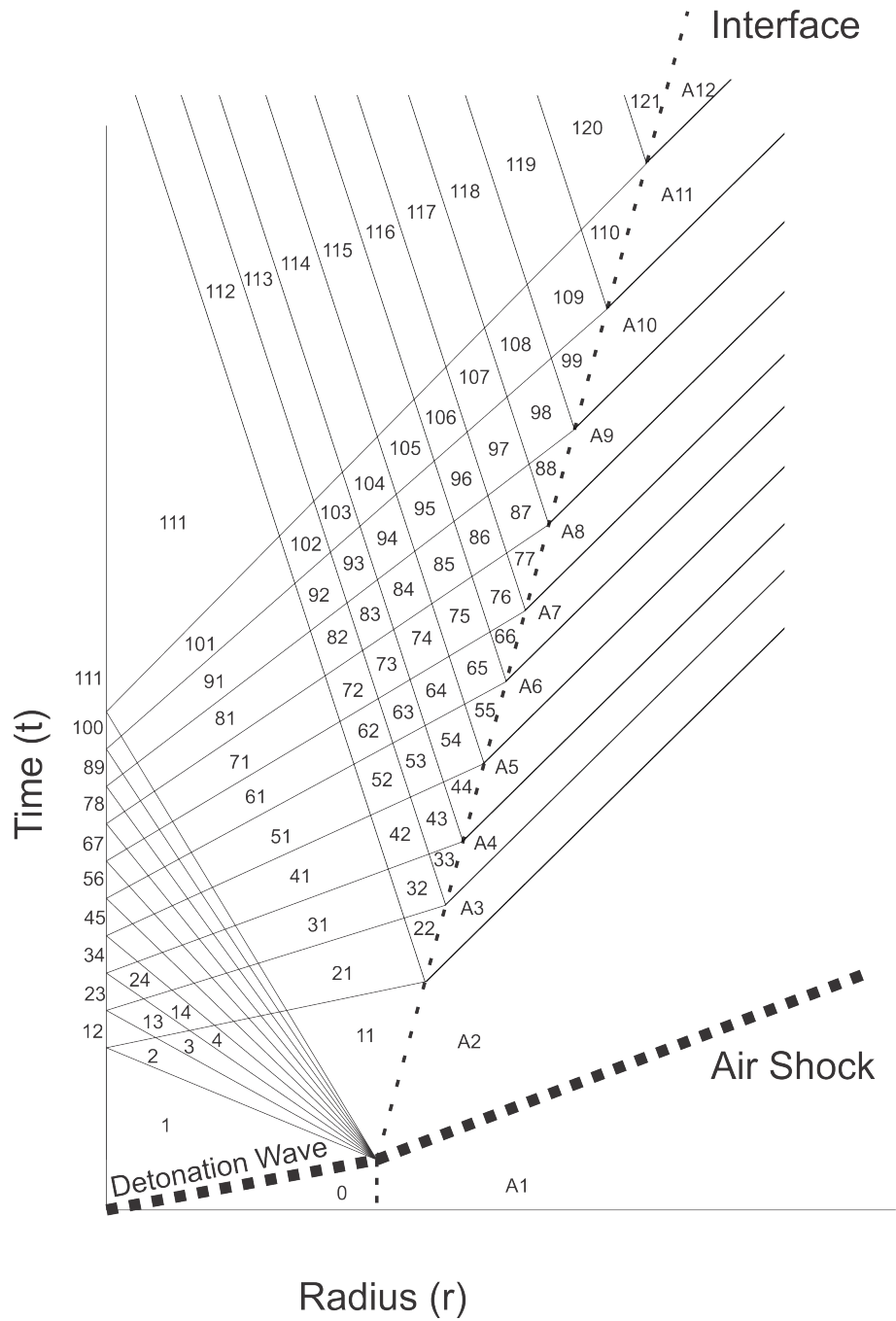


Figure 4.29: Simple 1D wave diagram of the detonation and expansion of a high explosive. The rarefaction fan generated at shock wave breakout is divided into 10 wavelet.

so the point of zero over pressure can not be identified from the images. Analytical models and computational simulations will not have these problems as turbulence is omitted from many simulations and models and the pressure can be plotted at all points from simulations or models.

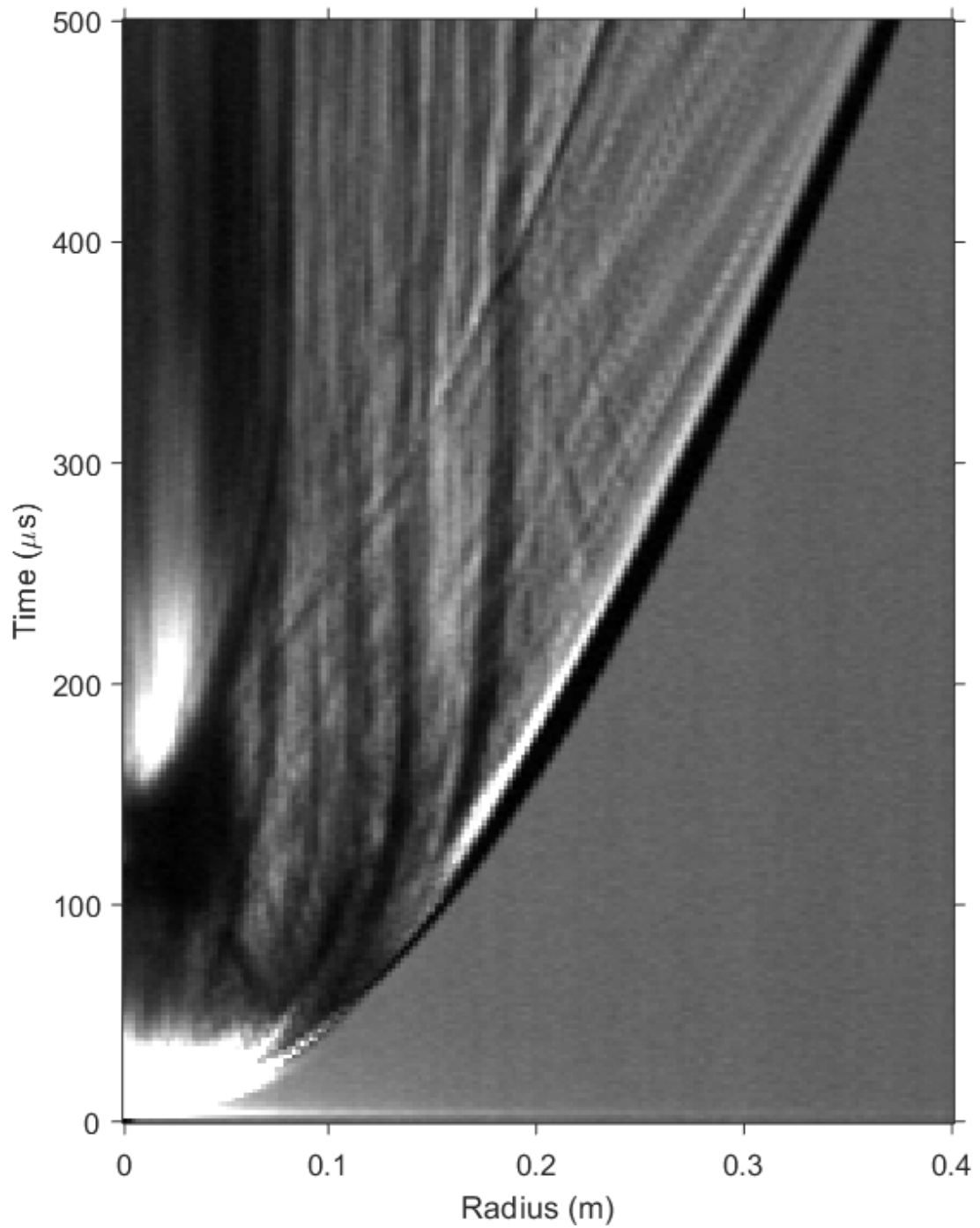


Figure 4.30: Streak shadowgraph image from test N5. The zero radius point is at the center of the charge and the streak image was generated from a horizontal line.

A method of characteristics approach can be used to develop an analytical model of the expansion process of the PETN pellet immediately after detonation. This approach divides the area of interest into regions of uniform properties separated by lines of constant change. Using this approach allows a continuous process, like an expansion fan, to be discretized. Further details on application of method of characteristics to compressible flow problems can be found in [91, 93].

To complete the analytical model requires calculating the boundary conditions at the centerline and interface. These boundary conditions can be found by plotting and manipulating the pressure-particle-velocity (P-u) Hugoniot. The unreacted Hugoniot for PETN is shown as the blue line in Figure 4.31 and the detonation products as the red line. The intersection of these two lines is the equilibrium conditions after the detonation wave but before the rarefaction fan, state 1 in Figure 4.29. The intersection of the air Hugoniot, the yellow line in Figure 4.31, and the detonation products is the conditions after the rarefaction fan, state 11. The transition across the rarefaction fan, states 2-10, can be closely approximated by following the PETN products line from the CJ condition to the interface condition [74]. In the following analysis each of these steps will be defined as having an equal change in particle velocity. States 2-10 are shown as the light blue dots in Figure 4.31.

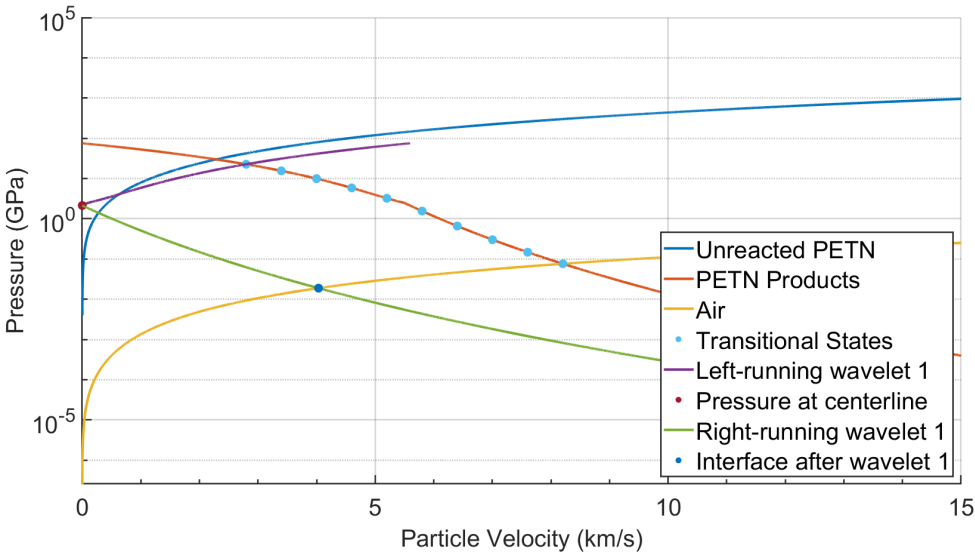


Figure 4.31: The solution for the pressure and particle velocity for the first wavelet at the center line and interface.

The locus of the first left-running wavelet is shown as the purple line in Figure 4.31. The locus of the left-running wavelet was determined by horizontally flipping the detonation products about the first transition state, state 2. Assuming symmetry at the centerline requires a velocity of zero on the centerline. The result of this assumption is that the centerline condition, state 12, is the y-intercept

of the left-running wavelet which is shown as the red dot in Figure 4.31. Horizontally flipping the detonation products about the centerline condition gives the locus of the right-running wavelet, the green line. The intersection between the right-running wavelet and the air Hugoniot is the conditions at the interface after the first wavelet, state 22.

The velocity of the intermediary states between the centerline and interface, states 13 through 21 in Figure 4.29, were determined using the method of characteristics approach of constant change across characteristic lines. The CJ velocity, state 1, was  $2.2 \text{ km/s}$  and the velocity at the initial interface, state 11, was  $8.2 \text{ km/s}$ . Dividing this change evenly across 10 lines gives each a change in velocity of  $0.6 \text{ km/s}$ . The velocity of states 13 through 21 was then determined by adding this change in velocity to the prior state, i.e. state 12 had a velocity of zero then state 13 has a velocity of  $0.6 \text{ km/s}$  and state 14 a velocity of  $1.2 \text{ km/s}$ . Once the velocity of each state was known its pressure was determined by finding the corresponding value on the right-running wavelet. The remaining state properties, speed of sound, the specific heat ratio or gamma, and density, are functions of pressure which was determined using the JonesWilkinsLee (JWL) equations of state for PETN detonation products [94]. The isentropic JWL equations of state and coefficients for PETN can be found in [95].

This process was repeated to determine the properties of each state for the remaining wavelets. Figure 4.32 shows the fifth wavelet as an additional example of the Hugoniot process. The Hugoniot were used to determine the velocity and pressure of each state and the JWL equation of state was used to determine the speed of sound, density, and gamma.

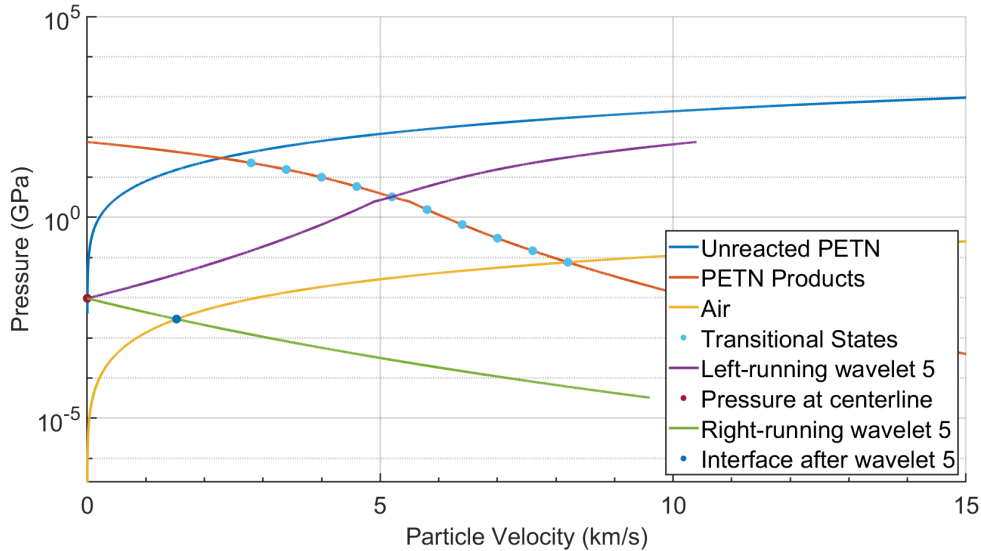


Figure 4.32: The solution for the pressure and particle velocity for the fifth wavelet at the center line and interface.

Using the P-u Hugoniot to find boundary conditions and the symmetry assumption resulted in an invalid solution. The net velocity of each wavelet is the local speed of sound plus or minus the local particle velocity. For a wave moving with the particle flow, the total velocity is the sum of the particle velocity and speed of sound and the difference for waves moving against the flow. The interface was assumed to move outward at the particle velocity of the region bordering it. Since the rarefaction fan is a continuous process the velocity of the characteristic lines were the average of the states on either side of the line. Using these assumptions, the characteristic line for the first wavelet never interacts with the interface. The wavelet had a total velocity of  $7.8 \text{ km/s}$ , an average of state 11 and 21, and the interface, state 11, expands at a velocity of  $8.2 \text{ km/s}$ .

To make a functional solution the symmetry assumption was re-evaluated. An issue with the original problem setup is that State 1 is defined as the CJ condition for PETN, having a particle velocity of the CJ velocity, but is also adjacent to the centerline which was defined as having no velocity. One method to account for the inconsistency, without changing the assumption of uniform regions or initial particle velocity, is to change the problem geometry. If the problem is redefined as the impact of a sandwich plate, shown in Figure 4.33, the rear face of the explosive can have a non-zero velocity. In the modified geometry, a slab of PETN with a width that matches the radius of pellets is impacted from one side at the CJ velocity. A detonation wave then moves from the impacted face towards the interfaces with air. The  $X = 0$  line is then the rear surface of the detonation products moving at the CJ velocity. The properties of each state were then recalculated with this set of assumption. Figures 4.34 and 4.35 are the resulting P-u Hugoniot for each of the wavelets. The particle velocity of each state is then taken as the velocity found via the Hugoniot analysis minus the CJ velocity.

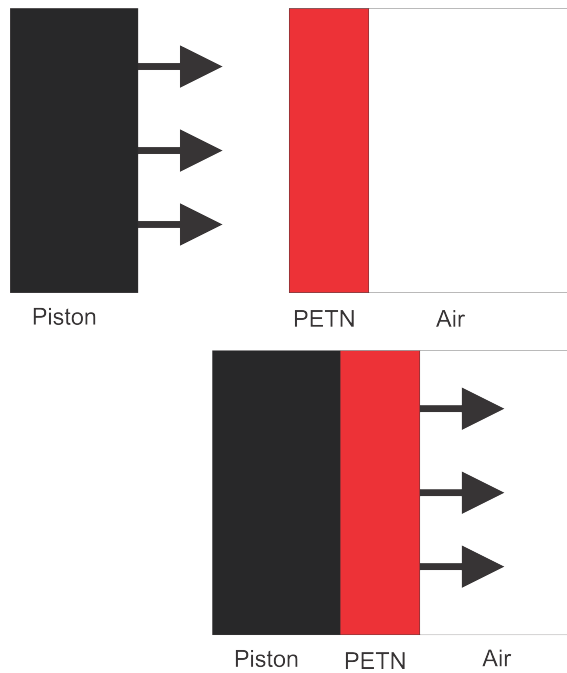


Figure 4.33: Diagram of the impact of a sandwich plate problem geometry.

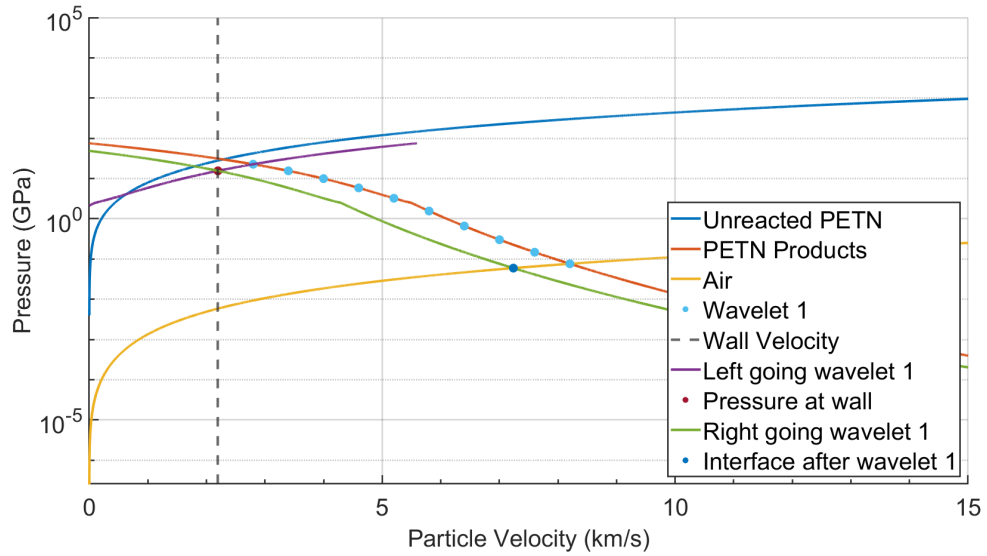


Figure 4.34: The solution for the pressure and particle velocity for the first wavelet at the center line and interface using the modified centerline assumption.

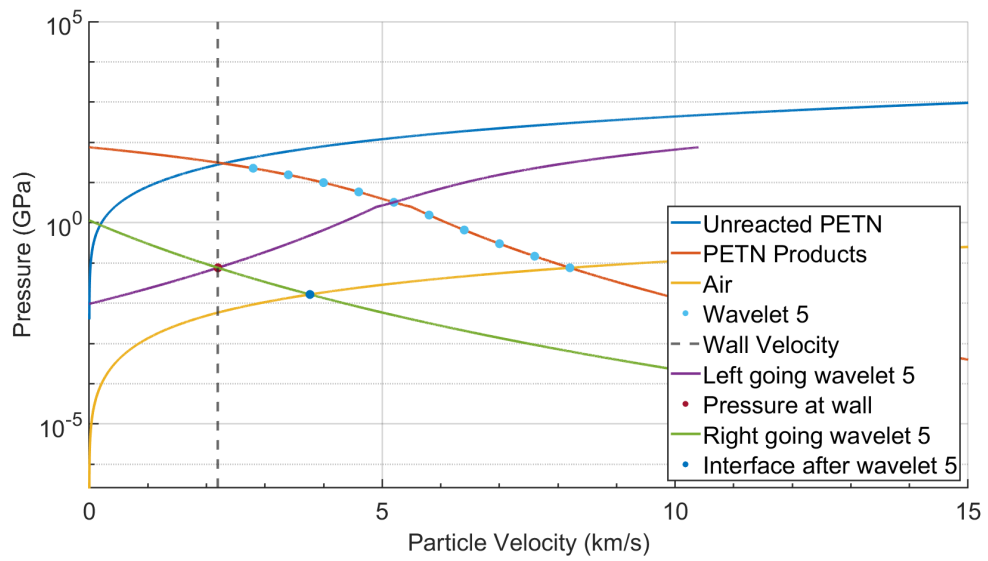


Figure 4.35: The solution for the pressure and particle velocity for the fifth wavelet at the center line and interface using the modified centerline assumption.

Using the sandwich plate impact assumption resulted in a functional model and the resulting wave diagram was plotted. A scale wave diagram was made using the particle velocity and speed of sound of each region defined in Figure 4.29. Figure 4.36 shows the first 20  $\mu\text{s}$  of the wave diagram. The leading edge of the rarefaction fan moves inward while the trail of rarefaction fan moves away from the centerline. This outward movement of the rarefaction fan tail is due to the local speed of sound being lower than the local particle velocity.

Figures 4.37, 4.38, and 4.39 show the wave diagram with a longer time axis. In Figure 4.37 the leading edge of the rarefaction fan reflected from the interface slowing the expansion rate of the interface. Since the detonation products have a higher shock impedance than the shocked air, the expansion wavelets are reflected as compression wavelets. By 600  $\mu\text{s}$ , in Figure 4.38, the first three compression waves have coalesced and several of the expansion wavelets that were initially expanding outwards have changed direction and begun to move towards the centerline. Figure 4.39 shows the furthest extent of the wave diagram that was plotted. At 2.5  $\text{ms}$  the detonation product have expanded to over 2 m which is over an order of magnitude larger than experimentally measured from the streak image in Figure 4.30. Note that in Figure 4.30 the wavelets are not drawn after their interactions with the last expansion line.

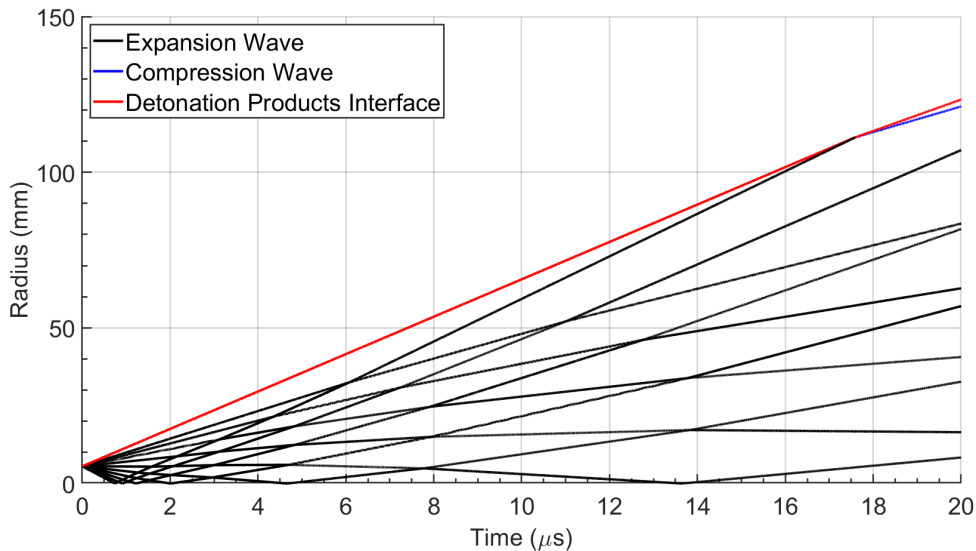


Figure 4.36: The first 20  $\mu\text{s}$  of a scale wave diagram of the expansion of a PETN pellet with a radius of 5.5 mm.

The largest difference between the analytical wave diagram in Figure 4.39 and the experimental results shown in Figure 4.30 is that the analytical model is a one dimensional rectangular model and the pellet has spherical symmetry. To examine if the one dimensional rectangular assumption is the main cause of the discrepancy between the experimental and analytical results, the detonation of a PETN pellet was simulated using the Sandia National Laboratory code CTH.

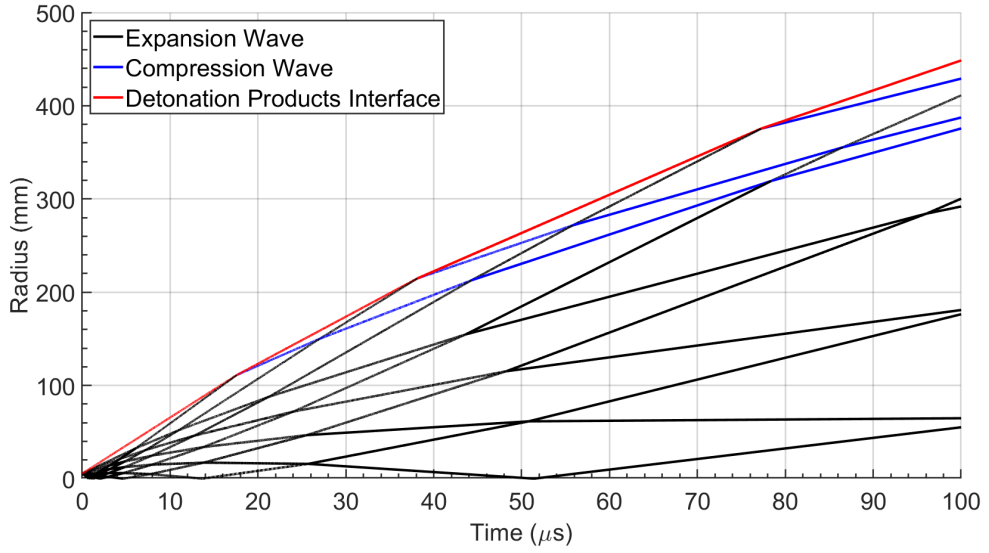


Figure 4.37: The first 100  $\mu\text{s}$  of a scale wave diagram of the expansion of a PETN pellet with a radius of 5.5 mm.

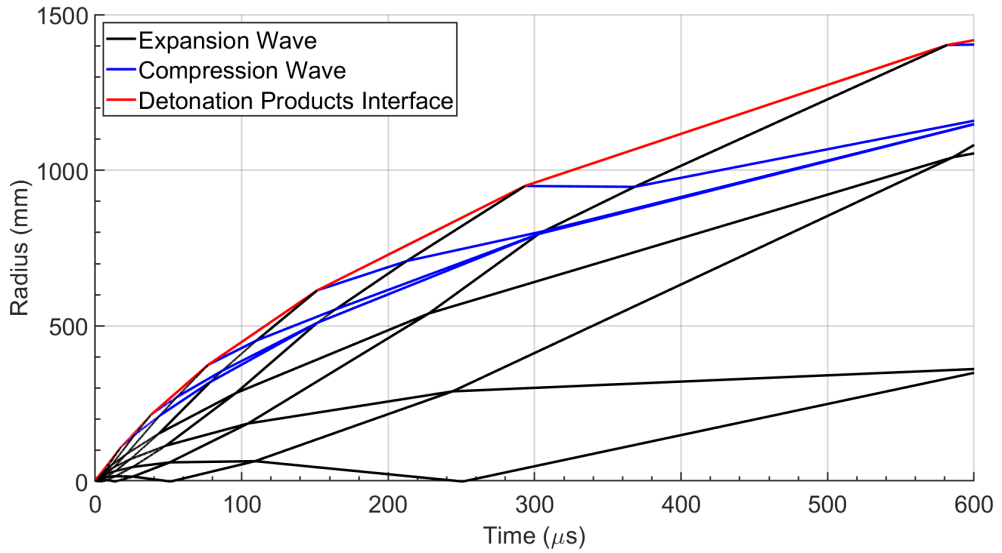


Figure 4.38: The first 600  $\mu\text{s}$  of a scale wave diagram of the expansion of a PETN pellet with a radius of 5.5 mm.

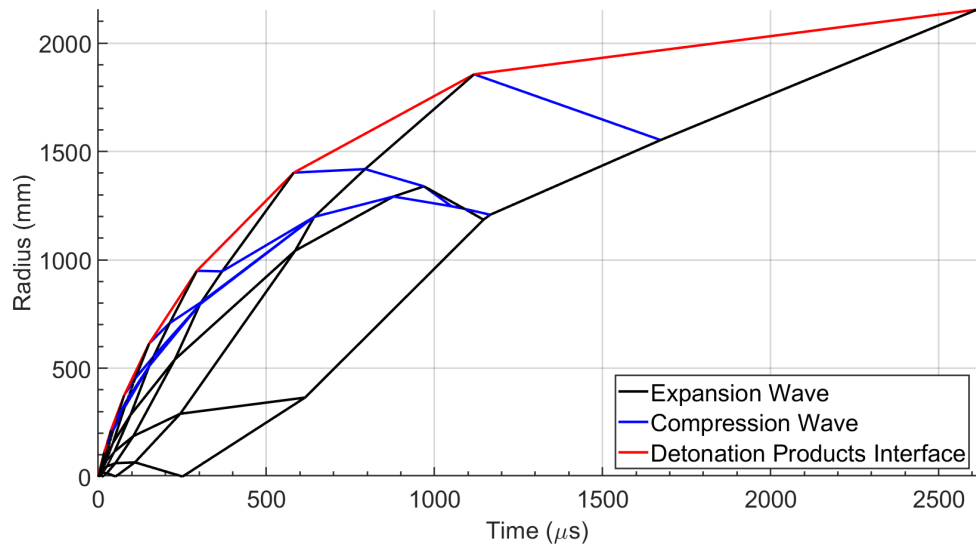


Figure 4.39: A scale wave diagram of the expansion of a PETN pellet with a radius of 5.5 mm.

#### 4.4.4 CTH Simulation of the Pulse Duration Release Wave

CTH is hydro-code capable of simulating strong shock and detonation for multi-material multi-phase problems in one, two, or three dimensions. More information on CTH can be found in [96, 97].

The one dimensional rectangular simulations were carried out at two different scales: a short simulation to look at the leading edge of the rarefaction fan and a long simulation to look at the expansion of the detonation products. The short simulation used a 50000 point mesh over 5 cm (1000 mesh points/mm) and the long simulation used a 40000 point mesh over 40 m (1 mesh point/mm). In both simulations the PETN pellet had a radius of 5.5 mm and air at 25° C and 1 atmosphere filled the remaining area. The PETN was initiated at time 0 from a region between 0 and 0.65 mm, which is the size of detonators used in the experimental work. The remaining PETN was reacted using a History Variable Reactive Burn (HVRB) model. For the short simulation the pressure, density and particle velocity at each point were recorded at 5 ns increments. For the long simulation pressure and density were recorded at 5  $\mu$ s increments. The zero radius boundary was a reflective boundary and the max radius boundary was a transmissive boundary. The transmissive boundary gave a numerical error when the primary shock reached it that resulted in a weak shock wave reflection. To eliminate this error the simulation was ended before the weak reflection reached the area of interest.

An important difference between the simulation and the analytical model is that the model assumes uniform states and the simulation does not. Figures 4.40 show a time step from the short simulation prior to shock wave break out. In the analytical model it was assumed that the region behind the detonation front was a uniform region at the CJ conditions. In the simulation, the PETN was shocked up to the CJ conditions and then a Taylor expansion wave reduces particle velocity to zero and the pressure to below the CJ pressure. This is a more realistic assumption of the detonation process but it is more difficult to represent analytically.

The one dimensional rectangular simulation shows similar results to the analytical model. Figure 4.41 is a synthetic density streak image that was generated from the long simulation by plotting the density at each point as a function of time. Figure 4.42 is the pressure plotted as function of time and radius. The primary shock is the thin dark band at the bottom of the figure, indicated with point 1. The interface between the detonation products and the shocked air, which is indicated at by point 2, is sharp discontinuity from dark to light (from left to right) behind the primary shock. The interface has a maximum radius of 10.2 m at 14.2 ms which is later than was analytically calculated. At early time in Figure 4.41 it is difficult to distinguish between the primary shock and the interface, so to compare the simulation to the model the density was plotted at 2.5 ms, Figure 4.43. The first density spike in Figure 4.43 is the primary shock and the second density spike is the location of the interface which is located at 5.3 m. Analyzing Figure 4.39 shows at 2.5 ms the analytical model predicts the interface to have a

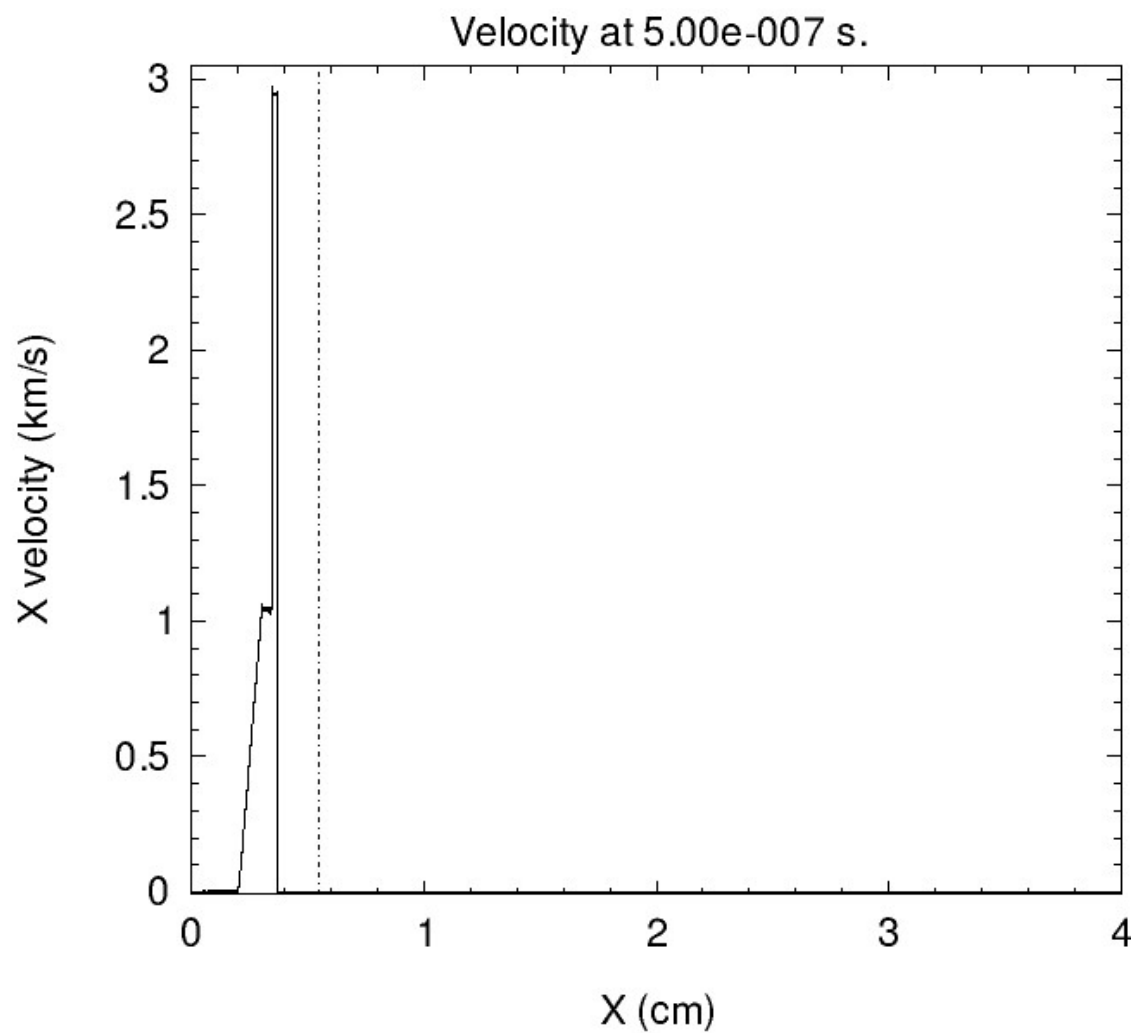


Figure 4.40: Plot of particle velocity as a function radius for a 1D rectangular simulation of the PETN pellet. The dashed line denotes the boundary between the PETN or PETN detonation products and air.

radius of 2.1 m. This shows that both the one dimensional rectangular analytical model and computational simulation results in the detonation products interface expanding much further than was observed in Figure 4.30.

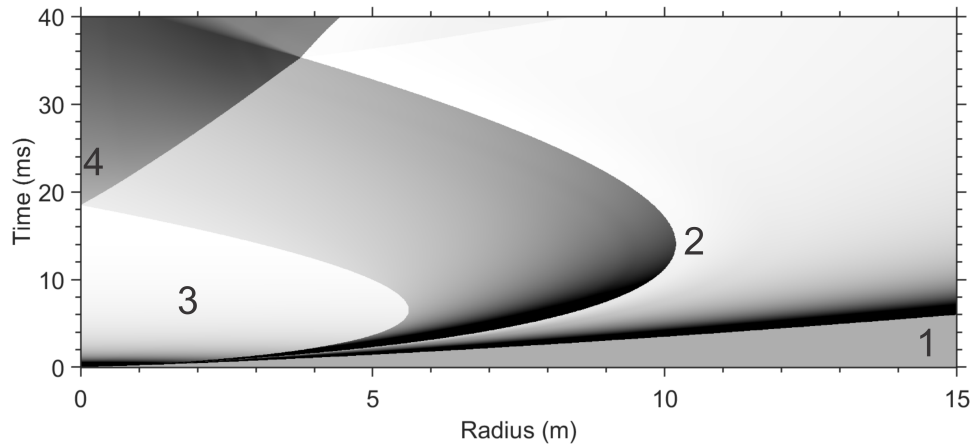


Figure 4.41: Plot of density as a function of time and distance for a 1D rectangular simulation of the PETN pellet. Four points of interest are labeled. Point 1 is the air shock. Point two is the point of maximum expansion of the air-detonation products interface. Point 3 indicates the region where the density and pressure of the detonation products drops to effectively zero. Point 4 is after the detonation products have rebounded against the  $x = 0$  boundary.

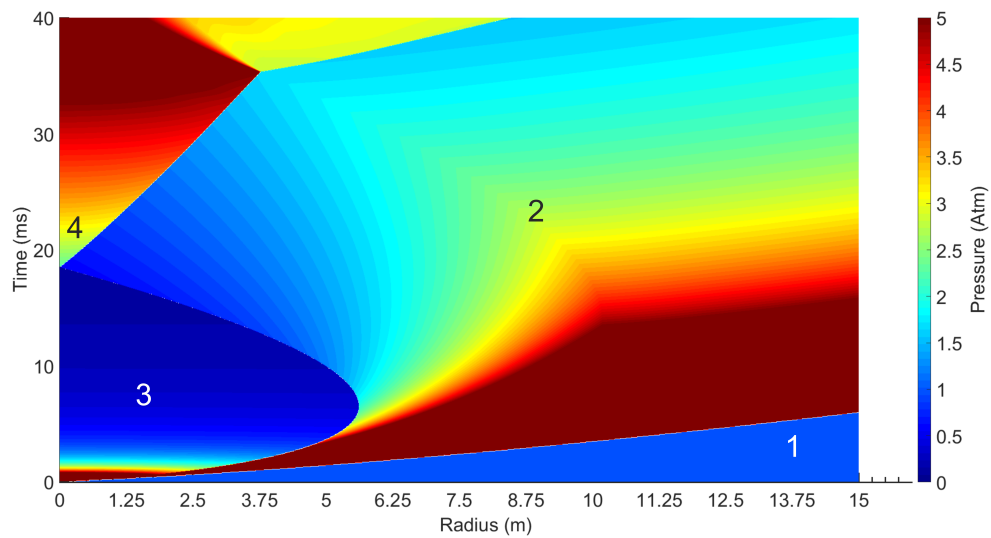


Figure 4.42: Plot of pressure as a function of time and distance for a 1D rectangular simulation of the PETN pellet. Four points of interest are labeled. Point 1 is the air shock. Point two is the approximate location of the air-detonation products interface. The product interface cannot support a pressure differential which is why there is no discontinuity. Point 3 indicates the region where the density and pressure of the detonation products drops to effectively zero. Point 4 is after the detonation products have rebounded against the  $x = 0$  boundary.

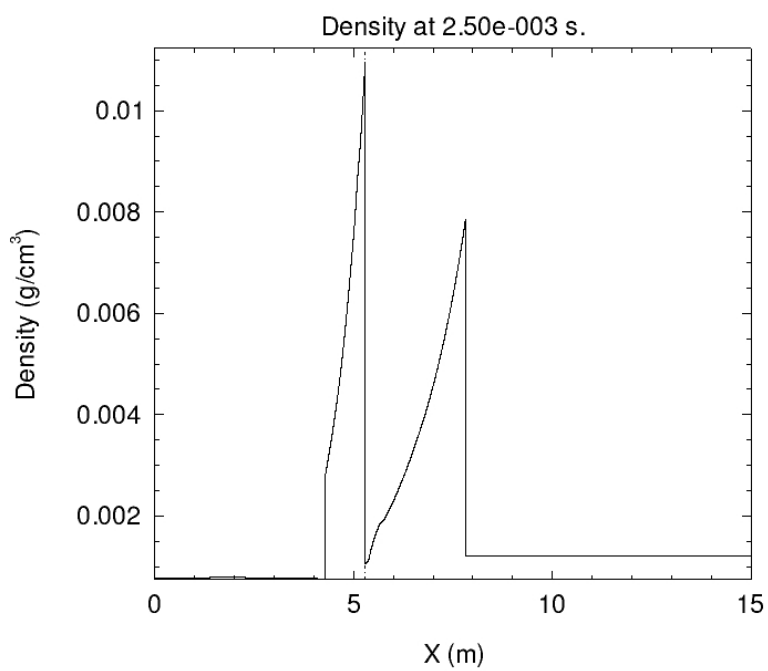


Figure 4.43: Plot of density at 2.5 ms for a 1D rectangular simulation of the PETN pellet.

To better match the experimental geometry the CTH simulation was repeated with spherical symmetry instead of rectangular symmetry. The one dimensional spherical simulation used a 6000 point mesh over 60 cm (10 mesh points/mm). The PETN explosive had a radius of 5.5 mm and air at 25° C and 1 atmosphere filled the remaining area. The PETN was initiated at time 0 from a region between 0 and 0.65 mm. The remaining PETN was reacted using a HVRB model. The pressure, density and particle velocity at each point was recorded at 0.5  $\mu\text{s}$  increments. The zero radius boundary was a reflective boundary and the max radius boundary was a transmissive boundary. To prevent numerical errors the simulation was ended before the primary shock crossed the transmissive boundary. A synthetic density streak image was generated from the spherical simulation by plotting the density as a function of radius and time, Figure 4.44. Since the primary interest of this simulation is the interface, Figure 4.45 shows the synthetic density image cropped to 10 cm Figure. 4.46 is the pressure plotted as a function of radius and time. To better show the expansion and contraction of the detonation products the plots were cropped to 200  $\mu\text{s}$ , Figure 4.47 and 4.48.

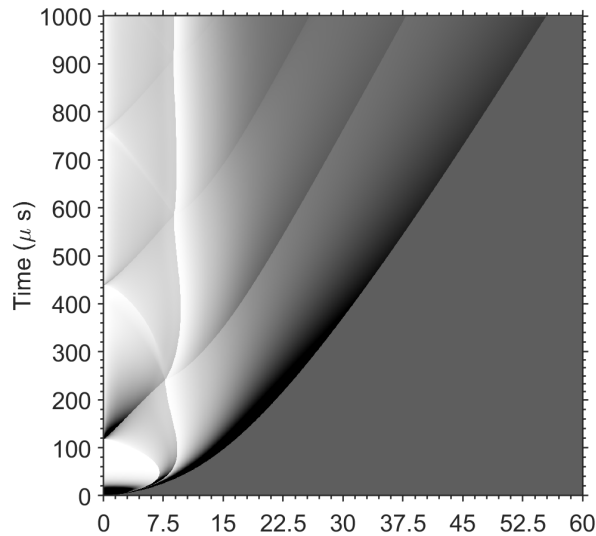


Figure 4.44: Plot of density as a function of time and radius for a 1D spherical simulation of the PETN pellet.

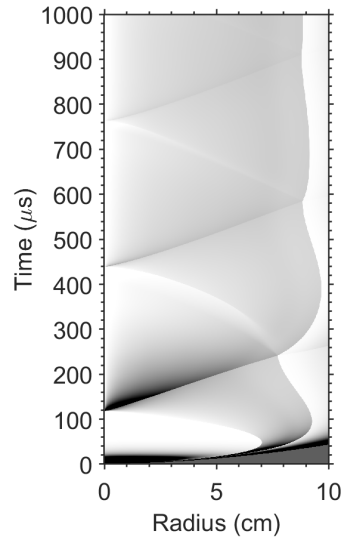


Figure 4.45: Plot of density as a function of time and radius for a 1D spherical simulation of the PETN pellet.

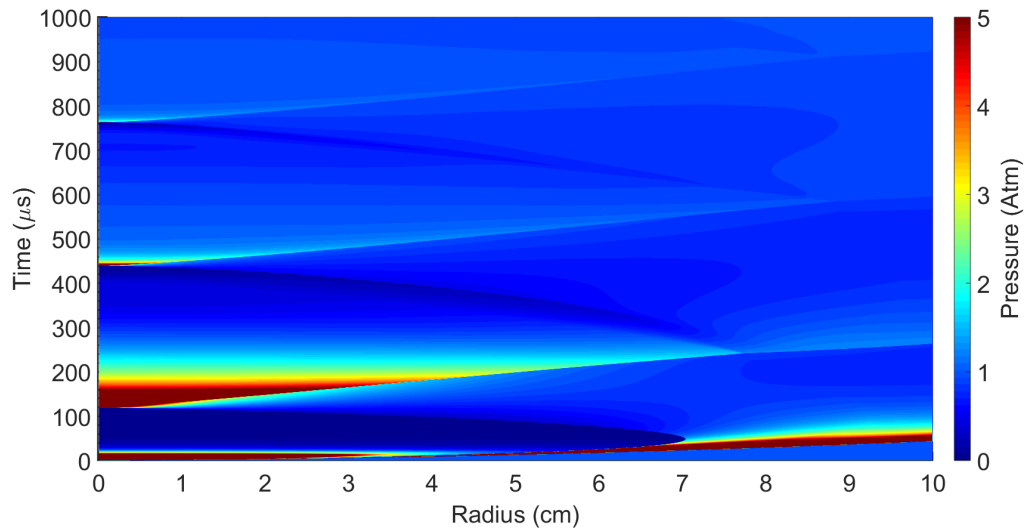


Figure 4.46: Plot of pressure as a function of time and radius for a 1D spherical simulation of the PETN pellet.

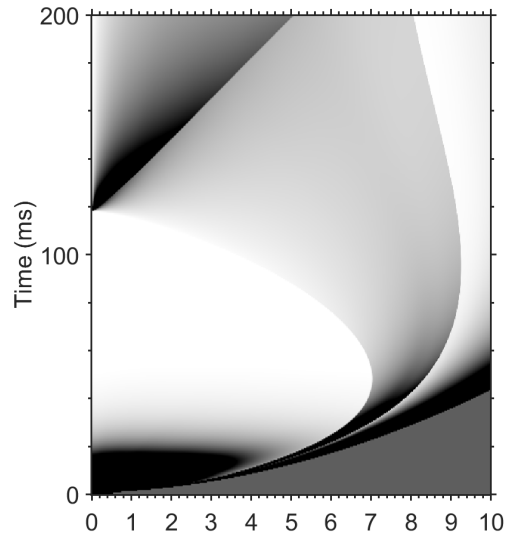


Figure 4.47: Plot of density as a function of time and radius for a 1D spherical simulation of the PETN pellet. The figure has been cropped to 10 *cm* and 200  $\mu$ s.

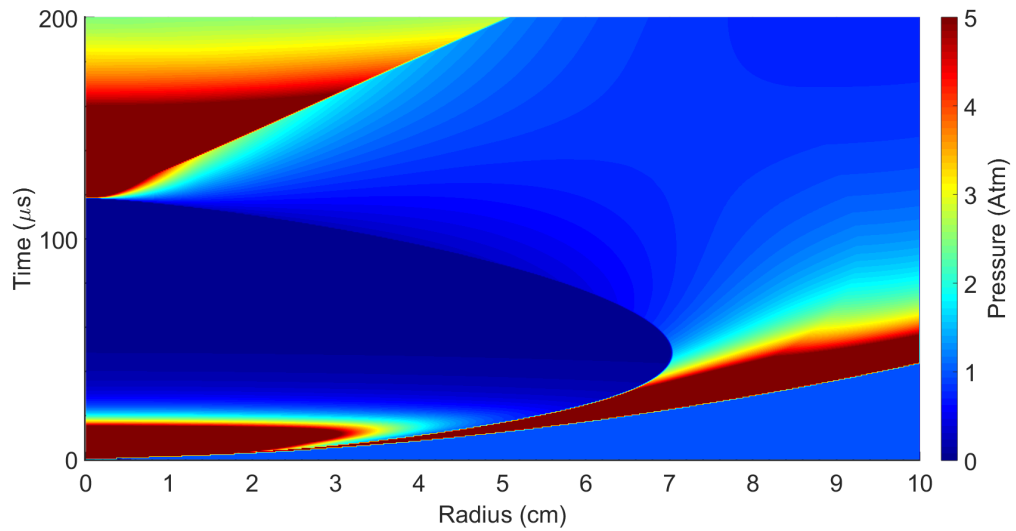


Figure 4.48: Plot of pressure as a function of time and radius for a 1D spherical simulation of the PETN pellet. The figure has been cropped to 10 *cm* and 200  $\mu$ s.

The spherical simulation was compared to the experimental streak image by merging the images together in Figure 4.49. Figure 4.49a is the experimental streak image. The synthetic streak schlieren image, Figure 4.44, was then cropped to size of the experimental image. A Canny edge detection was performed on the synthetic streak image to detect the points of change, Figure 4.49b. The edge detection resulted in a few artifacts which were manually removed. The edges were then visually thickened with an image dilatation. The edges were then overlaid onto the experimental image, Figure 4.49c. Comparing the edges and the experimental image shows good agreement between the spherical simulation and the experimental streak image. The primary shock matches well for the first 15 cm. After 15 cm the simulation under-predicts the shocks radius by up to 5 %. Similarly, the location of the secondary shock is under-predicted but has reasonable agreement. The large shadowgraph distortions around the predicted location of the detonation products makes direct comparison difficult. Comparison of the detonation products radius between the experimental and simulation shows that the simulation may over predict the radius while under predicting the time of the maximum expansion. Figure 4.49 shows that the inclusion of spherical symmetry is important to accurately represent the spherical pellets.

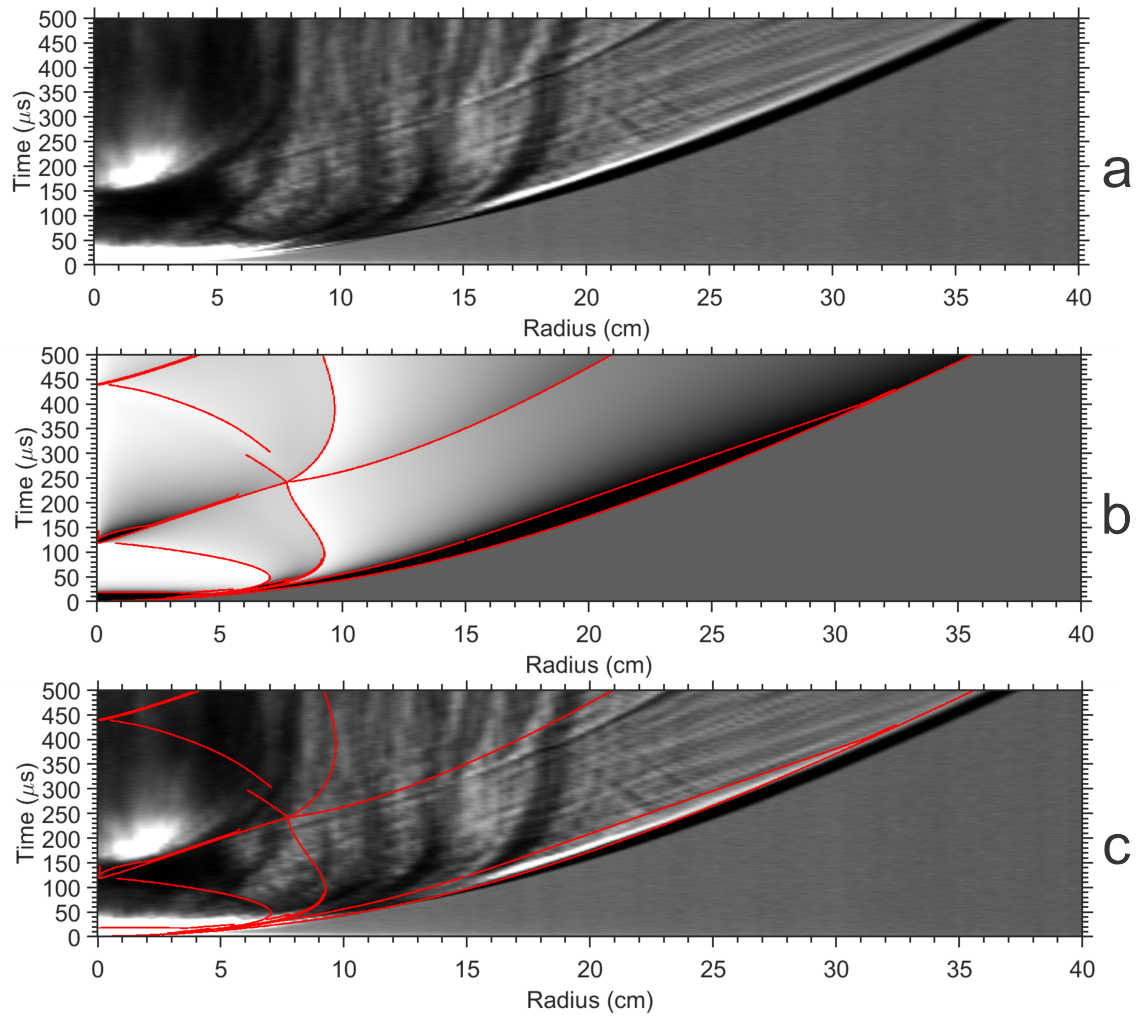


Figure 4.49: a is the experimental streak image. b is the synthetic streak image with a Canny edge detection overlaid. c is the edges of the synthetic streak image overlaid onto the experimental streak image.

The spherical simulation was used to determine the point of maximum product expansion and zero over pressure at the interface. Figure 4.47 shows the point of maximum product expansion at 9.27 cm and 96  $\mu\text{s}$ . Figures 4.47 and 4.48 were combined using 'imfuse' to generate Figure 4.50 which shows the pressure as a function of color and density as a function of brightness. The point along the interface where the pressure first reaches an absolute pressure of one atmosphere was found, 9.15 cm and 120  $\mu\text{s}$ , and plotted on Figure 4.50.

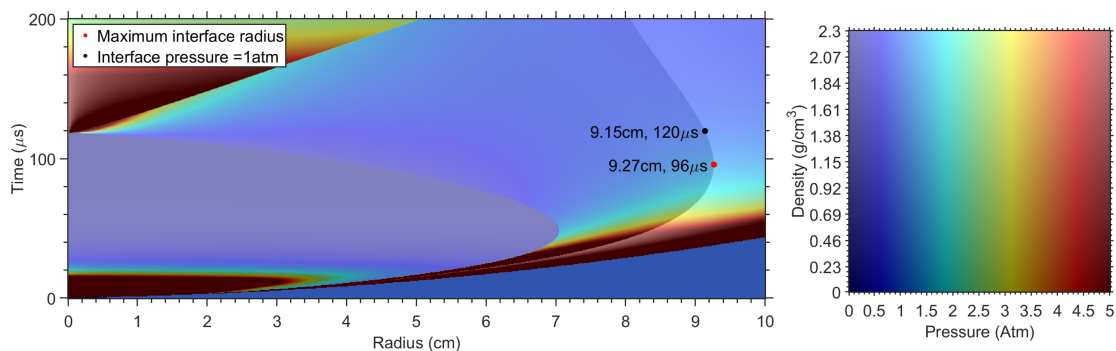


Figure 4.50: Composite image generated from the density and pressure data from the spherical simulation. A color legend for the pressure and density is shown.

Using the two potential starting locations of the release wave found via the CTH simulation, the pulse duration was recalculated. The delayed pulse duration was calculated by starting the release wave at the time and radius of either the point of maximum product expansion and zero over pressure and moving the release wave outward at the local speed of sound. This procedure is similar to what was used in Figure 4.27 but started at a later time and radius. The red line in Figure 4.51 shows the pulse duration with the release wave started at the point of zero over pressure as well as the experimentally found pulse duration. The yellow line in Figure 4.51 shows the pulse duration with the release wave started at the point of maximum product expansion. Comparing the two lines, shows that starting at the maximum product radius better matches the experimental data at smaller radii and starting at the point of zero over pressure better matches at larger radii. Neither line perfectly match the data. The zero over pressure pulse duration curve has an  $R^2$  value of 0.80. The maximum product expansion pulse duration curve has an  $R^2$  value of 0.84. For comparison the non-delayed pulse duration curve, Figure 4.28, has an  $R^2$  value of 0.49.

Neither starting location for the release wave, the point of zero overpressure or the point of maximum product expansion, perfectly predict the experimental pulse duration. Both starting locations better predicted one region and both had very similar  $R^2$  value. The more physical starting location of the release wave is the point of zero overpressure so in the following calculations and analysis it will be used but more work is needed to refine the analytical model of pulse duration

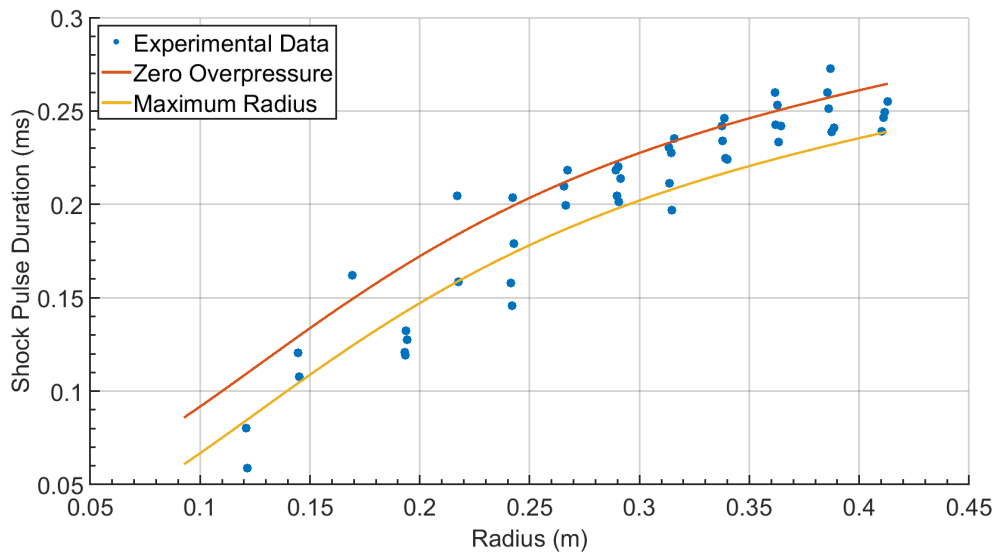


Figure 4.51: Comparison of the experimental pulse duration and the analytical pulse duration were the release wave has been started at either the point of zero over pressure or the point of maximum product expansion.

to better match experiments. This analysis also shows that if in future works with different explosive materials only the location of the maximum product expansion can be determined, then the pulse duration can be reasonably predicted by starting the release wave at the point of maximum expansion.

#### 4.4.5 Decay Coefficient

The  $\alpha$  term is the final Friedlander parameter required to calculate impulse. The  $\alpha$  term can be referred to as either the wave shape factor or decay coefficient as it controls the rate of exponential decay. Many prior researchers have studied how  $\alpha$  varies as a function of scaled distance but none have developed physical model explaining what causes the change in wave shape [98]. Currently all models of  $\alpha$  are numerical fits to experimental data with notable work being presented by Brode in 1955 [99], Baker in 1983 [100], Kinney and Graham in 1985 [70], Lan in 2004 [101], Dharaneepathy in 2006 [102], Larcher in 2007 [103] and Borger in 2008 [104], with most models being power law fits [105]. Figure 4.52 shows the proposed  $\alpha$  curves by Larcher, Lan, Borgers, and Dharaneepathy as a function of standard scaled distance ( $Z$ ), which is  $m/kg^{1/3}$ . None of these fits agree at small scaled distance and even at larger scaled distances still disagree by up to 50%. The discrepancy between the different fitting values can be contributed to different factors, two factors that have been previously explored in literature are charge shape and height of burst [105]. Difference in explosive charge composition will also have an major impact on the  $\alpha$  function. Since there is not a model that clearly is suited for the given experimental setup, the  $\alpha$  values determined in Figure 4.19 were fit to a power law function. The Friedlander  $\alpha$  values and resulting fit is shown in Figure 4.53. Figure 4.54 shows the experimental  $\alpha$  values and their fit along with the proposed literature curves. The literature curves have been scaled from a charge mass of 1 kg to the experimental charge mass. The fit of experimental data did not closely match any literature curve so the experimental power law fit was be used in calculation of impulse.

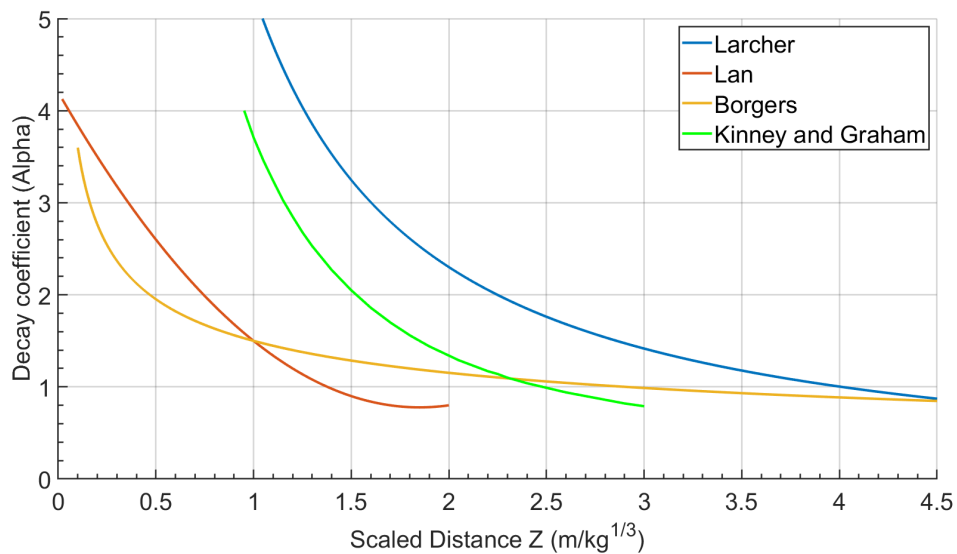


Figure 4.52: Predicted  $\alpha$  values as function of scaled distance ( $Z$ ) reproduced from multiple literature sources.

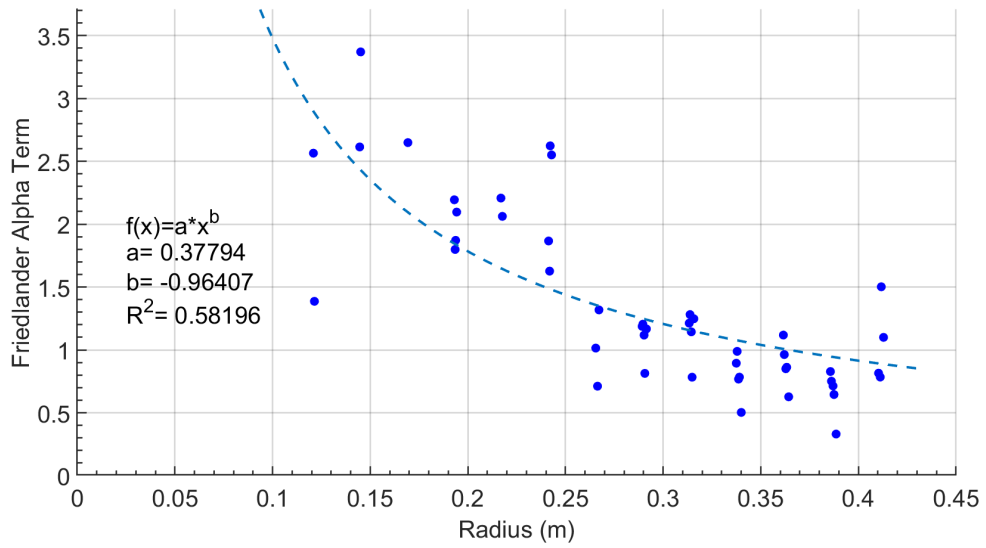


Figure 4.53: The decay coefficient  $\alpha$  as a function of radius for the fit experimental data and the resulting numerical power law fit of the data.

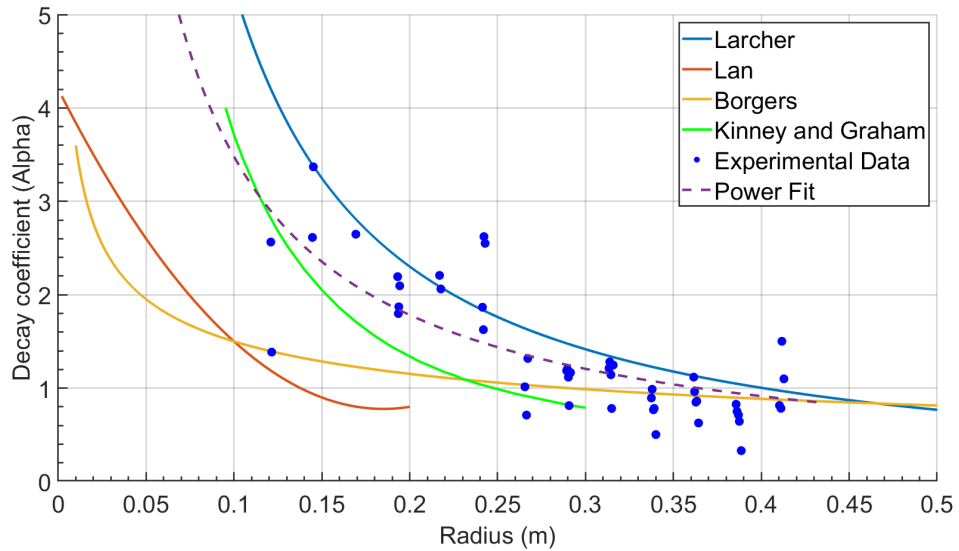


Figure 4.54: The decay coefficient  $\alpha$  and the resulting numerical power law fit of the data. Additionally the  $\alpha$  curve from multiple literature sources.

#### 4.4.6 Analytical Impulse

Using the three Friedlander terms, peak pressure  $P_s$ , pulse duration  $t_d$ , and the decay coefficient  $\alpha$ , the shock impulse can be calculated using Equation 1.15. The experimental pressure probe data was fit to the Friedlander equation with the resulting terms shown as a function of radius in Figures 4.17-4.19. The Friedlander terms were also analytically derived from the radius-Mach number curve, Figure 4.7. The peak pressure,  $P_s$ , was directly calculated from the Mach number using Equation 1.13. The analytical peak pressure as a function of radius is shown in Figure 4.22. Since the pressure curve was in terms of pressure ratio of peak pressure over atmospheric pressure, the impulse was calculated using a standard atmosphere, 101.3 kPa, as the pressure before the shock. The pulse duration,  $t_d$ , was calculated by determining the relative wave speeds of the shock wave and a sound wave behind the shock, the pulse duration is shown in Figure 4.51. Several models of decay coefficient,  $\alpha$ , were presented but no model matched the experimental data. The experimental  $\alpha$  values were fit to a power law function and is shown in Figure 4.53. Figure 4.55 shows both the experimental and the analytically calculated impulse per unit area. The analytical curve was calculated using the analytical pressure and pulse duration and  $\alpha$  from the power law fit to experimental data.

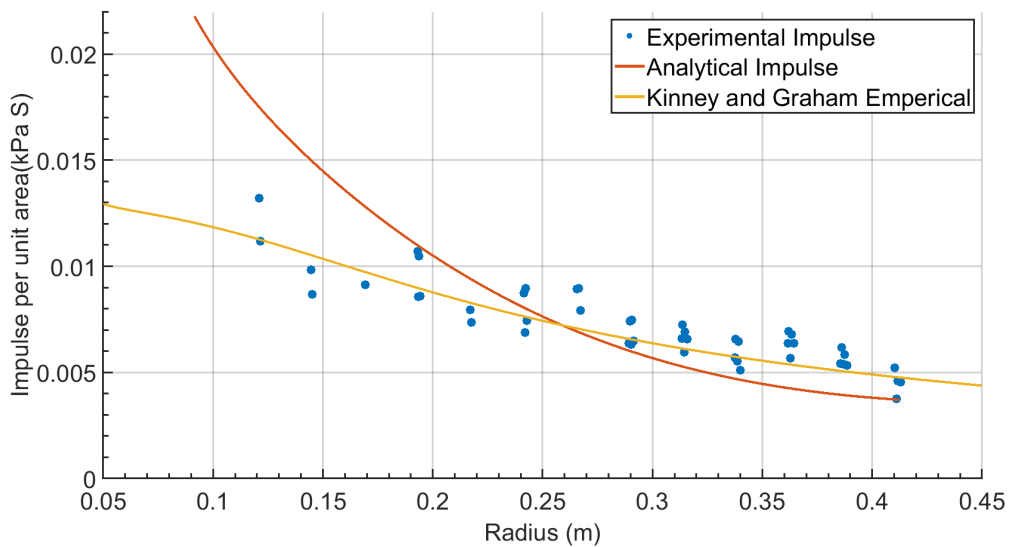


Figure 4.55: Shock impulse as a function of radius for experimental data and analytical. The Kinney and Graham empirical equation for impulse per unit area is shown.

In Figure 4.55 the analytical impulse per unit area curve starts above the first set of data points and then ends just below a furthest data points. For comparison, the Kinney and Graham empirically derived equation relating scaled distance to impulse per unit area is shown in Figure 4.55 [70]. To simplify comparison with

prior or future work, Figure 4.56 shows the impulse data scaled to the standard charge mass of 1 kg. The Kinney and Graham empirically equation agrees well with the experimental data. This shows that the analytical method used to predict impulse can still be improved.

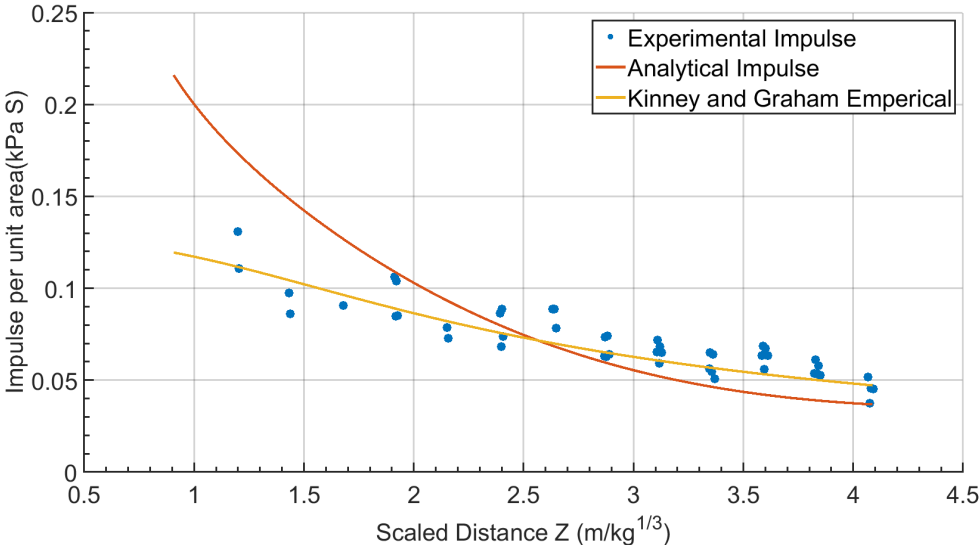


Figure 4.56: Shock impulse as a function of radius for experimental data and analytical. The Kinney and Graham empirical equation for impulse per unit area is shown. Data scaled to 1kg

Since there are only three terms in the Friedlander impulse equation the discrepancy between the analytical and experimental results must stem from one or more of those terms. Equation 1.15 shows that peak pressure and pulse duration are directly proportional to impulse but the relationship between  $\alpha$  and impulse is not immediately apparent. To show the effect of the  $\alpha$  term on the impulse, the  $\alpha$  section of the Friedlander impulse equation was isolated and Figure 4.57 shows how the value of the section varies as a function of  $\alpha$ . Figure 4.57 shows that as  $\alpha$  increases the value of the section decreases. The exact value of the  $\alpha$  section of the Friedlander equation as a function of radius is shown in Figure 4.58. Figure 4.53, which is the experimental data and fit of  $\alpha$ , shows that below 0.25 m the fit line is below the median of experimental data. Above 0.25 m the fit line is above the median of the experimental data. Accounting for this difference could result in a 5 to 10% change in impulse.

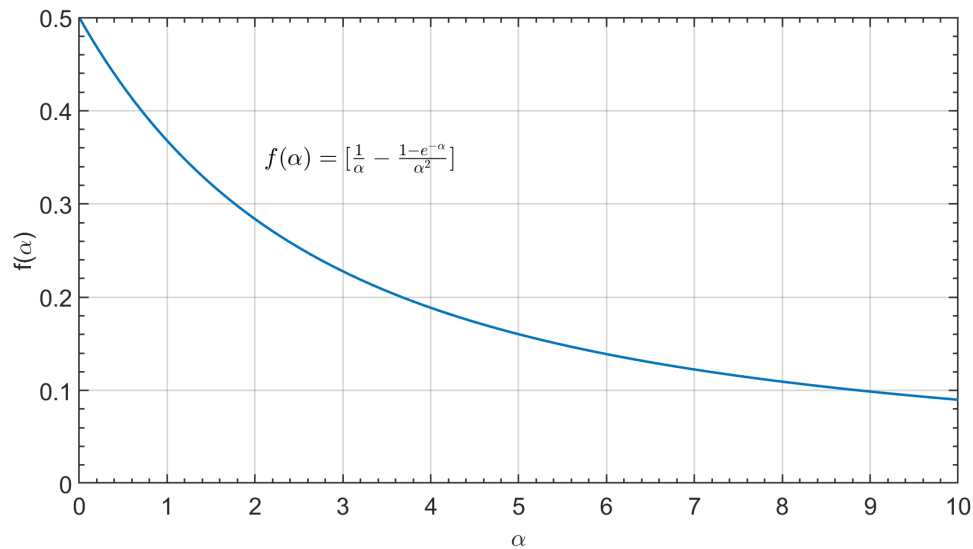


Figure 4.57: The value of part of the Friedlander impulse equation that contains the  $\alpha$  variable as a function of  $\alpha$ .

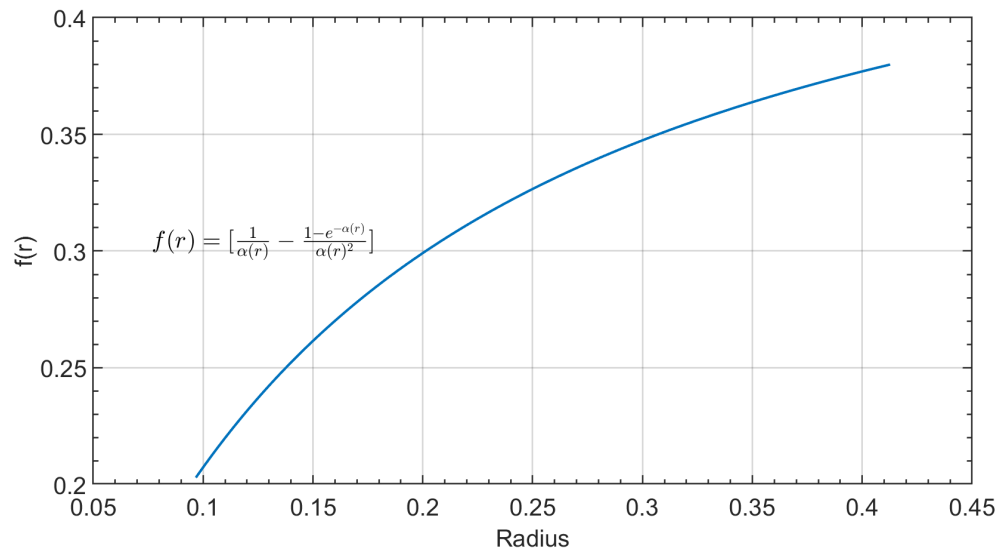


Figure 4.58: The value of part of the Friedlander impulse equation that contains the  $\alpha$  variable as a function of radius.

The peak pressure term was calculated by applying Equation 1.13 to the Mach radius curve, Figure 4.7. Equation 1.13 is derived from first principles and the underlying assumptions are valid over the region studied. For this reason it is assumed that the discrepancy between the experimental results and analytical lie either in the Mach radius curve or in the experimental data. The Mach radius curve is a fit of approximately  $7.5 * 10^4$  individual data point over fifteen tests, both non-reflected and reflected tests. There is variation from test to test with the curve being the average of all the tests. As a result the variation is assumed to be a result of scatter within the experimental data.

The pulse duration calculation has two major pieces, the starting location of the release wave and the wave velocity of the release wave. Comparing Figure 4.51 and Figure 4.28 shows that delaying the start of the release wave results in better agreement with experimental data. Two proposed starting locations of the release wave were examined via simulation. Both starting points matched the experimental data well but the zero overpressure location is more physical but further work is required to fully investigate the correct origin of the release wave. An ideal option for further investigation is the development of spherical analytical models. An analytical model was developed to study the expansion process but comparison with simulation and experimental results show that the use of spherical characteristic equations are required to improve the utility of the model. The results of a spherical analytical model will be applicable to a wider range of cases than the simulation.

Rarefaction waves propagate within a material at the local speed of sound. If the material is moving the net velocity of the wave is the sum of the speed of sound and particle velocity. The analytical model assumed that the air behind the shock wave has no velocity. This assumption is based off of the time delay between the shock and the release wave allowing the blast wind, or the velocity of the gas behind the shock, to dissipate. This assumption could be further investigated by using simulations to directly track the velocity behind the shock as a function of time or experimentally by tracking turbulent structures or with tracer particles, similar to [68]. Since the velocity of the gas after the shock is radially outward, the net effect will be to increase the release wave velocity and decrease the pulse duration. The model also assumes that the temperature is constant from the shock to the arrival of the release wave. This assumption is reasonable at larger radii due to the lower temperature. The temperature grows exponentially at smaller radii, so radiation and outward convection will play a larger roll. The net effect of cooling at small radii is an additional delay.

The analytically predicted impulse agrees well with the experimental data with the majority of the deviations attributable to pulse duration. Of the three terms in the Friedlander impulse equation, peak pressure had the best agreement with experimental data, contributing little to the overall inaccuracy in the impulse. The  $\alpha$  curve fit under predicts at lower radii and over predicts  $\alpha$  at higher radii. This contributes between 5 and 10 % to the overall discrepancy. The majority of discrepancy comes from the pulse duration. Improving the analytical model of pulse duration will have the greatest improvement in the ability to pre-

dict impulse.

## CHAPTER 5

### RESULTS AND DISCUSSION OF THE REFLECTED GRAM-SCALE TEST SERIES

A series of gram scale pellets of PETN were detonated above an instrumented reflecting plate which was placed within two shadowgraph imaging systems. A series of pressure probes were flush mounted in the reflecting plate to record the pressure and impulse from the shock reflection as a function of distance. The shadowgraph systems consisted of a 1-meter-diameter system that focused on the expansion of the shock wave and a 30-centimeter-diameter system that focused on the shock wave reflection. The shadowgraph systems recorded at between 250,000 and 1,000,000 frames per second.

#### 5.1 Shock Reflection Transition

##### 5.1.1 Analytical Shock Reflection Transition

Figure 5.1 shows the path of a shock wave from 1 g of PETN detonated at 0.1 m above a reflecting surface plotted as a function of effective wedge angle and Mach number. The shock path starts at a high Mach number and an effective wedge angle of  $90^\circ$  for the normal shock wave impact on the surface directly under the explosive charge. This point is shown as the green dot in Figure 5.1. As the shock wave expands, the Mach number and effective wedge angle decrease with the final plotted point shown as a magenta dot in Figure 5.1. Figure 5.2 shows the shock wave path overlaid on the reflection type domain diagram, previously shown as Figure 2.7. This diagram predicts the points where the reflection type will change [106]. The analysis techniques used in this work, high speed imaging and pressure transducers, are discretized, so Figure 5.3 shows the points along the shock path where each frame occurs for a 500,000 fps imaging system. The time of several frames is shown, with zero time being first light.

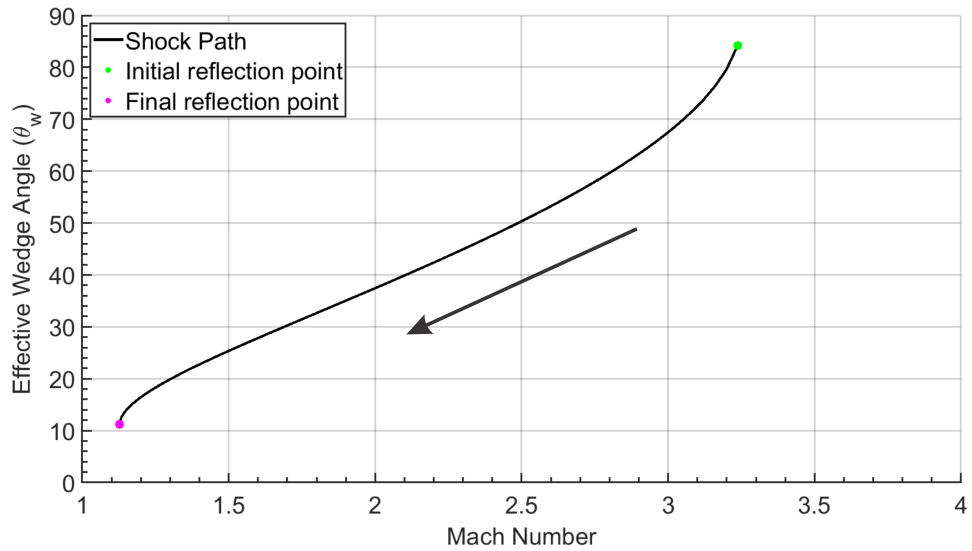


Figure 5.1: The Mach number and effective wedge angle path of the shock wave from 1 g of PETN detonated 0.1 m above a reflecting surface. The initial reflection point is shown as a green dot and the final point shown is highlighted with a magenta dot. An arrow was added to indicate the progression of the reflection.

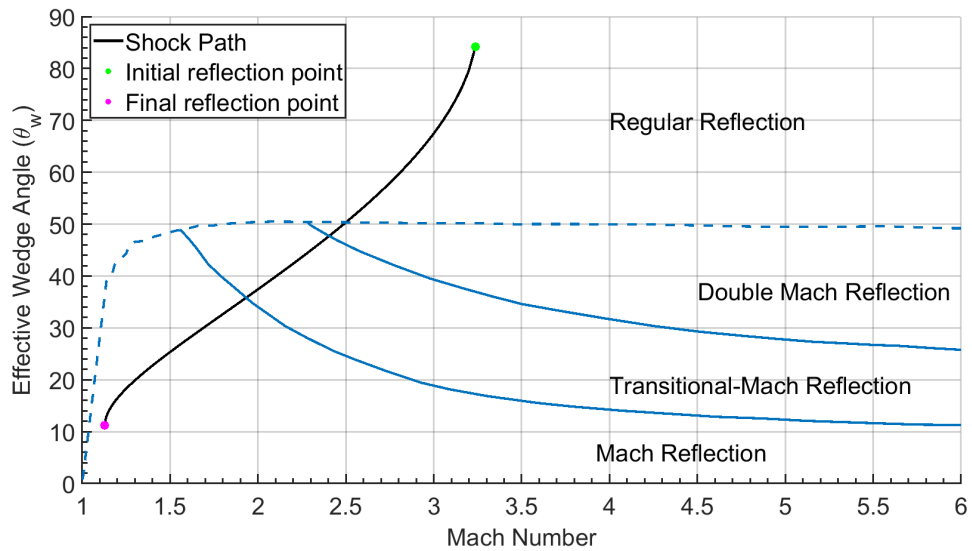


Figure 5.2: The Mach number and effective wedge angle path of the shock wave from test R1 overlaid on the shock reflection type domain map.

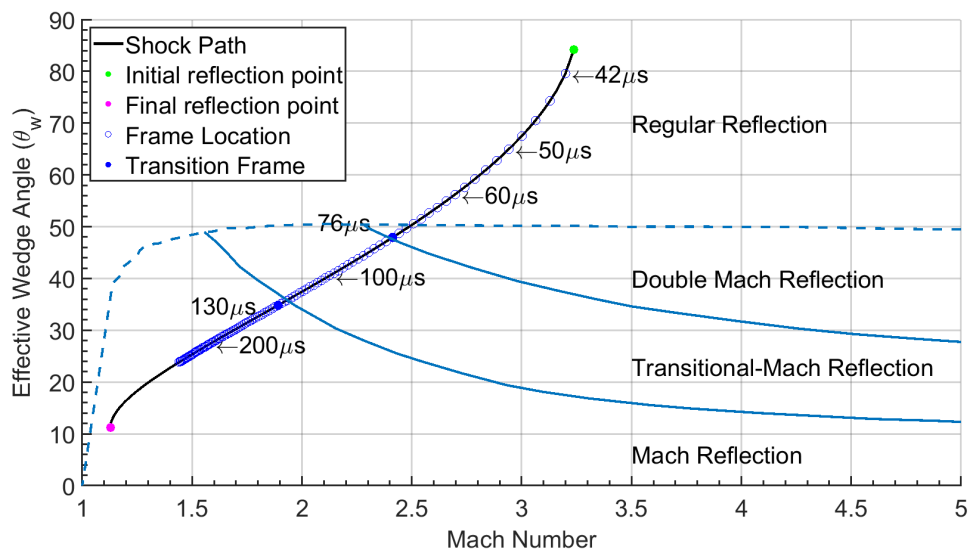


Figure 5.3: The Mach number and effective wedge angle path of the shock wave from test R1 overlaid on the shock reflection type domain map. The location of the frames from the 30 cm schlieren system are shown as blue circles. The first frame following the predicted transition from a regular reflection to irregular reflection is shown as a solid blue dot.

### 5.1.2 Refractive Imaging of Shock Reflection Transitions

To study the transition between reflection types, a series of tests were conducted where PETN pellets were detonated over a rigid reflecting surface. Table 5.1 summarizes all tests and results for the reflection test series. The reflection transition data from the majority of the tests were determined to be unusable due to oblique shocks from fragments interacting with the primary shock near the reflection transition point. An example of a test with unusable reflection transition data is shown in Figure 5.4. In the first frame of Figure 5.4, at  $33 \mu s$ , several fragments can be seen to have propagated faster than the primary shock wave. At  $50 \mu s$  some of the fragments have impact the reflecting surface. In the frames at  $65 \mu s$  and  $80 \mu s$  the primary shock is visibly disrupted at the reflection point. The disruption is visualized in the difference between the undisturbed shock, which is visualized as a thick dark smooth curve, and the area around the reflection point which has a thin transition and is highly noisy. The result of this disruption can be seen as an added bulge at the bottom of the Mach stem at  $112 \mu s$ . By  $123 \mu s$  a classic Mach reflection has formed but it is unknown if its properties are identical to the properties of an undisturbed reflection. A test with a usable reflection transition is characterized as having no disruptions to the primary shock wave immediately before or during the transition. Significant effort was expended to make the explosive charges as free of particles and irregularities as possible, but some variations on individual tests still occurred.

Table 5.1: Summary of the reflection tests series.

Test ID	30 cm Schlieren System		Pressure Data
	Frame Rate (kfps)	Visualization of Transition	Usable Pressure Traces
R1	500	Usable	15
R2	N/A	No Refractive Data	15
R3	1,000	Unusable Transition	15
R4	1,000	Unusable Transition	15
R5	1,000	Unusable Transition	15
R6	1,000	Transition Not Observed	12
R7	500	Unusable Transition	15
R8	500	Usable	15
R9	500	Unusable Transition	No pressure data
R10	250	Unusable Transition	12
R11	500	Usable	14
R12	500	Unusable Transition	13
R13	1,000	Unusable Transition	14
R14	1,000	Unusable Transition	15
R15	1,000	Unusable Transition	15

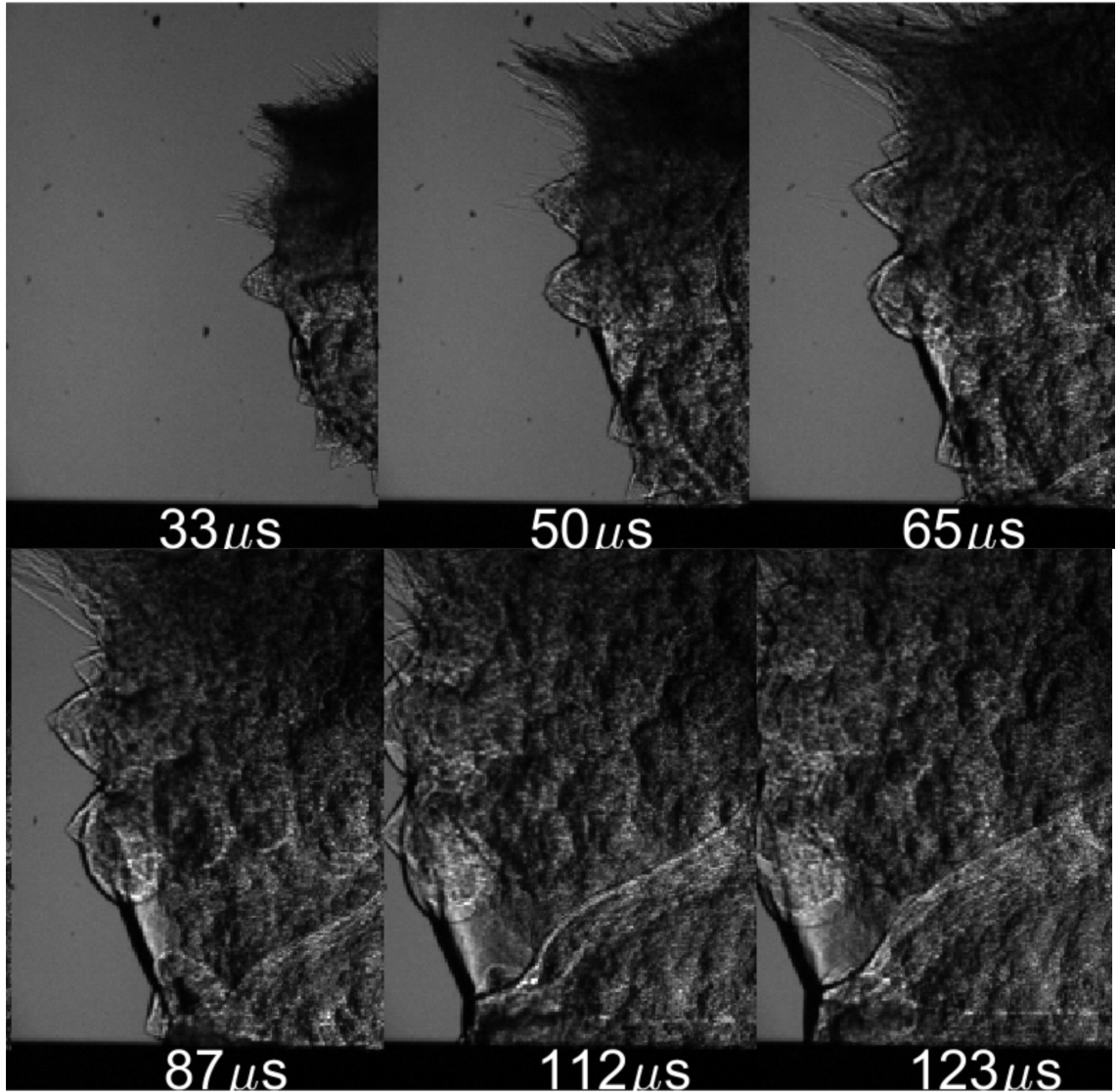


Figure 5.4: Frames from a test with an unusable shock reflection transition. Oblique shocks disrupt the primary shock immediately prior to the reflection transition. This figure will be broken into two rows to make it more easily seen.

Figure 5.5 shows the transition of the shock wave reflection from a regular reflection to an irregular reflection. The first frame of Figure 5.5, at  $86\mu s$ , shows a regular reflection with the initial and reflected shock meeting at the reflecting surface. The reflection in the final frame of Figure 5.5, at  $98\mu s$ , is an irregular reflection with a short Mach stem visible. The exact frame where the transition occurs is difficult to identify due to a slight misalignment in the experimental setup between the Z schlieren system and the reflection plate. The misalignment between the refractive imaging systems and the reflection plate had two causes: curvature of the surface of the reflection plate and the surface of the reflection plate and the light rays of the imaging systems not being parallel. The result of the misalignment was the reflection plates cast a shadow in the schlieren system causing a black area above reflection plate that was not visualized.

The welding of the reflection plate resulted in the system having a slight concave curvature. The result of this was a small un-visualized area directly above the center of the plate, the area the reflection transitions were expected to occur. To minimize the concave curvature the edges of the reflection plate were tensioned downwards while the center was supported. Eliminating the curvature in the direction of both cameras was found to be impracticable. Since the 30 cm system had a higher spatial resolution than the 1 m system, the 30 cm system was optimized. Tensioning the reflection plate to eliminate the curve resulted in the surface of the reflection plate being non-parallel with the 30 cm system Z schlieren system. To allow adjustment of reflection plate and increase the parallelism of the system, the feet of the reflection plate were placed on laboratory scissor jacks. The height of the scissor jacks were adjusted to minimize the non-visualized area over the reflecting surface. After minimizing the curvature of the plate and aligning the surface and schlieren system, the maximum height of the area which was not visualized in the 30 cm system Z schlieren system was limited to approximately 2-3 mm (3-4 pixels). This was measured in the center of the test section where the non-visualized height was the greatest. The height of the non-visualized area steadily decreased to zero height at the edges of the reflection plate. The system was inspected between tests to verify the non-visualized area did not increase.

Due to the unvisualized area, the Mach stem is not the first sign of the transition between a regular and irregular reflection in the R1 test. As the Mach stem forms the point where the initial and reflected shock meets moves away from the reflecting surface. Tracking this point gives the first sign that an irregular reflection has formed. Figure 5.6 shows an enlarged section of the frames near the transition point. To improve identification, the lowest visible pixel of the right edge of the primary shock is highlighted in red. In the first two frames of Figure 5.6,  $86\mu s$  and  $88\mu s$ , the primary shock ends at the bottom of the visualization area. At  $90\mu s$  the bottom right edge of the primary shock is visible and a region connecting the primary and reflected shock is visible. The implication of this is that the transition from regular and irregular reflection occurred prior to  $90\mu s$ . The final frame before the transition was visualized, at  $88\mu s$ , is shown in Figure 5.7 as the green dot. The frame where the transition is expected to occur is shown in solid blue.

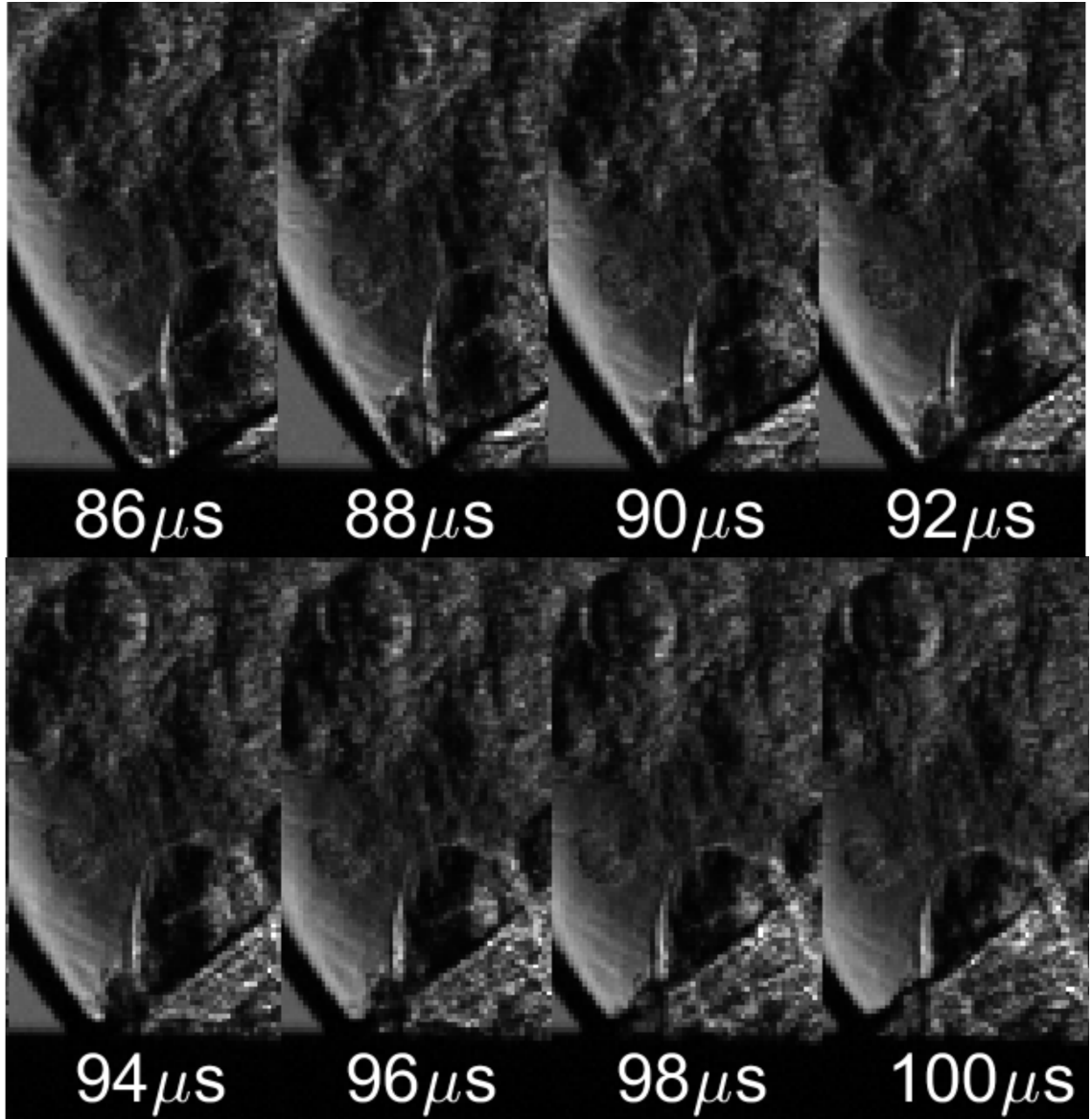


Figure 5.5: Frames, with time stamp added, from test R1 to show the shock reflection transition.

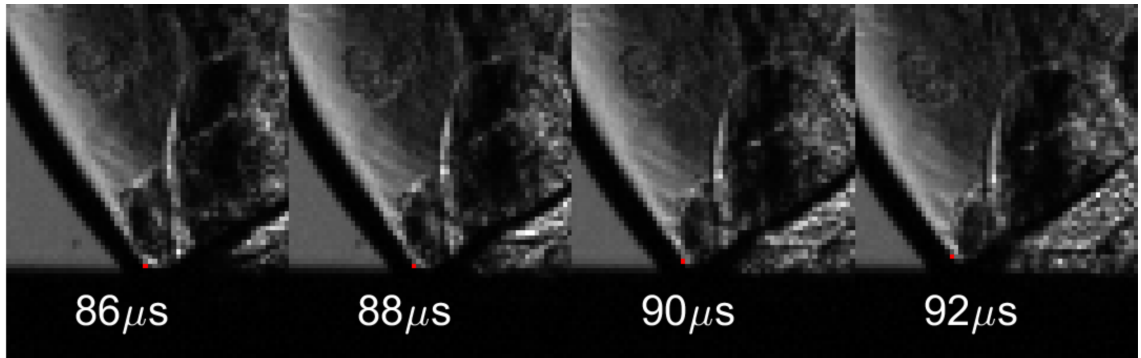


Figure 5.6: Select frames from Figure 5.5 enlarged to show the lower right edge of the primary shock lifting off of the reflection surface.

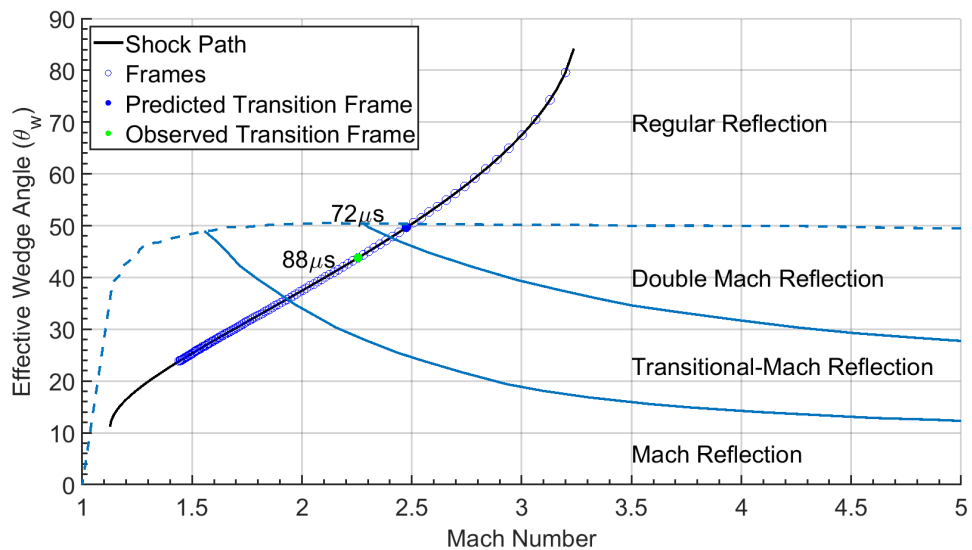


Figure 5.7: The Mach number and effective wedge angle path of the shock wave from R1 overlaid on the shock reflection type domain map. The predicted reflection transition is shown in solid blue and the observed transition is shown in solid green.

Due to the increased height of burst in tests R8 and R11 the formation of the Mach stem occurred further from the center of the plate. Near the edges of the plate the height of the non-visualized area was much less than the maximum. As a result the Mach stem formation was better visualized allowing Mach stem formation to be used to identify the transition from regular to irregular reflection. Figure 5.8 shows a series of enlarged images from test R8. The top left frame in Figure 5.8 is a regular reflection since the primary shock intersects the reflection plate. The final frame in Figure 5.8 is a irregular reflection since a Mach stem connects the primary shock to the reflection plate. The exact location of the transition from regular to irregular is difficult to identify as Mach stem growth is a gradual process and the pixelized nature of digital photography results in the infinitely thin shock front being visualized by multiple pixels. To standardize the manual identification of the transition between tests, the shock front location is defined as the first pixel which shows a decrease in intensity below the average background intensity. This definition is demonstrated in Figure 5.9 with the point where the shock front intersects the bottom of the visualized area highlighted in red. Figure 5.10 shows the frames from  $124 \mu s$  to  $130 \mu s$  with the bottom most portion of the shock front highlighted in red. At  $124 \mu s$  and  $126 \mu s$  the bottom of the shock has a constant slope. At  $128 \mu s$  the bottom two pixels are vertical followed by a constant slope. Over time the bottom pixels remain vertical and grow which indicates that the Mach stem is being visualized and not noise. Since the Mach stem was visualized at  $128 \mu s$  and the Mach stem growth is slow, the transition is expected to have occurred closer to the frame at  $126 \mu s$ . Figure 5.11 shows conditions of the observed transition and the predicted transition. The time of the transition from regular to irregular reflection was identified for test R11 using the same procedure as for test R8 with the results shown in Figure 5.12. Figure 5.13 shows the conditions of the observed transition as well as the predicted transition conditions.

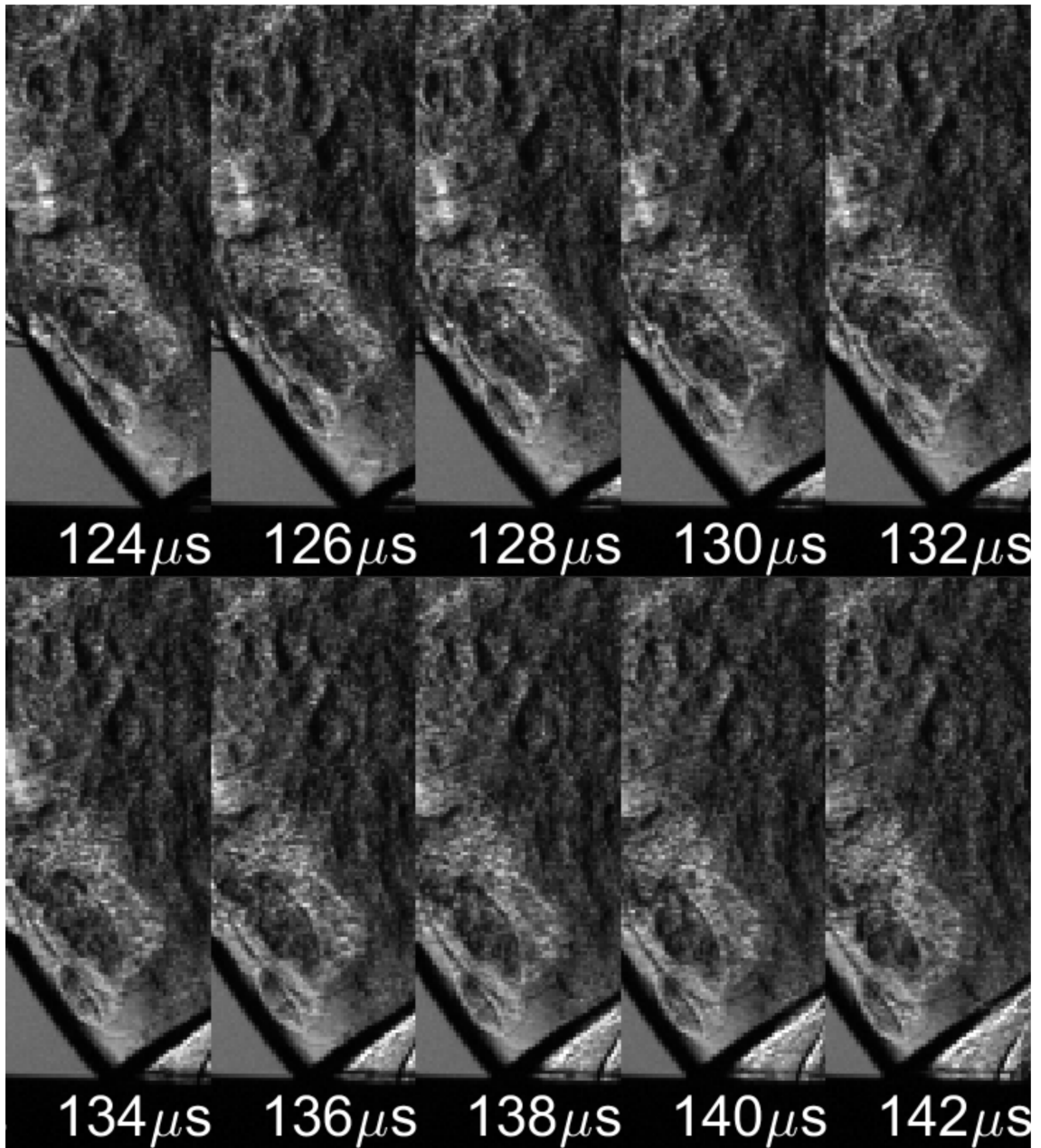


Figure 5.8: Frames from R8 showing the transition of regular to irregular reflection.

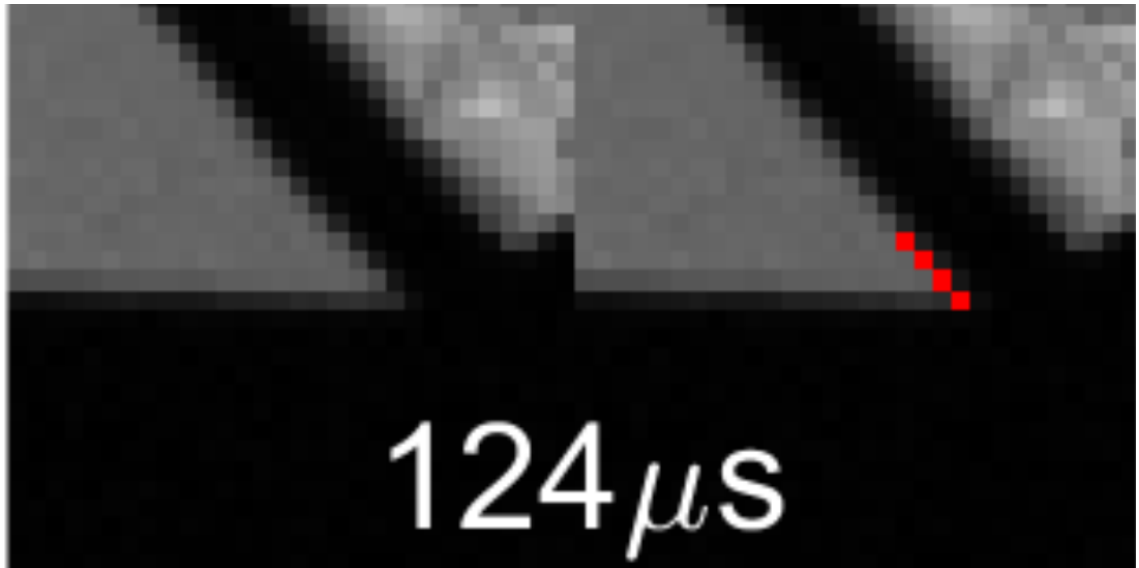


Figure 5.9: An enlarged view from Figure 5.10 to show how the leading edge of the shock is being defined in the refractive images.

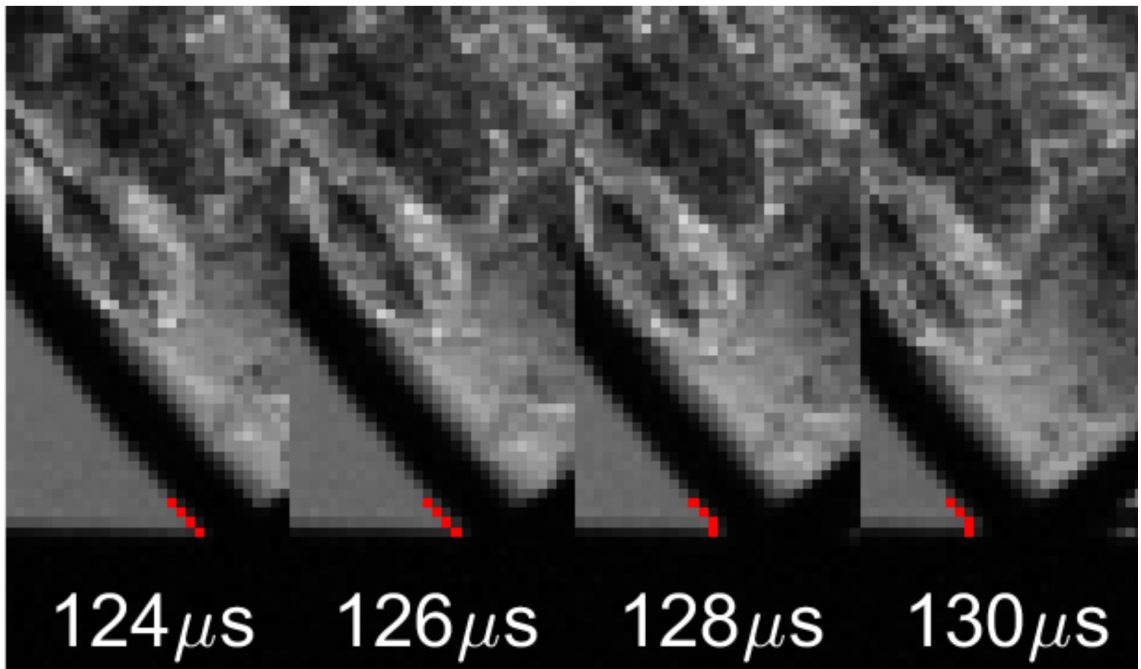


Figure 5.10: Frames from R8 showing the transition of the primary shock to a Mach stem.

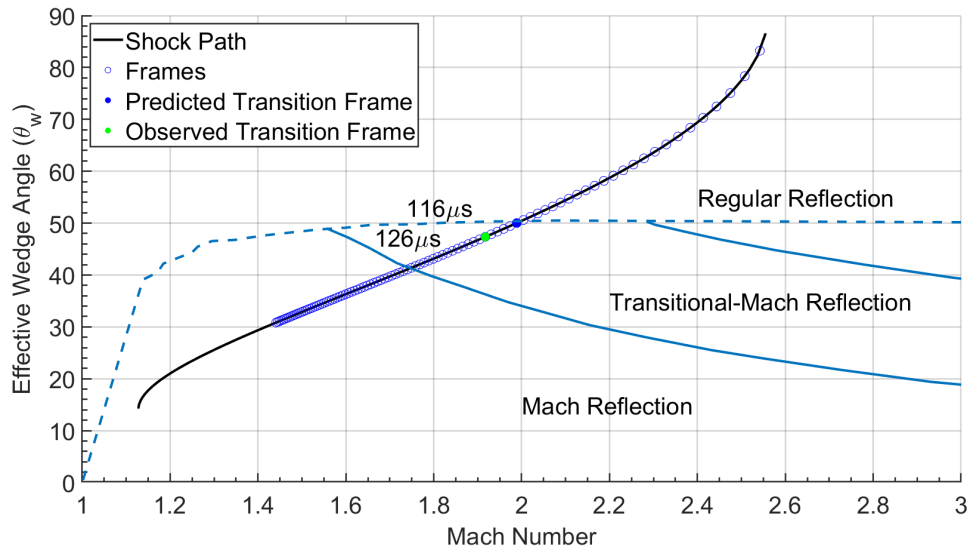


Figure 5.11: The Mach number and effective wedge angle path of the shock wave from R8 overlaid on the shock reflection type domain map. The predicted reflection transition is shown in solid blue and the observed transition is shown in solid green.

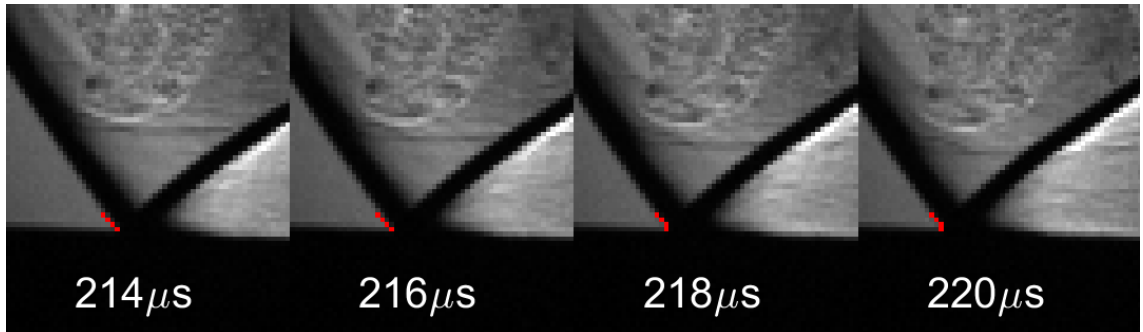


Figure 5.12: Frames from R11 showing the transition of the primary shock to a Mach stem.

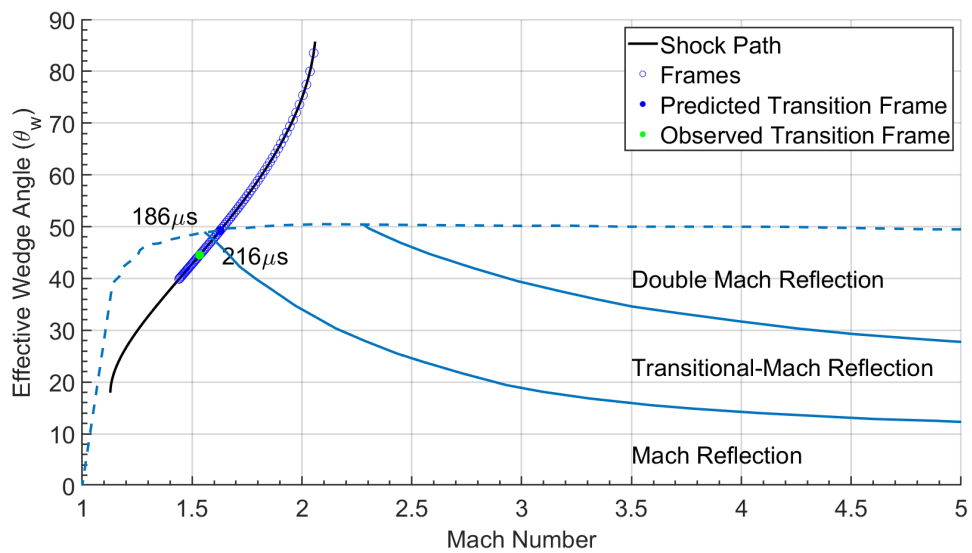


Figure 5.13: The Mach number and effective wedge angle path of the shock wave from R11 overlaid on the shock reflection type domain map. The predicted reflection transition is shown in solid blue and the observed transition is shown in solid green.

### 5.1.3 Mach Stem Growth Effect on Visualization of Mach Reflection

In the three cases studied the transition from regular to irregular reflection occurred at a lower effective wedge angle than predicted. In test R1 the transition was predicted to occur at an effective wedge angle of  $50^\circ$  and was observed at  $44^\circ$ . In test R8 the transition was predicted to occur at an effective wedge angle of  $50^\circ$  and was observed at  $47^\circ$ . In test R11 the transition was predicted to occur at an effective wedge angle of  $49^\circ$  and was observed at  $45^\circ$ . In each case the transition occurs between  $3 - 6^\circ$  lower than predicted. The  $3 - 6^\circ$  delay is greater than the  $1 - 2^\circ$  discrepancy shown for the transition of planar pseudo-steady shock waves [6]. A possible cause of this delay is the time required for the Mach stem to grow large enough to be observed by the imaging system.

The Mach stem growth was analytically modeled to estimate the time required for the Mach stem to be visible in the refractive imaging system. The properties of an irregular reflection for a given Mach number and effective wedge angle can be determined by simultaneously solving Equations 2.9 through 2.17. The property required to predict the Mach stem height is  $\chi$ , which is the slope at which the triple point moves away from the reflecting surface. The height of the Mach stem at any point along a path can be predicted analytically by integrating  $\chi$  from the transition to an irregular reflection to the desired point. Using the Mach number and effective wedge angle from in Figure 5.1,  $\chi$  was calculated by simultaneously solving Equations 2.9 through 2.17.  $\chi$  was then plotted as a function of time, Figure 5.14. By integrating  $\chi$ , the Mach stem height was then plotted as a function of time, Figure 5.15.

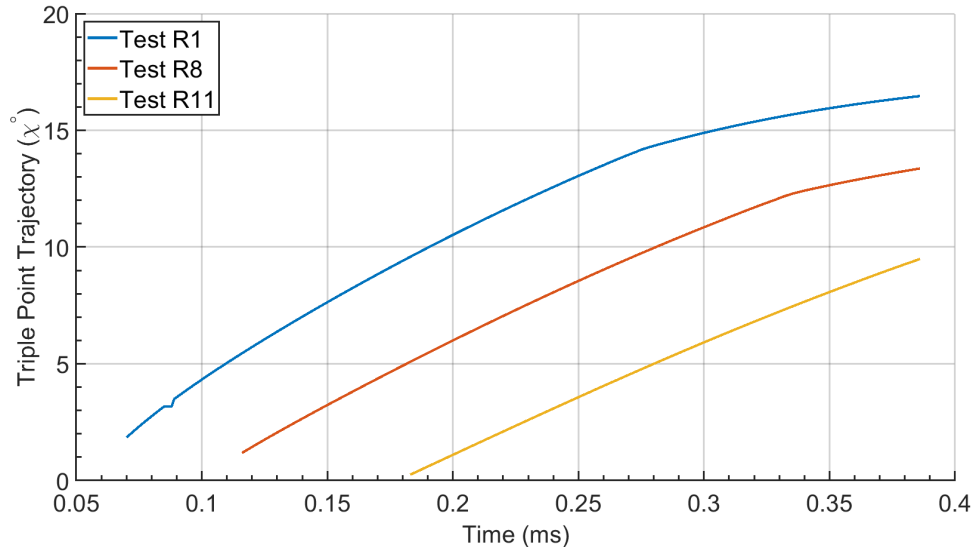


Figure 5.14: The triple point trajectory  $\chi$  as a function of time for tests R1, R8, R11.

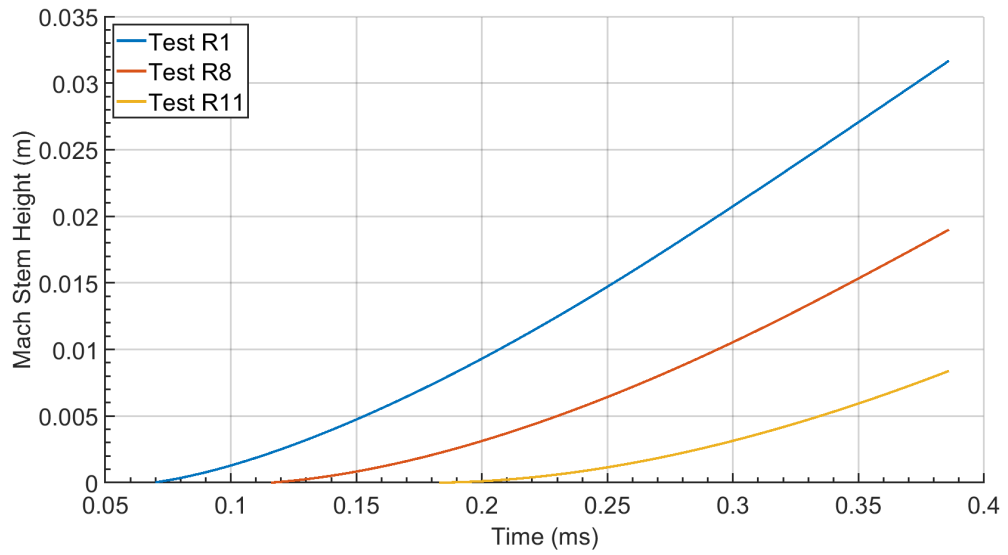


Figure 5.15: The Mach stem height as a function of time for tests R1, R8, R11.

Assuming the entire Mach stem is visualized by the schlieren system, the Mach stem may not be visualized until it has grown to the height of approximately 1 pixel. The 30 cm system Z schlieren system had a spatial resolution of  $0.7 \frac{mm}{pix}$ . Figure 5.15 shows that for test R1 the reflection transitions from regular to irregular at approximately  $70 \mu s$  but the Mach stem doesn't reach 0.7 mm in height until  $88 \mu s$ . One problem with this methodology is that the Mach stem may be observed prior to it reaching the height of 1 full pixel. The intensity of each pixel is the average of the brightness of everything in the imaged area over the time the camera shutter is open. Theoretically, over the frames between Mach stem formation and when it reaches a full pixel height the pixel corresponding to the bottom of the reflection will gradually decrease in intensity. This gradual visual transition is not seen for a number of reasons. The primary reason is the noise in the image background, which varies between normalized values of 0.30 and 0.38. Additionally the visual transition from the reflection surface to the background occurs over 2 pixels, as shown in Figure 5.9. Due to this noise it is not possible to observe the sub pixel growth of the Mach stem. A more reasonable assumption is that the Mach stem is observed when it is between a half and full pixel in height. For test R1 the analytical model predicts the Mach stem to reach a height of a half pixel, 0.35 mm, at  $80 \mu s$  and a full pixel, 0.7 mm, at  $88 \mu s$ . The Mach stem was observed in test R1 between  $88 \mu s$  and  $90 \mu s$ . For test R8, Figure 5.15, the Mach stem should be a half pixel tall at  $134 \mu s$  and a full pixel at  $146 \mu s$ . Figure 5.10 shows that the Mach stem is observed between  $126 \mu s$  and  $128 \mu s$  which is slightly after the half pixel height. For test R11, the Mach stem should be half pixel tall at  $217 \mu s$  and a full pixel at  $234 \mu s$ . The Mach stem in R11 was observed between  $216 \mu s$  and  $218 \mu s$  which is the half pixel time. In the above calculation it was assumed the Mach stem was fully in view of the schlieren system. If part of the Mach stem was obscured by the non-visualized area this would delay its observation.

The maximum height of the non-visualized area occurred at the center of the reflection surface and decreased to full visualization at the edges of the reflection structure. The height of the non-visualized area was not measured directly at any other locations. It is not possible to interpolate the height of the non-visualized area at other locations due to the non-uniform construction of the reflection structure. The center plate was the test section plate which was 6.25 mm (0.25 inch) thick and attached to the substructure at its edges, approximately 150 mm (6 inch) apart. The extension plates, where the reflections were visualized, was 0.5 mm thick and bolted to the substructure at its edges, approximately 600 mm (2 feet) apart. The extension plates were mounted on rubber sheets to raise them to the same height as the test section plate. Due to the wide difference in plate thickness and difference in mounting these plates are not deformed uniformly.

Since the height of the non-visualized area cannot be interpolated from the system geometry another method was used to estimate the height of the non-visualized area. A regular reflection is characterized by the primary and reflected shock meeting at the reflecting surface. Figure 5.16 shows the final regular reflection frame for tests R1, R8 and R11, with the bottom pixels of the primary and

reflected shock highlighted. The bottom pixels of the shocks were then fit to a line and those lines plotted over the image. Only the very bottom pixels were fit to minimize impact from the curvature of the shock. Being regular reflections, the fit lines should intersect at the reflecting surface. In Test R1, Figure 5.16A, the intersection is 3 pixels below the visualized surface. This implies that the local height of the non-visualized area is approximately 3 pixels. This matches the expectation of a large amount of the reflection being obscured and is why the visualization of the Mach stem was not used as the transition criteria in Figure 5.6. In Test R8, Figure 5.16B, the intersection of the lines is under half a pixel from the visualized surface. Similarly, in Test R11, Figure 5.16C, the lines intersect at the visualized surface. This shows that in Tests R8 and R11 the local height of the non-visualized area is less than half a pixel. In these cases, the uncertainty due to the Mach stem growth will dominate over the uncertainty due to the local height of the non-visualized area.

The transition from regular to irregular reflection matched theory to within the uncertainty of the imaging system. Of the three tests with good data, the transition to an irregular reflection was observed when the Mach stem was between a half to full pixel in height, a range between  $8 \mu s$  and  $17 \mu s$ . This gives an uncertainty in the effective wedge angle of the transition of  $\pm 5^\circ$ .

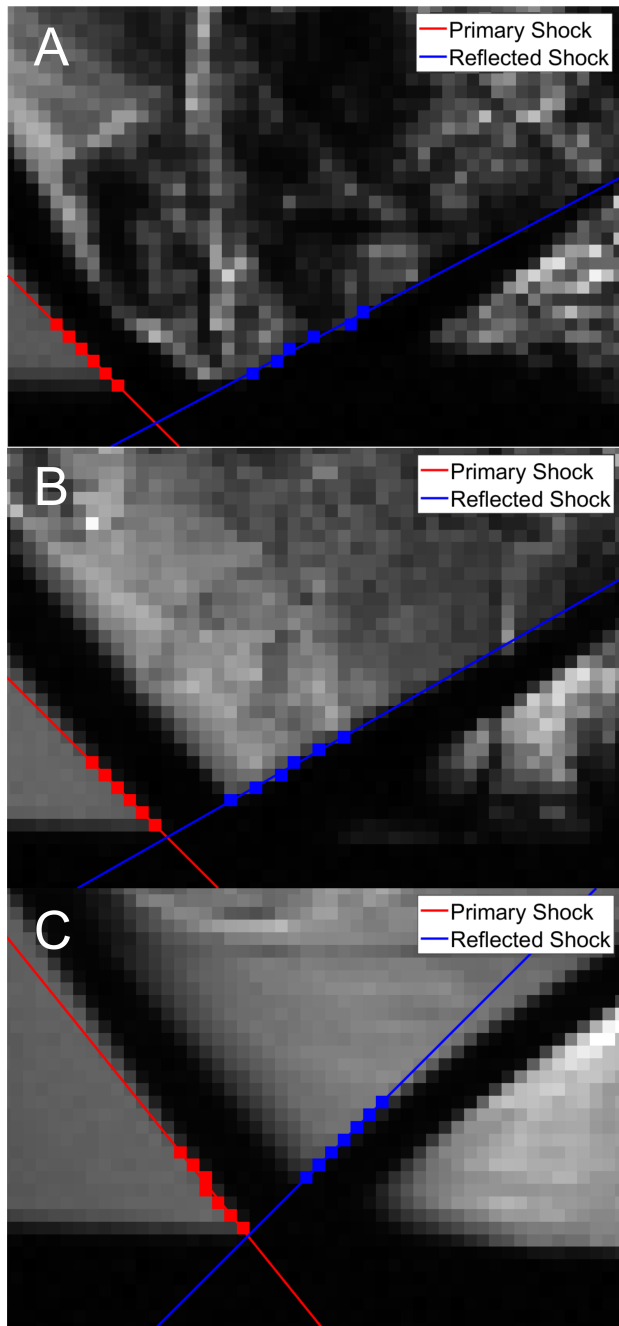


Figure 5.16: The final frame of the regular reflections from Tests R1, R8, and R11. The bottom pixels of the primary and reflected shocks are highlighted and a fit line shown.

## 5.2 Experimental Peak Pressure and Impulse

### 5.2.1 Fitting Experimental Pressure Data

Pressure traces were recorded for each of the shock reflection tests so that the peak pressure and impulse could be evaluated. Figure 5.17 is a flow diagram that outlines the process used to fit the pressure data to the Friedlander equation, Equation 1.14. Similar to the non-reflected case, the first step was to crop the data from the time of arrival to approximately the first time the pressure trace returns to zero. The pressure traces had two general forms where the pressure either asymptotically decayed to zero overpressure, Figure 5.18, or passed zero overpressure to have a negative phase, Figure 5.19. The Friedlander equation assumes there will be a negative phase which allows the root of the pressure trace to be found. When the pressure traces without a negative phase were fit to the Friedlander equation the resulting fitting parameters were unrealistic.

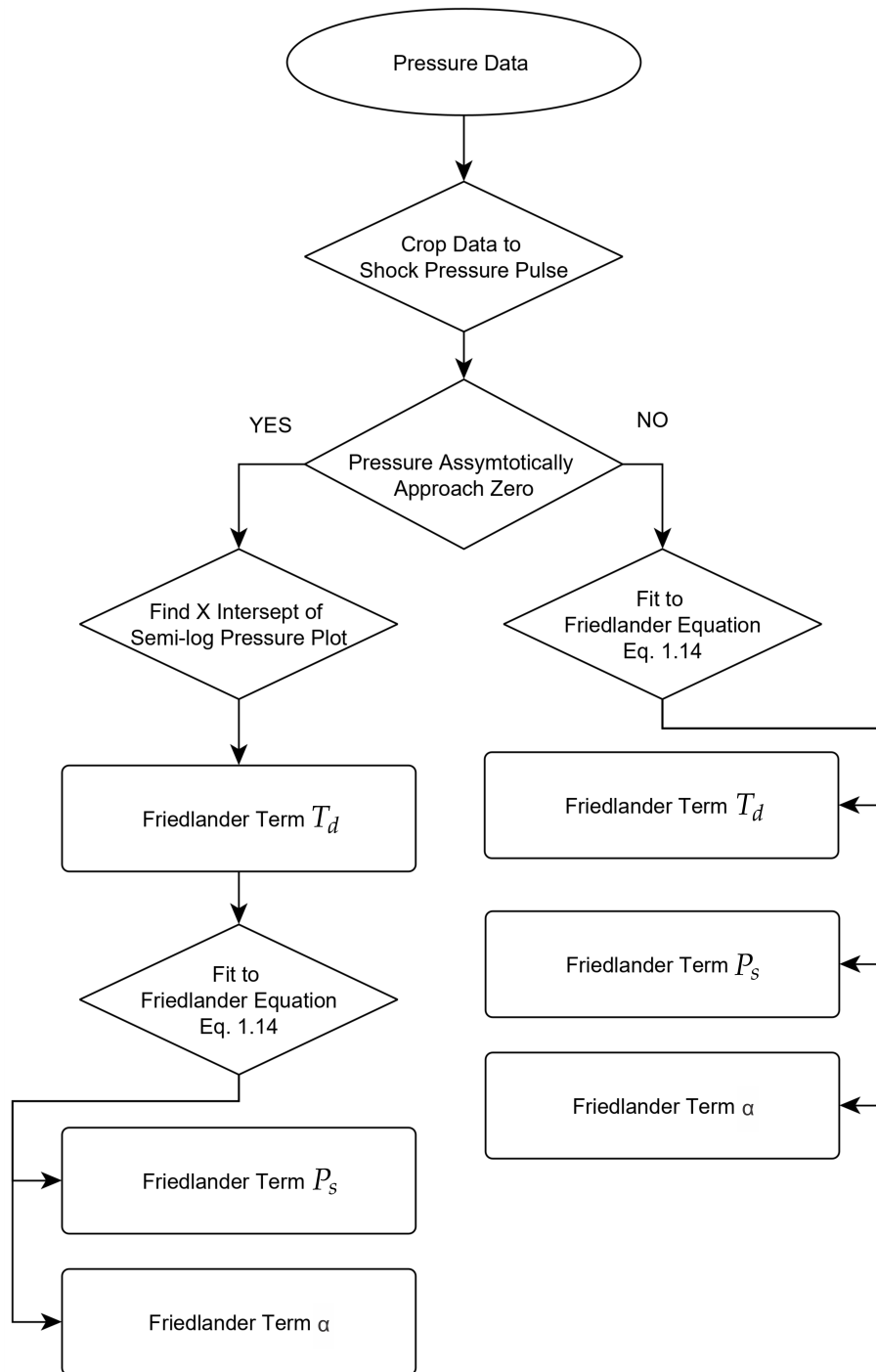


Figure 5.17: Flow chart outlining the calculation of the Friedlander parameters for a reflected shock.

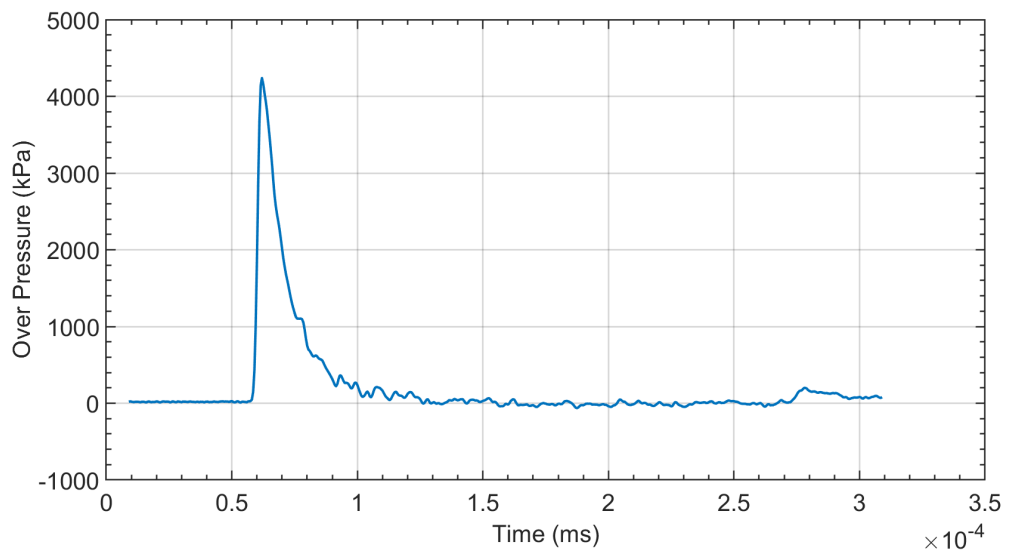


Figure 5.18: Raw pressure trace from the pressure probe at  $X=-5.1$  cm from Test R1.

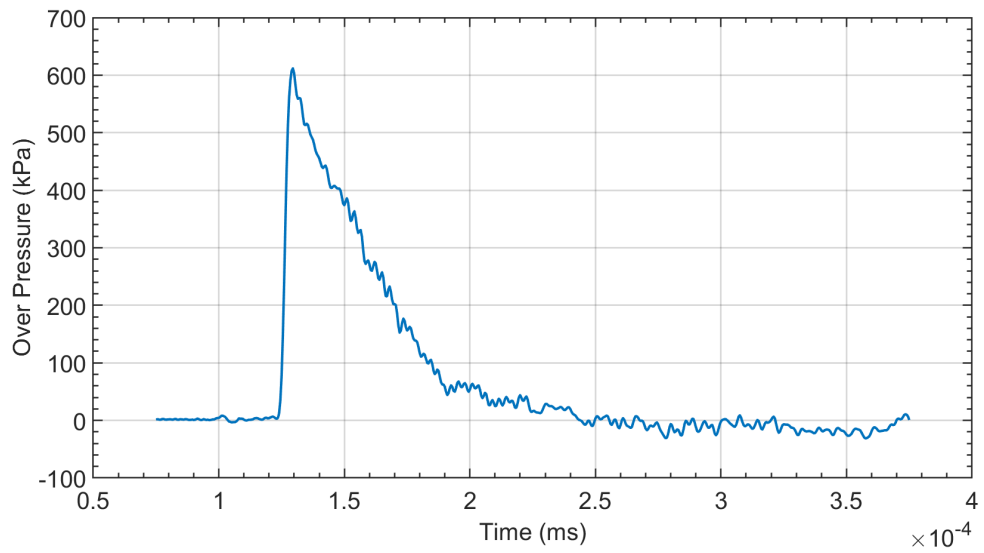


Figure 5.19: Raw pressure trace from the pressure probe at  $X=-15.2$  cm from Test R1

To improve the fit of the reflected pressure data that gave unrealistic values, the pulse duration was first determined then the data was fit to the Friedlander equation with a fixed pulse duration. The pulse duration was found by plotting the pressure trace as a function of logarithmic time and linear pressure and performing a linear fit to the lower portion of the pressure trace. The semi-log fit was performed from a pressure of 40% of the raw peak to the lowest pressure point. The resulting X intercept of the linear fit is taken as the pulse duration [70, 107]. This process is shown in the left half of Figure 5.20. The pulse duration was then used as a fixed value in the Friedlander fit and the peak pressure and decay coefficient,  $\alpha$ , found using a non-linear least squares approach, Figure 5.20 right.

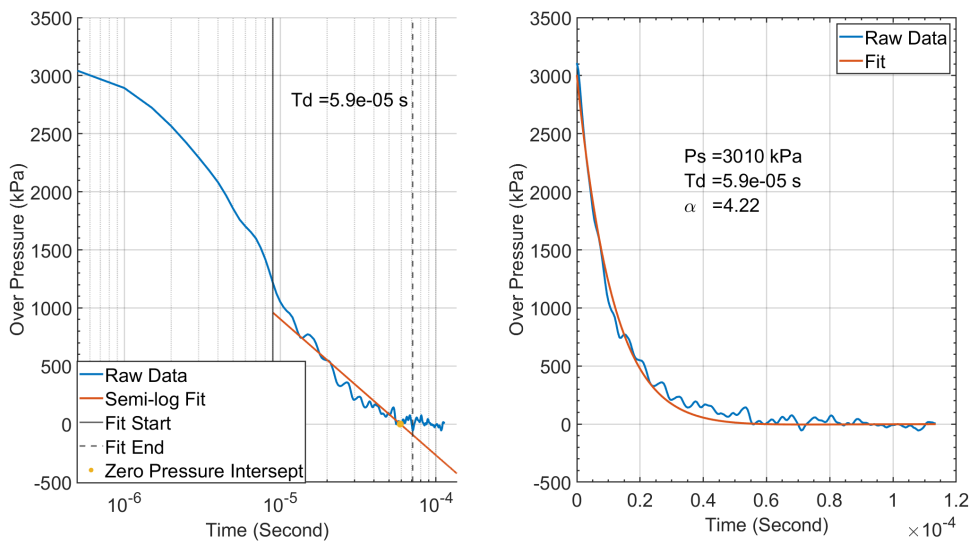


Figure 5.20: Two step fitting to the pressure trace from the pressure probe at  $X = -7.6$  cm from Test R1. The left plot is the linear fit to the semi-log data to find the pulse duration. The right plot is the Friedlander fit to determine the remaining two variables.

In the reflection testing, the explosive pellet was suspended at four different heights of 8, 9, 11 and 14 charge diameters (0.088, 0.102, 0.123 and 0.155 m). The fitted peak pressure from each height of burst (HOB) is shown in Figures 5.21 through 5.24. The X axis of Figures 5.21 through 5.24 is the radius from the charge center to the pressure probe location which was determined using the measured HOB for each test. The fitted pulse duration for each height of burst are shown in Figures 5.25 through Figure 5.28. The decay coefficient did not appear to be a function of HOB, but is only a function of radius from the charge. The decay coefficient,  $\alpha$ , for all reflection tests are shown in Figure 5.29.

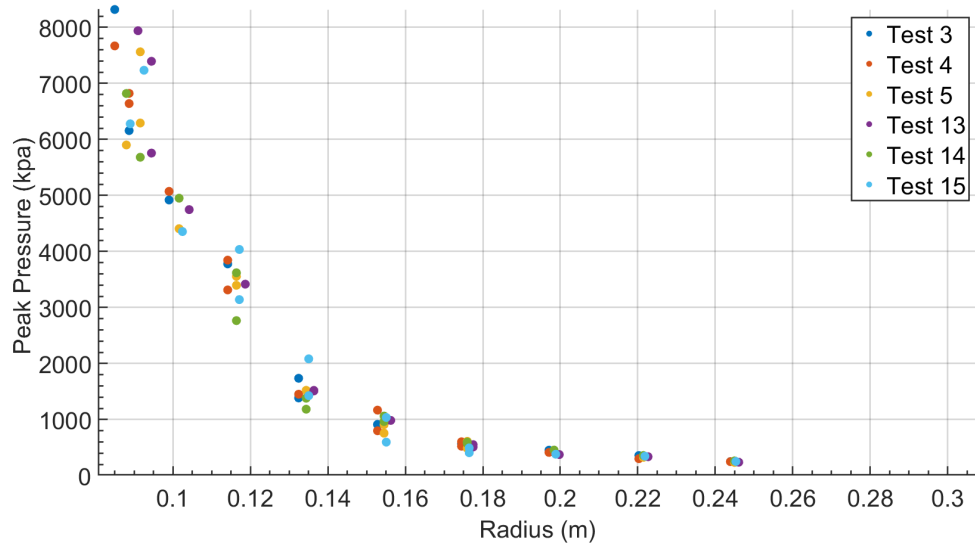


Figure 5.21: Peak pressure values for the 8 charge diameter HOB tests.

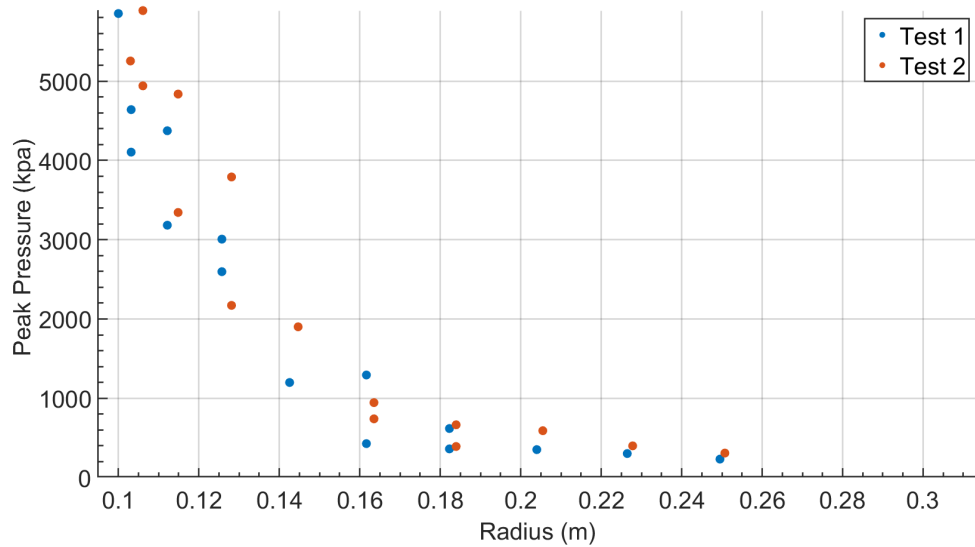


Figure 5.22: Peak pressure values for the 9 charge diameter HOB tests.

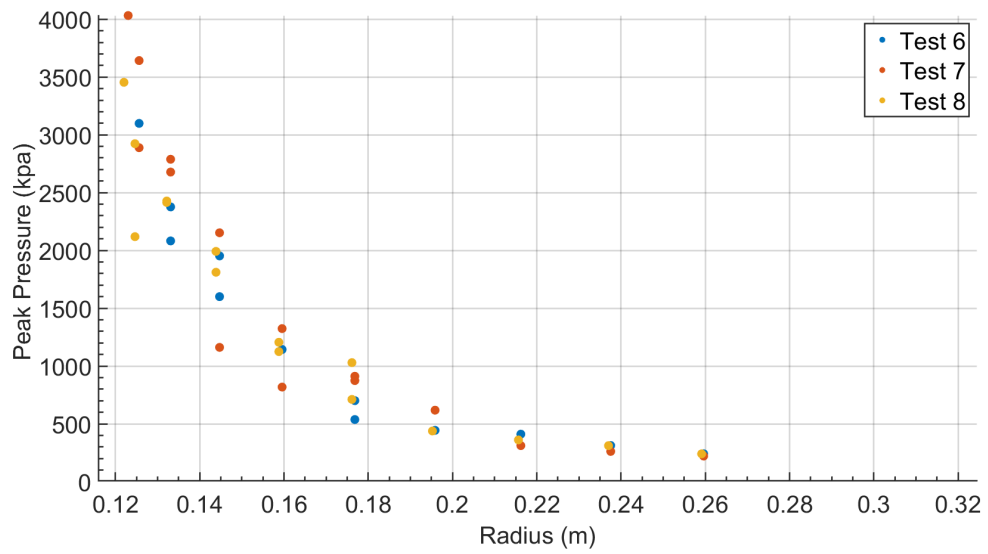


Figure 5.23: Peak pressure values for the 11 charge diameter HOB tests.

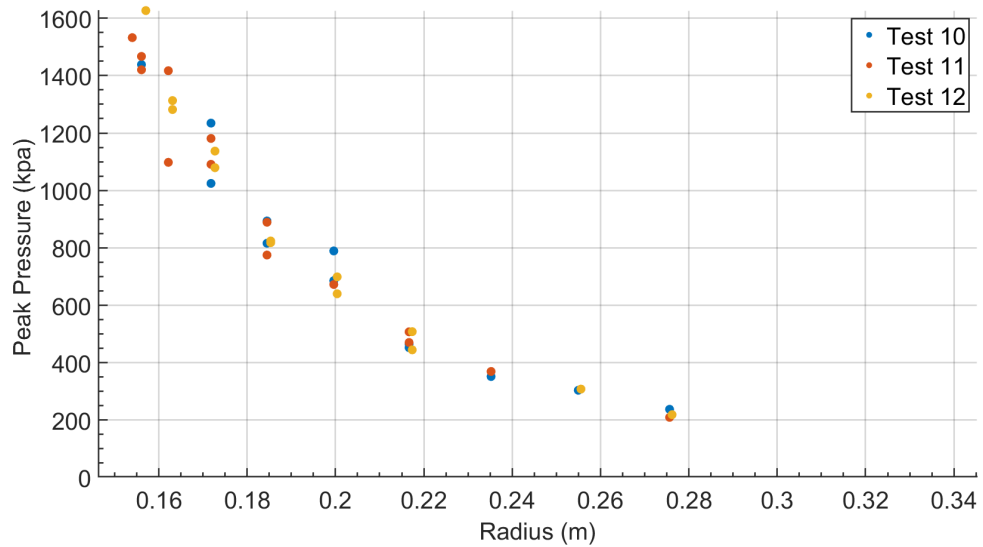


Figure 5.24: Peak pressure values for the 14 charge diameter HOB tests.

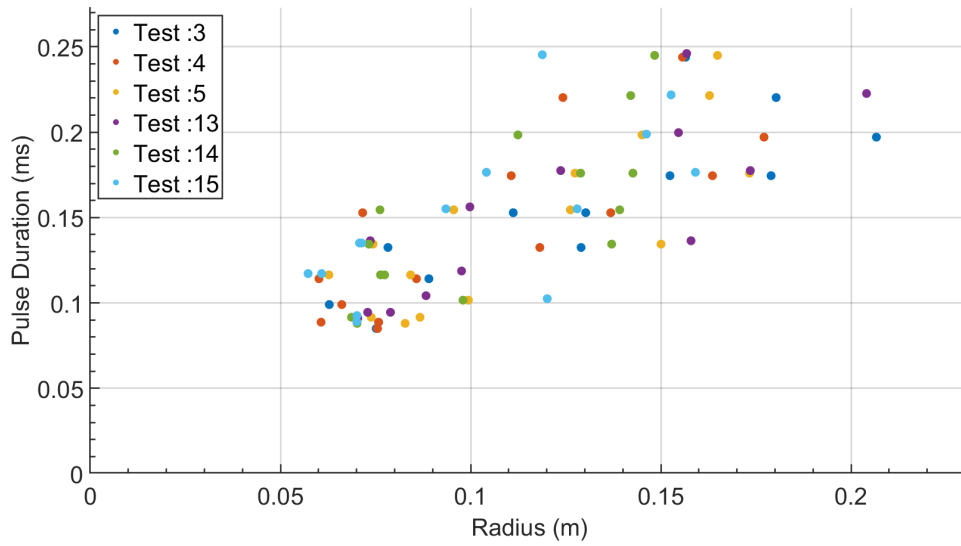


Figure 5.25: Pulse duration values for the 8 charge diameter HOB tests.

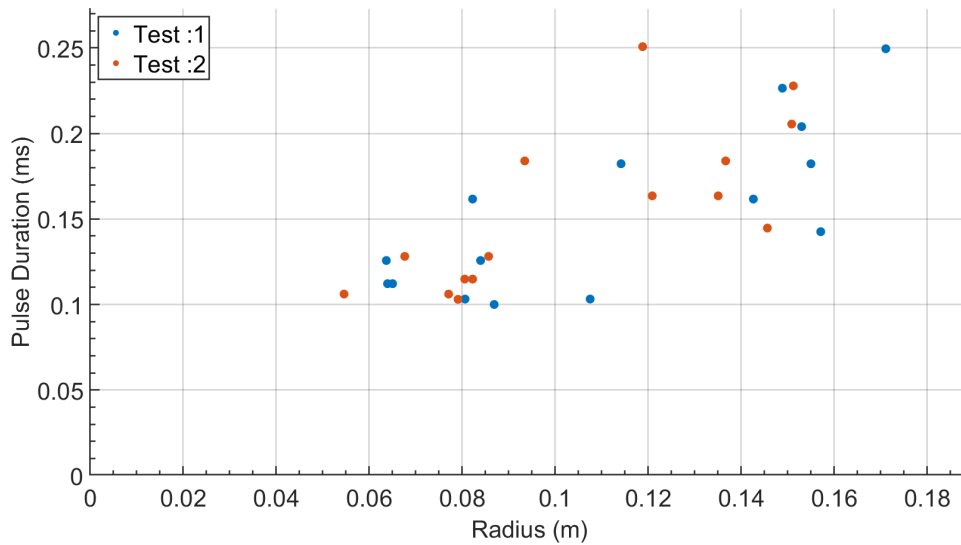


Figure 5.26: Pulse duration values for the 9 charge diameter HOB tests.

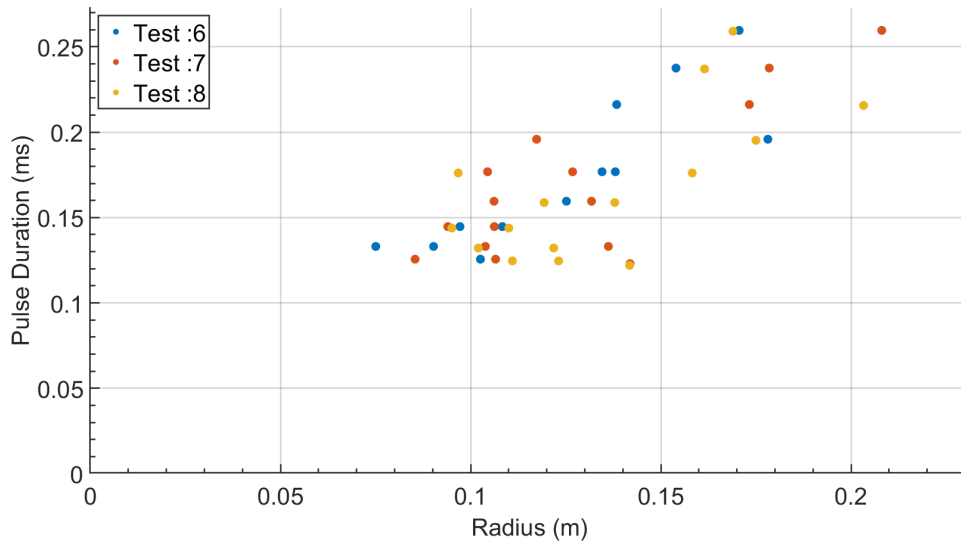


Figure 5.27: Pulse duration values for the 11 charge diameter HOB tests.

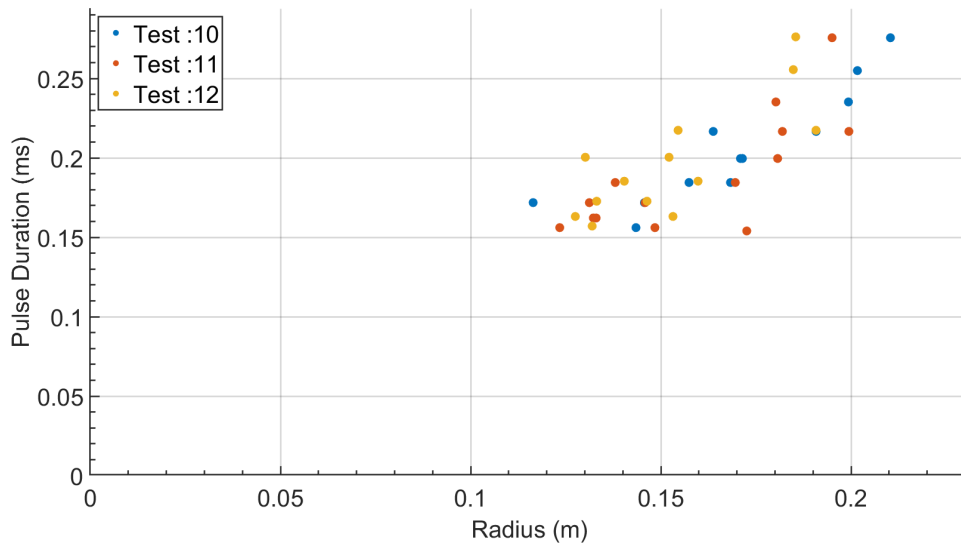


Figure 5.28: Pulse duration values for the 14 charge diameter HOB tests.

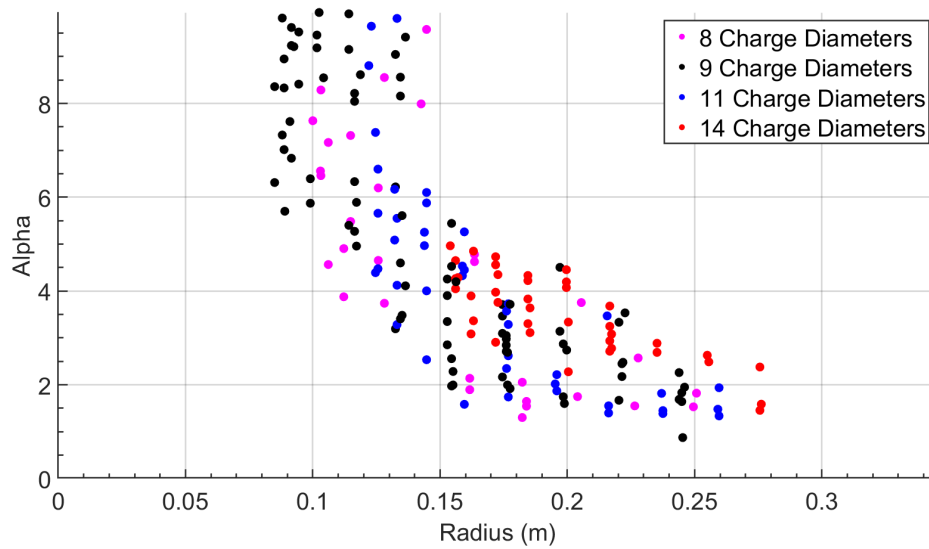


Figure 5.29: Decay coefficient,  $\alpha$ , for all tests.

## 5.2.2 Uncertainty In Pressure Data

The pressure data had two sources of error, mis-calibration and errors in the dynamic measurement. To calibrate the pressure probes, the voltage response of each pressure probe was recorded and a linear fit determined. The deviation from the fit was recorded at 20%, 40%, 60%, 80%, and 100% of the probes range. The vast majority had an error below 1%. The error in the dynamic measurement is more difficult to measure but the objective of fitting the data to the Friedlander equation is to reduce this error. To quantify the uncertainty in the resulting fitting parameters the standard deviation was calculated as a function of radius. For the decay coefficient, ( $\alpha$ ), the data was separated into 2-cm regions and the uncertainty of each region was calculated. In Figure 5.30, the uncertainty is shown about the local mean. This process was repeated for the peak pressure, Figure 5.31 through Figure 5.34, and pulse duration data, Figure 5.35 through Figure 5.38, for each height of burst with the uncertainty calculated for each probe location.

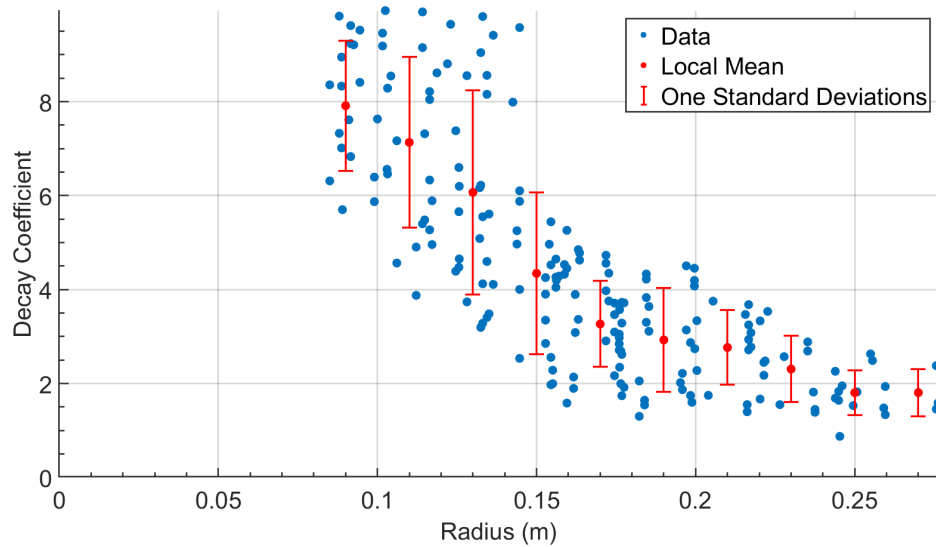


Figure 5.30: Uncertainty as a function of radius for the decay coefficient,  $\alpha$ .

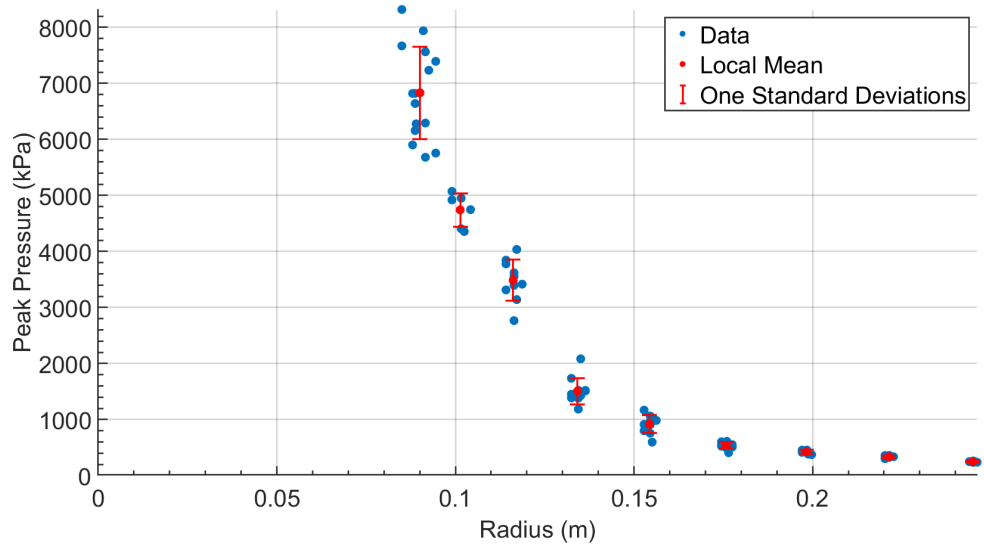


Figure 5.31: Uncertainty as a function of radius for the peak pressure for 8 charge diameters.

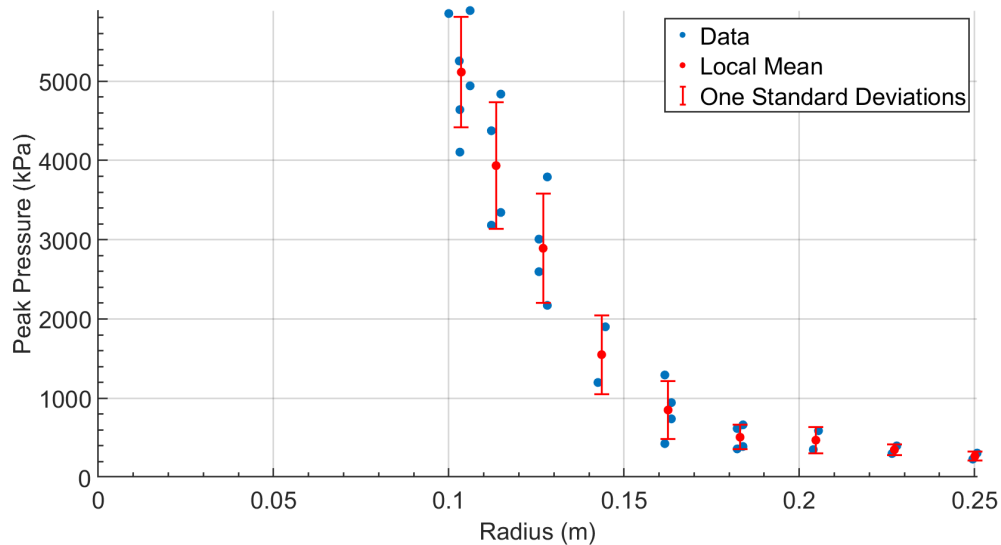


Figure 5.32: Uncertainty as a function of radius for the peak pressure for 9 charge diameters.

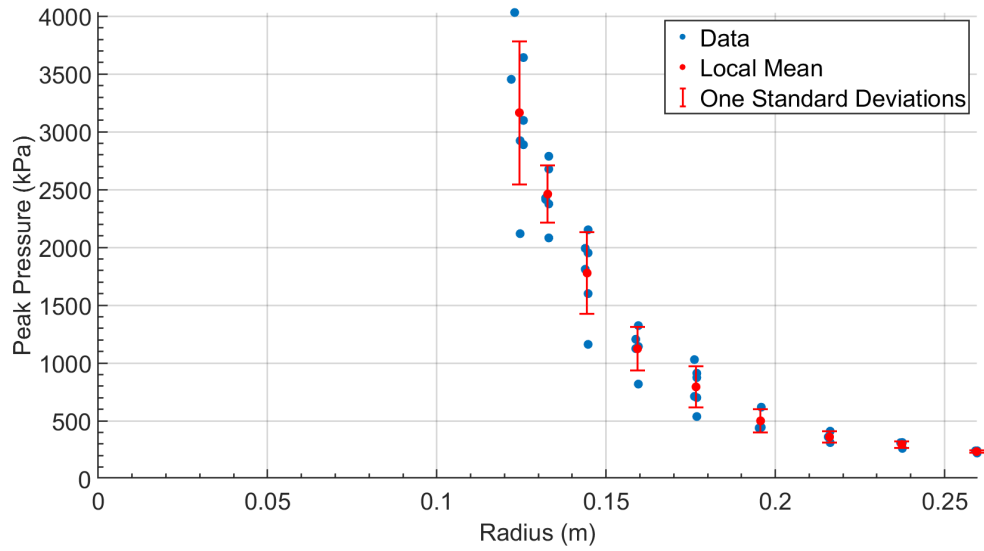


Figure 5.33: Uncertainty as a function of radius for the peak pressure for 11 charge diameters.

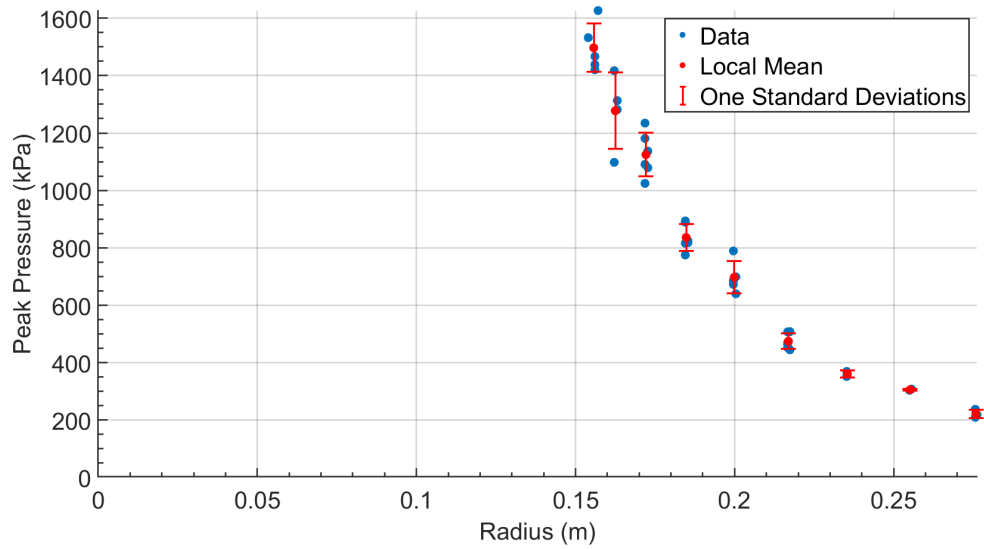


Figure 5.34: Uncertainty as a function of radius for the peak pressure for 14 charge diameters.

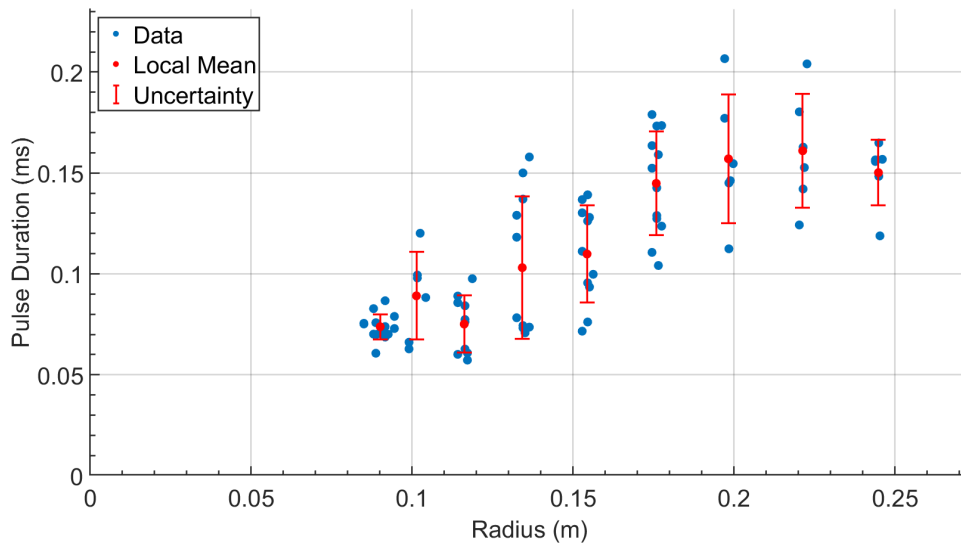


Figure 5.35: Uncertainty as a function of radius for the pulse duration for 8 charge diameters.

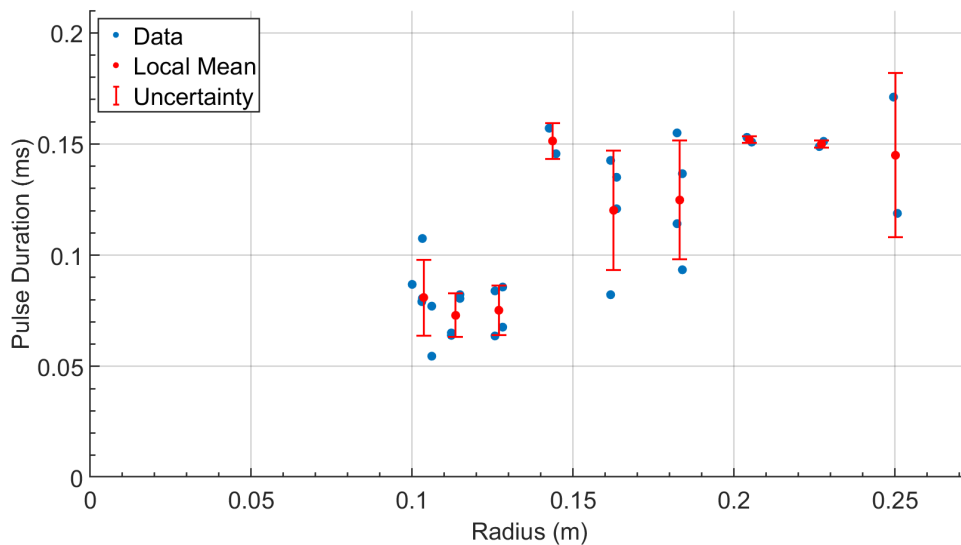


Figure 5.36: Uncertainty as a function of radius for the pulse duration for 9 charge diameters.



The uncertainty of each term was propagated through the Friedlander impulse equation, Equation 1.15, to find the uncertainty in the final impulse values. The propagation of uncertainty for an arbitrary function  $Q = f(x, y, \dots)$  is given as [108]

$$\Delta Q = \sqrt{\left(\frac{\partial f}{\partial x} \Delta x\right)^2 + \left(\frac{\partial f}{\partial y} \Delta y\right)^2 + \dots} \quad (5.1)$$

where  $\Delta Q$  is the uncertainty of the total function and  $\Delta x$  and  $\Delta y$  are the uncertainty of each variable. Starting from Equation 1.15, the partial derivatives for peak pressure and pulse duration are

$$\frac{\partial I/A}{\partial P_s} = T_d \left[ \frac{1}{\alpha} - \frac{1 - e^{-\alpha}}{\alpha^2} \right] \quad (5.2)$$

$$\frac{\partial I/A}{\partial t_d} = P_s \left[ \frac{1}{\alpha} - \frac{1 - e^{-\alpha}}{\alpha^2} \right] \quad (5.3)$$

which can be rewritten as

$$\frac{\partial I/A}{\partial P_s} = \frac{I/A}{P_s} \quad (5.4)$$

$$\frac{\partial I/A}{\partial t_d} = \frac{I/A}{t_d} \quad (5.5)$$

The partial derivative for  $\alpha$  is

$$\frac{\partial I/A}{\partial \alpha} = P_s t_d \left[ -\frac{1}{\alpha^2} - \frac{e^{-\alpha}}{\alpha^2} + \frac{2(1 - e^{-\alpha})}{\alpha^3} \right] \quad (5.6)$$

Combining Equations 5.4, 5.5, and 5.6 into Equation 5.1 gives

$$\Delta I/A = \sqrt{\left(I/A \frac{\Delta P_s}{P_s}\right)^2 + \left(I/A \frac{\Delta t_d}{t_d}\right)^2 + \left(P_s t_d \left[-\frac{1}{\alpha^2} - \frac{e^{-\alpha}}{\alpha^2} + \frac{2(1 - e^{-\alpha})}{\alpha^3} \Delta \alpha\right]\right)^2} \quad (5.7)$$

Using Equation 5.7 the uncertainty was calculated for the impulse per area at each pressure probe location. This uncertainty was plotted about the local mean along with the calculated impulse in Figures 5.39 through 5.42. The propagated uncertainty was much greater than the uncertainty calculated based on the impulse values themselves. This is due to the interaction between the pulse duration and decay coefficient terms. When the semi-log fit over calculated the pulse duration the Friedlander fit gave an overly large  $\alpha$  to maintain a good overall fit. The result is that the large scatter in the pulse duration term forces large scatter in the decay coefficient term. The large uncertainty in pulse duration and decay coefficient cause a larger overall uncertainty.

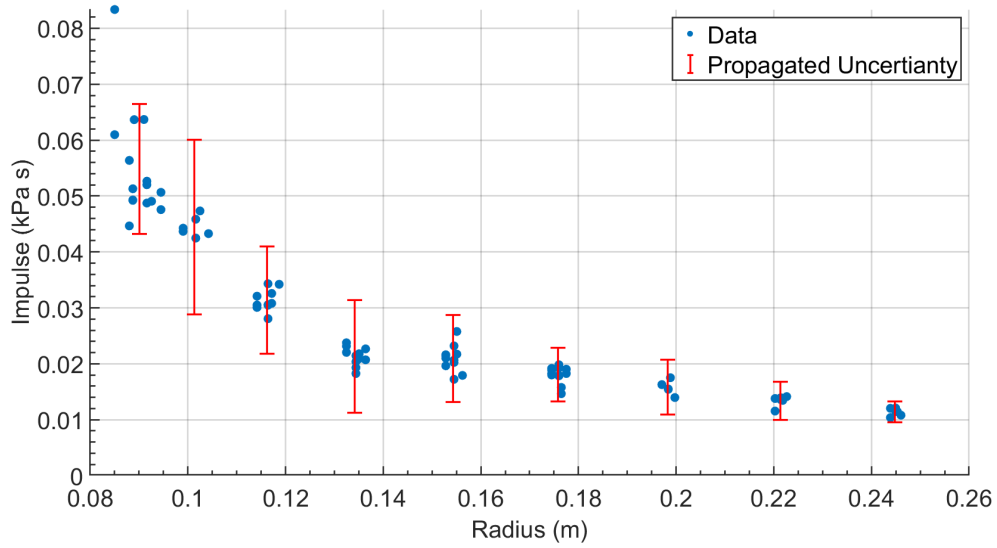


Figure 5.39: Experimental values and uncertainty of impulse as a function of radius for the 8 charge diameter tests.

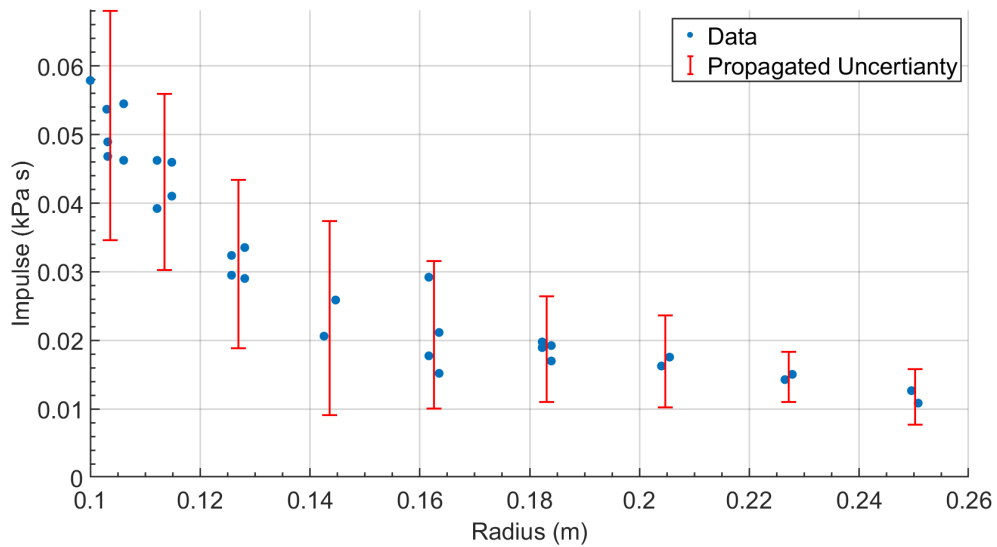


Figure 5.40: Experimental values and uncertainty of impulse as a function of radius for the 9 charge diameter tests.

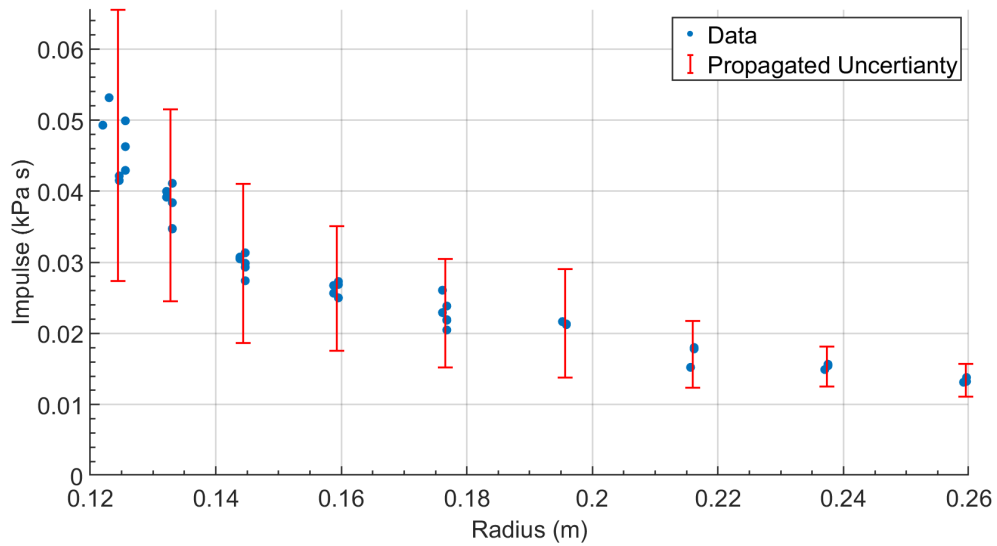


Figure 5.41: Experimental values and uncertainty of impulse as a function of radius for the 11 charge diameter tests.

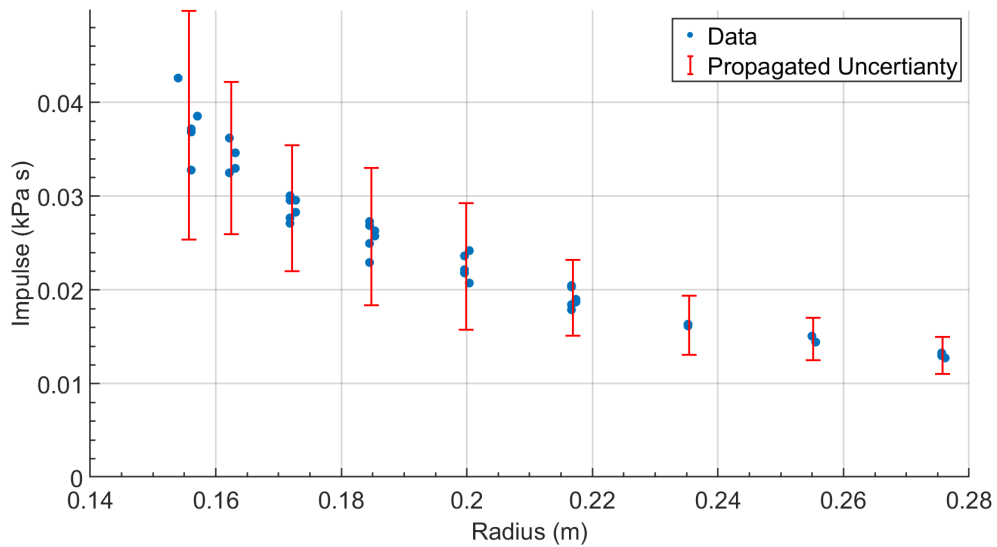


Figure 5.42: Experimental values and uncertainty of impulse as a function of radius for the 14 charge diameter tests.

### 5.3 Analytical Peak Pressure and Impulse

Figure 5.43 is a flow chart to summarize the process that will be detailed in the following section to analytically calculate the peak pressure and impulse for a reflected shock wave. Inputs such as data and assumptions are shown in ovals. Calculations and fits are shown in diamonds. There are three terms that are used to calculate impulse: peak pressure, pulse duration and decay coefficient. The sub-process for each term is grouped and outlined. The flow chart summarizing the analytical pulse duration was separated into Figure 5.44.

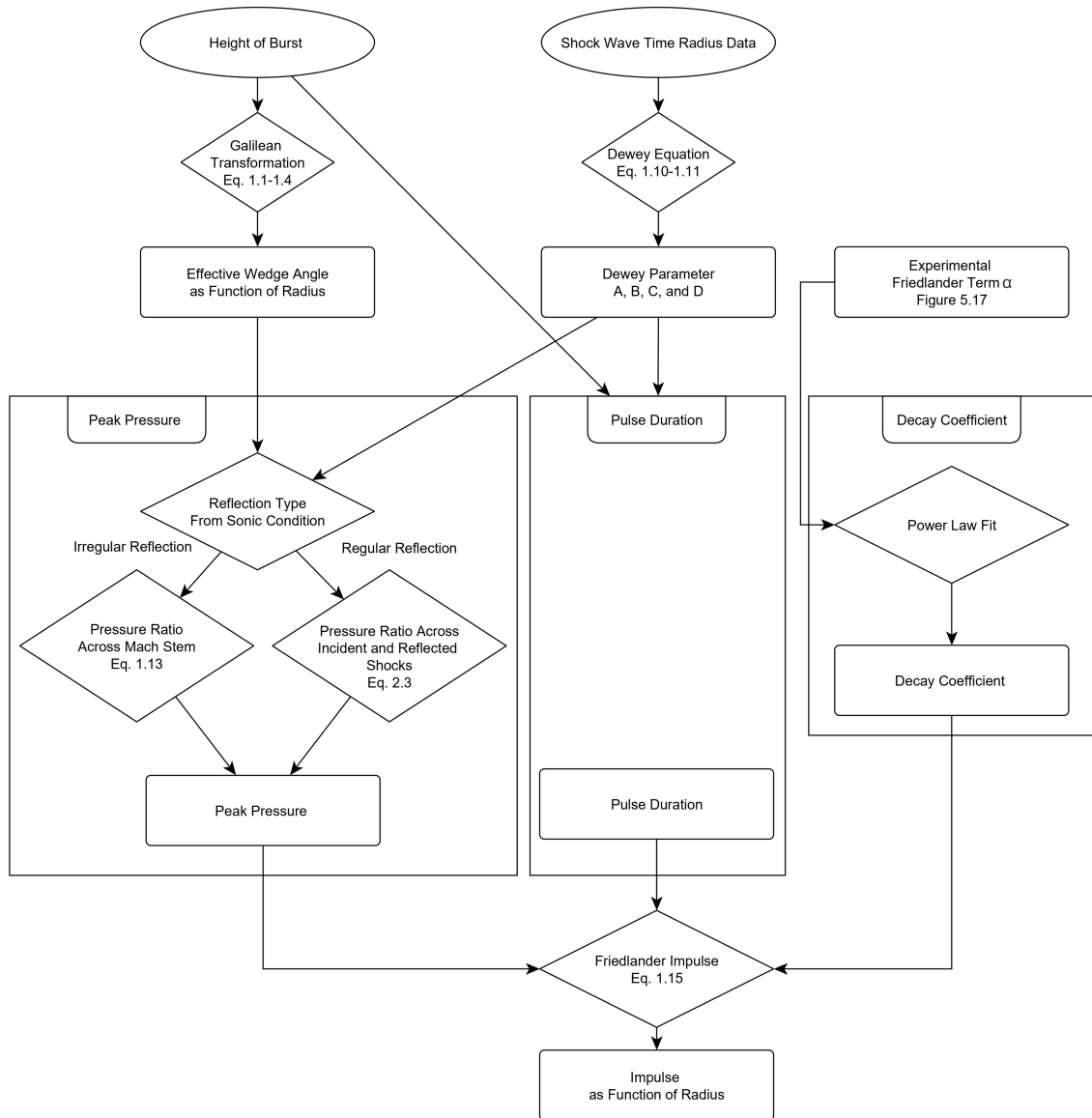


Figure 5.43: Flow chart outlining the calculation of analytical impulse for a reflected shock. The subprocess used to calculate pulse duration is shown in the following figure.



### 5.3.1 Analytical Peak Pressure

To calculate the impulse analytically required determining the three underlying terms: peak pressure, pulse duration and decay coefficient. The peak pressure is calculated by first determining the reflection type and then solving for the conditions across each of the reflected shocks. For a given reflection location the primary shock wave's Mach number is used to find the effective wedge angle corresponding to the sonic condition, as discussed previously in Section 2.4. If the effective wedge angle is greater than the sonic condition then a regular reflection will occur. The reflection details are solved by matching the angle of deflection of the flow across the primary and reflected shock. The pressure ratio across the reflection is then the product of the pressure ratios across the primary and secondary shock wave. If the effective wedge angle is less than the sonic condition an irregular reflection will occur which is solved by simultaneously solving Equations 2.9 through 2.17. The pressure ratio at the reflecting surface is then the pressure ratio across the Mach stem. Using this process, the pressure across the reflection can be determined for any point along the reflection path.

The pressure was analytically determined for the four heights of burst and showed good agreement with experimental data. The analytical peak pressure is shown as a function of radius from the charge center for a height of burst of 8 charge diameters in Figure 5.45. The reflection begins at low radius as a regular reflection at high over pressure and as the shock expands the Mach number and changing angle decrease the over pressure. When the reflection reaches the sonic condition the reflection transitions to an irregular reflection, the vertical dashed line. The analytical peak pressure then drops after the transition. The peak pressure then continues to decrease at increasing radius but at a lower rate than for the regular reflection. Comparing the analytical peak pressure with the experimental peak pressure shows that initially the analytical result is in the middle of the experimental data. The analytical result then slightly underpredicts the pressure around 0.1 m. Immediately after the transition, the analytical result underpredicts the peak pressure by approximately 50%. The analytical result then slightly underpredicts the pressure data around 0.135 m. At 0.155 m the analytical peak pressure is within the scatter of the experimental data but below the mean of the data. Between 0.17 m and 0.24 m the analytical result is near the mean of the experimental data and slightly overpredicts the peak pressure of the final group of experimental data. This is the general trend between the analytical and experimental peak pressure for the other three heights of burst, Figure 5.46 through Figure 5.48. Initially the analytical peak pressure under predicts the experimental data. At the transition from regular to irregular reflection the analytical pressure drops. The analytical pressure of the irregular reflection then under predicts the mean of the experimental pressure immediately after the transitions but then slightly over predicts the mean of the experimental pressure in the far field.

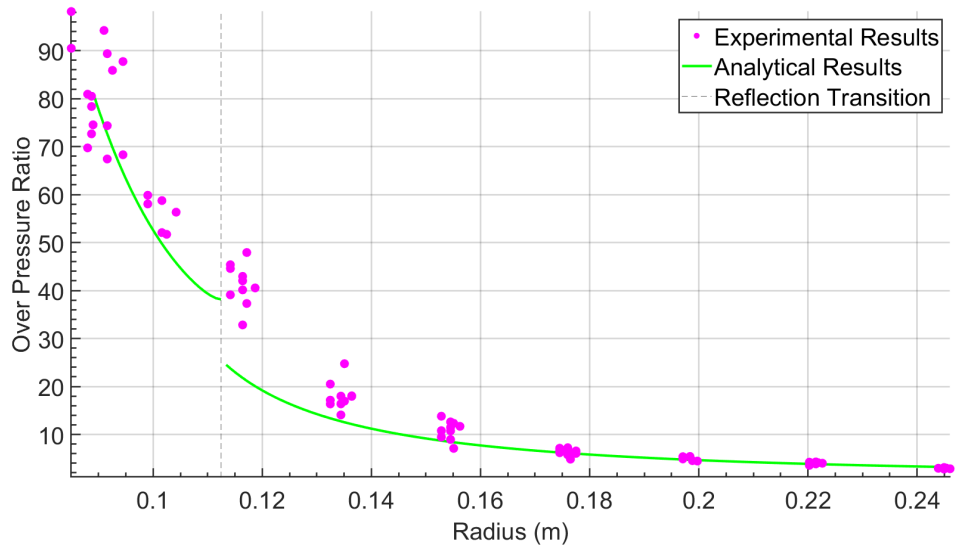


Figure 5.45: Comparison between the analytical and experimental values for peak pressure for the 8 charge diameter tests.

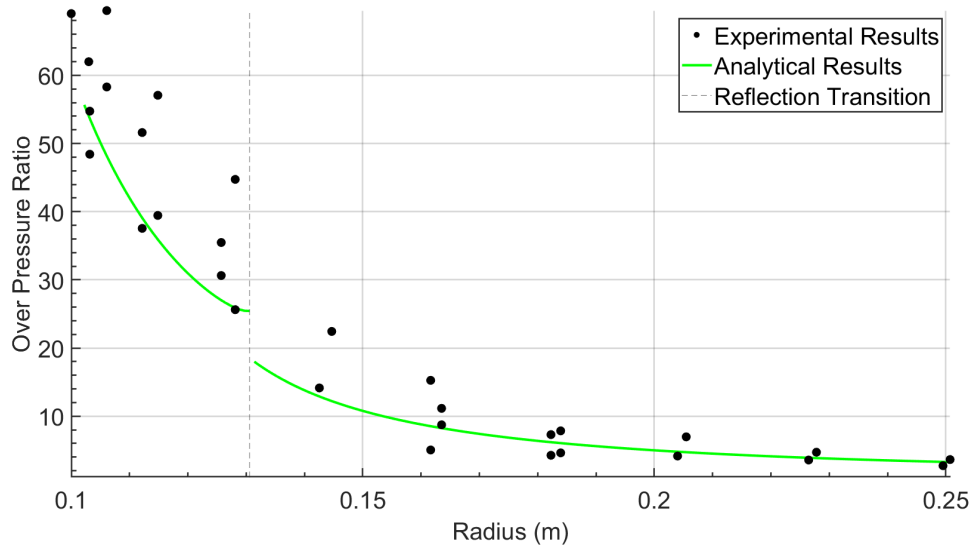


Figure 5.46: Comparison between the analytical and experimental values for peak pressure for the 9 charge diameter tests.

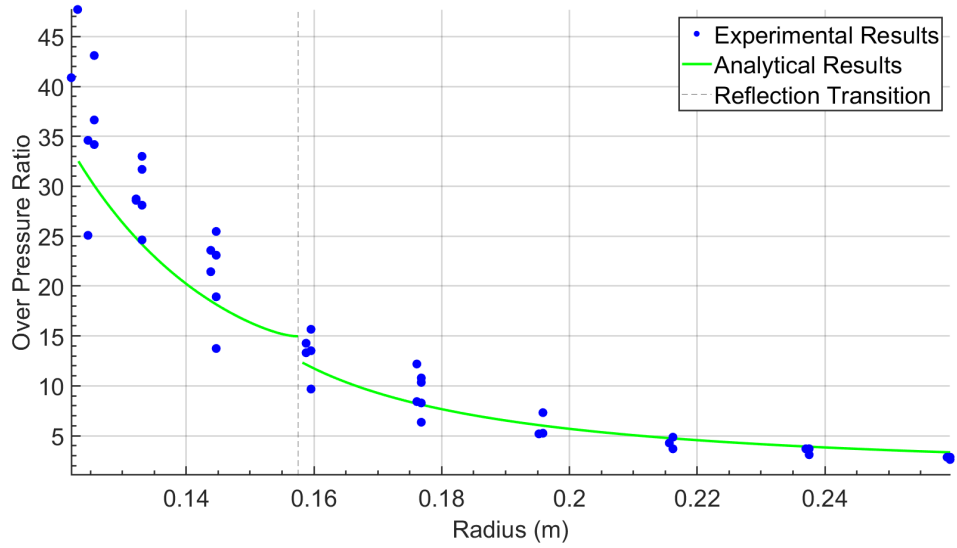


Figure 5.47: Comparison between the analytical and experimental values for peak pressure for the 11 charge diameter tests.

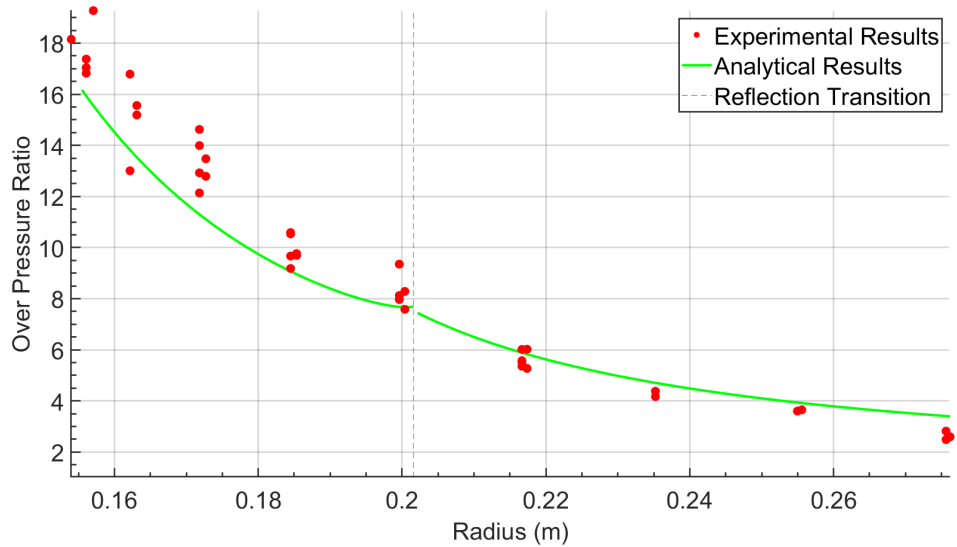


Figure 5.48: Comparison between the analytical and experimental values for peak pressure for the 14 charge diameter tests.

### 5.3.2 Analytical Pulse Duration

Figure 4.51 showed that the pulse duration of a shock wave expanding into free air can be predicted by tracking a wave released in the expansion process of the product gasses. Tracking the wave's path is fairly straight-forward since the geometry is spherically symmetric in free air. The spherical symmetry is broken for the case of a shock reflection. After the release wave detaches from the product gases it will begin by expanding uniformly behind the primary shock, similar to the free air case. At some point, depending on the wave path and height of burst, the release wave will reach the reflected shock. After the reflected shock the release wave moves through non-symmetric regions of temperature and speed of sound.

To calculate the speed of sound field behind the reflected shock requires an additional assumption to govern the movement of the reflected shock into the already shocked air. Since a shock wave reflection from a perfect surface is equivalent to a symmetry line between two identical charges, the reflected shock will be assumed to move with the same radius time curve as the shock propagating through unshocked air. This is demonstrated in Figure 5.49 where the radius of the primary and reflected shock have radii of  $r$ . This assumption, causes the reflected shock to have the same velocity as the primary shock.

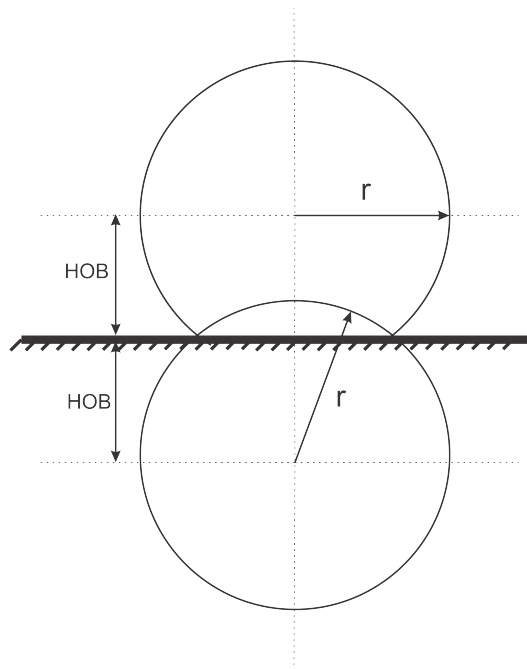


Figure 5.49: Schematic of how the radius of the reflection shock is defined.

After the primary shock, the shocked air will have a higher temperature than ambient and as a result will have a higher speed of sound. Assuming the reflected shock has the same velocity as the primary shock but moving through

an environment with a higher temperature, and thus speed of sound, will cause it to have a lower Mach number. The Mach number was then used to determine the temperature ratio across the reflected shock with Equation 4.10. Figure 5.50a is the temperature ratio across the primary shock. Using the atmospheric temperature before the primary shock and Equation 4.9 the speed of sound was calculated at all points in Figure 5.50a. This was used with the radius time curve to determine the Mach number of the reflected shock at all points. Areas with high temperatures had correspondingly high speeds of sound which decreased the Mach number of the reflected shock. Areas near or in the fireball had very high temperatures and thus speeds of sound. In these very high speed of sound areas the Mach number was calculated to be below 1 so the Mach number was rounded to 1. Using the Mach number of the reflected shock, the temperature ratio across the reflected shock was calculated, Figure 5.50b. The product of the temperature ratio across the primary and reflected shock gives the temperature ratio from atmospheric to behind the reflected shock, Figure 5.50c. The combined temperature ratio is then used to find the speed of sound behind the reflected shock, Figure 5.51. The final speed of sound field was calculated on a square 0.1 mm grid.

To verify the methodology and underlying assumptions used to generate the speed of sound profile in Figure 5.51, the temperature ratio was examined at two points on the reflecting surface. The first point examined was directly under the charge, at  $X = 0$  in Figure 5.50. Using the Mach-radius profile, the Mach number at  $X = 0$  was determined to be 3.2. Using the Mach number, the equations for a normal shock reflection from [70] and compressible flow relations [72], the temperature ratio across the reflection was analytically determined to be 5.2. Figure 5.50c shows a predicted temperature ratio of 4.5 across the reflected shock wave.

The second point examined was at  $X = 50$  mm which would generate a regular reflection. From the Mach-radius profile the Mach number at this point was determined to be 2.8 at an effective wedge angle of  $63^\circ$ . The Mach number and wave angle across each shock was determined using the process outlined in Section 2.2. The temperature ratio across each shock was then determined using the compressible flow equations across an oblique shock [72]. This gave a temperature ratio across the reflection of 4.1 compared to the predicted temperature ratio of 3.8 shown in Figure 5.50c. This analysis shows that the new methodology and assumptions used to calculate the temperature field and then speed of sound field are reasonable and agree with prior analytical methods.

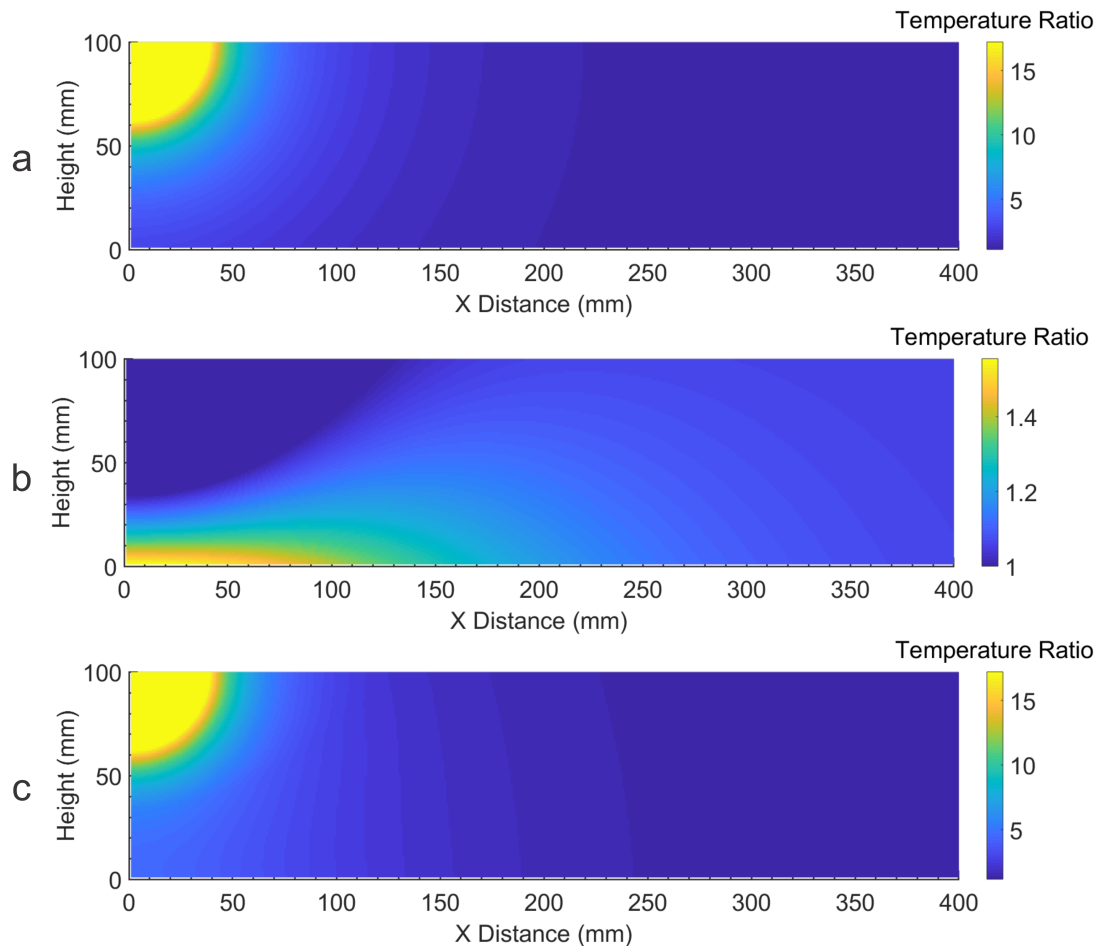


Figure 5.50: a) plot of the temperature ratio across primary shock. b) Plot of the temperature ratio across the reflected shock. c) Plot of the temperature ratio across the primary and reflected shock.

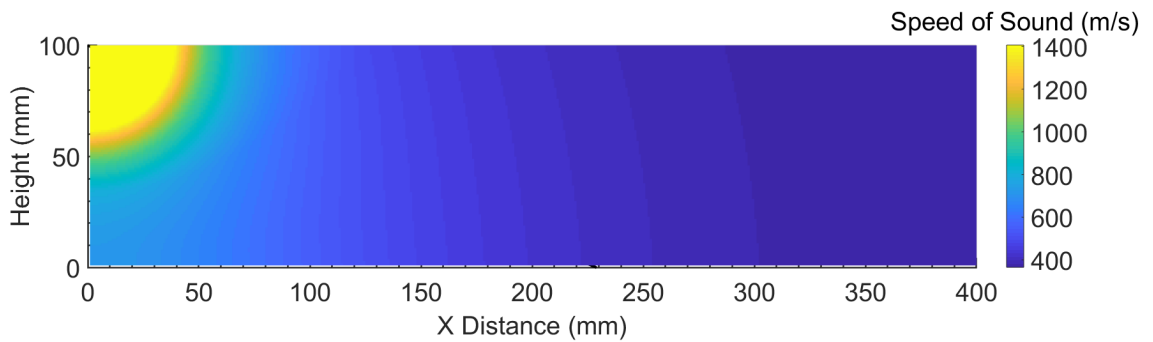


Figure 5.51: Plot of the speed of sound after the reflected shock.

The pulse duration at any point on the reflecting surface should be the time between the arrival of the shock wave and the release wave. The time of arrival of the shock wave at a pressure probe is found by matching the radius of the pressure probe and the radius time curve for PETN. Calculating the time of arrival of the release wave starts with the radius and time of the release wave detaching from the detonation products, Figure 4.50. Next the time at which the release wave intersects with the reflected shock was calculated using the assumption of constant radius time curve for the reflected shock. At this point the release wave began propagating through the non-uniform speed of sound in Figure 5.51. The path behind the reflected shock was divided into a series of line segments with each line segment being in only one of the 0.1 mm grid spaces. The time for the wave to travel each line segment was then just the segment length divided by the speed of sound. The time of arrival of the release wave is then calculated by adding the time to reach the reflected shock and the sum of the time to travel all the line segments after the reflected shock. Using this process the pulse duration is calculated for the 4 heights of burst, Figure 5.52. The pulse duration assuming there is no reflection is also shown.

The reflected pulse duration does a better job of predicting the experimental pulse duration than the non-reflected pulse duration. The reflected shock increases the local speed of sound allowing the release wave to travel faster. This is highlighted in Figure 5.52a where in both the reflected and non-reflected case the wave starts at the same location which is the origin of the release wave. The non-reflected pulse duration continues at the upper edge of the experimental data while the reflected pulse duration moves to more closely approximate the mean of the experimental pulse duration. This trend continues in the other 3 heights of burst studied, Figure 5.52b through 5.52d, with the non-reflected pulse duration being at the upper edge of the experimental data and the reflected pulse duration near the mean pulse duration.

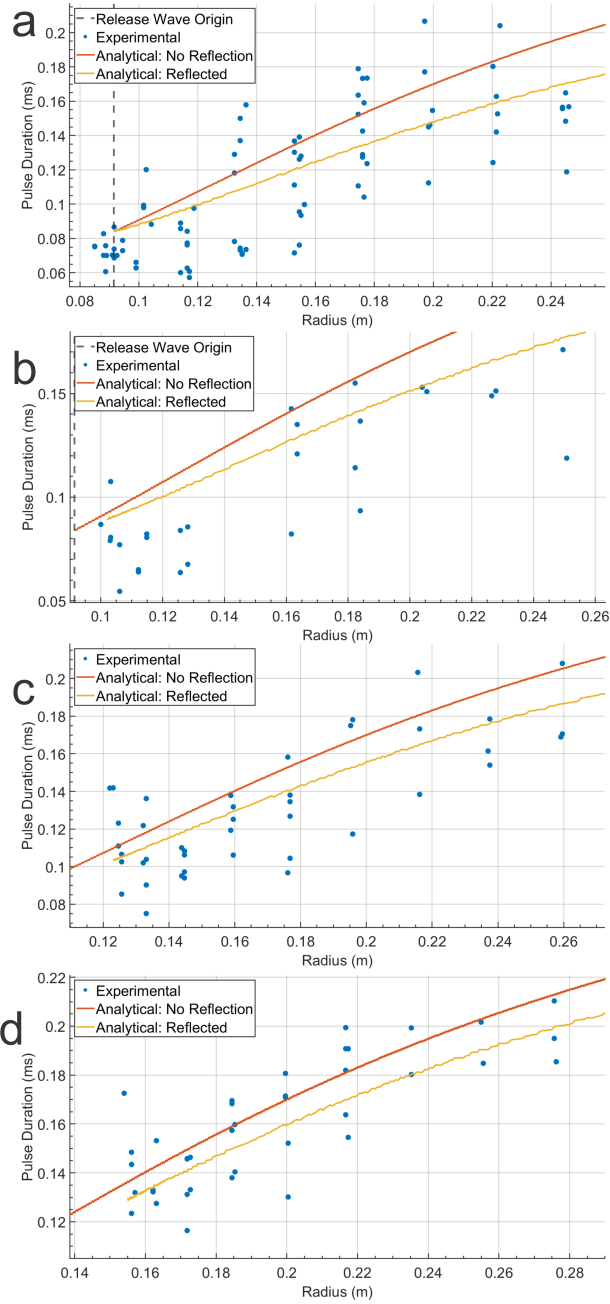


Figure 5.52: Comparison between the analytical pulse duration, for both a non-reflected and reflected shock, and experimental pulse duration. a) is the 8 charge diameter tests. b) is the 9 charge diameter tests. c) is the 11 charge diameter tests. d) is the 14 charge diameter tests.

Figure 5.53 compares the experimental pulse duration and its uncertainty with the analytical reflected pulse duration. At the majority of locations in Figure 5.53 the analytical pulse duration is within the uncertainty of the experimental data. The large variance within the experimental data makes it difficult to determine if the analytical method under or over predicts the pulse duration.

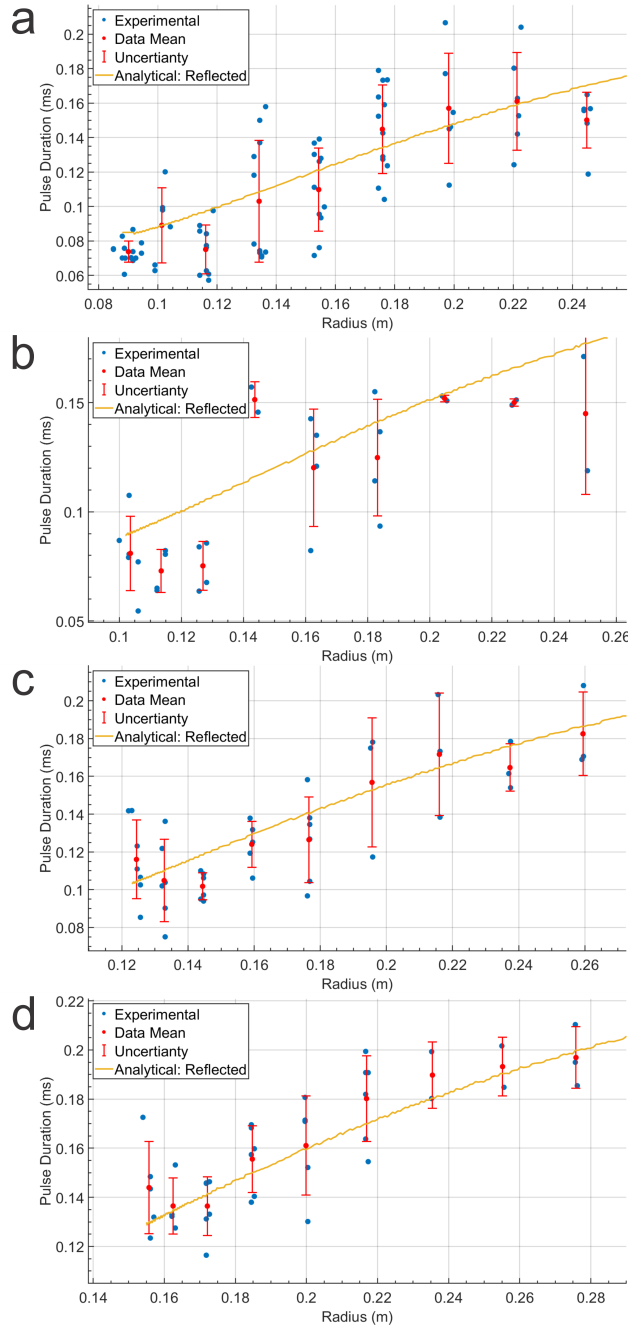


Figure 5.53: Comparison between the analytical pulse duration, for both a non-reflected and reflected shock, and experimental pulse duration. a) is the 8 charge diameter tests. b) is the 9 charge diameter tests. c) is the 11 charge diameter tests. d) is the 14 charge diameter tests.

At all heights of burst studied the reflected pulse duration better matched the experimental data than the non-reflected pulse duration but the non-reflected pulse duration may still be a useful tool. Calculating the reflected pulse duration is more computationally expensive than calculating the non-reflected pulse duration. In the present work, the reflected pulse duration was more computationally expensive by 4 orders of magnitude. Future work could increase the efficiency with how the reflected pulse duration is calculated but it will always be more expensive than the non-reflected duration. In some applications, where only a first order approximation or upper limit is required, the non-reflected pulse duration may be the more useful tool. In Figure 5.54 the experimental pulse duration for all the reflection tests and the analytical non-reflected pulse duration is plotted. The analytical non-reflected pulse duration is at the upper limit of the experimental data. The experimental data for the non-reflected test is added in Figure 5.55. Figure 5.55 shows that for limited applications where only an order of magnitude accuracy is required the analytical non-reflected pulse duration may be a useful tool.

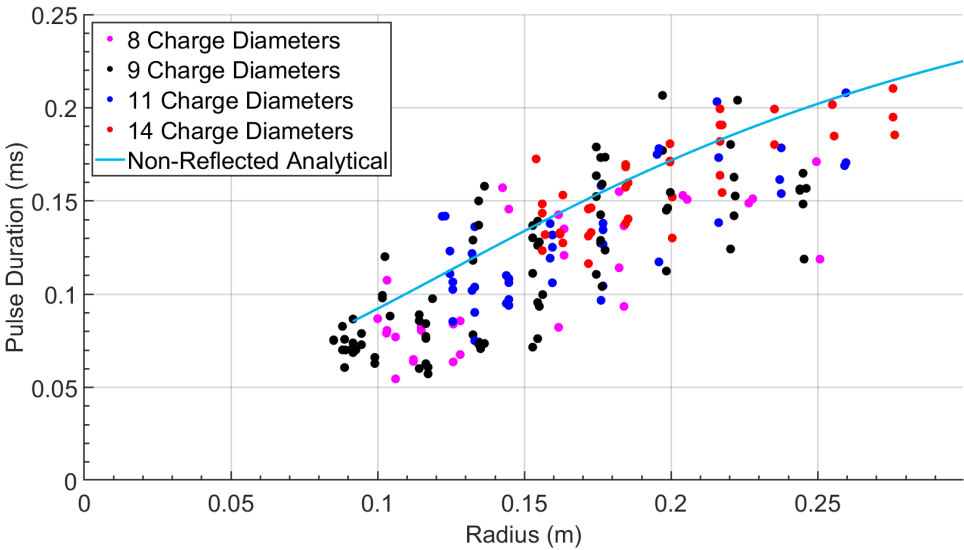


Figure 5.54: Comparison between the analytical non-reflected pulse duration and the experimental pulse duration for all the shock reflection tests.

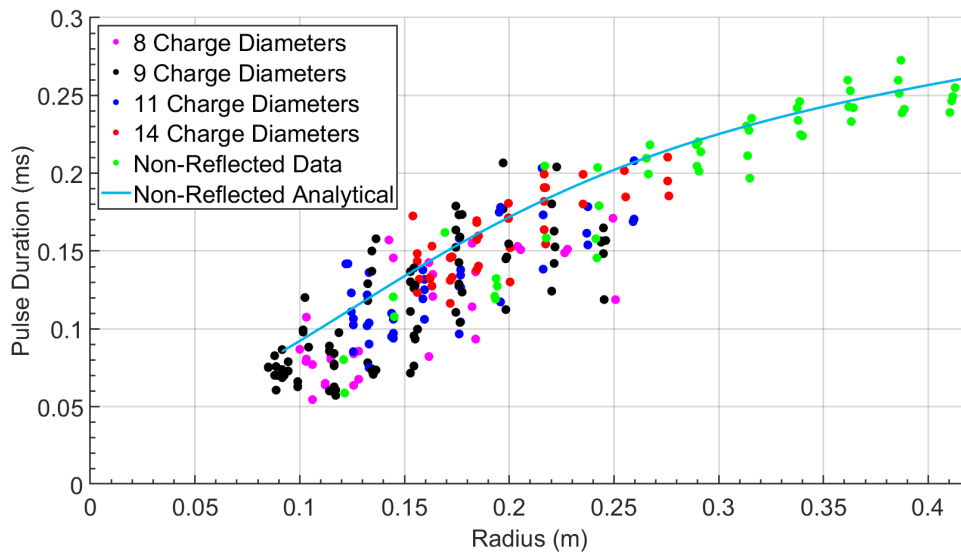


Figure 5.55: Comparison between the analytical non-reflected pulse duration and the experimental pulse duration for all tests, both shock reflection and the non-reflected tests.

### 5.3.3 Decay Coefficient

Since there is not a physical model for the decay coefficient,  $\alpha$ , the parameter was determined by fitting the experimental data. To define  $\alpha$  as a function of radius, the experimental data was fit to a power law function, as shown in Figure 5.57. The power law fit was chosen as it has been used in literature previously to describe the decay coefficient [105] and as it was used to describe  $\alpha$  for the non-reflection case, Figure 4.19. The data was fit to other curve fitting equations but the other equations either yielded worse results or only marginal improvements that did not justify the change from the literature method. The main reason for the poor coefficient determination is the large amount of scatter in the  $\alpha$  data. Less noisy data would allow for the better determination of the optimum fitting method for the decay coefficient.

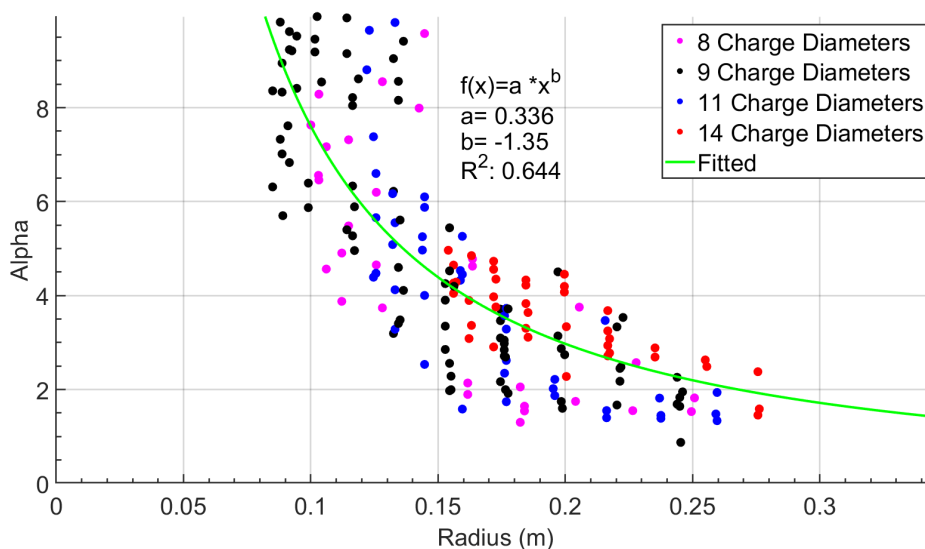


Figure 5.56: The experimental decay coefficient,  $\alpha$ , for the reflection tests and power law fit to the data.

Comparing the decay coefficient,  $\alpha$ , between the reflected and non-reflected tests shows a large amount of overlap. Figure 5.57 shows the decay coefficient for the non-reflection tests as well as their associated power law fit and the data from the reflected tests with their fit. The maximum radius of the detonation products, determined via CTH in Section 4.4.4, is also shown. Comparing the two fits of the reflected and non-reflected cases shows that each starts at a different value at the edge of the fireball and seems to decay to a common value. Additional data, paired with better data collection and analysis, to limit uncertainty, would show if these two fits do asymptotically approach a single value in the far field or stay separated.

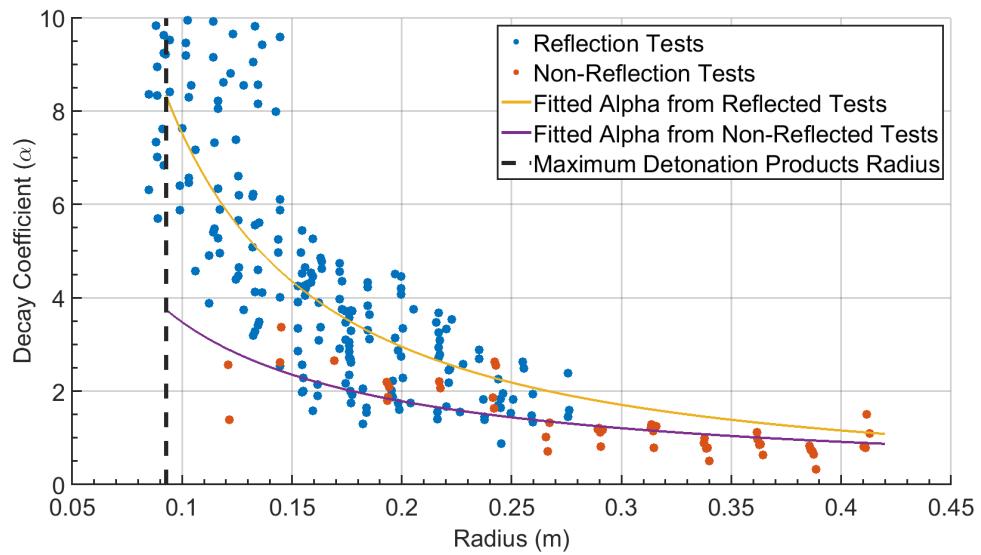


Figure 5.57: The experimental decay coefficient,  $\alpha$ , for all tests and the power law fit to both the reflected and non-reflected data .

### 5.3.4 Analytical Impulse

Using the three terms of the Friedlander equation, peak pressure, pulse duration and decay coefficient, the impulse was analytically determined as a function of radius. Figures 5.58 through 5.61 show the analytical impulse as a function of radius from the charge center for the 4 heights of burst. In Figure 5.58 the impulse starts at its highest value and then as the shock wave expands the impulse begins to decrease. Shortly before reaching the reflection transition the impulse reaches a local minimum and then increases until it reaches the reflection transition. This local minimum is caused by the interaction between the pressure and pulse duration. In Figure 5.45 the peak pressure decreases from the normal reflection to the reflection transition but the slope decreases as it approaches the transition. In contrast the pulse duration, Figure 5.55, increases at a mostly constant rate across the entire area studied. Thus the local minimum is caused by a point where the decreasing derivative of peak pressure matches the increasing derivative of pulse duration. The reflection transition from regular to irregular reflection causes a drop in the impulse that is caused by the drop in peak pressure across the transition. After the reflection transition the impulse continues to decrease with increasing radius. This pattern is repeated at all charge heights, Figures 5.59 through 5.61. The impulse starts high, decreases to a local minimum and then rises until it reaches the reflection transition where it drops and decreases with increasing radius. With increasing HOB the drop in impulse across the reflection transition decreases until at a height of 14 charge diameters the two lines almost meet.

Comparing the analytical and experimental impulse shows that the analytical impulse is within the uncertainty of the data. In Figures 5.58 through 5.61 the experimental data are shown as dots with the uncertainty shown at the experimental mean.

In the 8-charge-diameter tests, Figure 5.58, prior to the reflection transition the analytical impulse is within the experimental data. Just after the reflection transition the analytical impulse is below the experimental data but within the uncertainty. With increasing radius the analytical impulse moves closer to the mean of the experimental data until at 0.22 m the analytical impulse is at the experimental mean. Finally at approximately .25 m the analytical impulse is slightly over the experimental mean. For the 9- and 11-charge-diameter cases, Figure 5.59 and Figure 5.60, the analytical impulse is within the uncertainty of the experimental impulse over the entire range studied. For the majority of the probe locations, it is within the experimental data. For the 14-charge-diameter tests the analytical impulse was within the uncertainty of the experimental impulse except for the final two sets of data points at 0.25 m and 0.27 m, for which the analytical impulse is slightly above the uncertainty

The analytical impulse well predicts the experimental data. Over the majority of the regions studied the analytical impulse is within the spread of the experimental data. In only 2 of the 36 regions studied was the analytical impulse outside of the uncertainty for the data. This shows that the method used to predict the 3 terms underlying impulse are valid. That being said, both the analytical

models and experimental method can be improved. The large uncertainty in the experimental data makes it difficult to identify the cause of the discrepancy between the experimental and analytical impulse. Further research should focus on reducing the uncertainty of the experimental results and decreasing radial distance between probes. The analytical results predict a discontinuity in pressure and impulse across the reflection transition but the large spacing between pressure probes do not allow the differentiation between a smooth transition and sharp discontinuity in impulse.

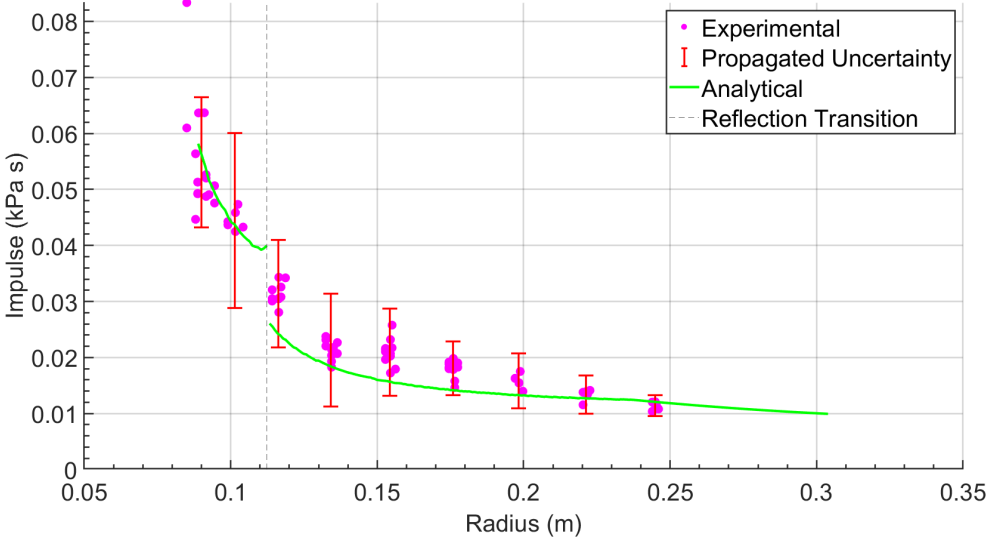


Figure 5.58: The experimental impulse with one standard deviation and the analytical impulse for the 8 charge diameter tests shown as a function of total radius from the charge. The transition from regular reflection to irregular reflection is shown as the vertical dotted line.

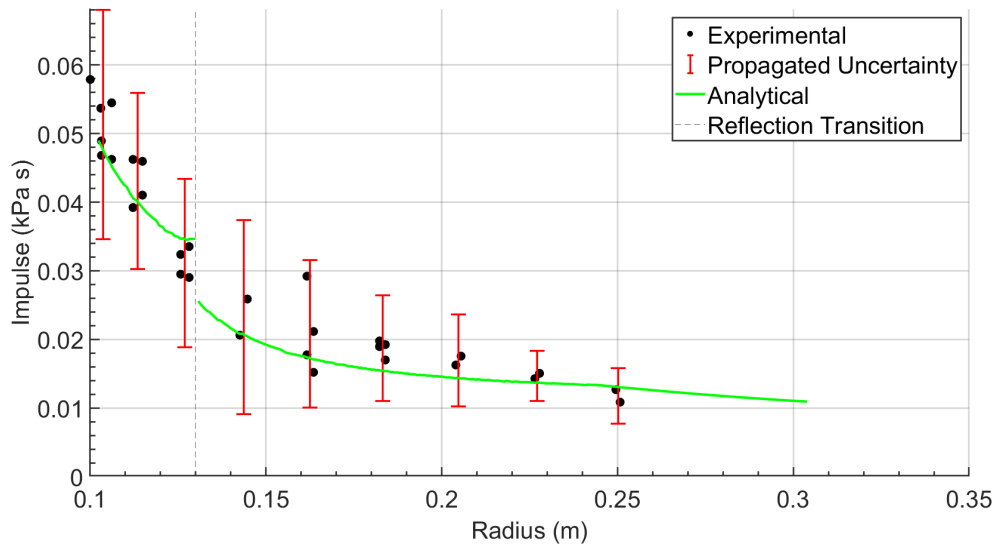


Figure 5.59: The experimental impulse with one standard deviation and the analytical impulse for the 9 charge diameter tests shown as a function of total radius from the charge. The transition from regular reflection to irregular reflection is shown as the vertical dotted line.

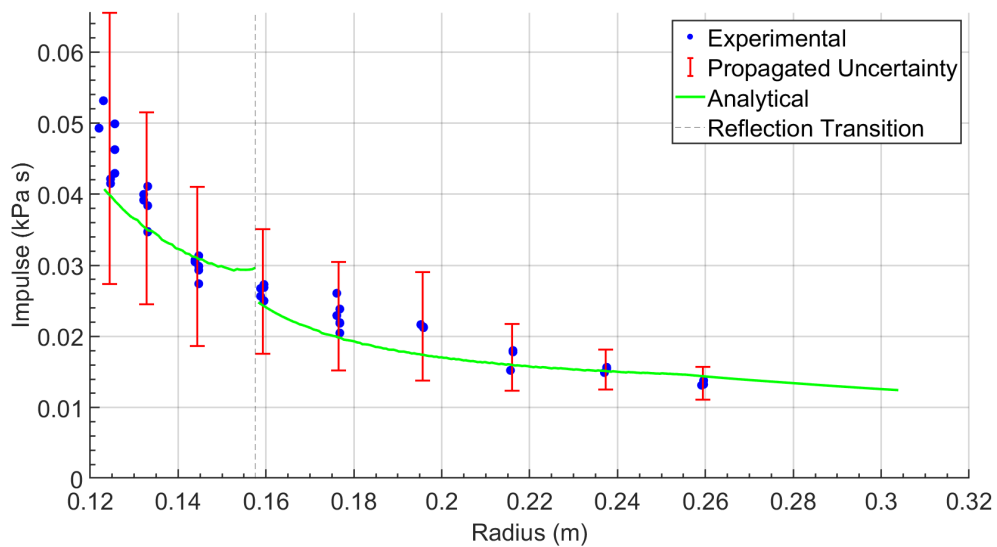


Figure 5.60: The experimental impulse with one standard deviation and the analytical impulse for the 11 charge diameter tests shown as a function of total radius from the charge. The transition from regular reflection to irregular reflection is shown as the vertical dotted line.

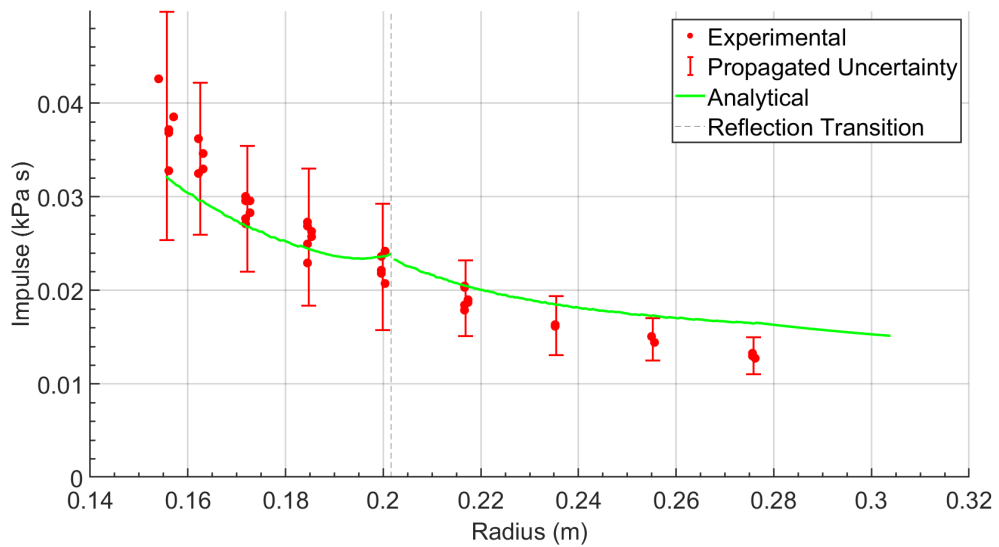


Figure 5.61: The experimental impulse with one standard deviation and the analytical impulse for the 14 charge diameter tests shown as a function of total radius from the charge. The transition from regular reflection to irregular reflection is shown as the vertical dotted line.

### 5.3.5 Surface Plots of Peak Pressure, Pulse Duration and Impulse

The analytical techniques used to calculate the impulse at the 4 heights of burst can be applied to any height of burst. Figure 5.62 is a surface plot of the peak pressure from a 1 g PETN charge as a function of X distances and heights of burst. The black line in the figure denotes the location of the transition from regular reflection to irregular reflection. Comparing the pressure on either side of the transition for various height of burst shows that at a low height of burst the pressure drop across the transition is quite large. At higher heights of burst there is a pressure increase across the transition. Figure 5.63 shows the pulse duration as a function of X distances and heights of burst. Between the origin and a radius of 93 mm nothing is plotted as this area is inside of the product gases which is beyond the scope of this work. Figure 5.64 is the surface plot of impulse at varying heights of burst. The black line denotes the transition from regular to irregular reflection.

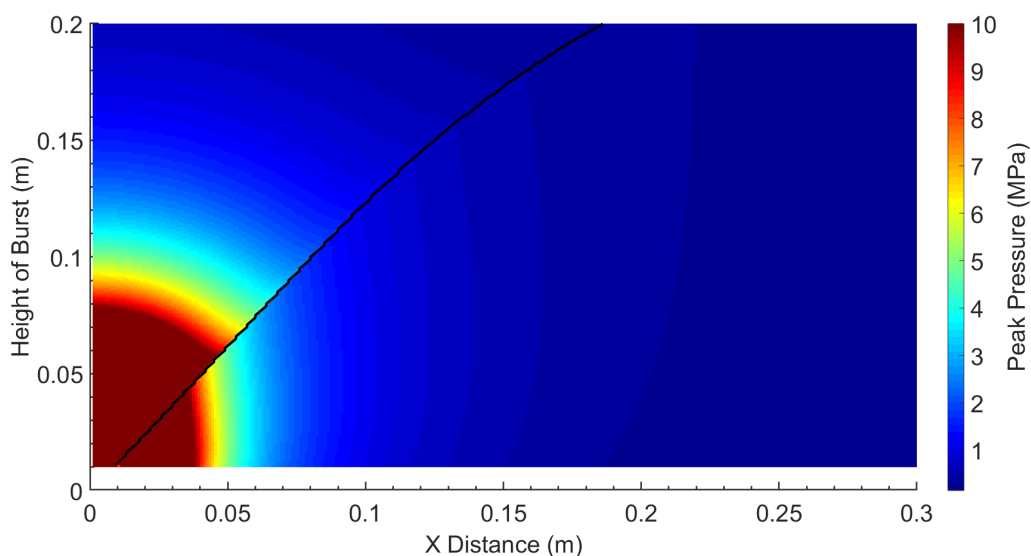


Figure 5.62: Surface plot of peak pressure as function of height of burst and X distance from the charge. The transition from regular to irregular reflection is shown as the black line.

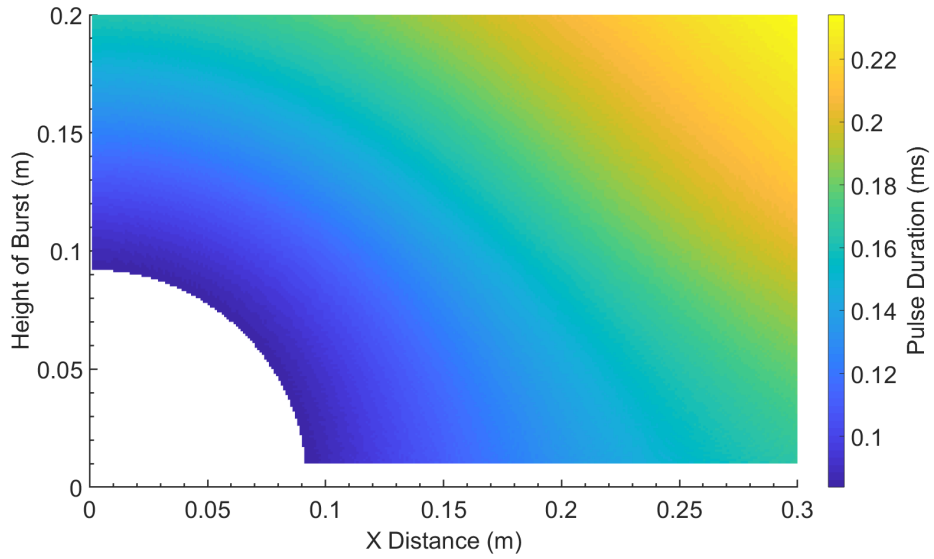


Figure 5.63: Surface plot of pulse duration as function of height of burst and X distance from the charge. The areas inside of the product gasses are not shown.

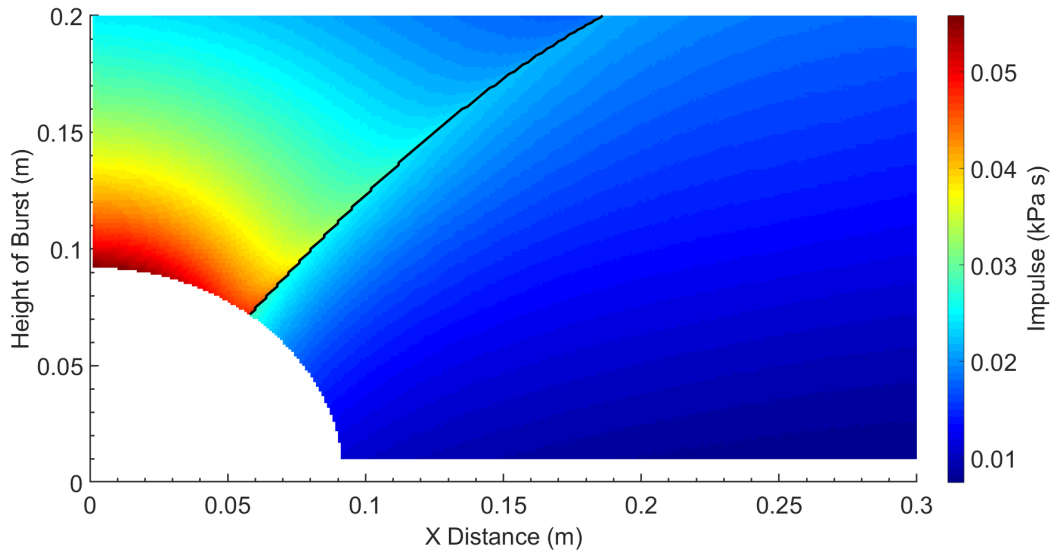


Figure 5.64: Surface plot of impulse per unit area as function of height of burst and X distance from the charge.

Using Figure 5.64 the impulse at a given point or region on a reflecting surface can be predicted for a given height of burst. There are several points that can be learned from Figure 5.64. The most important point is that in many cases reducing the distance to the charge does not increase the impulse. As an example, if the X distance to the charge is fixed at 0.1 m, the minimum radius to the charge is at the lowest height of burst (HOB), 0.01 m, but the highest impulse,  $0.0297 \text{ N s} / \text{M}^2$ , is at a HOB of 0.124 m which is just before the transition from regular reflection to irregular reflection. This shows a second interesting point that for a fixed X distance to the charge, the highest impulse is adjacent to the transition from regular to irregular reflection. For a HOB less than 0.164 m the regular reflection side of the reflection transition has a higher impulse but at larger HOB the irregular reflection side has the higher impulse. This point of inflection is caused by the change in the pressure across the reflection transition as a function of HOB. At 8 charge diameters there is a substantial drop in pressure across the reflection, Figure 5.45. As HOB is increased the drop in pressure across the transition decreases until at 14 charge diameters there is a minimal drop across the transition. At a HOB of 0.164 m there is no change in pressure across the transition and increasing the HOB above 0.164 m results in an increase in pressure across the transition.

For most cases of a fixed height of burst, decreasing the X distance to the charge increases the impulse but there are few exceptions. There is a local minimum of impulse prior to the reflection transition. Within this region increasing the X distance will increase the impulse until the reflection transitions to an irregular reflection. After the transition, increasing the X distance will decrease the impulse.

## CHAPTER 6

### EXPERIMENTAL METHODS OF KILOGRAM-SCALE TEST SERIES

Experiments were conducted at Eglin Air Force Bases Advanced Warhead Experimentation Facility (AWEF). This test series consisted of the detonation of kilogram-scale PBXN-110 charges over a reflection platform instrumented with pressure probes. Five high speed cameras were placed in a 120° arc around the charges. Four cameras were configured as BOS imaging systems with frame rates set between 15,000 and 60,000 frames per second (fps). The final camera recorded at between 50,000 and 60,000 fps and was used in a retroreflective shadowgraph system.

The explosive charges were cast spheres of PBXN-110 which are listed in Table 6.1. All charges were center initiated with an RP-1 detonator into a cylindrical 12.7 mm (0.5 inch) diameter by 12.7 mm (0.5 inch) long PBXN-5 booster. The charges were cast as single units with a cavity for the initiation train. The booster and detonator were glued into the cavity immediately prior to use. Three sizes of spherical charges were used. The smaller charges had a mass of 0.45 kg (1 lb.) and a diameter of 40.6 mm (1.6 inches). The middle charges had a mass of 1.36 kg (3 lb.) and a diameter of 58.3 mm (2.295 inches). The largest charges had a mass of 2.72 kg (6 lb.) and a diameter of 147 mm (5.8 inches). Each test was denoted using a letter and number: spherical charges have the prefix "S" and individual tests were then numbered sequentially.

The charges were suspended over a steel reflection platform with flush mounted pressure probes in a star-burst pattern, which is shown in Figure 6.1. The star-burst pattern was centered below the charge and comprised of eight lines of pressure transducers placed at 45 degree rotations and named A through H. The A line, pointing towards the shadowgraph camera, had a gauge located directly under the charge. Each line had a gauge at a radius of 152, 381, 686, 1067 and 1397 mm (6, 15, 27, 42, and 55 inches) from the center gauge. The A and E lines had gauges at 165 mm (6.5 inches) instead of 152 mm (6 inches). The B, D, F, and H lines had 45° off-sets from the shadowgraph camera, and an additional gauge at 1778 mm (70 inches). The exact transducer used at each gauge location varied on individual tests based on the expected pressure at that location as a function of the charge height and weight.

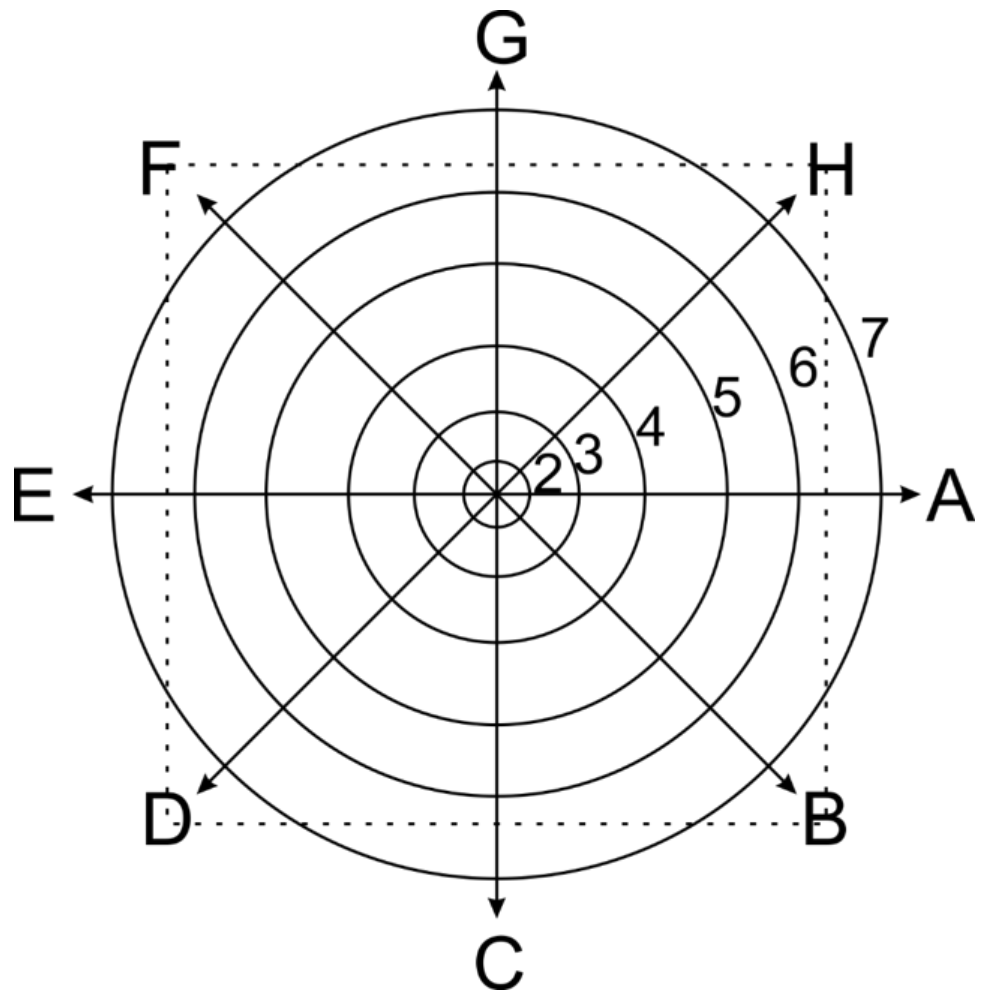


Figure 6.1: Diagram of the pressure probe locations for the kilogram-scale test series. A pressure gauge was located at the intersection of each ring and radial line.

Table 6.1: Details of the explosive charge used in each test. The rounded charge weight denotes which of the three weight ranges the charge falls in: 0.45 kg (1 lb.), 1.36 kg (3 lb.), or 2.72 kg (6 lb.).

Test Name	Rounded Charge Weight (kg)	Exact Charge Weight (kg)	Height of Burst (cm)
S1	1.36	1.298	116
S2	1.36	1.303	116
S3	1.36	1.301	116
S4	1.36	1.298	174
S5	1.36	1.309	174
S6	0.45	0.457	116
S7	0.45	0.454	116
S8	1.36	1.275	116
S9	2.72	2.723	116
S10	2.72	2.730	116

## 6.1 Refractive Imaging Systems

Two types of refractive imaging systems were used to visualize each test: retro-reflective shadowgraph and BOS. The light source for the retro-reflective system was a 1000 watt arc lamp focused onto a rod mirror. The rod mirror was secured to a lens cover on a fixed focal length lens on the high speed camera which was approximately 13 m (44 ft.) from the charge. The arc lamp light was then projected onto the retro-reflective screen placed approximately 4.6 m (15 ft.) behind the charge. The cameras used for BOS were placed at similar distances, approximately 13 m, from the charge. The ambient lighting conditions were not sufficient for the natural landscape to act as a high contract background, so speckle boards were used as a background. These boards were placed approximately 4.6 m (15 ft.) behind the charge in a semi-circle opposite the BOS cameras. All but one camera was placed at a similar elevation to the charge. The elevated camera, which was used for BOS, was elevated by placing it on the roof of a nearby one-story structure. To provide a background for the elevated camera, the reflection platform was speckle painted. The speckle boards and platform are visible in Figure 6.2. The refractive screen is shown in Figure 6.3.



Figure 6.2: Photograph of part of the setup for the large scale tests. In the center of the image is the reflection platform in which the starburst pattern of the pressure gauges can be seen. The speckle boards used as a background for BOS are positioned behind the reflection platform. The non-speckled space is where the retro-reflective shadowgraph screen is placed prior to the test.

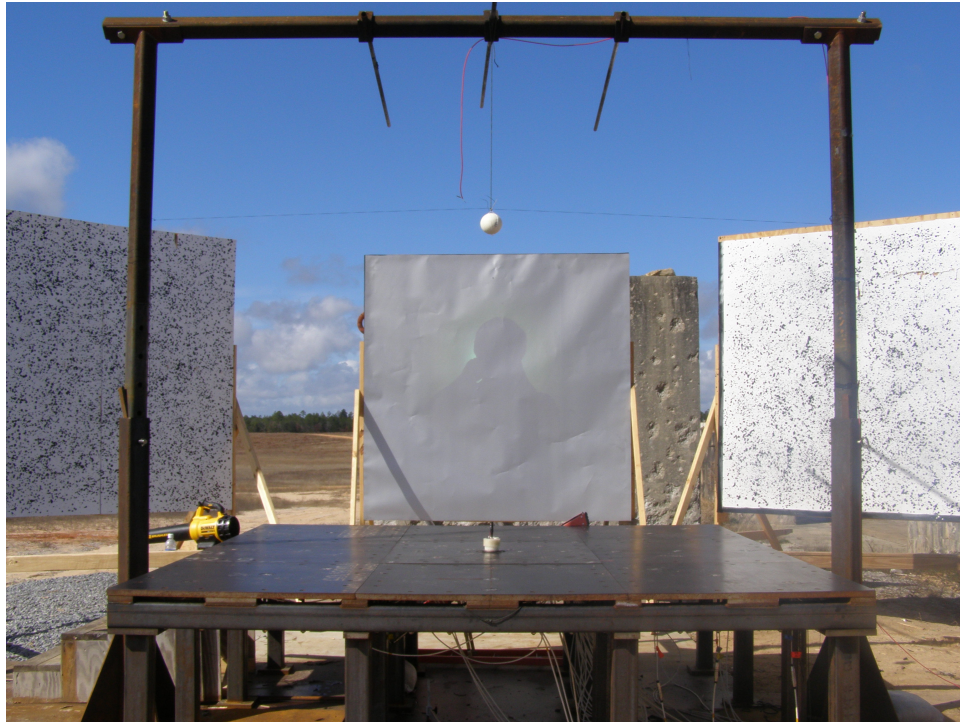


Figure 6.3: Photograph of part of the setup for the large scale tests. A 1.36 kg (3 lb.) sphere charge is hanging from the gantry. Behind the charge is the retro-reflective shadowgraph screen.

## 6.2 Camera Synchronizing

The method used to synchronize the cameras for the large scale test was to supply each camera with a timing signal from a pulse generator. This was done as an attempt to provide more accurate synchronization than IRIG. To determine the accuracy of the synchronization, the data from five cylindrical charge tests were examined with the results shown in Tables 6.2 and 6.3. Table 6.2 lists the time, reported by the camera in  $\mu\text{s}$ , between when the camera receives the trigger signal and when it begins to record the next image which is listed as frame 0. In a system of perfectly synchronized cameras, all cameras would report the same time. In a system with no synchronization, each camera will have a time between 0 and the inverse of the frame rate. At the bottom of the table is the maximum time difference between cameras within a test. Table 6.3 lists the frame in which first light is seen in each camera where frame 0 is the first frame after the trigger signal was received. First light is defined as the first frame where any change is seen in the explosive article. At the bottom of Table 6.3 is the maximum frame difference between the first light frame in number of frames and in  $\mu\text{s}$ .

Table 6.2: The difference, in  $\mu s$ , between the time the camera receives a trigger signal and when it opens its digital shutter for the frame 0 for five individual tests.

Test	C1	C2	C3	C4	C5
Camera 1 ( $\mu s$ )	7.87	4.94	19.5	7.75	2.52
Camera 2 ( $\mu s$ )	8.9	6.3	19.64	8.48	3.02
Camera 3 ( $\mu s$ )	9.19	6.06	19.81	7.94	3.2
Camera 4 ( $\mu s$ )	8.82	5.84	19.77	8.61	2.5
Camera 5 ( $\mu s$ )	8.77	5.57	20.12	8.19	1.72
Max Difference ( $\mu s$ )	1.32	1.36	0.62	0.86	1.3

Table 6.3: The difference, in frames, between the time the camera receives a trigger signal and when any light is seen from the explosive. All cameras were recording at 50,000 fps so the time between each frame is 20  $\mu s$ .

Test	C1	C2	C3	C4	C5
Camera 1 (frame)	0	0	0	0	1
Camera 2 (frame)	0	0	-1	0	0
Camera 3 (frame)	-1	-1	-2	0	0
Camera 4 (frame)	-2	-2	-2	-2	-1
Camera 5 (frame)	0	0	0	0	1
Max Difference (frames)	2	2	2	2	2
Max Difference ( $\mu s$ )	40	40	40	40	40

Table 6.2 and Table 6.3 give contradictory views of the accuracy of the synchronization. The reported time between frames and trigger listed in Table 6.2 show that the cameras should be synchronized to within  $\pm 1\mu s$ , this is half the maximum discrepancy to a whole frame rate period. Using the difference in frame numbers shown in Table 6.3, the cameras should be synchronized to within  $\pm 20\mu s$ , this is half the maximum discrepancy rounded up. An additional check was to compare frames to estimate the discrepancy in time between cameras. Figure 6.4 shows the frame of first light for test C1 from each camera view. In four of the views, the fireball has consumed only part of the charge. The other camera view was over exposed so no determination can be made. Given the length from the center of the charge to the end is 89 mm and PBXN-110 has a detonation velocity of  $8.39\text{ mm }\mu s^{-1}$  [109]. If it is assumed that the detonation wave has reached steady state, it should take  $10.6\ \mu s$  for the entire charge to be consumed. Because the fireball has only consumed a fraction of the charge, it can be assumed that the synchronization is well below  $10\ \mu s$  for this test. The conclusion from Table 6.2 and 6.3 and Figure 6.4 is that the cameras are synchronized to within about  $\pm 5\ \mu s$ , but frame 0 is not well defined. As such, the frame that first light is observed will be taken as frame 0 moving forward and the synchronization will be conservatively taken as  $\pm 20\mu s$ .

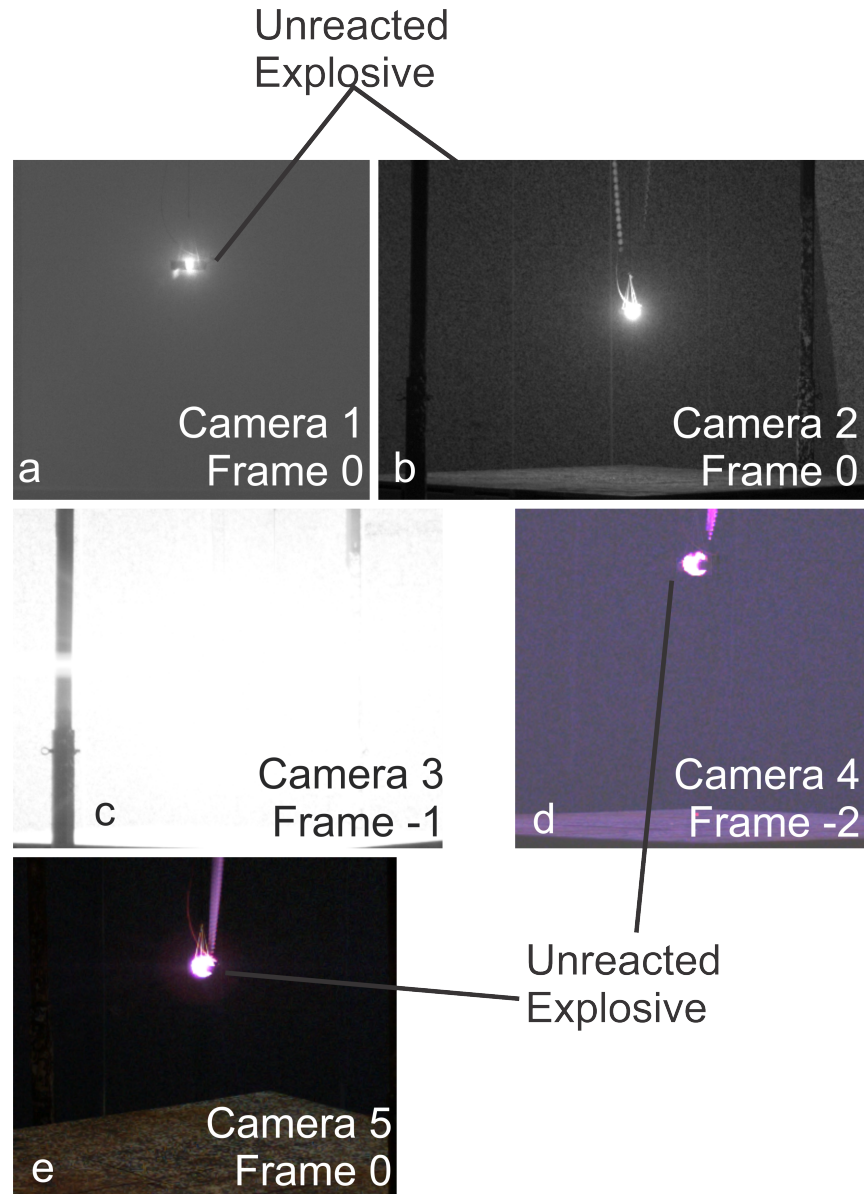


Figure 6.4: The frame at which first light was observed for cylinder test C1. Frame 0 is defined by the camera as the first frame after it receives the trigger signal. The images have been image processed to improve visibility of the charge. a) Frame 0 for camera 1, the shadowgraph camera. b) Frame 0 for camera 2. c) Frame -1 for camera 3. d) Frame -2 for camera 4. e) Frame 0 for camera 5.

### 6.3 Camera Calibration Techniques

Camera calibration is used to relate images taken with a digital camera to the physical objects recorded. The camera calibration used in this work is single camera calibration. Single camera calibration techniques are used to determine the size of refractive objects in shadowgraph and BOS images. The camera calibration was calculated by analyzing images of a checkerboard pattern.

Single camera calibration techniques allow for measurements to be made in a single plane. A MATLAB script was written to perform these calibrations by automatically detecting the pixel locations of the corners of a checkerboard pattern of known size. This was used to generate a series of pixel-per-unit-length calibrations for each square in the checkerboard pattern. The mean calibration value is used to make measurements within the plane the calibration was taken; two standard deviations from the mean was used as the uncertainty in each calibration value.

In BOS imaging the shock wave is assumed to be imaged in a fixed plane. Since the background is sufficiently far behind the object, the diffuse light coming from the background was assumed to be effectively parallel and thus the shock wave was visualized in a single plane that is perpendicular to the camera that contains the shock source. For this reason the system is calibrated in the plane that contains the shock source.

In retro-reflective shadowgraph imaging, the shock wave is assumed to be visualized on a spherical surface which contains the shock source and the camera lens. Retroreflective shadowgraph imaging visualizes the shock wave where the diverging light rays are perpendicular to the shock propagation direction [50]. As a result, a geometric correction is required to measure the radius of shock waves in shadowgraph images. This correction uses the geometry of the imaging system and a calibration taken in the plane of the retro-reflective screen.

### 6.4 BOS Processing

The BOS image subtraction processing technique is used to improve detection of refractive objects [47]. In this work, the technique is used to compare two images from an individual camera at different times. The two images compared will be a reference image, referred to as a "cold image", and the image which is being analyzed, or "hot image". In the image subtraction process used, the values of the pixels in the cold images are compared on a pixel-by-pixel basis to the pixel values from the hot images using:

$$pic(x, y) = \frac{[hot(x, y) - cold(x, y)]^2}{\frac{hot(x, y) + cold(x, y)}{2} + 1} \quad (6.1)$$

where  $hot(x, y)$  is the value of a pixel at location  $x, y$  in the analyzed image,  $cold(x, y)$  is the value of a pixel at the same location in the reference image, and  $pic(x, y)$  is the value recorded for that pixel location in the new image [60]. The value of any pixel change determines the brightness of the pixel in the new image. When imaging refractive objects, the magnitude of change in pixel values tends to be small, so the resulting image is processed with a manual histogram stretch to make the shock wave more visible. The values used in each histogram stretch are manually determined to produce an image with a clearly visible shock wave with minimal background noise.

The image subtraction method can be optimized for shock wave tracking by careful selection of the reference image, which is described in Figure 6.5. In traditional BOS, which is shown in the left column of Figure 6.5, the reference image is taken before the event. When subtracted from the test image, the resulting image shows everything that has changed since detonation including the fireball, changes in lighting due to the fireball, lens glare, fragments, and the shock wave. In Figure 6.5c neither the reflected or secondary shock is visible and the area near the fireball is also washed out due to the lighting from the fireball. One method to reduce this noise and increase the detail of the shocks is to use the previous image in the high-speed imaging sequence as the reference image [87]. This sequential subtraction approach is illustrated in the right column of Figure 6.5. By subtracting the previous image from the test image, the resulting BOS image shows only high velocity features such as fragments and shock waves that have changed in the time between frames and does not show slower objects such as the fireball. This also increases the apparent density with which the shock wave is visualized because artifacts from the shock position at both times appear in the image. This makes automated detection of the shock easier without changing the location of the shock front [86, 87]. The difference made by selection of a proper reference frame can be seen in the difference between Figure 6.5c and f. These images have been processed using the same method except that Figure 6.5f used sequential subtraction.

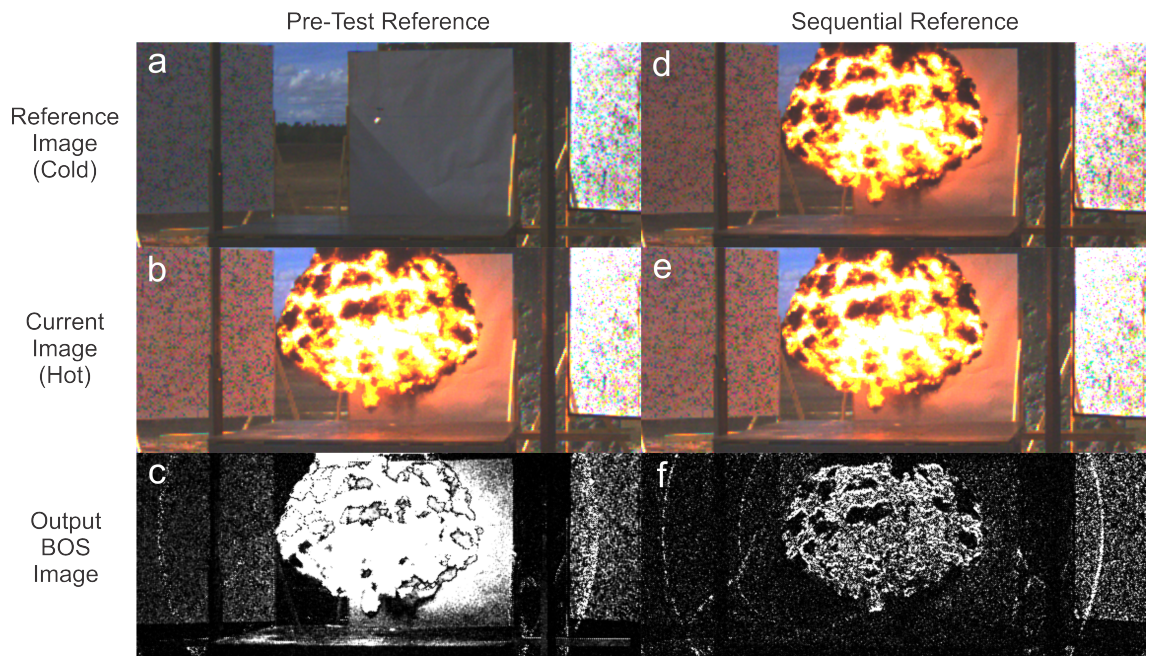


Figure 6.5: (a) Reference image before detonation. (b) Hot image 3.34 ms after detonation. (c) BOS image created by image subtracting (a) and (b). (d) Reference image recorded 1 frame (0.017 ms) before hot image. (e) Hot image, identical to (b), 3.34 ms after detonation. (f) Sequential BOS image created by image subtracting (d) and (e). All images are from test S6.

## CHAPTER 7

### RESULTS AND DISCUSSION OF KILOGRAM-SCALE TEST SERIES

A kilogram-scale test series was performed at the AWEF at Eglin Air Force Base. The test series used spherical charges with masses between 0.45 kg and 2.72 kg (1 lb. and 6 lb.).

Refractive imaging was used to track the radius of the shock wave from the spherical charges as a function of time. The direct high speed images from spherical tests were processed into BOS images using the process outlined in Section 6.4. The shadowgraph images were adjusted to improve brightness and contrast but did not require further image processing. The location of the shock front was determined either manually or automatically at multiple points in each frame of each camera view. The shock locations were then used to determine the shock wave radius at each point in pixel units. The pixel units were scaled to meters and used to generate a time radius curve. This analysis was performed on a 0.45 kg and 1.36 kg (one and three pound) spherical charge test. The data from each test was scaled to 1 kg at standard temperature and pressure using the Sac's Scaling Equations, 1.6 thru 1.9. The scaled data was then fit to the Dewey Equation, 1.10, which gave the fitting parameters of  $A=0.0146$ ,  $B=1$ ,  $C=-0.628$ , and  $D=2.51$ . The averaged scaled radius from each camera view and the curve fit is shown in Figure 7.1. The shock wave reflection characteristics for each test were then examined, similar to the analysis performed on the gram-scale charges.

#### 7.1 Shock Reflection Transition

The spherical tests only produced regular reflections over the range visualized by the shadowgraph system. The reflection should transition from regular to irregular below an effective wedge angle of  $50^\circ$ . Due to the height of burst of the charges, the edge of the screen was at  $52^\circ$  relative to the center of the charge, this angle is equivalent to the effective wedge angle at the screen edge. As a result, the regular to irregular reflection transition is expected to occur outside the shadowgraph field of view. Figure 7.2 shows that the shock wave from test S3, a spherical 1.36 kg charge, produced a regular reflection at the edge of the shadowgraph system. This result was similar to all of the spherical tests, in that the shadowgraph system only visualized regular reflections. The BOS cameras had

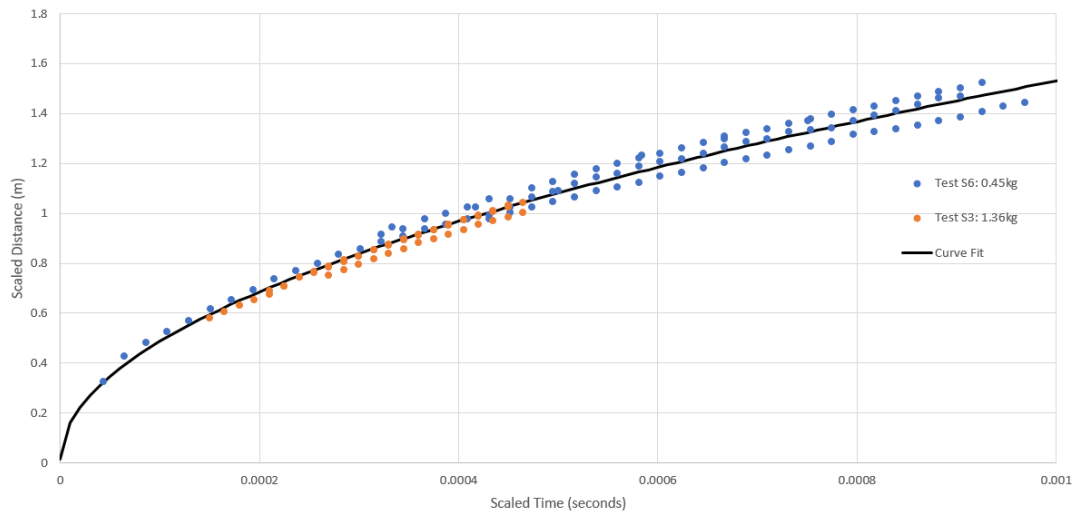


Figure 7.1: Radius-time plot for 1 kg of PBXN-110. The data from the 0.45 kg and 1.36 kg is shown along with the Dewey Curve fit.

a wider field of view than the shadowgraph system but the higher noise levels in the BOS images prevent the identification of the shock reflection.

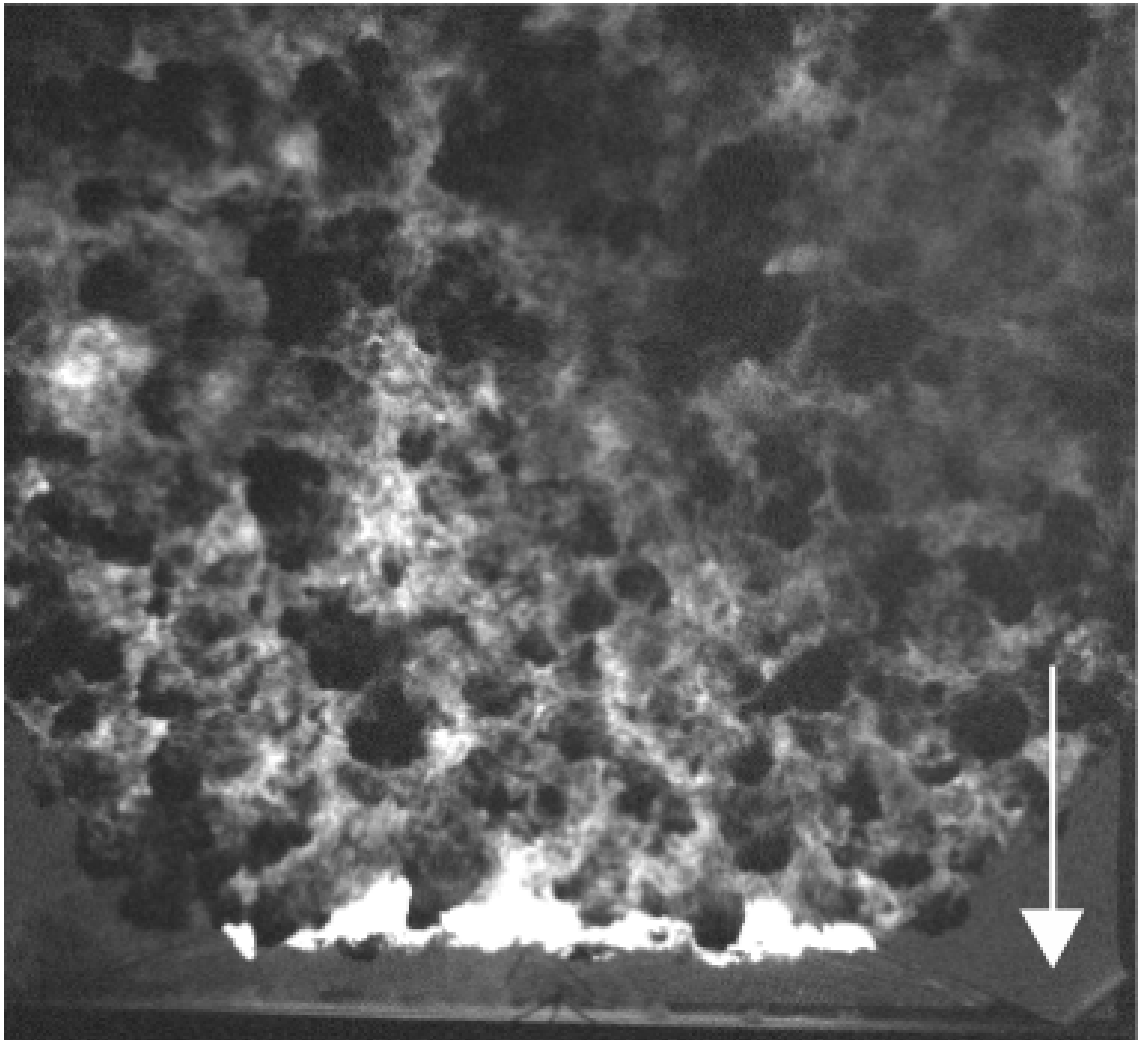


Figure 7.2: Shadowgraph of a regular shock wave reflection from test S3 0.87 ms after detonation. The location of regular reflection is indicated by the arrow. The charge used was 1.36 kg of PBXN-110.

## 7.2 Experimental Peak Pressure and Impulse

### 7.2.1 Frequency Filtering Pressure Data

The pressure traces from the kilogram test series had more noise than the gram scale tests. Figure 7.3 shows that in addition to the expected random noise, many pressure traces had a strong oscillation around a mean at a regular interval, which will be referred to as 'ringing'. The ringing noise was most prominent in probes between the 3 to 5 pressure probe rings, as labeled in Figure 6.1. One method to remove this type of noise is frequency filtering.

To perform the frequency filtering, the pressure trace was converted from the time domain to the frequency domain with a fast Fourier transform (FFT). The resulting frequency plot is shown as the blue line in the left of Figure 7.4. The frequency analysis showed a strong peak at approximately 160 kHz and a lesser peak at 150 kHz. To remove these peaks, the frequencies between 140 to 180 kHz were removed, the orange line in Figure 7.4. The filtered frequency data was then transformed back to the time domain via an inverse FFT. The unfiltered and filtered pressures traces are shown in the right of Figure 7.4.

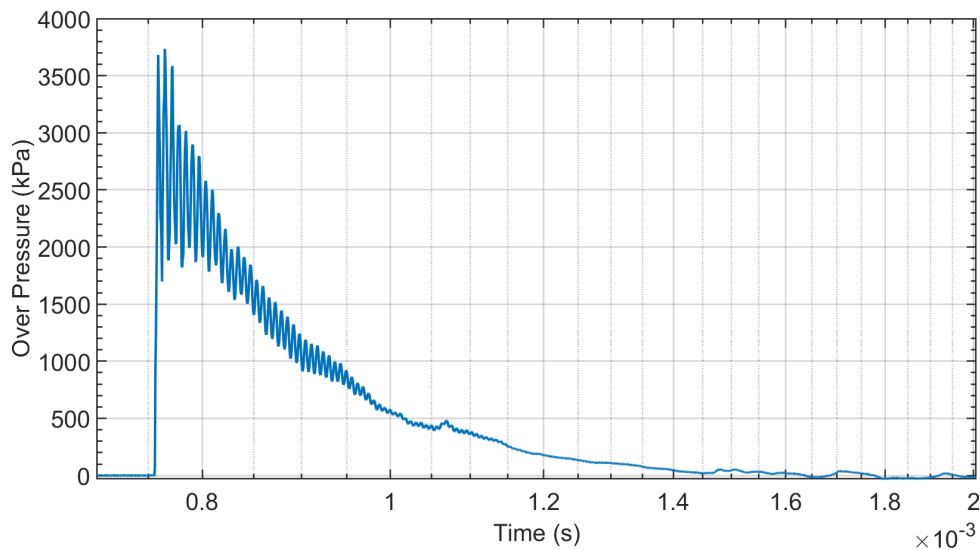


Figure 7.3: Pressure trace from probe A4 from tests S3 which was a 1.36 kg (3 lb) charge at a height of burst of 1.16 m (46 inches).

The frequency filtering eliminated the ringing noise but did not affect the random noise. To handle the random noise the filtered pressure data was fit to the Friedlander equation, Equation 1.14. Since the pressure asymptotically approached 0 overpressure, the two step fitting approach, discussed in Section 5.2.1, was used to fit the data. The resulting fit and the fitting parameters are shown in Figure 7.5. The original, un-frequency filtered, pressure trace was also

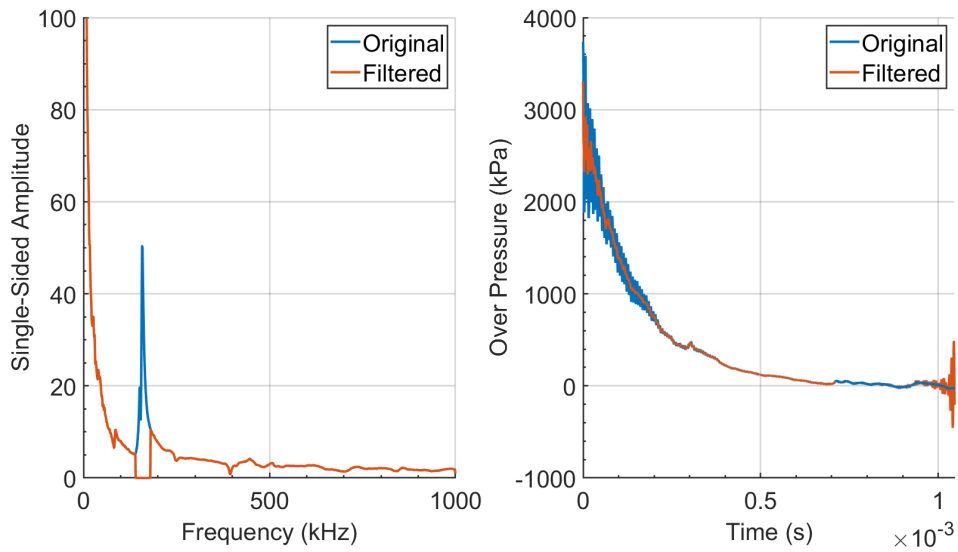


Figure 7.4: Left, frequency analysis of the pressure trace from test S3 probe A4 before and after filtering. Right, the pressure trace before and after frequency filtering.

fit to the Friedlander equation to determine the effect of frequency filtering prior to fitting to the Friedlander equation, Figure 7.6. The frequency filtering had a negligible effect in the found values for peak pressure, pulse duration and the decay coefficient. The frequency filtering changed the found values by less than 1% for test S3 probe A4, Figures 7.5 and 7.6. This analysis was repeated for 4 other probes which had prominent ringing noise. In each case, the frequency filtering changed the found values by 1% or less. This shows that the Friedlander fitting process is able to remove the ringing noise without pre-processing required and for this reason only the Friedlander fitting will be used in the following analysis.

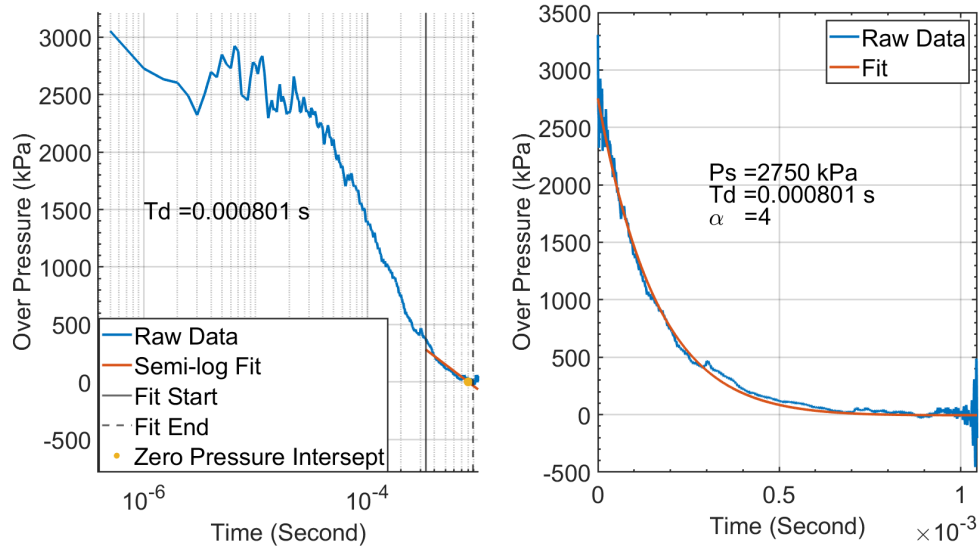


Figure 7.5: The frequency filtered pressure trace from test S3 probe A4 fit to the Friedlander equation via the two step process.

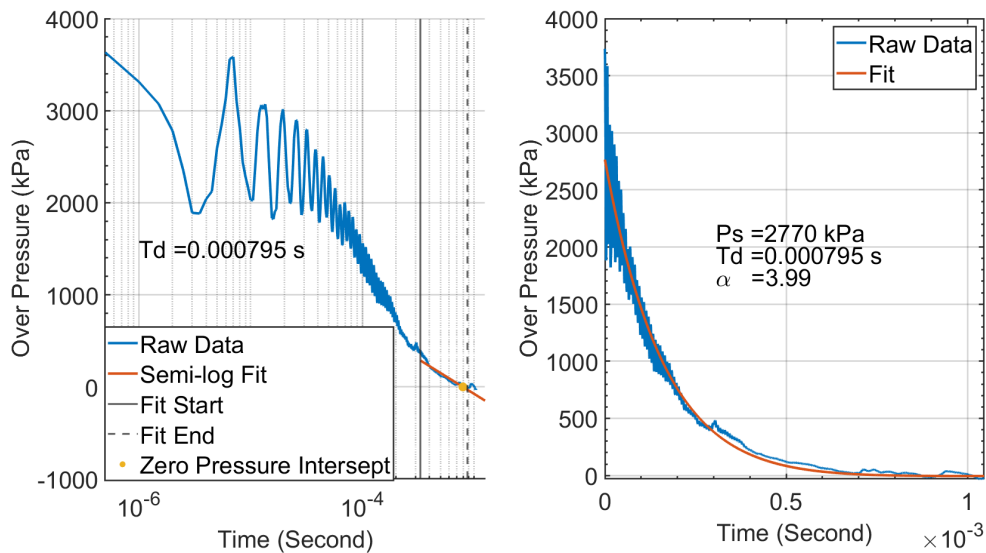


Figure 7.6: The unfiltered pressure trace from test S3 probe A4 fit to the Friedlander equation via the two step process.

## 7.2.2 Fitting and Uncertainty of Experimental Pressure Data

Pressure traces for each spherical test were recorded at up to 45 positions for each test and the data were fit to the Friedlander equation to reduce noise. There were 4 configurations of the kilogram scale spherical tests; the base line tests, abbreviated as 'B', had a mass of approximately 1.36 kg (3 lb.) and a height of burst of 1.16 m (46 inches), the elevated tests ('E') had a mass of approximately 1.36 kg (3 lb.) and a height of burst of 1.74 m (69 inches), the light tests ('L') had a mass of 0.45 kg (1 lb.) and a height of burst of 1.16 m (46 inches), the heavy tests ('H') had a mass of 2.72 kg (6 lb.) and a height of burst of 1.16 m (46 inches). The peak pressure values for each test configuration are shown in Figure 7.7. The uncertainty at each pressure probe location was calculated and shown at the local mean. The pulse duration and corresponding uncertainty are shown for each test configuration in Figure 7.8.

The decay coefficient,  $\alpha$ , was determined to not be a function of height of burst in the gram-scale tests, so it is possible to directly compare all of the test configurations. The  $\alpha$  term and the radius was found for each probe, then the radii of the tests were scaled to 1 kg using Sachs scaling, Equations 1.6 through 1.9. The found  $\alpha$  values and scaled radius are shown in Figure 7.9 along with the uncertainty which was calculated for each 0.2 m region.

The found values of the Friedlander equation were combined in Figure 7.10 to calculate the impulse at each point. The uncertainty for the impulse was found by propagating the uncertainties of peak pressure, pulse duration and decay coefficient. The full discussion of how uncertainty propagated for impulse was presented in Section 5.2.2. The large uncertainties and interaction between the pulse duration and decay coefficient terms result in the propagated uncertainty for impulse being much larger than if the uncertainty was calculated on the final impulse values.

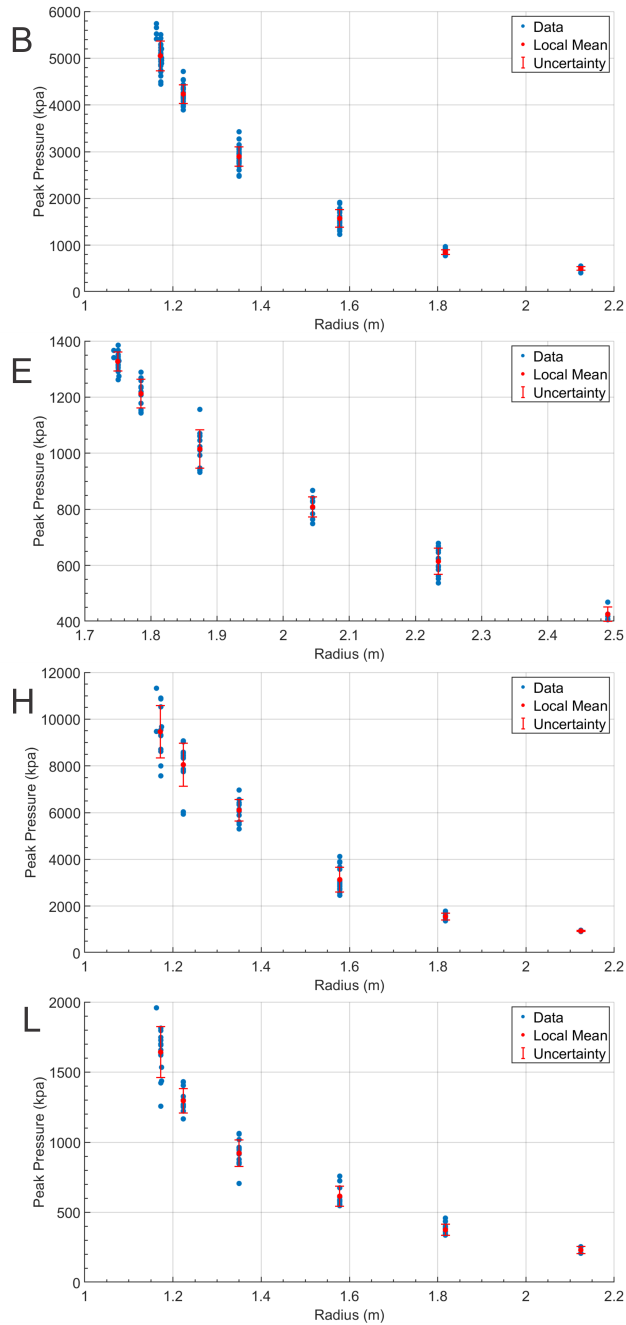


Figure 7.7: Peak pressure values for the 4 spherical test configurations. 'B' are the base line tests, 'E' are the elevated tests, 'L' are the light tests and 'H' are the heavy tests.

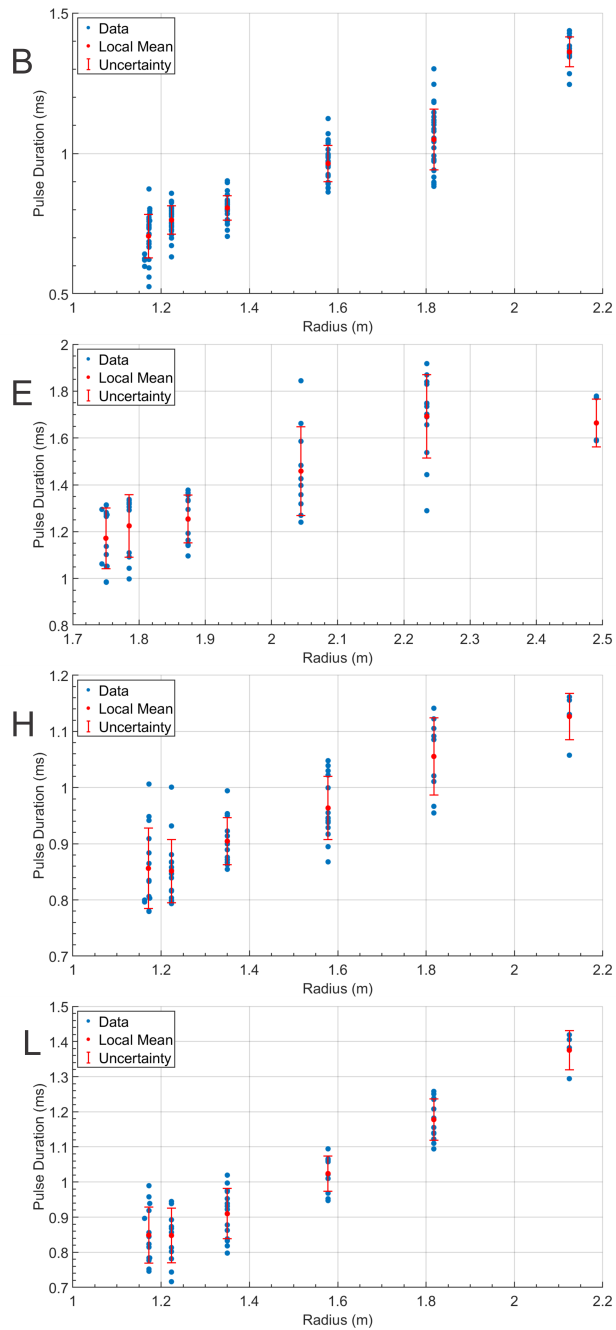


Figure 7.8: Pulse duration values for the 4 spherical test configurations. 'B' are the base line tests, 'E' are the elevated tests, 'L' are the light tests and 'H' are the heavy tests.

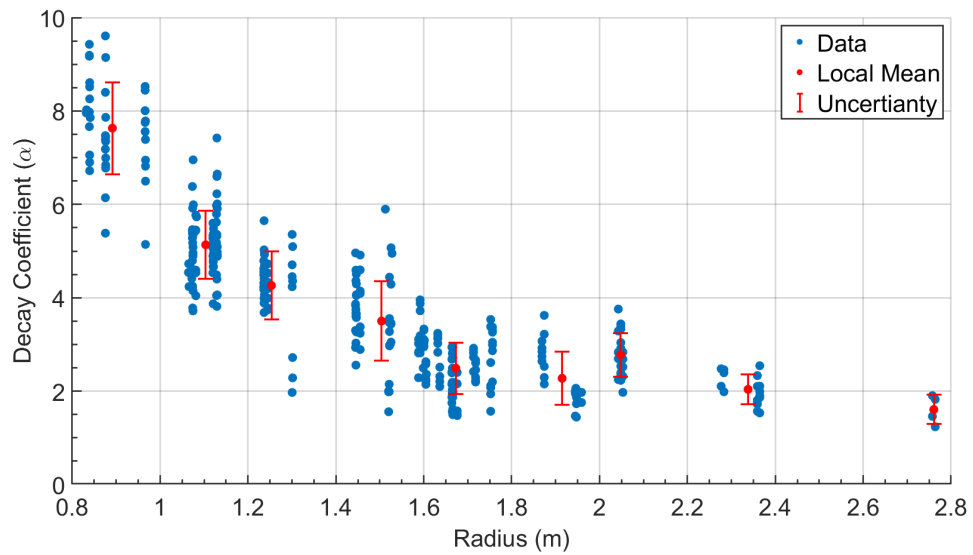


Figure 7.9: Decay coefficient,  $\alpha$ , for all spherical tests. 'B' are the base line tests, 'E' are the elevated tests, 'L' are the light tests and 'H' are the heavy tests.

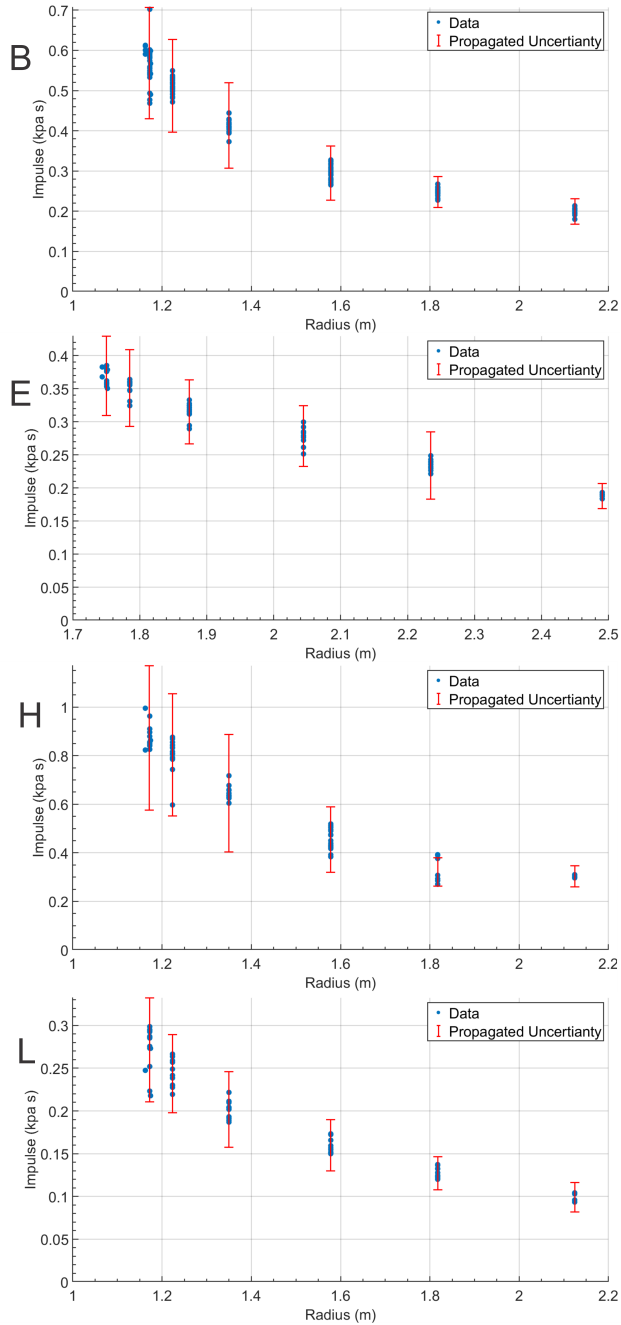


Figure 7.10: Experimental impulse for all spherical tests and the uncertainty found by propagating the uncertainties of peak pressure, pulse duration and decay coefficient. 'B' are the base line tests, 'E' are the elevated tests, 'L' are the light tests and 'H' are the heavy tests.

## 7.3 Analytical Peak Pressure and Impulse

### 7.3.1 Analytical Peak Pressure

The analytical peak pressure was calculated as a function of radius for each of the 4 charge configurations and compared to the experimental data. Using the Dewey parameters found from Figure 7.1, the Mach-radius curve was calculated and the radius scaled for the charge mass for each configuration. Using the charge height and scaled Mach-radius curve the analytical peak pressure was then calculated with the procedure laid out in Section 5.3.1. The analytical pressure was then compared to the experimental peak pressure found from the Friedlander fits in Figure 7.11. In almost all cases the analytical peak pressure over predicts the Friedlander fitted peak pressure.

The ringing noise in the pressure trace may be causing the Friedlander fit to underpredict the peak pressure. The blue line in Figure 7.12 is the un-modified pressure trace from test S2 probe A1. This probe was chosen as it was directly under the charge and the well understood normal reflection would occur. The Friedlander peak pressure is shown as the yellow dot which is well below the peak pressure of the un-fitted data. The analytical pressure is shown as the purple dot which is between the Friedlander peak pressure and the un-fitted peak pressure. Pressure traces of a regular and irregular reflection are shown in Figure 7.13. The reflection type at each location was determined analytically. In each case the analytical peak pressure was between the Friedlander and the raw peak pressure. Figure 7.14 shows that the analytical peak pressure is within the experimental data for the un-fitted peak pressure for all configurations.

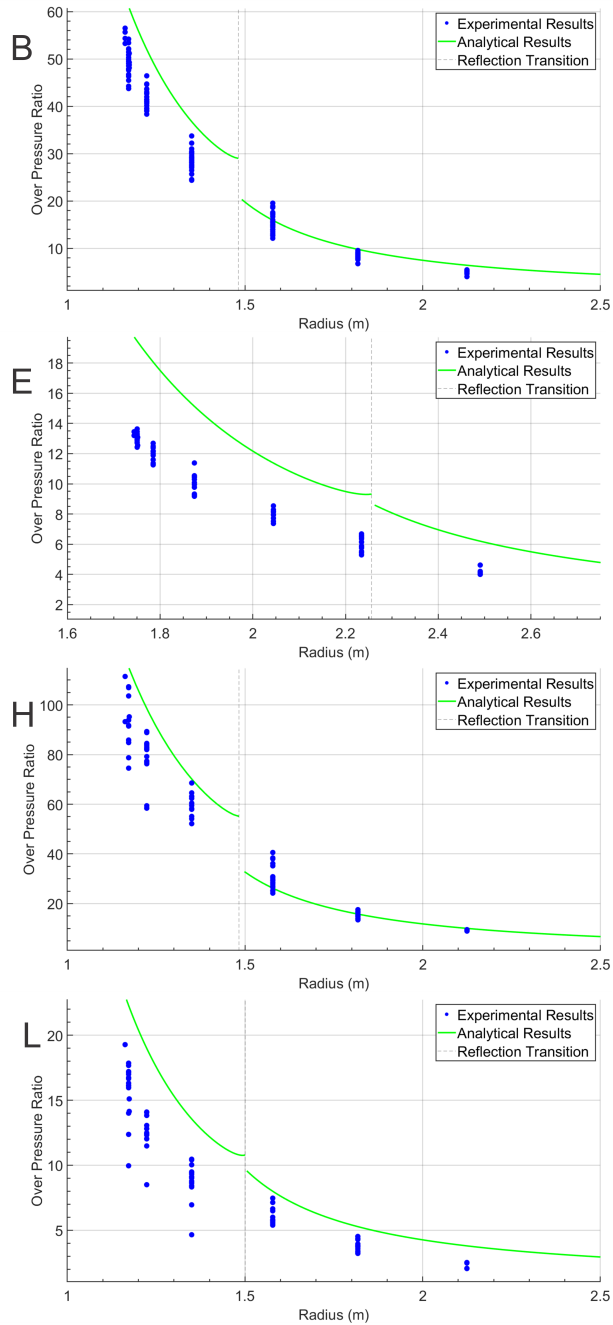


Figure 7.11: Analytical peak pressure and the Friedlander experimental peak pressure for each test configuration. 'B' are the base line tests, 'E' are the elevated tests, 'L' are the light tests and 'H' are the heavy tests.

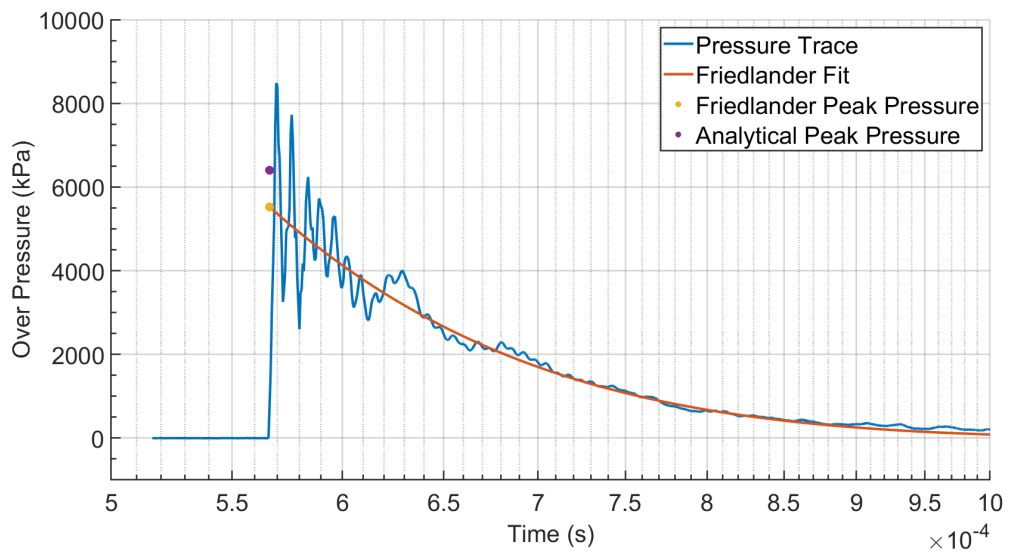


Figure 7.12: Pressure trace from the A1 pressure probe from the S2 test which is a baseline configuration. The Friedlander fit and resulting peak pressure is shown along with the analytical peak pressure.

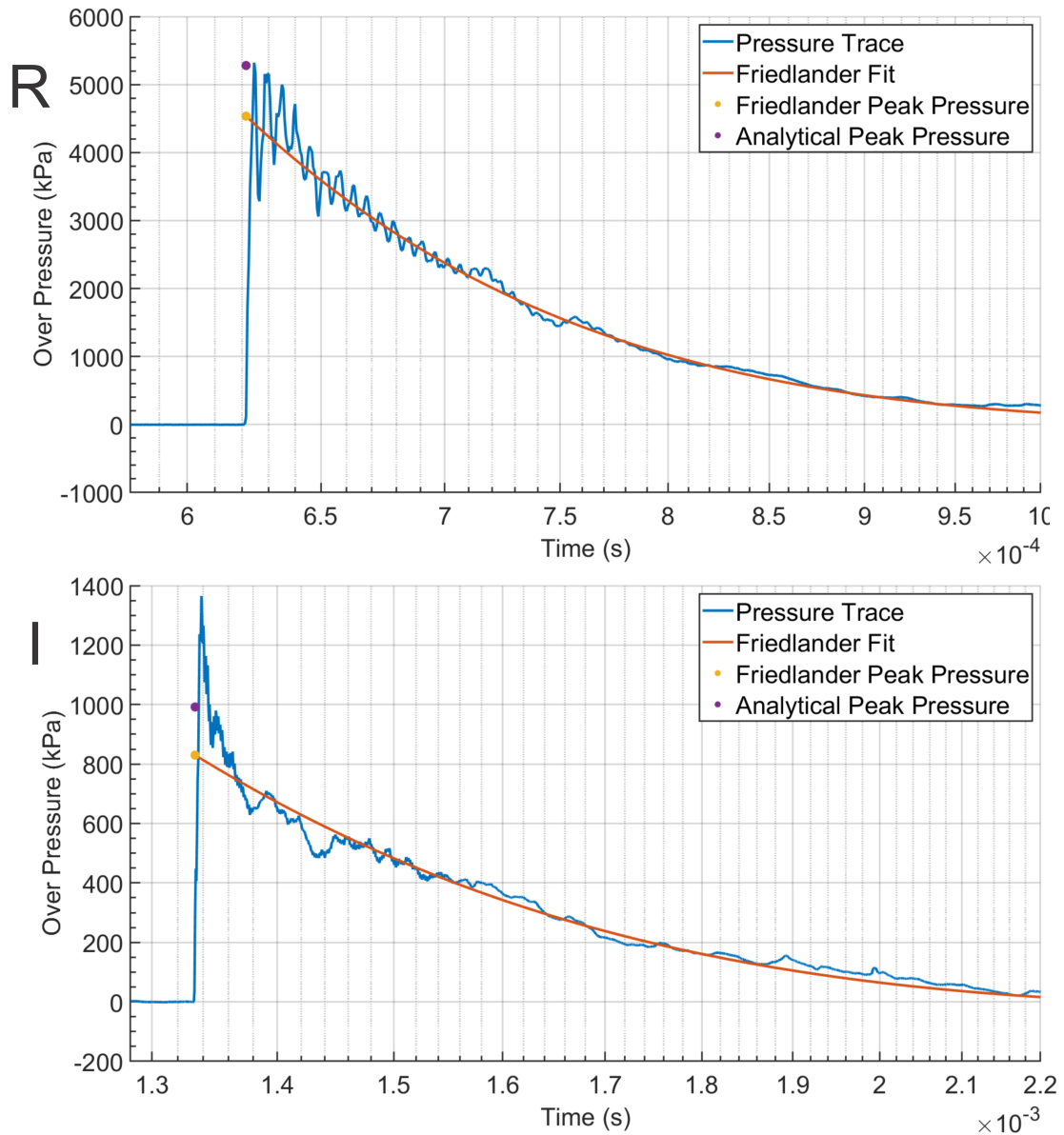


Figure 7.13: R is the pressure trace from the A3 pressure probe from the S2 test which is a baseline configuration. The reflection at this location was analytically predicted to be a regular reflection. I is the pressure trace from the A6 pressure probe from the S2 test which is a baseline configuration. The reflection at this location was analytically predicted to be an irregular reflection. The Friedlander fit and resulting peak pressure is shown along with the analytical peak pressure.

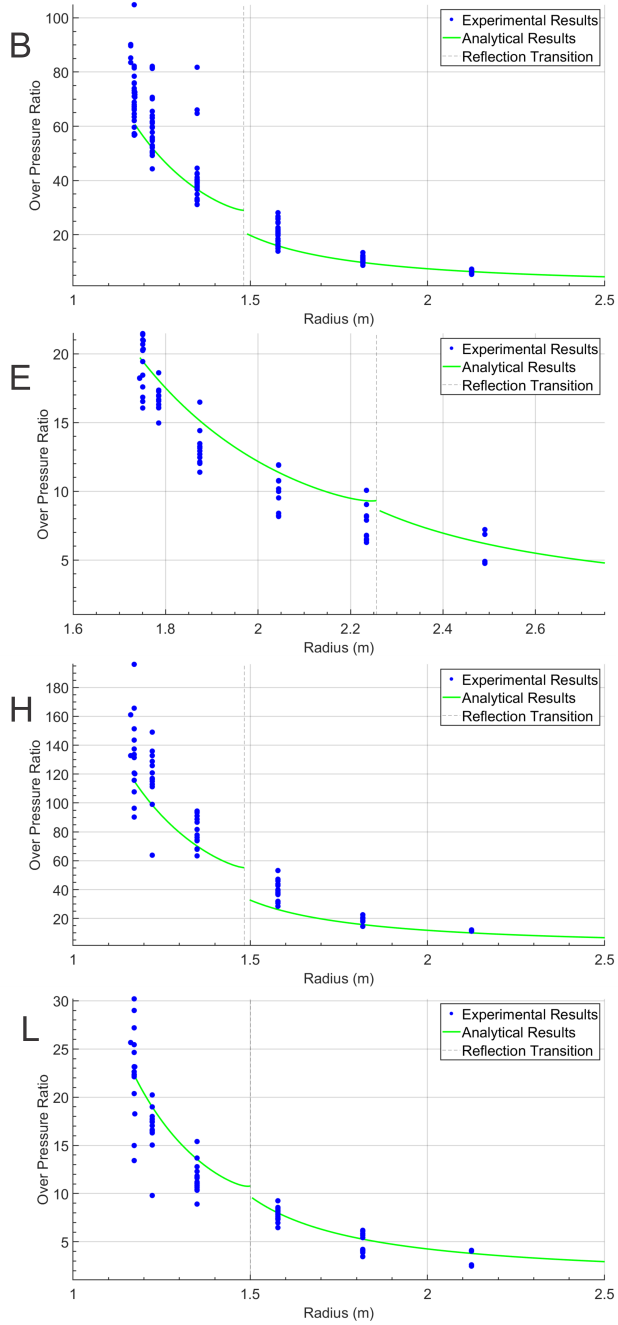


Figure 7.14: Analytical peak pressure and the unfitted experimental peak pressure for each test configuration. 'B' are the base line tests, 'E' are the elevated tests, 'L' are the light tests and 'H' are the heavy tests.

### 7.3.2 Analytical Pulse Duration

The analytical pulse duration starts at the origin of the release wave, which is covered in detail in Section 5.3.2. The theoretical origin of the release wave is the point of zero overpressure at the detonation products interface but this point can only be determined with an analytical model or computational simulation. The point of maximum detonation product expansion should be near the point of zero overpressure but can be determined experimentally. Figure 7.15 is a streak image of the detonation products from test S4 which was a 1.3 kg (3 lb.) charge. The streak image was made with the radial direction parallel to the reflection surface and zero radius at the charge center. PBXN-110 is comprised of 88% HMX with the balance being binders [110]. During the detonation process the binders do not fully oxidize which make the detonation products appear either black or glowing red. In Figure 7.15,  $t = 0$  is first light, which whites out the field of view. When the detonation products become visible they are rapidly expanding. At 1.3 m and 1.5 ms the expansion rate of the detonation products drops to effectively zero. At 2.7 ms a secondary shock from within the fireball reaches the detonation products interface and the fireball begins to expand again. After the secondary shock the detonation products goes through a second expansion process and then slows and stops expanding. Following this the reflected shock reaches the field of view forcing the detonations products upwards and outwards.

The point where the detonation products first stopped expanding, 1.3 m and 1.5 ms, is the point of maximum expansion. Using this point as the origin of the release wave the pulse duration can be analytically determined. Figure 7.16 shows the experimental and analytical pulse duration for the 'B' test configuration. The vertical dotted line is the maximum radius of the detonation products. The pulse duration inside of the detonation products is outside the scope of this work but if the analytical pulse duration line is extrapolated backwards the extrapolated line would be within the uncertainty of the experimental pulse duration. At the first three pressure probe radii that are outside the detonation products, the analytical pulse duration is within the uncertainty of the experimental data. At the final probe radius the analytical pulse duration is outside of the uncertainty but is within the experimental data. Figure 7.17 shows the experimental and analytical pulse duration for the 'E' test configuration which also used a 1.3 kg (3 lb.) charge. Over the entire range shown the analytical pulse duration underpredicts the experimental pulse duration. At the first 4 probe radii the analytical pulse duration is at the bottom of the uncertainty region. The analytical pulse duration is below the uncertainty at 2.25 m and below the experimental data at 2.5 m.

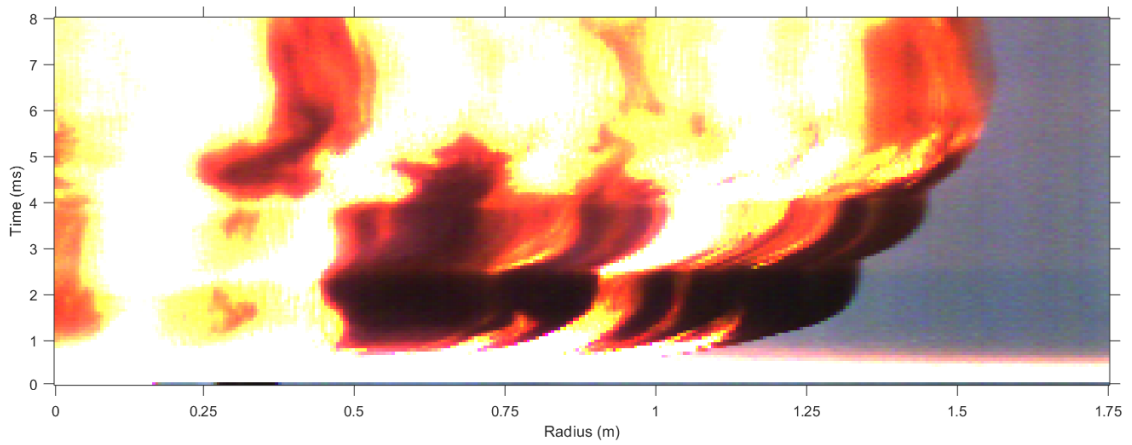


Figure 7.15: Streak image from test S4 which was a 1.3 kg (3 lb.) charge. The radial direction is parallel to the reflection plane.

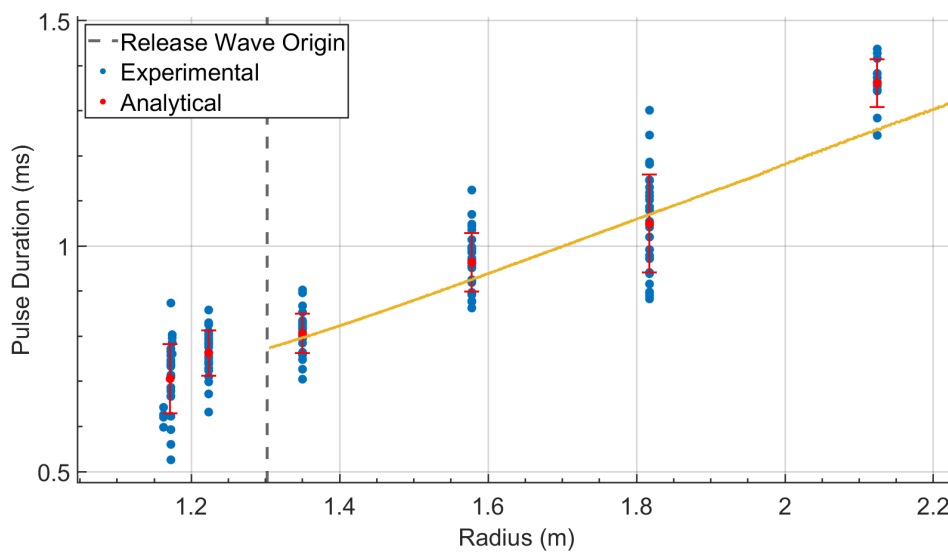


Figure 7.16: Comparison of the experimental, experimental uncertainty, and analytical pulse duration for the 'B' test configuration.

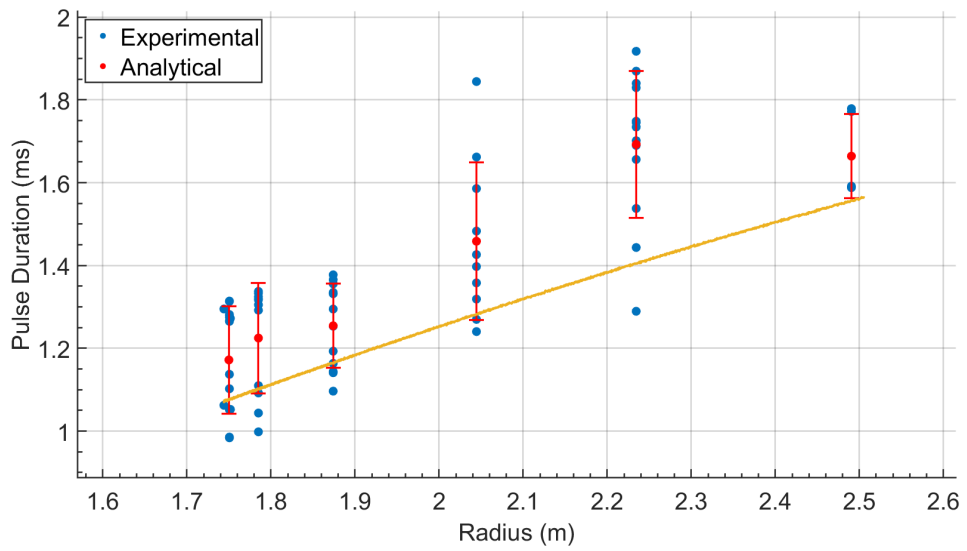


Figure 7.17: Comparison of the experimental, experimental uncertainty, and analytical pulse duration for the 'E' test configuration.

Figure 7.18 is a streak image of the detonation products from test S6 which was a 0.45 kg (1 lb.) charge. Similar to the 1.3 k (3 lb.) charge there is an initial section of rapid expansion which ends at the maximum expansion at 0.9 m and 0.97 ms. Figure 7.19 shows the experimental and analytical pulse duration for the 'L' test configuration. At all radii the analytical pulse duration is within the uncertainty but it is at the edges of the uncertainty region for all but one of the radii. Due to the larger fireball from the 2.72 kg charge no camera fully captured the expansion process and the point of maximum expansion could not be experimentally determined.

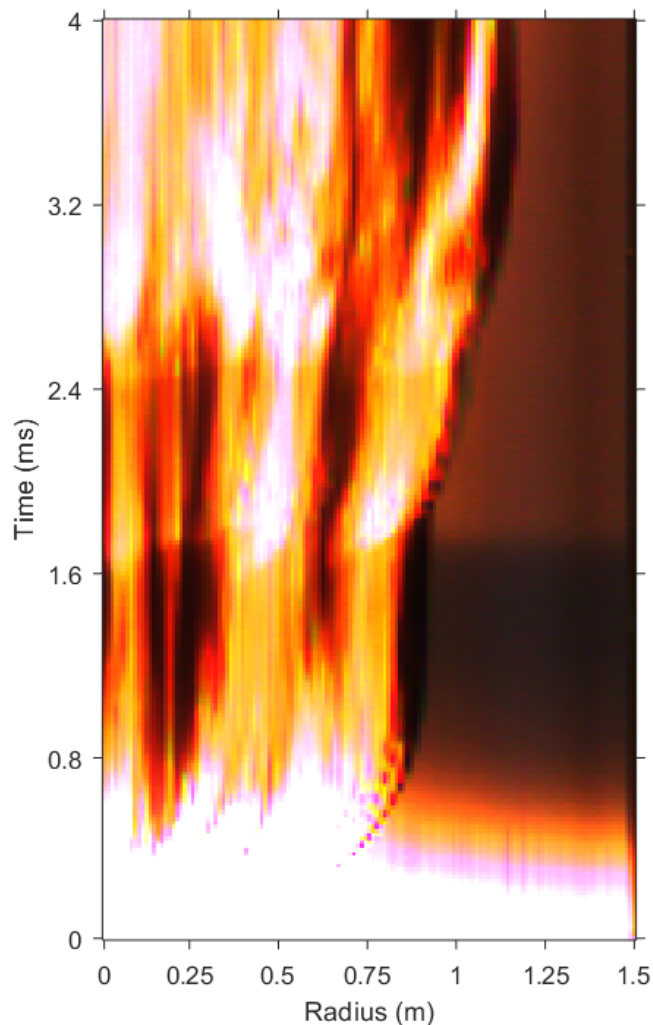


Figure 7.18: Streak image from test S6 which was a 0.45 kg (1 lb.) charge. The radial direction is parallel to the reflection plane.

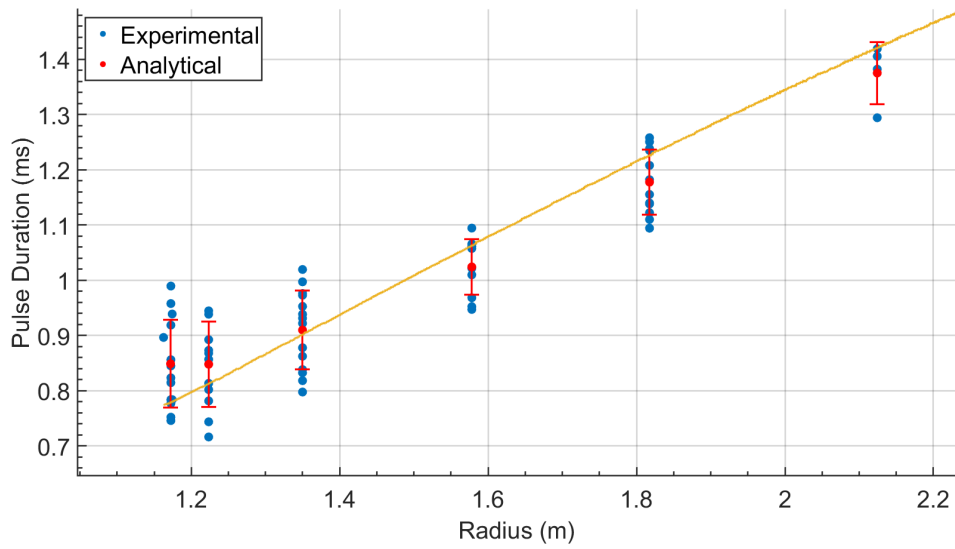


Figure 7.19: Comparison of the experimental, experimental uncertainty, and analytical pulse duration for the 'L' test configuration.

### 7.3.3 Decay Coefficient

Since no physical model for decay coefficient exists, the alpha values for all the spherical kilogram scale tests were plotted as a function of scaled radius and fit to a power law function, as shown in Figure 7.20. Further details on the decay coefficient or power law fit can be found in Section 5.3.3. Since the decay coefficient is not a function of height of burst and Figure 7.20 shows that Sachs scaling can be used to scale the radius term it is possible to directly compare the  $\alpha$  terms from the kilogram scale test series and the gram scale test series. Figure 7.21 shows experimental data and power series fits of  $\alpha$  for both test series. The two curve fits have very similar shapes but are slightly offset.

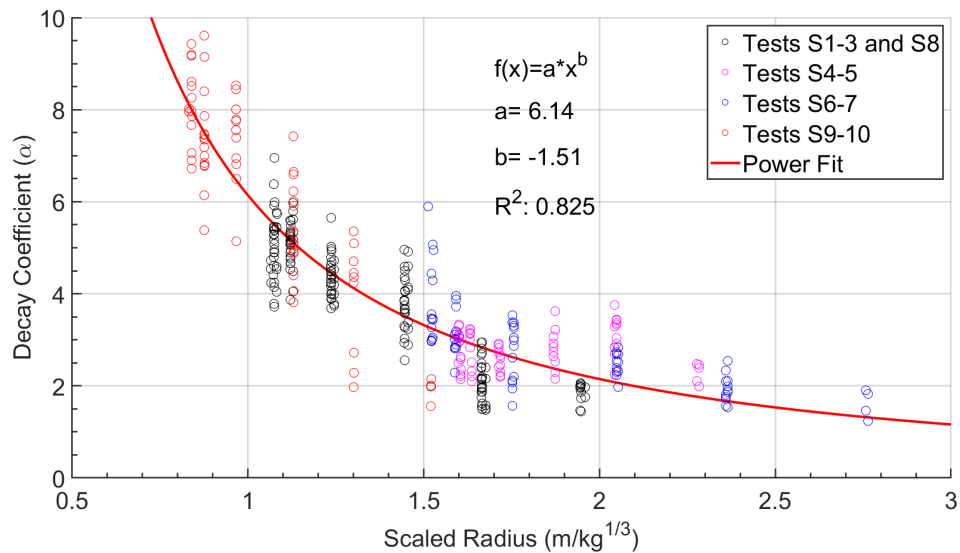


Figure 7.20: Plot of the decay coefficient  $\alpha$  for all the kilogram scale sphere tests as a function of scaled radius. The power fit to the data is shown with the resulting parameters.

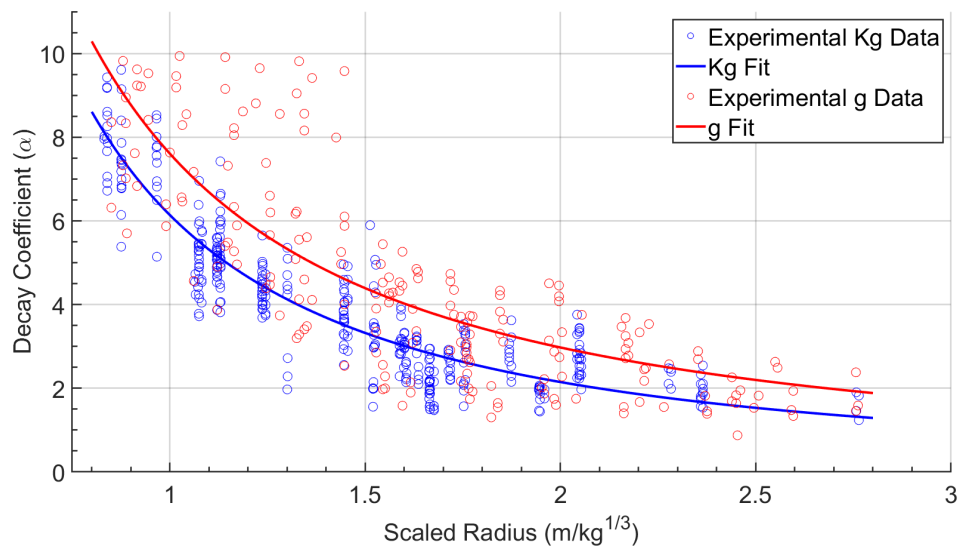


Figure 7.21: Comparison of the reflected decay coefficient  $\alpha$  between the gram and kilogram scale test series. Only the radius has been scaled using Sachs scaling. The power fits are also shown.

A potential cause of the offset between the two fits in Figure 7.21 is the difference between the explosive used in the gram scale tests and the kilogram scale tests. The charges in the gram scale tests were effectively pure PETN. The PBXN-110 used in the kilogram tests was only 88% HMX with the remaining 12% being a binder system, the main component of which was hydroxyl-terminated polybutadiene polymer (HTPB) [110]. One method to account for the differences in explosives is by comparing their internal energy or specifically energy release.  $E_0$  is the JWL term that describes the total heat of reaction of an explosive [111]. To compare decay coefficient  $\alpha$  between two explosive materials a scaling approach was developed which is given by:

$$E_s = \frac{E_0}{E_{ref}} \quad (7.1)$$

$$\alpha_s = \alpha / E_s \quad (7.2)$$

where  $E_s$  is the heat of reaction scale factor,  $E_{ref}$  is a reference heat of reaction, and  $\alpha_s$  is the scaled decay coefficient.

Using the new  $\alpha$  scaling equations, Equations 7.1 and 7.2 and Sachs scaling equations, Equations 1.6 through 1.9, the decay coefficients were compared between the gram and kilogram tests and shown to have good agreement. PETN was used as the reference heat of reaction to which the PBXN-110 data was scaled to. PETN has a heat of reaction of  $E_0 = E_{ref} = 10.8$  (GPa  $cm^3/cm^3$  g) [111] and PBXN-110 has a heat of reaction of  $E_0 = 8.7$  (GPa  $cm^3/cm^3$  g) [112]. The data was scaled using both  $\alpha$  and Sachs scaling and fit to a power law function and is shown in Figure 7.22. Accounting for the heat of reaction of the explosives caused the gram and kilogram fits to collapse. The combined gram and kilogram data was fit power law function and is shown in Figure 7.23. The fit values and  $R^2$  of the unscaled  $\alpha$  data from Figure 7.21 and the scaled  $\alpha$  data from Figure 7.22 are shown in Table 7.1. The fit values and  $R^2$  for the combined g and kg data is also listed in Table 7.1. For comparison, the combined g and kg un-scaled  $\alpha$  data was fit to a power law function and the resulting values listed in Table 7.1.

Four literature curves for the decay coefficient  $\alpha$  as a function of scaled radius are presented in Figures 4.52 and 4.54. The Kinney and Graham data is from TNT charges [70] and the Larcher curve is based off of data from a 1984 report which used hemispheres and spheres of TNT [103, 113]. The internal energy of TNT is  $E_0 = 6$  (GPa  $cm^3/cm^3$  g) [114]. Using Equation 7.1 and 7.2 the Kinney and Graham and Larcher curves were scaled to the same internal energy as PETN and are plotted in Figure 7.24 along with the gram and kilogram data and the fit to the combined data. The data used to generate the Lam curve was calculated from a 1955 numerical solution for the shock wave from a sphere of high pressure gas [101, 99]. Currently the  $\alpha$  scaling approach is only applicable to explosive charges and so the Lam curve is omitted. The full details of the Borgers experimental data were unavailable so it is also omitted.

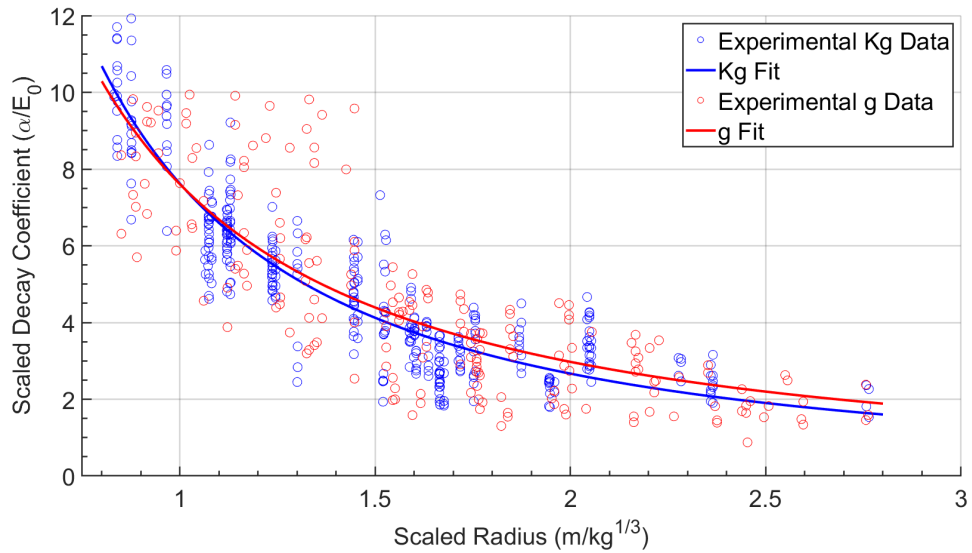


Figure 7.22: Comparison of the scaled reflected decay coefficient  $\alpha$  between the gram and kilogram scale test series. Both the  $\alpha$  term and radius have been scaled. The power law fits are also shown.

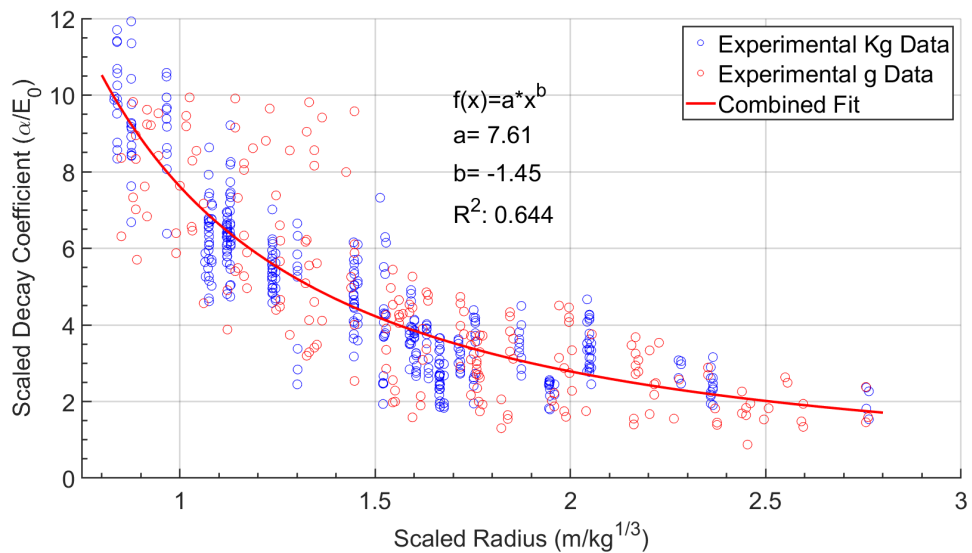


Figure 7.23: The combined gram and kilogram scaled data of the reflected decay coefficient  $\alpha$  and resulting power law fit. Both the  $\alpha$  term and radius have been scaled.

Table 7.1: List of the power law fit terms from the scaled and un-scaled gram, kilogram and combined tests. The  $\alpha$  scaling factor for the scaled gram and kilogram tests is shown.

Data Set	$E_s$ Value	a Fit Value	b Fit Value	$R^2$
Kilogram Unscaled	N/A	6.14	-1.51	0.825
Gram Unscaled	N/A	7.61	-1.35	0.644
Combined Data Unscaled	N/A	6.53	-1.40	0.678
Kilogram Scaled	0.806	7.62	-1.51	0.825
Gram Scaled	1	7.60	-1.35	0.644
Combined Data Scaled	N/A	7.61	-1.45	0.756

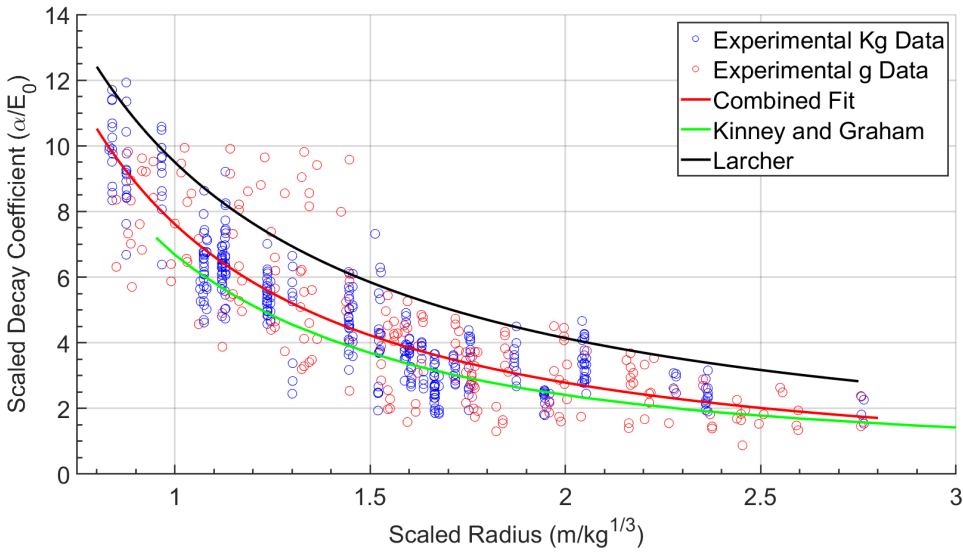


Figure 7.24: The combined gram and kilogram scaled data of the reflected decay coefficient  $\alpha$  and resulting power law fit with two  $\alpha$  curve from literature shown. Both the  $\alpha$  term and radius have been scaled.

Figure 7.24 shows that there may be a universal decay coefficient curve for reflected shocks. The Kinney and Graham curve is a close match for the combined fit to the gram and kilogram data. The Larcher curve has the same shape as the combined fit curve but is offset while still being within the spread of the experimental data. A potential cause for the offset between the two curves is the different methods used to determine  $\alpha$ , since the method used to calculate  $\alpha$  has been shown to have an impact on the found value [105]. In the present work  $\alpha$  was determined by fitting the pressure trace data to the Friedlander equation. In the Larcher work, first the impulse, peak pressure and pulse duration was determined and then  $\alpha$  was calculated from the Friedlander impulse equation, Equation 1.15 [103]. By scaling the  $\alpha$  term to account for the differences in heat of reaction of the explosives and applying Sachs scaling to the radii, all the data from the gram and kilogram tests overlap and agree with historical data.

### 7.3.4 Analytical Impulse

Using the analytically determined peak pressure, pulse duration and the fitted decay coefficient the analytical impulse was calculated for 'B', 'E' and 'L' test configurations. Since the point of maximum expansion for the 2.72 kg charges could not be found, the pulse duration for the 'H' test configuration could not be determined. Figure 7.25 shows the analytical and experimental pulse duration for the 'B' test configuration which consisted of a 1.36 kg (3 lb.) charge at a height of burst of 1.16 m (46 inches). In the current model for pulse duration, the pulse duration is undefined below the radius of maximum product expansion. This is why the analytical impulse is not shown below the line of maximum expansion. At 1.35 m the analytical impulse is at the mean of the experimental data. At the first probe radii after the reflection transition the analytical impulse underpredicts the experimental analytical results but is still within the uncertainty bound. At 1.8 m the analytical solution is below the bounds of the experimental uncertainty. At 2.15 m the analytical results are back to within the uncertainty but slightly below the experimental data.

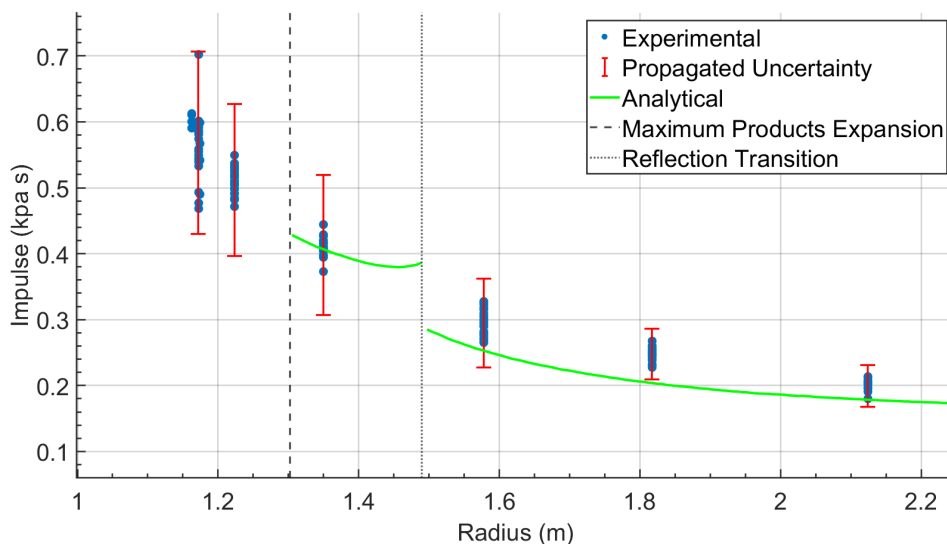


Figure 7.25: Comparison between the experimental and analytical impulse for the 'B' test configuration. The impulse is undefined below the maximum product expansion.

Figure 7.26 compares the analytical and experimental impulse for the 'E' configuration which had a 1.36 kg (3 lb.) charge at a height of burst of 1.74 m (69 inches). From the first probe radii to 2.1 m the analytical agrees very well with the experimental data being near the mean of the data. After 2.1 m the analytical overpredicts the experimental but is within the uncertainty. After the reflection transition the analytical overpredicts the experimental impulse by 25%.

Figure 7.27 compares the analytical and experimental impulse for the 'L' configuration which had a 0.45 kg (1 lb.) charge at a height of burst of 1.16 m (46 inches). At all points the analytical impulse dramatically overpredicts the experimental results. This is due to the discrepancy between the raw peak pressure values and those found by the Friedlander fit. In Figure 7.28 the experimental impulse is calculated using the unfitted peak pressure. Using the unfitted peak pressure the analytical impulse is within the experimental data.

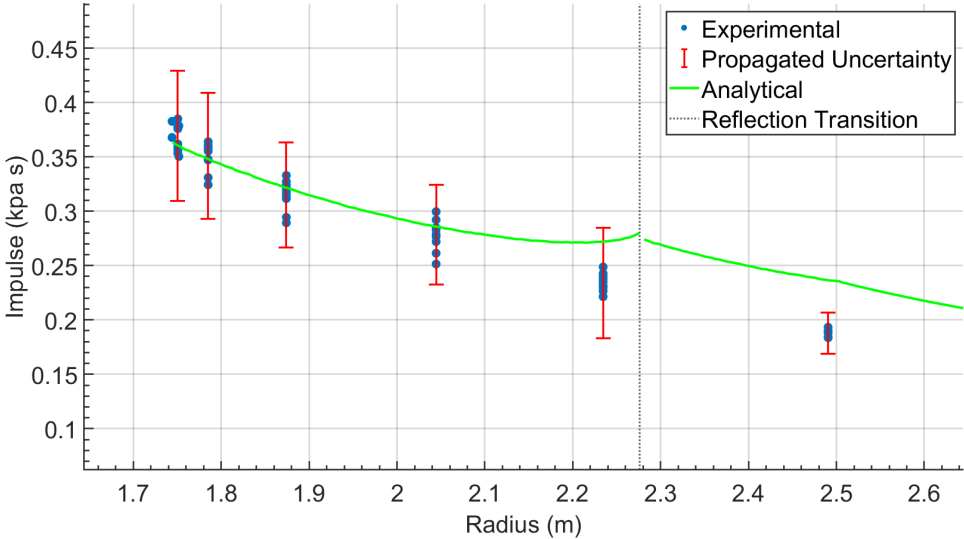


Figure 7.26: Comparison between the experimental and analytical impulse for the 'E' test configuration.

Figures 7.25, 7.26, and 7.28 show that the techniques developed from the gram scale test series can be used to predict the impulse of kilogram scale charges of the same spherical geometry. The ringing noise in the kilogram scale pressure trace data caused the Friedlander fitting equation to underpredict the peak pressure. The pulse duration was calculated using the point of maximum product expansion as an approximation of the location of the point of zero overpressure and decay coefficient was found by fitting the experimental data to a power law. Using these techniques, over the majority of the region studied the impulse was predicted to within the uncertainty of the data.

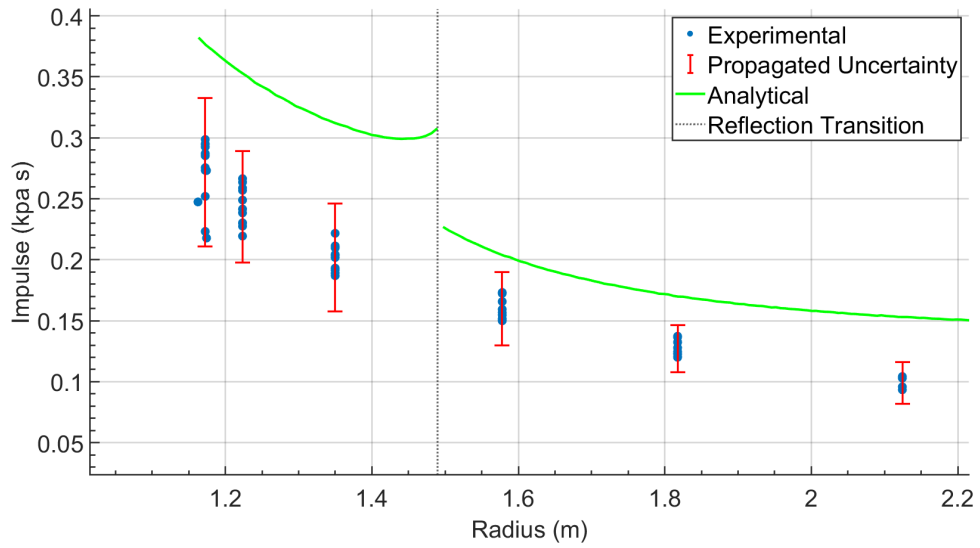


Figure 7.27: Comparison between the Friedlander experimental and analytical impulse for the 'L' test configuration.

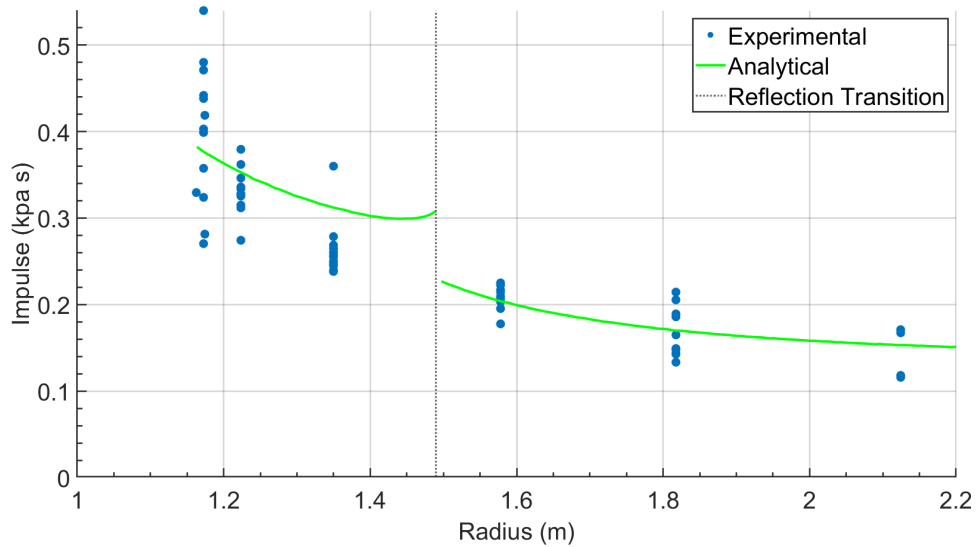


Figure 7.28: Comparison between the experimental and analytical impulse for the 'L' test configuration. The peak pressure term is the unfitted peak pressure.

## CHAPTER 8

# CONCLUSIONS AND RECOMMENDATIONS FOR FUTURE RESEARCH

### 8.1 Summary and Conclusions

The majority of prior research in the field of shock wave reflections has focused on pseudo-steady reflections which are fundamentally different from the most common case of explosively-driven unsteady shock waves. The present work combines prior pseudo-steady reflection theory with new models, methodologies, and scaling to better predict and understand unsteady shock waves and their reflections. A new model for the pulse duration of free air shocks, where the origin of the release wave is at the point of zero overpressure, is applied and shown to better predict experimental results than the prior model. A novel methodology to calculate the pulse duration of reflected shocks is shown to accurately predict the experimental results. A novel scaling approach was developed for the Friedlander decay coefficient  $\alpha$  of shock reflections based on the heat of reaction of the explosive is shown to collapse the data from two different explosive materials. Using these new models, methodologies, and scaling the overpressure, decay coefficient, and impulse from a shock wave reflection can be analytically predicted for any charge size, height of burst, or distance from the charge.

The sonic condition model predicts that a shock wave reflection will change types when the flow behind the reflection becomes sonic. The present work demonstrated that the sonic condition model was able to predict the reflection type of explosively driven shock waves to within the accuracy of the refractive imaging systems used to document the experiments. The slow growth rate of Mach stems was also discussed and shown to be an important factor in when an irregular reflection will be visualized.

The impulse from a shock wave can be expressed as a function of three parameters: the peak overpressure, the pulse duration and the path between those two points which is mathematically described as a decay coefficient. For a regular reflection the overpressure is the product of the pressure change across primary and reflected shock. For an irregular reflection the peak pressure is the pressure across the Mach stem. The value of the pressure change across these shocks was found by solving the boundary condition and continuity equations for each reflection type. This was shown to predict the overpressure of explosively driven

shock waves at the gram and kilogram scale and over a wide range of reflection conditions.

Pulse duration is the time between the arrival of the shock wave and when the overpressure returns to zero. The point when the overpressure returned to zero was found by tracking a release wave traveling behind the primary shock moving at the local sound speed. The prior model placed the origin of the release wave at the shock wave breakout but wave diagram analysis of the expansion of the detonation products was developed to show this to not be a viable origin. The proposed model uses an origin for the release wave which is the point of zero overpressure across the detonation products. A one dimensional rectangular analytical model of the expansion of the detonation products was developed and shown to not be applicable to spherical geometries. The hydro-code CTH was used to computationally simulate the expansion of the detonation products and the point of zero overpressure across the detonation products interface was determined for a spherical gram charge. The point of maximum product expansion was also determined in the simulation and shown to be located near the point of zero overpressure across the detonation products. This point of maximum expansion can thus be used as a proxy for the zero overpressure point. This is useful because the maximum expansion point can be experimentally visualized. The point of maximum product expansion was then determined for kilogram scale charges of different composition through streak images of the explosive fireballs.

The release wave was tracked from its origin outwards as function of time to determine the pulse duration for a variety of configurations. The simplest configuration was of a shock wave expanding into free air. The speed of sound field which the release wave moved through was spherically symmetric and calculated from basic compressible relations. This approach was shown to accurately predict the pulse duration of gram scale non-reflected shocks. Calculating the pulse duration of reflected shocks requires accounting for the non-symmetric fields behind the reflection. After the release wave detached from the detonation products it would start by traveling through the symmetric field behind the primary shock. The release wave then intersects the reflected shock. After passing the reflected shock the release wave moves through the non-uniform speed of sound field. A new methodology to track the release wave through the non-symmetric field is proposed and shown to accurately predict the pulse duration of gram and kilogram charges at a range of heights of burst and angles.

The final term need to calculate impulse is the decay coefficient which was found experimentally by fitting the experimental data to a power law function. The Friedlander decay coefficient was found to vary between reflected and non-reflected shock wave. The decay coefficient of a reflected shock was shown to be independent of charge height. The reflected decay coefficient was also shown to scale well across different explosives by applying a novel scaling approach based on the heat of reaction of the explosive and across orders of magnitude differences in charge mass by applying Sach's scaling to the radius from the charge. This novel scaling approach shows that it may be possible to analytically calculate the decay coefficient of an arbitrary explosive and size.

The impulse was analytically determined by combining the three terms: peak overpressure, pulse duration, and decay coefficient. Over the majority of the range studied the analytically determined impulse was within the uncertainty of the experimental impulse. This analysis shows that the analytical methodology used to calculate the impulse is an accurate and useful tool. The analytical methodology was then used to create surface plots of the peak pressure, pulse duration, and impulse for a wide range of heights of burst and horizontal distances. These surface plots show regions of local minimums and maximums and can be used to discuss effect of changing height of burst has on impulse for a given location.

## 8.2 Recommendations for Future Research

This dissertation covers only a fraction of the research possible with explosively driven shock wave reflections. A few areas that were identified during the course of this work that warrant further research and experimentation include development of a physical model for the decay parameter and investigating more near-field effects of explosions where the fireball plays a more prominent role.

The decay coefficient of the Friedlander equation,  $\alpha$  does not have a physical model. Current methodology for predicting  $\alpha$  is built on the fitting of experimental data to an arbitrary curve. This work has shown that using a standard methodology to calculate the Friedlander parameters caused  $\alpha$  from multiple charge materials and heights to collapse when scaled for charge mass and internal energy. This work should be expanded to develop either a physical model of the decay coefficient.

A potential model for the decay coefficient could be developed by treating the pressure decay process with the same methodology as the pulse duration. The pulse duration is calculated by propagating a specific pressure from the detonation products interface outwards. It may be possible to approximate the pressure decay process as a series of fractions of the peak overpressure propagated outward from the detonation products.

Prior to the development of a physical model of decay coefficient it may be possible to generate a universal scaling law of  $\alpha$  for shock wave reflections. This work showed that the scaled decay coefficient of the reflection of a spherical charge of PETN and PBXN-110 had very similar shapes and values. By repeating these experiments with a wider range of explosive materials, charge masses and most importantly charge geometries it may be possible to show that  $\alpha$  has a predictable scalable form for specific charge geometries.

One limitation of the current work is that the analytical model of pulse duration is undefined for radii less than the origin of the release wave. Development of a model for the pulse duration inside of the detonation products would allow the calculation of pulse duration and impulse for any point in the experimental field. This may be achieved by tracking the rarefaction waves inside of the detonation products.

A one dimensional rectangular analytical model of the expansion of the detonation products was developed and shown to not be applicable to spherical geometries. Development of a spherical analytical model of the detonation products will allow the origin of the release wave to be determined for an arbitrary explosive material without the need for detailed computer simulations or experiments. A spherical analytical model could also be used to determine the pulse duration inside of the detonation products.

## REFERENCES

- [1] H. Reichenbach. Contributions of ernst mach to fluid mechanics. *Annual Review of Fluid Mech*, 15:1–28, 1983.
- [2] John Von Neumann. Theory of shock waves. Technical Report 1140, Institute for Advanced Study, Princeton, New Jersey, 1943.
- [3] Wayland C. Griffith. Shock waves. *Journal of Fluid Mechanics*, 106:81–101, 1981.
- [4] Ryuma Kawamura and Haruo Saito. Reflection of shock waves - 1 pseudo-stationary case. *Journal of the Physical Society of Japan*, 11(5):584–592, 1956.
- [5] D. C. Pack. The reflexion and diffraction of shock waves. *Journal of Fluid Mechanics*, 18(4):549–576, 1964.
- [6] G. Ben-Dor. *Shock Wave Reflection Phenomena*. Springer, 2 edition, 2007.
- [7] E. Mach and J. Sommer. Über die fortpflanzungsgeschwindigkeit von explosionsschallwellen. *Anzeiger der Akademie der Wissenschaften in Wien. Mathematische-naturwissenschaftliche Klasse. Wien*, 75:101–130, 1877.
- [8] John von Neumann. Oblique reflection of shocks. Technical Report Explosive Research Report 12, Navy Department, Bureau of Ordnance, Washington, DC, USA., 1943.
- [9] H. Hornung. Regular and mach reflections of shock waves. *Annual Review of Fluid Mechanics*, 18:33–58, 1986.
- [10] P. C. Keenan and R. J. Seeger. Analysis of intersections of shockwaves. Technical Report Research Report 15, US Navy Bureau Ordnance Explos., 1944.
- [11] Lincoln G. Smith. Photographic investigation of the reflection of plane shocks in air : final report. Technical Report Report Number 6271 NB: 20190119, National Defense Research Committee of the Office of Scientific Research and Development, 1945.
- [12] Donald R. White. *A Experimental Survey of the Mach Reflection of Shock Waves*. PhD thesis, Princeton University, 1951.
- [13] G. Ben-Dor and I. I. Glass. Domains and boundaries of non-stationary oblique shock-wave reflexions. 1. diatomic gas. *Journal of Fluid Mechanics*, 92(3):459–496, 1979.

- [14] John von Neumann. Refraction, intersection and reflection of shock waves. Technical report, Navy Department, Bureau of Ordinance, 1943.
- [15] W. Bleakney and A. H. Taub. Interaction of shock wave. *Reviews of Modern Physics*, 21(4):584–604, 1949.
- [16] G. Birkhoff. *Hydrodynamics: A study in fact logic and similitude*. Princeton University Press, 1950.
- [17] P. Colella and L. F. Henderson. The von neumann paradox for the diffraction of weak shock waves. *Journal of Fluid Mech.*, 213:71–94, 1990.
- [18] E. I. Vasilev and A. N. Kraiko. Numerical simulation of weak shock diffraction over a wedge under the von neumann paradox conditions. *Zhurnal Vychislitel'noi Matematiki i Matematicheskoi Fiziki*, 39(8):1393–1404, 1999.
- [19] K. G. Guderley. Considerations on the structure of mixed subsonic-supersonic flow patterns. Technical Report F-TR-2168-ND, T-2 Technical Intelligence, 1947.
- [20] Jason T. Ashworth and Beric W. Skews. The physical nature of weak shock wave reflection. *Journal of Fluid Mechanics*, 542:105–114, 2005.
- [21] L. D. Landau and E. M. Lifshitz. *Fluid Mechanics*, volume 6. Institute of Physical Problems, U.S.S.R. Academy of Sciences, 2 edition, 1959.
- [22] L. F. Henderson and A. Lozzi. Experiments on transition of mach reflexion. *Journal of Fluid Mechanics*, 68(1):139–155, 1975.
- [23] G. Ben-Dor. *Shock Wave Reflection Phenomena*. Springer, 1 edition, 1992.
- [24] G. D. Lock and J. M. Dewey. An experimental investigation of the sonic criterion for transition from regular to mach reflection of weak shock waves. *Experiments in Fluids*, 7:289–292, 1989.
- [25] H. G. Hornung, H. Oertel, and R. J. Sandeman. Transition to mach reflexion of shock waves in steady and pseudosteady flow with and without relaxation. *Journal of Fluid Mechanics*, 90(3):541–560, 1979.
- [26] Dewey J. M. and van Netten A. A. Observations of the initial stages of the mach reflection process. In *Proceedings of the 18th International Symposium on Shock Waves*, pages pp 227–232, Sendai, Japan, 1992.
- [27] Dewey J. M. and van Netten A. A. Non-self-similarity of the initial stages of mach reflection. In *Shock Waves - Proceedings Of The 20th International Symposium (In 2 Volumes)*, pages 399–404, 1995.
- [28] C. K. Law and I. I. Glass. Diffraction of strong shock waves by a sharp compressive corner. *C. A. S. I. Transactions*, 4:2–12, 1971.

- [29] Ben-Dor G. Regions and transitions of nonstationary oblique shock-wave diffractions in perfect and imperfect gases. Technical Report ASA064967, Institute for Aerospace Studies University of Toronto, 1978.
- [30] Galileo Galilei. *Dialogues concerning Two New Sciences*. Macmillan Company, 1638.
- [31] Doris M. Jones, P. Moira, E. Martin, and C. K. Thornhill. A note on the pseudo-stationary flow behind a strong shock diffracted or reflected at a corner. *Proceedings of the Royal Society of London*, 209(1097):238–248, 1951.
- [32] T. Kawauchi G. Ben-Dor, K. Takayama. The transition from regular to mach reflexion and from mach to regular reflexion in truly non-stationary flows. *Journal of Fluid Mechanics*, 100(1):147–160, 1980.
- [33] Heilig WH. Diffraction of a shock wave by a cylinder. *The Physics of Fluids*, 12(5):1–154, 1969.
- [34] I. P. Ginzburg and Iu. S. Markov. Experimental investigation of the reflection of a shock wave from a two-facet wedge. *Fluid Mechanics - Soviet Research*, 1975.
- [35] Ben-Dor G. and Dewey J. M. The reflection of a planar shock wave over a double wedge. *Journal of Fluid Mechanics*, 176:483–520, 1987.
- [36] Li H. and Ben-Dor G. Interaction of two mach reflections over concave double wedges-analytical model. *Shock Waves*, 9:259–268, 1999.
- [37] Skews B. and Blitterswijk A. Shock wave reflection off coupled surfaces. *Shock Waves*, 21:491–498, 2011.
- [38] Soni V., Hadjadj A., Chaudhuri A., and Ben-Dor G. Shock-wave reflections over double-concave cylindrical reflectors. *Journal of Fluid Mechanics*, 813:70–84, 2017.
- [39] W. R. Smith. Mutual reflection of two shocks waves of arbitrary strength. *Physics of Fluids*, 2(3):533–541, 1959.
- [40] Ralph E. Reisler, Lynn W. Kennedy, and John H. Keefer. High explosive multiburst airblast phenomena (simultaneous and non-simultaneous detonations). Technical Report ADA068462, US Army Armament Research and Development Command, 1979.
- [41] Kaman AviDyne. Calculation of multiple burst interactions for six simultaneous explosions of 120 ton anfo charges. Technical Report ADA091978, Defense Nuclear Agency, 1979.
- [42] V. Eliasson, N. Apazidis, N. Tillmark, and M. B. Lesser. Focusing of strong shocks in an annular shock tube. *Shock Waves*, 2006.

- [43] Eliasson V., Kjellander M., and Apazidis N. Regular versus mach reflection for converging polygonal shocks. *Shock Waves*, 17:43–50, 2007.
- [44] Qiu S. and Eliasson V. Interaction and coalescence of multiple simultaneous and non-simultaneous blast waves. *Shock Waves*, 26:287–297, 2016.
- [45] G.S. Settles. *Schlieren and Shadowgraph Techniques: Visualizing Phenomena in Transparent Media*. Experimental Fluid Mechanics. Springer-Verlag Berlin Heidelberg, 1 edition, 2001.
- [46] M. J. Hargather and G. S. Settles. A comparison of three quantitative schlieren techniques. *Optics and Lasers in Engineering*, 50:8–17, 2012.
- [47] G. S Settles and M. J Hargather. A review of recent developments in schlieren and shadowgraph techniques. *Measurement Science and Technology*, 28, 2017.
- [48] Michael John Hargather, Gary S. Settles, and Matthew J. Madalis. Schlieren imaging of loud sounds and weak shock waves in air near the limit of visibility. *Shock Waves*, 2010.
- [49] H. E. Edgerton. Shockwave photography of large subjects in daylight. *Review of Scientific Instruments*, 29(2):171–172, 1958.
- [50] M. J. Hargather and G. S. Settles. Retroreflective shadowgraph technique for large-scale visualization. *Applied Optics*, 48:4449–4457, 2009.
- [51] P. M. Giannuzzi, M. J. Hargather, and G. C. Doig. Explosive-driven shock wave and vortex ring interaction with a propane flame. *Shock Waves*, 26:851–857, 2016.
- [52] M. J. Hargather, G. S. Settles, and J. A. Gatto. Full-scale optical experiments on the explosive failure of a uld-3 air cargo container. In *4th International Aviation Security Technology Symposium*, Washington, D.C., November-December 2006.
- [53] M. Raffel. Background-oriented schlieren (bos) techniques. *Experiments in Fluids*, 56:60:1–17, 2015.
- [54] H. Schardin. Die schlierenverfahren und ihre anwendungen. *Ergebnisse der Exakten Naturwissenschaften*, 20:303–439, 1942. Translated as NASA TT F-12731.
- [55] S. B. Dalziel, G. O. Hughes, and B. R. Sutherland. Synthetic schlieren. In G. M. Carlomagno, editor, *Proc. 8th International Symposium on Flow Visualization*, volume 62, Sorrento, Italy, 1998.
- [56] G. E. A. Meier. Hintergrund-schlierenverfahren. Deutsche Patentanmeldung, 1999. DE 199 42 856 A1.

- [57] M. Raffel, H. Richard, and G. Meier. On the applicability of background oriented optical tomography for large scale aerodynamic investigations. *Experiments in Fluids*, 28:477–481, 2000.
- [58] K. Kindler, E. Goldhahn, F. Leopold, and M. Raffel. Recent developments in background oriented schlieren methods for rotor blade tip vortex measurements. *Experiments in Fluids*, 43(2-3):233 – 240, 2007.
- [59] M. J. Hargather and G. S. Settles. Natural-background-oriented schlieren. *Experiments In Fluids*, 48(1):59–68, 2010.
- [60] M. J. Hargather. Background-oriented schlieren diagnostics for large-scale explosive testing. *Shock Waves*, 23:529–536, 2013.
- [61] F. A. Mier and M. J. Hargather. Color gradient background-oriented schlieren imaging. *Experiments In Fluids*, 57(95), 2016.
- [62] G. E. A. Meier. Computerized background-oriented schlieren. *Experiments In Fluids*, 33(1):181–187, 2002.
- [63] O. K. Sommersel, D. Bjerketvedt, S. O. Christensen, O. Krest, and K. Vaagsaether. Application of background oriented schlieren for quantitative measurements of shock waves from explosions. *Shock Waves*, 18(4):291–297, 2008.
- [64] T. Mizukaki, H. Tsukada, K. Wakabayashi, T. Matsumaura, and Y. Nakayama. Quantitative visualization of open-air explosions by using background-oriented schlieren with natural background. In *28th International Symposium on Shock Waves*, Manchester, United Kingdom, 2011.
- [65] B. Hopkinson. British Ordnance Minutes, 13563, 1915.
- [66] R. G. Sachs. Dependence of blast on ambient pressure and temperature. Technical Report BRL-466, Army Ballistic Research Lab, Aberdeen Proving Ground, 1944.
- [67] H. Kleine, J. M. Dewey, K. Ohashi, T. Mizukaki, and K. Takayama. Studies of the TNT equivalence of silver azide charges. *Shock Waves*, 13(2):123–138, 2003.
- [68] J. M. Dewey. The properties of a blast wave obtained from an analysis of the particle trajectories. *Proceedings of the Royal Society of London Series A - Mathematical and Physical Sciences*, 324(1558):275–299, 1971.
- [69] J. M. Dewey. Expanding spherical shocks (blast waves). In G. Ben-Dor, O. Igra, and E. Elperin, editors, *Handbook of Shock Waves, Vol. 2*, pages 441–481. Academic Press, 2001.
- [70] G. F. Kinney and K. J. Graham. *Explosive shocks in air*. Springer-Verlag, 1985.

- [71] C. K. Thornhill. The shape of a spherical blast wave. Technical Report A.R.D.E Memorandum (B)41/59, Armament Research and Development Establishment, 1959.
- [72] AMES RESEARCH STAFF. Equations, tables, and charts for compressible flow. techreport 1135, National Advisory Committee for Aeronautics, 1953.
- [73] G. Ben-Dor and J. M. Dewey. The reflection of a planar shock wave over a double wedge. *Journal of Fluid Mechanics*, 176:483–520, 1987.
- [74] P. W. Cooper. *Explosives engineering*. Wiley-VCH, Inc, 1996.
- [75] RISI. *RP-3 EBW Detonator P/N 167-9225*.
- [76] Robert Weinheimer. Properties of selected high explosives. In *27th International Pyrotechnics Seminar*, 2000.
- [77] J. M. Walsh. Oblique interactions of detonation waves with explosive/metal interfaces. Technical Report LA-9612-MS, Los Alamos National Laboratory, 1982.
- [78] R. J. Bauer. An analysis of small scale gap test sensitivity data using porosity theory and nonreactive shock hugoniot. Technical Report NSWC/WOL/TR 75-67, Naval Surface Weapons Center, Silver Springs, Maryland, 1975.
- [79] S. G. Finnegan, J. W. Ferguson, M. J. Goff, J. C. F. Millett, and N. J. Whitworth. Development of a flyer design to perform plate impact shock-release shock experiments on explosives. In *AIP Conference Proceedings*, 1979.
- [80] M. Braithwaite and G.J. Sharpe. Non-ideal detonation behavior in commercial explosives. In *Performance of Explosives and New Developments*. Taylor and Francis Group, 2013.
- [81] Barry D. Fishburn. An analysis of impact initiation of explosives and the currently used threshold criteria. Technical Report ARAED-TR-90029, U. S. Army Armament Research, Development and Engineering Center, Armament Engineering Directorate, Picatinny Arsenal, 1990.
- [82] K. L. C. Nielsen, C. Craciun, T. R. Craig, and R. Turcotte. High-velocity projectile initiation of emulsion explosives. In *38th International Pyrotechnics Seminar*, 2012.
- [83] D. J. Idar, R. A. Lucht, R. Scammon, J. Straight, and C. B. Skidmore. Pbx 9501 high explosive violent response/low amplitude insult project: Phase i. Technical Report LA-13164-MS, Los Alamos National Laboratory, 1997.
- [84] Bob Smith Industries, 8060 Morro Road Atascadero, CA 93422. *Insta-Set Safety Data Sheet*, 2.01 edition, May 2018.

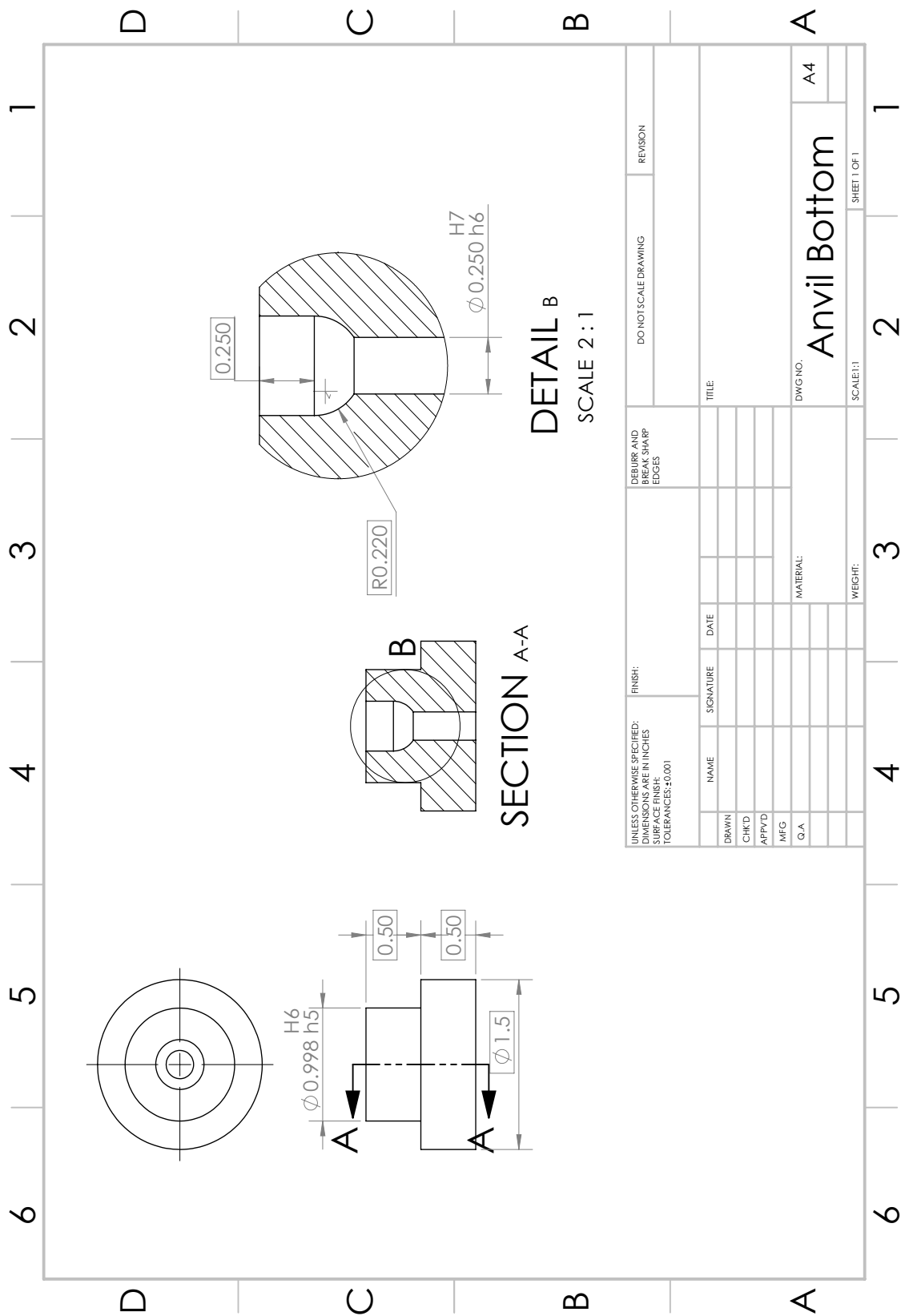
- [85] Mark Dewhirst, Benjamin L. Viglianti, Michael Lora-Michiels, P. Jack Hoopes D.V.M, and Margaret A. Hanson. Thermal dose requirement for tissue effect: experimental and clinical findings. In *Thermal Treatment of Tissue: Energy Delivery and Assessment II*, volume SPIE 4954, 2003.
- [86] Kyle O. Winter. Three-dimensional shock wave reconstruction using multiple high-speed digital cameras and background oriented schlieren imaging. Master's thesis, New Mexico Institute of Mining and Technology, 2018.
- [87] Kyle O. Winter and Michael J. Hargather. Threedimensional shock wave reconstruction using multiple highspeed digital cameras and backgroundoriented schlieren imaging. *Experiments in Fluids*, 60(93), 2019.
- [88] Matthew M. Biss and Gary S. Settles. On the use of composite charges to determine insensitive explosive material properties at the laboratory scale. *Propellants, Explosives, Pyrotechnics*, 35(5):452–460, 2010.
- [89] Gary S. Settles Michael J. Hargather. Optical measurement and scaling of blasts from gram-range explosive charges. *Shock Waves*, 17:215–223, 2007.
- [90] Matthew M. Biss, Kathryn E. Brown, and Christopher F. Tilger. Ultrahigh fidelity laserinduced air shock from energetic materials. *Propellants, Explosives, Pyrotechnics*, 45(3), 2020.
- [91] John Anderson. *Modern Compressible Flow With Historical Perspective*. Mc Graw Hill, 3 edition, 2003.
- [92] Michael J. Hargather. *Scaling, characterization, and application of gram-range explosive charges to blast testing of materials*. PhD thesis, Pennsylvania State University, 2008.
- [93] James E. A. John. *Gas Dynamics*. Prentice-Hall, 2 edition, 1984.
- [94] Ralph Menikoff. Jwl equation of state. Technical Report LA-UR-15-29536, Los Alamos National Laboratory, 2016.
- [95] Craig M. Tarver, Breithaupt R. Don, and John W. Kury. Detonation waves in pentaerythritoltetranitrate. *Journal of Applied Physics*, 81(7193), 1997.
- [96] McGlaun J.M, Thompson S.L, and Elrick M.G. Cth: A three-dimensional shock wave physics code. *International Journal of Impact Engineering*, 10(1-4):351–360, 1990.
- [97] Julio C. Peguero II. Measurement of shock and detonation propagation along pentaerythritol tetranitrate ( PETN ) thin films. Master's thesis, New Mexico Institute of Mining and Technology, 2019.
- [98] Vasilis Karlos, George Solomos, and Martin Larcher. Analysis of the blast wave decay coefficient using the kingerybulmash data. *International Journal of Protective Structures*, 7(3):409–429, 2016.

- [99] Harold L. Brode. Numerical solutions of spherical blast waves. *Journal of Applied Physics*, 26(6), 1955.
- [100] W.E. Baker, P.A. Cox, J.J. Kulesz, R.A. Strehlow, and P.S. Westine. *Explosion Hazards and Evaluation*, volume 5. Elsevier Science, 1983.
- [101] Nelson Lam, Priyan Mendis, and Tuan Ngo. Response spectrum solutions for blast loading. *Electronic Journal of Structural Engineering*, 4, 2004.
- [102] M. V. Dharaneepathy, M. N. Keshava Raot, and A. R. Santhakumarzf. Critical distance for blast-resistant design. *Computers & Structures*, 54(4), 1995.
- [103] Martin Larcher. Simulation of the effects of an air blast wave. Technical report, Institute for the Protection and Security of the Citizen, 2007.
- [104] Borgers J. and Vantomme J. Improving the accuracy of blast parameters using a new friedlander curvature alpha. In *DoD Explosives Safety Seminar*, Palm Springs, California, USA., 2008.
- [105] Vasilis Karlos, Martin Larcher, and George Solomos. Analysis of the blast wave decay coefficient in the friedlander equation using the kingery-bulmash data. Technical Report JRC94784, European Commission Joint Research Centre, Institute for the Protection and Security of the Citizen, 2015.
- [106] T.C.J. Hu and I. I. Glass. Blast wave reflection trajectories from a height of burst. *AIAA Journal*, 24(4):607–610, 1986.
- [107] W. E. Baker. *Explosions in air*. University of Texas Press, 1973.
- [108] John R. Taylor. *An introduction to error analysis*. University Science Books, 2 edition, 1997.
- [109] P. Clark Souers. A library of prompt detonation reaction zone data. Technical Report UCRL-ID-130055 Rev 1, Lawrence Livermore National Laboratory, 1998.
- [110] W. R. Blumenthal, D. G. Thompson, C. D. Cady, G. T. Gray III, and D. J. Idar. Compressive properties of pbxn-110 and its htpb -based binders as a function of temperature and strain rate. In *Proceedings of the 12th International Detonation Symposium*, San Diego, CA, USA, 2002.
- [111] C. M. Tarver. Jones-wilkins-lee (jwl) reaction products equations of state for overdriven petn detonation waves. In *21st Biennial Conference of the APS Topical Group on Shock Compression of Condensed Matter*, 2019.
- [112] Philip J. Miller. A simplified method for determining reactive rate parameters for reaction ignition and growth in explosives. In *Material Research Society Proceedings*. Material Research Society Proceedings, 1995.

- [113] C. N. Kingery and G. Bulmash. Airblast parameters from tnt spherical air burst and hemispherical surface burst. Technical Report ARBRL-TR-02555, Aberdeen Proving Ground, Maryland : US Army Armament and Development Center, Ballistic Research Laboratory, 1984.
- [114] E. Lee, M. Finger, and W. Collins. Jwl equation of state coefficients for high explosives. Technical Report UCID-16189, Lawrence Livermore Laboratory, 1973.

## **APPENDIX A**

### **SPHERE PRESSING DIE DESIGN**



**DETAIL B**  
SCALE 2 : 1

**SECTION A-A**

UNLESS OTHERWISE SPECIFIED: DIMENSIONS ARE IN INCHES SURFACE FINISH: TOLERANCES: ±0.001		FINISH:		DEBURR AND BREAK SHARP EDGES		DO NOT SCALE DRAWING		REVISION	
DRAWN	NAME	SIGNATURE	DATE	TITLE:		DWG NO.		A4	
CHK'D						Anvil Bottom			
APP'VD						SCALE: 1:1		SHEET 1 OF 1	
MEG						WEIGHT:			
Q.A.						MATERIAL:			

D

C

B

A

D

C

B

A

D

C

B

A

D

C

B

A

D

C

B

A

D

C

B

A

D

C

B

A

D

C

B

A

D

C

B

A

D

C

B

A

D

C

B

A

D

C

B

A

D

C

B

A

D

C

B

A

D

C

B

A

D

C

B

A

D

C

B

A

D

C

B

A

D

C

B

A

D

C

B

A

D

C

B

A

D

C

B

A

D

C

B

A

D

C

B

A

D

C

B

A

D

C

B

A

D

C

B

A

D

C

B

A

D

C

B

A

D

C

B

A

D

C

B

A

D

C

B

A

D

C

B

A

D

C

B

A

D

C

B

A

D

C

B

A

D

C

B

A

D

C

B

A

D

C

B

A

D

C

B

A

D

C

B

A

D

C

B

A

D

C

B

A

D

C

B

A

D

C

B

A

D

C

B

A

D

C

B

A

D

C

B

A

D

C

B

A

D

C

B

A

D

C

B

A

D

C

B

A

D

C

B

A

D

C

B

A

D

C

B

A

D

C

B

A

D

C

B

A

D

C

B

A

D

C

B

A

D

C

B

A

D

C

B

A

D

C

B

A

D

C

B

A

D

C

B

A

D

C

B

A

D

C

B

A

D

C

B

A

D

C

B

A

D

C

B

A

D

C

B

A

D

C

B

A

D

C

B

A

D

C

B

A

D

C

B

A

D

C

B

A

D

C

B

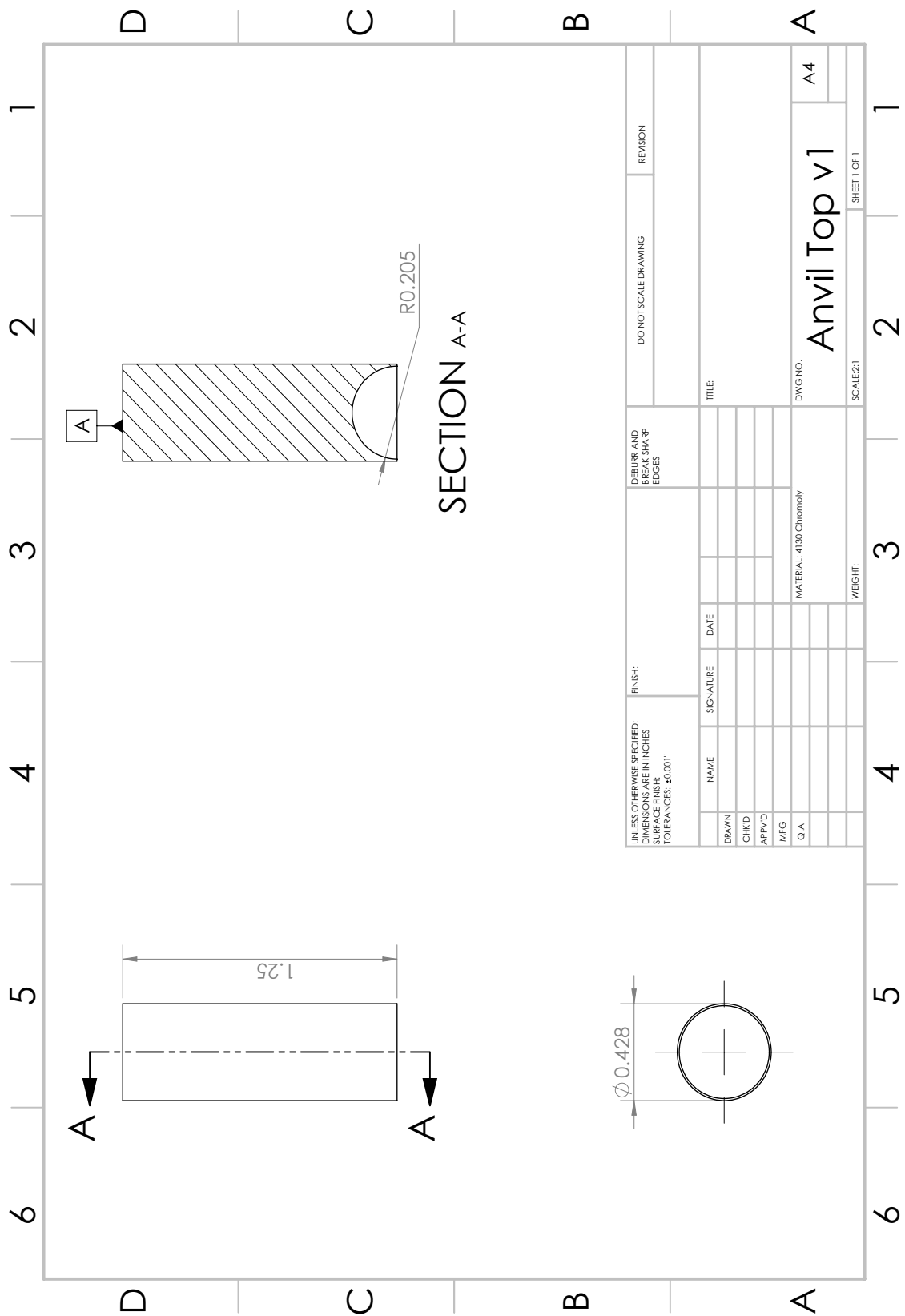
A

D

C

B

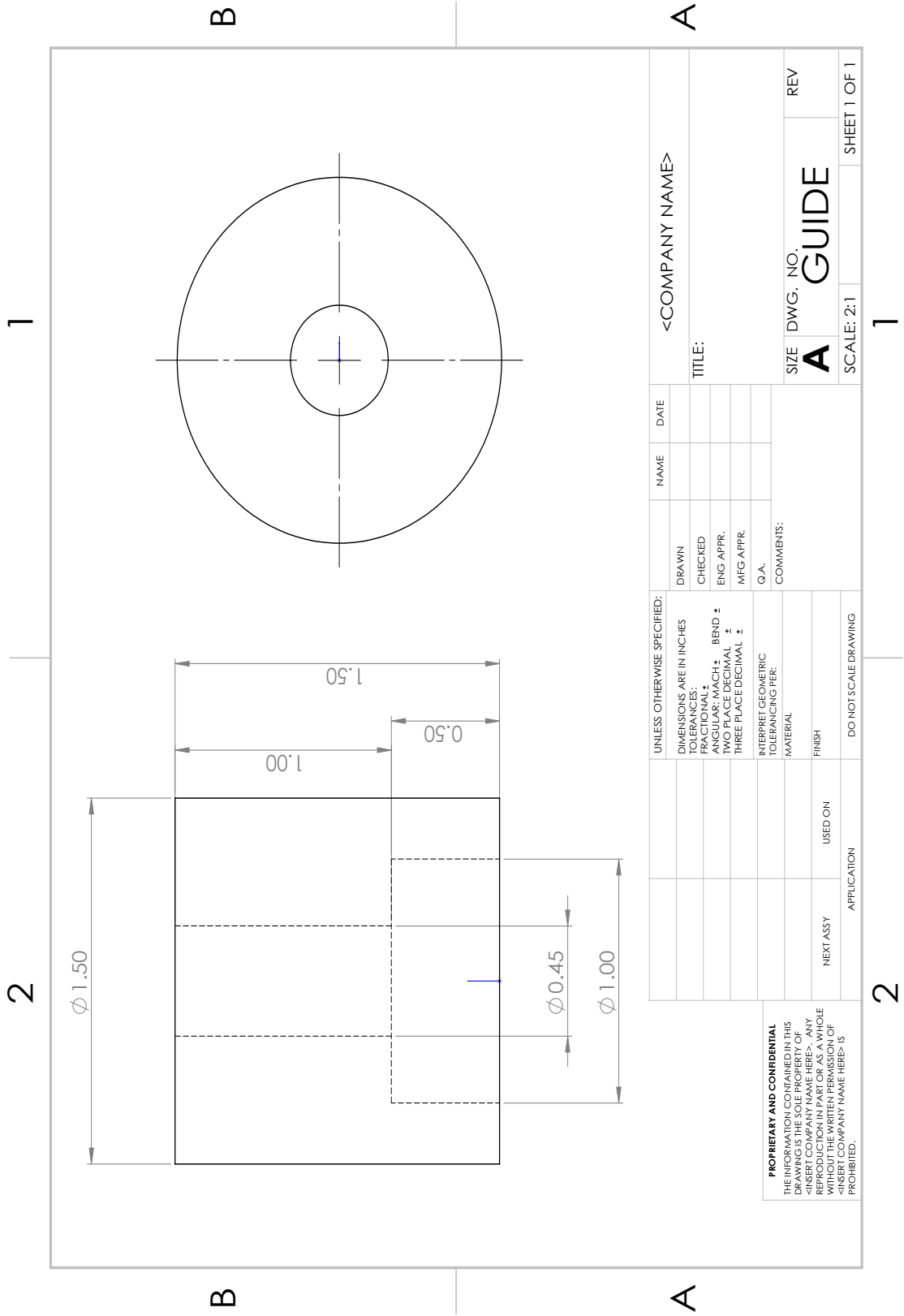




SECTION A-A

UNLESS OTHERWISE SPECIFIED: DIMENSIONS ARE IN INCHES SURFACE FINISH: TOLERANCES: ±0.001"		FINISH:		DEBURR AND BREAK SHARP EDGES		DO NOT SCALE DRAWING		REVISION	
DRAWN	NAME	SIGNATURE	DATE						
CHK'D									
APP'VD									
MEG									
Q.A.									
	MATERIAL: 4130 Chromoly			TITLE:		DWG NO.		A4	
	WEIGHT:			SCALE: 2:1		SHEET 1 OF 1			

Anvil Top v1



2

1

B

B

A

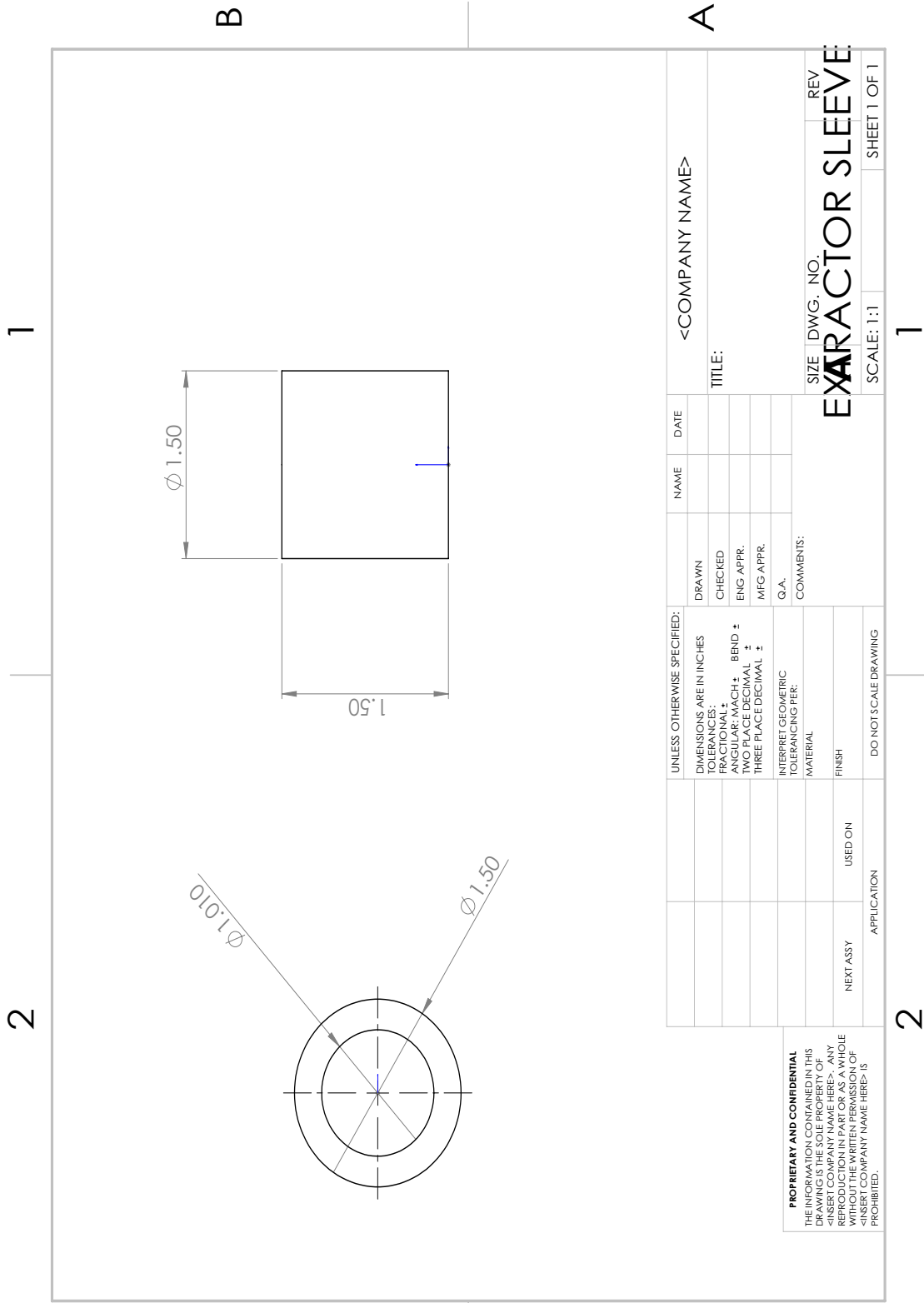
A

**PROPRIETARY AND CONFIDENTIAL**  
 THE INFORMATION CONTAINED IN THIS DRAWING IS THE SOLE PROPERTY OF <INSERT COMPANY NAME HERE> AND IS NOT TO BE REPRODUCED IN ANY MANNER WITHOUT THE WRITTEN PERMISSION OF <INSERT COMPANY NAME HERE>. IS PROHIBITED.

UNLESS OTHERWISE SPECIFIED: DIMENSIONS ARE IN INCHES FRACTIONS ANGULAR: MACH ± BEND ± TWO PLACE DECIMAL ± THREE PLACE DECIMAL ±		DRAWN	NAME	DATE	<COMPANY NAME>
INTERPRET GEOMETRIC TOLERANCING PER: MATERIAL FINISH		CHECKED			
NEXT ASSY		ENG APPR.			TITLE:
USED ON		MFG APPR.			SIZE DWG. NO. REV
APPLICATION		Q.A.			<b>A</b> <b>GUIDE</b>
DO NOT SCALE DRAWING		COMMENTS:			SCALE: 2:1 SHEET 1 OF 1

2

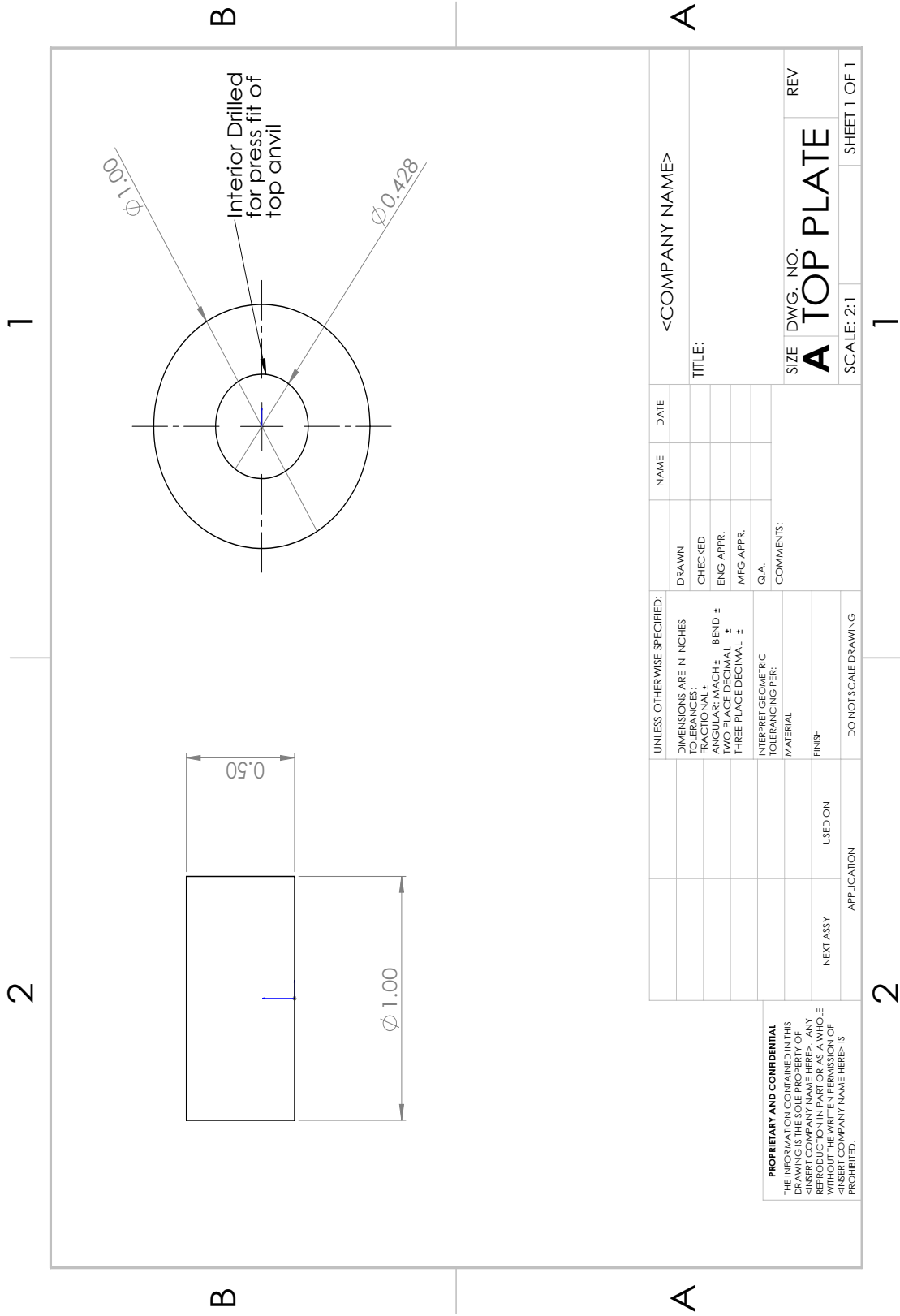
1



**PROPRIETARY AND CONFIDENTIAL**  
 THE INFORMATION CONTAINED IN THIS  
 DRAWING IS THE SOLE PROPERTY OF  
 THE COMPANY AND IS NOT TO BE  
 REPRODUCED IN ANY MANNER, IN  
 WHOLE OR IN PART, WITHOUT THE  
 WRITTEN PERMISSION OF THE  
 COMPANY. <INSERT COMPANY NAME HERE> IS  
 PROHIBITED.

UNLESS OTHERWISE SPECIFIED:		DRAWN	NAME	DATE	<COMPANY NAME>
DIMENSIONS ARE IN INCHES FRACTIONS ANGULAR: MACH ± BEND ± TWO PLACE DECIMAL ± THREE PLACE DECIMAL ±		CHECKED			
INTERPRET GEOMETRIC TOLERANCING PER:		ENG APPR.			SIZE DWG. NO. REV
MATERIAL		MFG APPR.			<b>EXTRACTOR SLEEVE</b>
FINISH		Q.A.			SCALE: 1:1 SHEET 1 OF 1
NEXT ASSY	USED ON	COMMENTS:			
APPLICATION		DO NOT SCALE DRAWING			

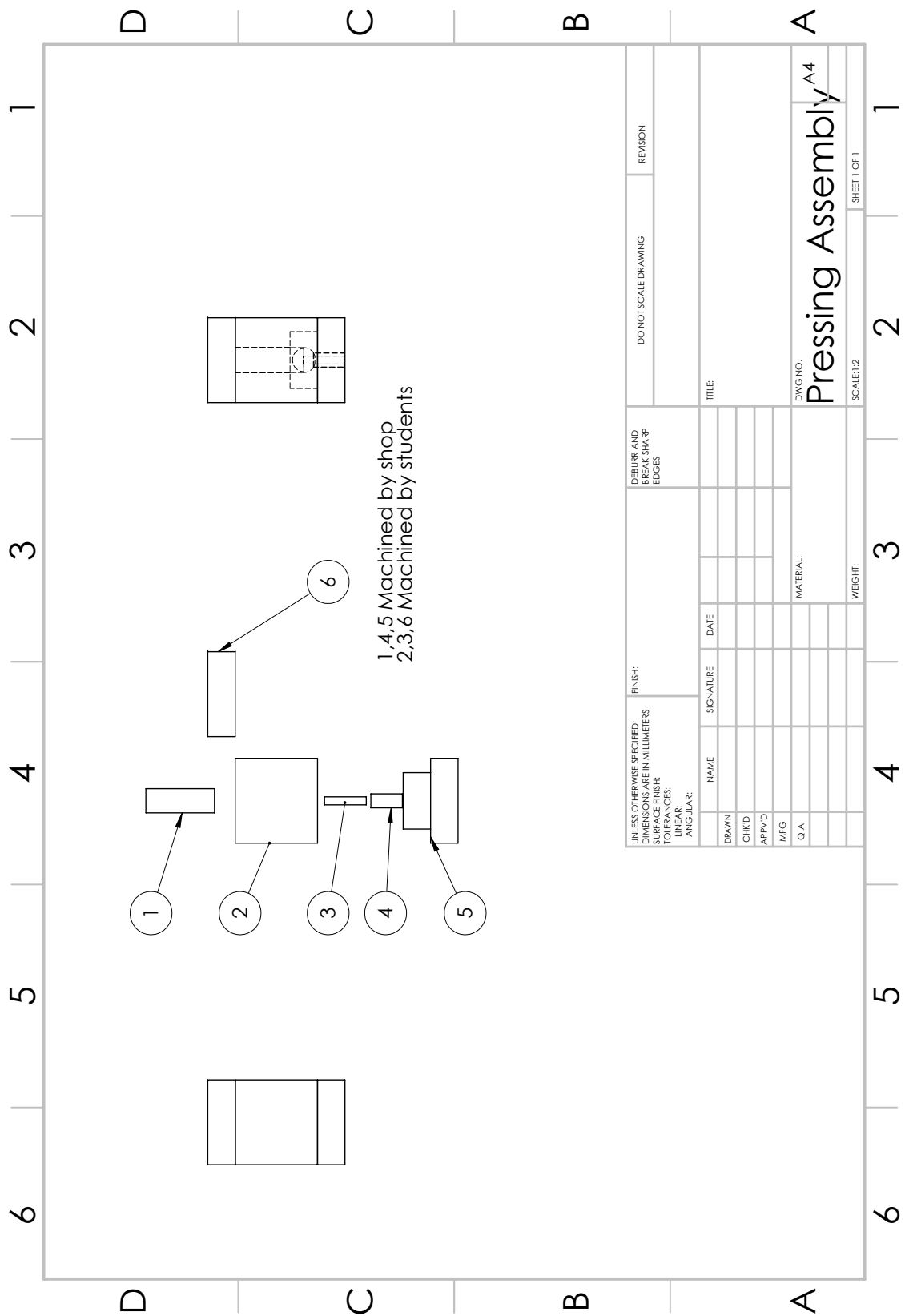
2 1 B A B A



**PROPRIETARY AND CONFIDENTIAL**  
 THE INFORMATION CONTAINED IN THIS  
 DRAWING IS THE SOLE PROPERTY OF  
 THE COMPANY AND IS NOT TO BE  
 REPRODUCED IN ANY MANNER, IN  
 WHOLE OR IN PART, WITHOUT THE  
 WRITTEN PERMISSION OF THE  
 COMPANY. <INSERT COMPANY NAME HERE> IS  
 PROHIBITED.

UNLESS OTHERWISE SPECIFIED:		DRAWN	NAME	DATE	<COMPANY NAME>
DIMENSIONS ARE IN INCHES FRACTIONS ANGULAR: MACH ± BEND ± TWO PLACE DECIMAL ± THREE PLACE DECIMAL ±		CHECKED			
INTERPRET GEOMETRIC TOLERANCING PER:		ENG APPR.			SIZE DWG. NO.
MATERIAL		MFG APPR.			<b>A TOP PLATE</b>
FINISH		Q.A.			REV
NEXT ASSY	USED ON	COMMENTS:			SCALE: 2:1
APPLICATION		DO NOT SCALE DRAWING			SHEET 1 OF 1

2 1 1 2



UNLESS OTHERWISE SPECIFIED: DIMENSIONS ARE IN MILLIMETERS		FINISH:		DEBURR AND BREAK SHARP EDGES		DO NOT SCALE DRAWING		REVISION	
SURFACE FINISH:		TOLERANCES:		LINEAR:		ANGULAR:		TITLE:	
DRAWN	NAME	SIGNATURE	DATE	MATERIAL:		DWG NO.		Pressing Assembly <sup>A4</sup>	
CHK'D						SCALE:1:2		SHEET 1 OF 1	
APP'VD									
MEG									
Q.A.									

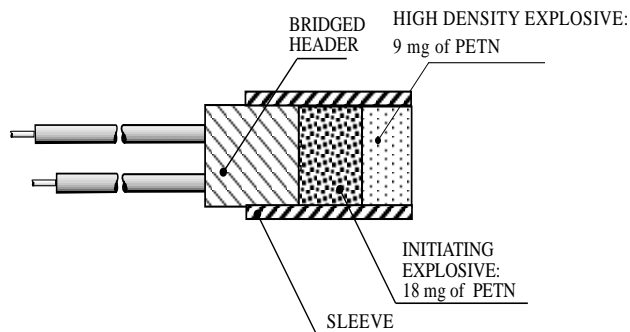
## RP-3 EBW Detonator

P/N 167-9225

The RP-3 EBW detonator is a miniature detonator containing less than 30 mg of PETN explosive. Although small this detonator will initiate most common military explosives. The RP-3 is used in situations which cannot tolerate blast or fragment damage but still requires the safety and reliability of an EBW detonator.



### RP-3 EXPLOSIVE TRAIN



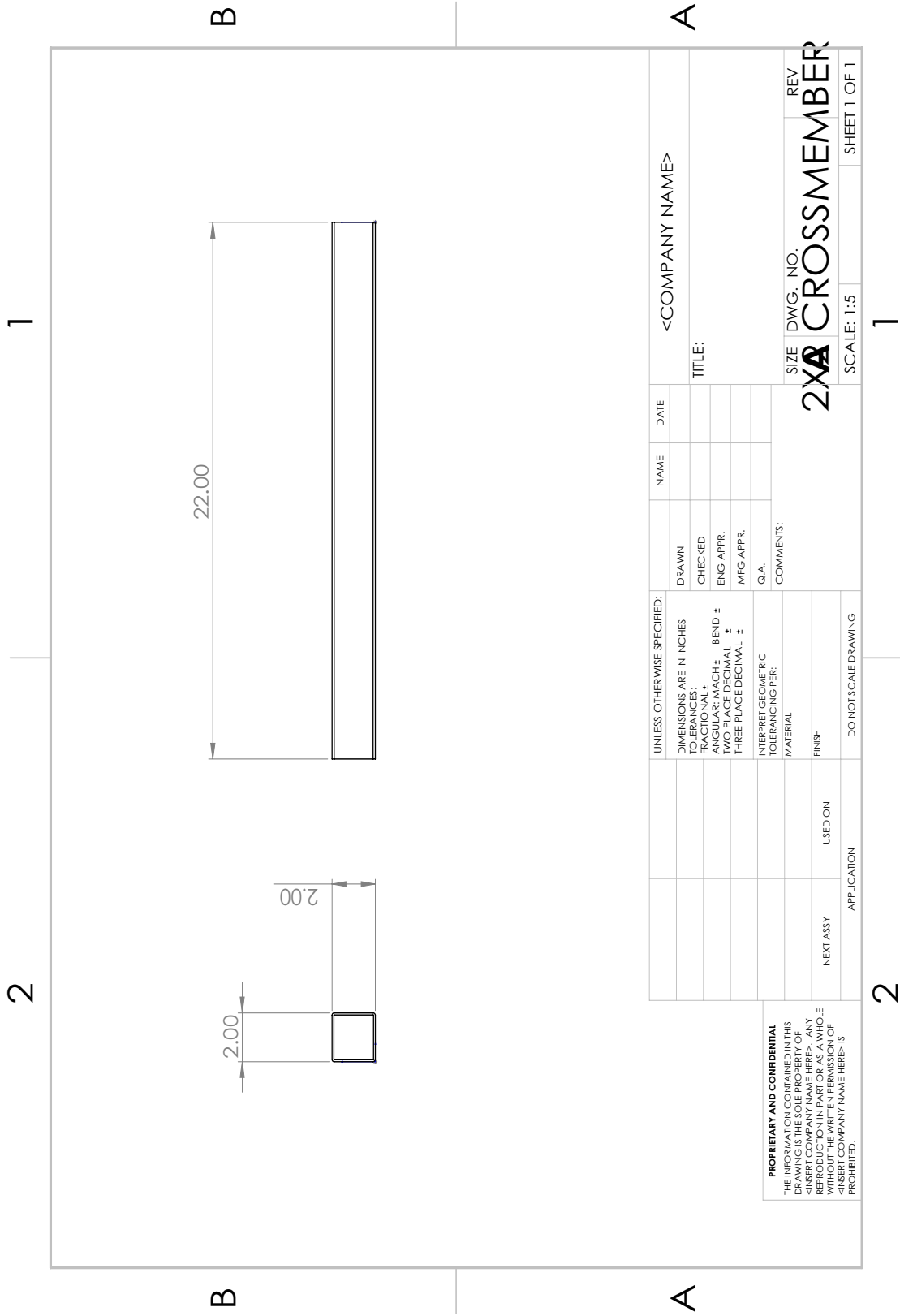
### RP-3 Firing Parameters

- Threshold Burst Current: 200 amps
- Threshold Voltage: Approx. 500 volts
- Threshold Voltage Std. Deviation: 25 volts maximum
- Function Time: 1.5  $\mu$ sec. typical
- Function Time Simultaneity Standard Deviation: 0.060  $\mu$ sec Max.

**Caution:** While EBW and EFI Initiators are inherently less susceptible to accidental detonation during handling and set-up than devices containing primary explosives, electrical and electronic firing systems are sensitive to transient electrical energies which could cause premature triggering or firing. The blasting area must be clear of personnel and equipment before the detonator leads are connected to any RISI Firing System. Only approved RISI Firing Systems should ever be used to initiate or detonate any explosive product manufactured and authorized for sale by RISI.

## **APPENDIX B**

### **REFLECTION PLATE DESIGN**



2 1

2

B

B

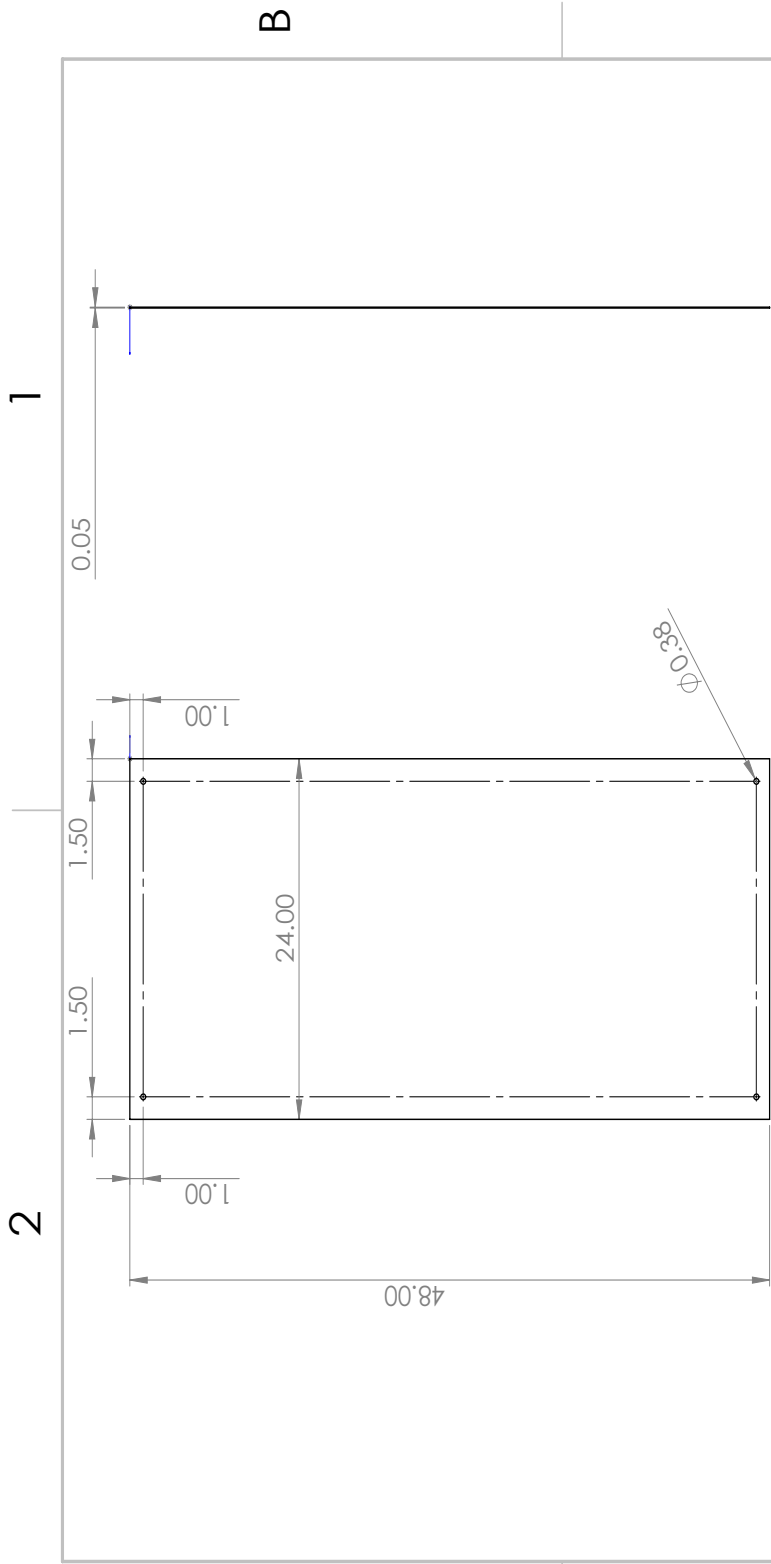
A

A

UNLESS OTHERWISE SPECIFIED:		DRAWN	NAME	DATE	<COMPANY NAME>
DIMENSIONS ARE IN INCHES		CHECKED			TITLE:
FRACTIONS		ENG APPR.			
ANGULAR: MACH ±		MFG APPR.			
BEND ±		Q.A.			
TWO PLACE DECIMAL ±		COMMENTS:			
THREE PLACE DECIMAL ±					
INTERPRET GEOMETRIC TOLERANCING PER:					SIZE DWG. NO. REV
MATERIAL					<b>2XA CROSSMEMBER</b>
FINISH					SCALE: 1:5 SHEET 1 OF 1
NEXT ASSY	USED ON				
APPLICATION					

**PROPRIETARY AND CONFIDENTIAL**  
 THE INFORMATION CONTAINED IN THIS DRAWING IS THE SOLE PROPERTY OF THE COMPANY. IT IS TO BE USED ONLY FOR THE PRODUCTION OF THIS PART AS A WHOLE WITHOUT THE WRITTEN PERMISSION OF THE COMPANY.   
 <INSERT COMPANY NAME HERE> IS PROHIBITED.

2 1



<p><b>PROPRIETARY AND CONFIDENTIAL</b>          THE INFORMATION CONTAINED IN THIS DRAWING IS THE SOLE PROPERTY OF [COMPANY NAME]. IT IS TO BE USED ONLY FOR THE SPECIFIC PART AND ASSEMBLY IDENTIFIED HEREON. REPRODUCTION IN ANY MANNER, IN WHOLE OR IN PART, WITHOUT THE WRITTEN PERMISSION OF [COMPANY NAME] IS PROHIBITED.</p>		UNLESS OTHERWISE SPECIFIED:		DRAWN		NAME		DATE		<COMPANY NAME>	
		DIMENSIONS ARE IN INCHES DECIMALS ANGULAR: MACH ± BEND ± TWO PLACE DECIMAL ± THREE PLACE DECIMAL ±		CHECKED		DATE		DATE		TITLE:	
NEXT ASSY		USED ON		ENG APPR.		MFG APPR.		Q.A.		SIZE DWG. NO. REV	
APPLICATION		DO NOT SCALE DRAWING		INTERPRET GEOMETRIC TOLERANCING PER:		COMMENTS:		MATERIAL		<b>AX4 FLAT SHEET</b>	
				FINISH						SCALE: 1:10 SHEET 1 OF 1	

2

2

1

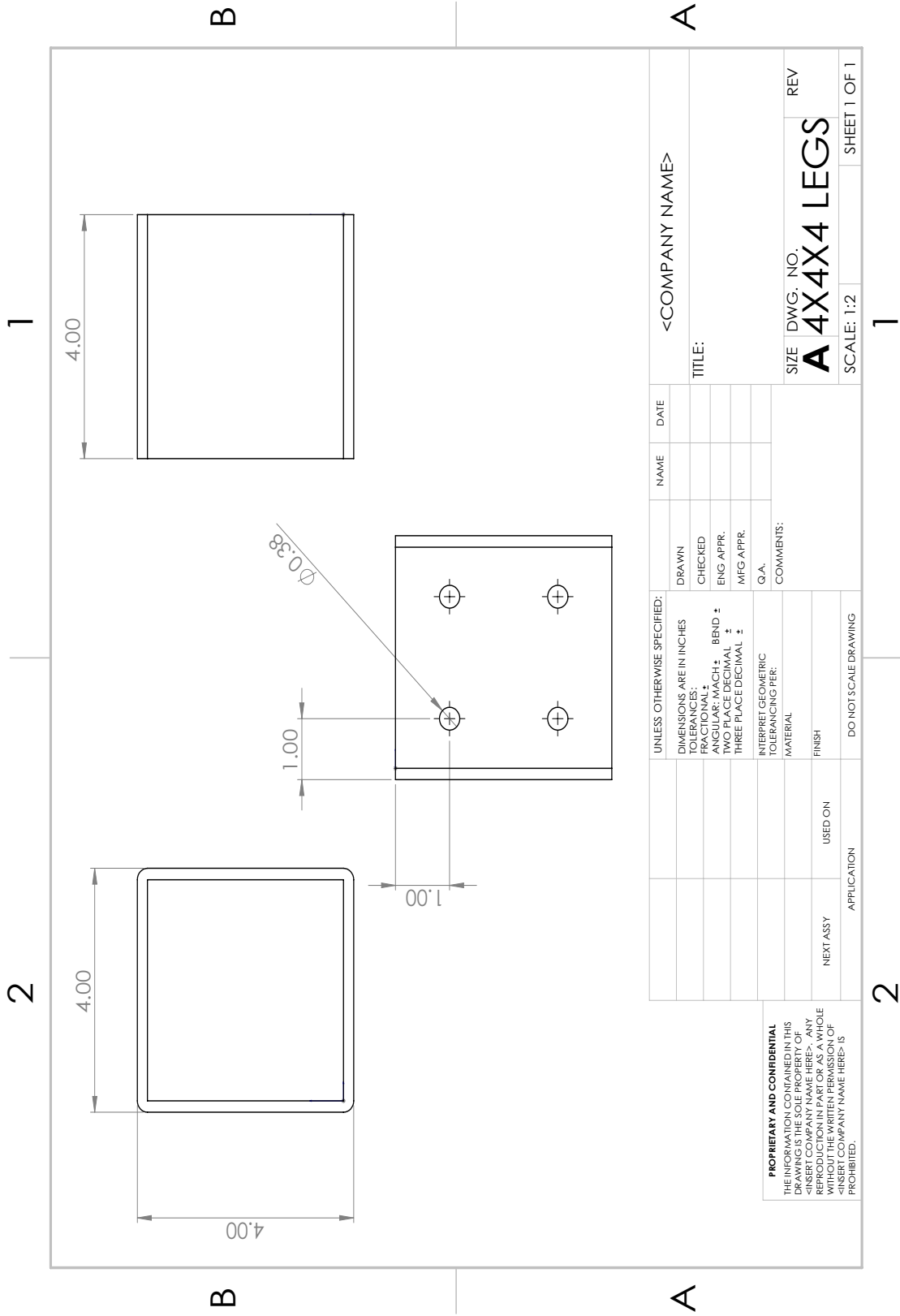
1

B

A

B

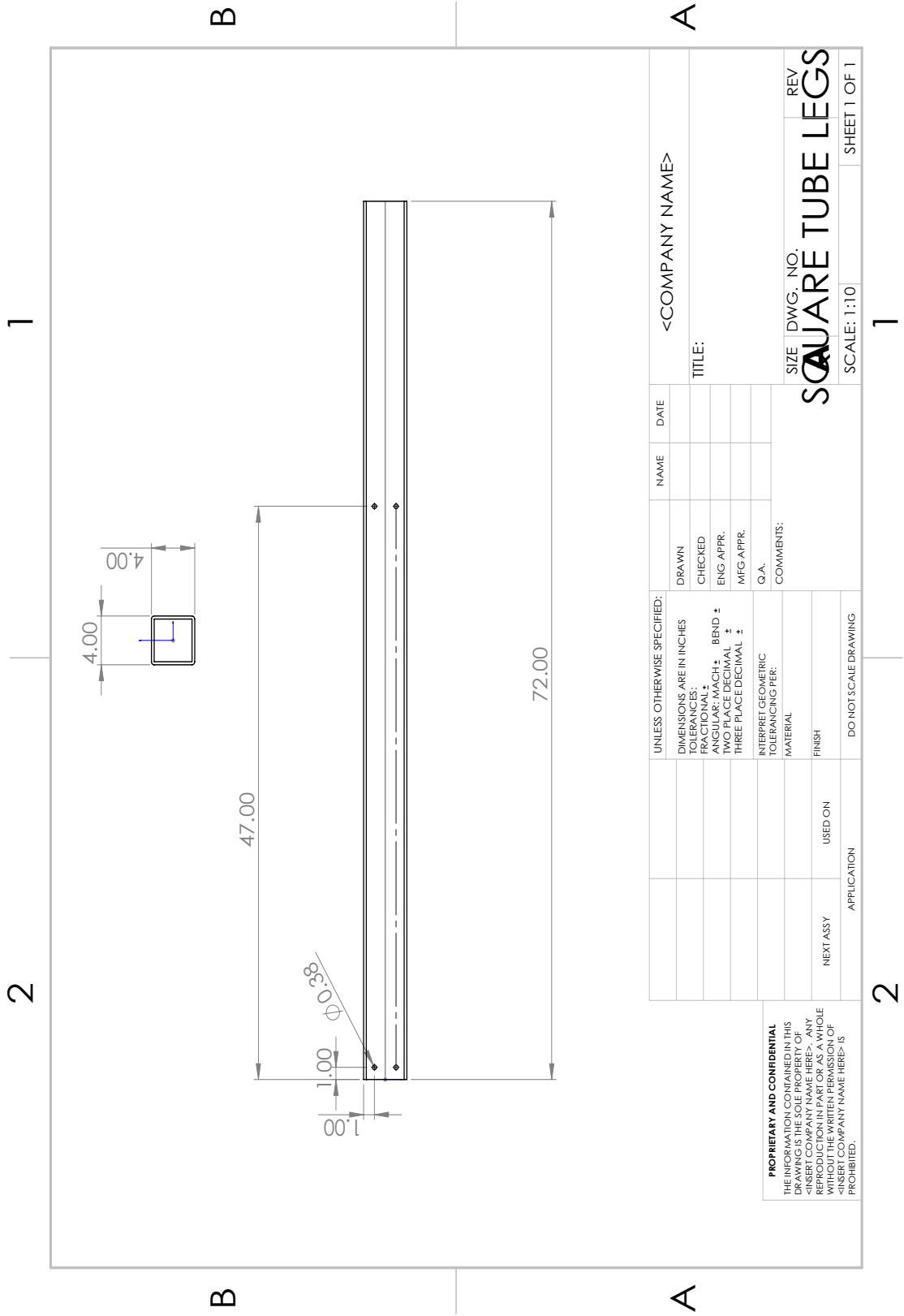
A



**PROPRIETARY AND CONFIDENTIAL**  
 THE INFORMATION CONTAINED IN THIS  
 DRAWING IS THE SOLE PROPERTY OF  
 AND IS NOT TO BE REPRODUCED OR  
 TRANSMITTED IN ANY FORM OR BY  
 ANY MEANS, ELECTRONIC OR MECHANICAL,  
 INCLUDING PHOTOCOPYING, RECORDING,  
 OR BY ANY INFORMATION STORAGE AND  
 RETRIEVAL SYSTEM, WITHOUT THE WRITTEN PERMISSION OF  
 <INSERT COMPANY NAME HERE> IS  
 PROHIBITED.

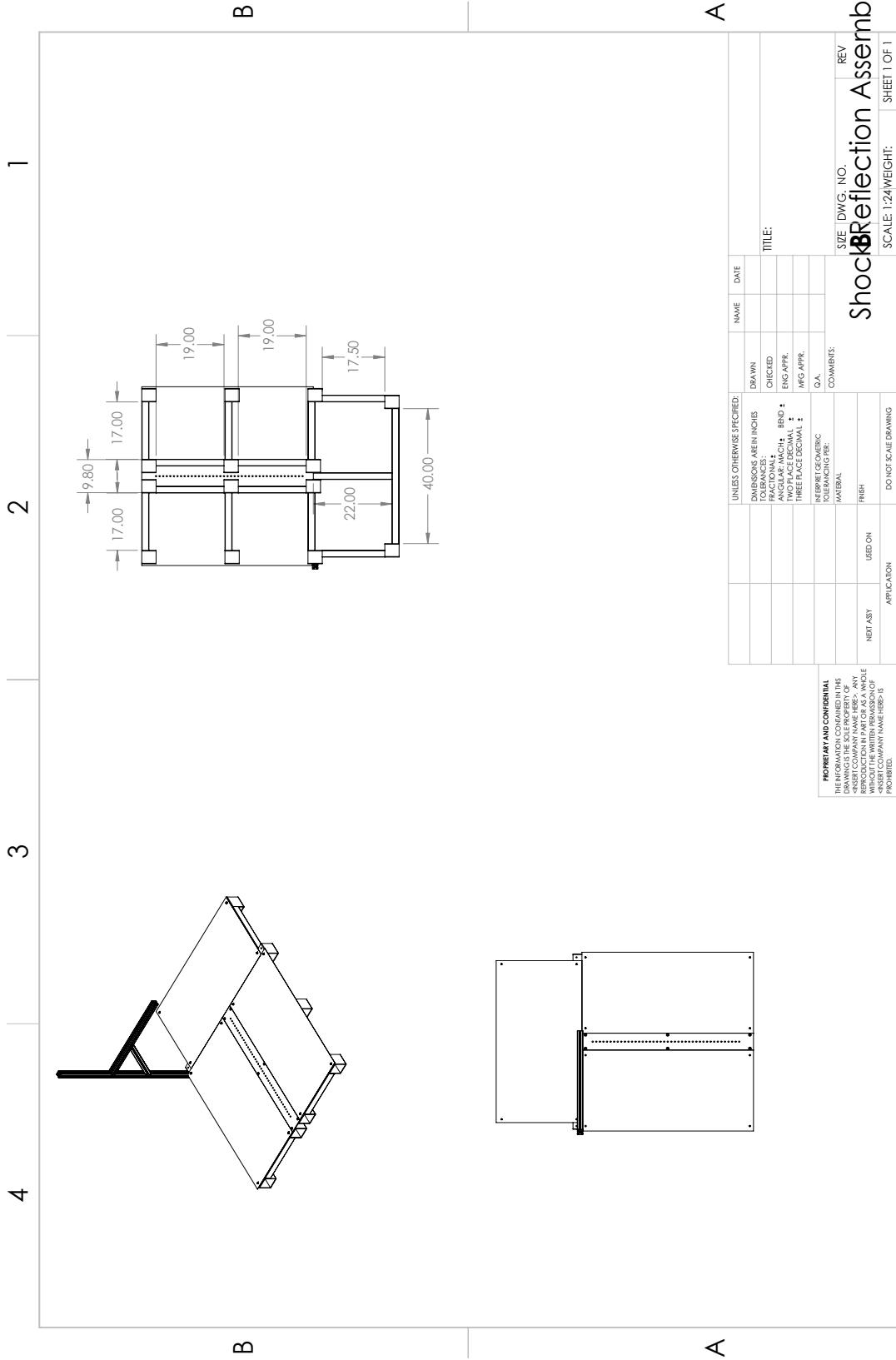
UNLESS OTHERWISE SPECIFIED:		DRAWN	NAME	DATE	<COMPANY NAME>
DIMENSIONS ARE IN INCHES		CHECKED			
FRACTIONS		ENG APPR.			TITLE:
ANGULAR: MACH ±		MFG APPR.			SIZE DWG. NO.
BEND ±		Q.A.			<b>A 4X4X4 LEGS</b>
TWO PLACE DECIMAL ±		COMMENTS:			REV
THREE PLACE DECIMAL ±					SCALE: 1:2
INTERPRET GEOMETRIC TOLERANCING PER:					SHEET 1 OF 1
MATERIAL					
FINISH					
NEXT ASSY					
USED ON					
APPLICATION					
DO NOT SCALE DRAWING					

2 1



UNLESS OTHERWISE SPECIFIED:		DRAWN	NAME	DATE	<COMPANY NAME>	
DIMENSIONS ARE IN INCHES		CHECKED			TITLE:	
FRACTIONS		ENG APPR.			SIZE DWG. NO. REV	
ANGULAR: MACH ± BEND ±		MFG APPR.			<b>SQUARE TUBE LEGS</b>	
TWO PLACE DECIMAL ±		Q.A.			SCALE: 1:10 SHEET 1 OF 1	
THREE PLACE DECIMAL ±		COMMENTS:				
INTERPRET GEOMETRIC TOLERANCING PER:						
MATERIAL						
FINISH						
NEXT ASSY		USED ON				
APPLICATION		DO NOT SCALE DRAWING				

**PROPRIETARY AND CONFIDENTIAL**  
 THE INFORMATION CONTAINED IN THIS DRAWING IS THE SOLE PROPERTY OF SQUARE TUBE LEGS. IT IS TO BE USED ONLY FOR THE MANUFACTURE AND REPRODUCTION IN PART OR AS A WHOLE WITHOUT THE WRITTEN PERMISSION OF SQUARE TUBE LEGS. <INSERT COMPANY NAME HERE> IS PROHIBITED.



4 3 2 1

B A

**PROPRIETARY AND CONFIDENTIAL**  
 THE INFORMATION CONTAINED IN THIS DRAWING IS THE SOLE PROPERTY OF SHOCK REFLECTION ASSEMBLY, INC. REPRODUCTION IN PART OR AS A WHOLE WITHOUT THE WRITTEN PERMISSION OF SHOCK REFLECTION ASSEMBLY, INC. IS PROHIBITED.

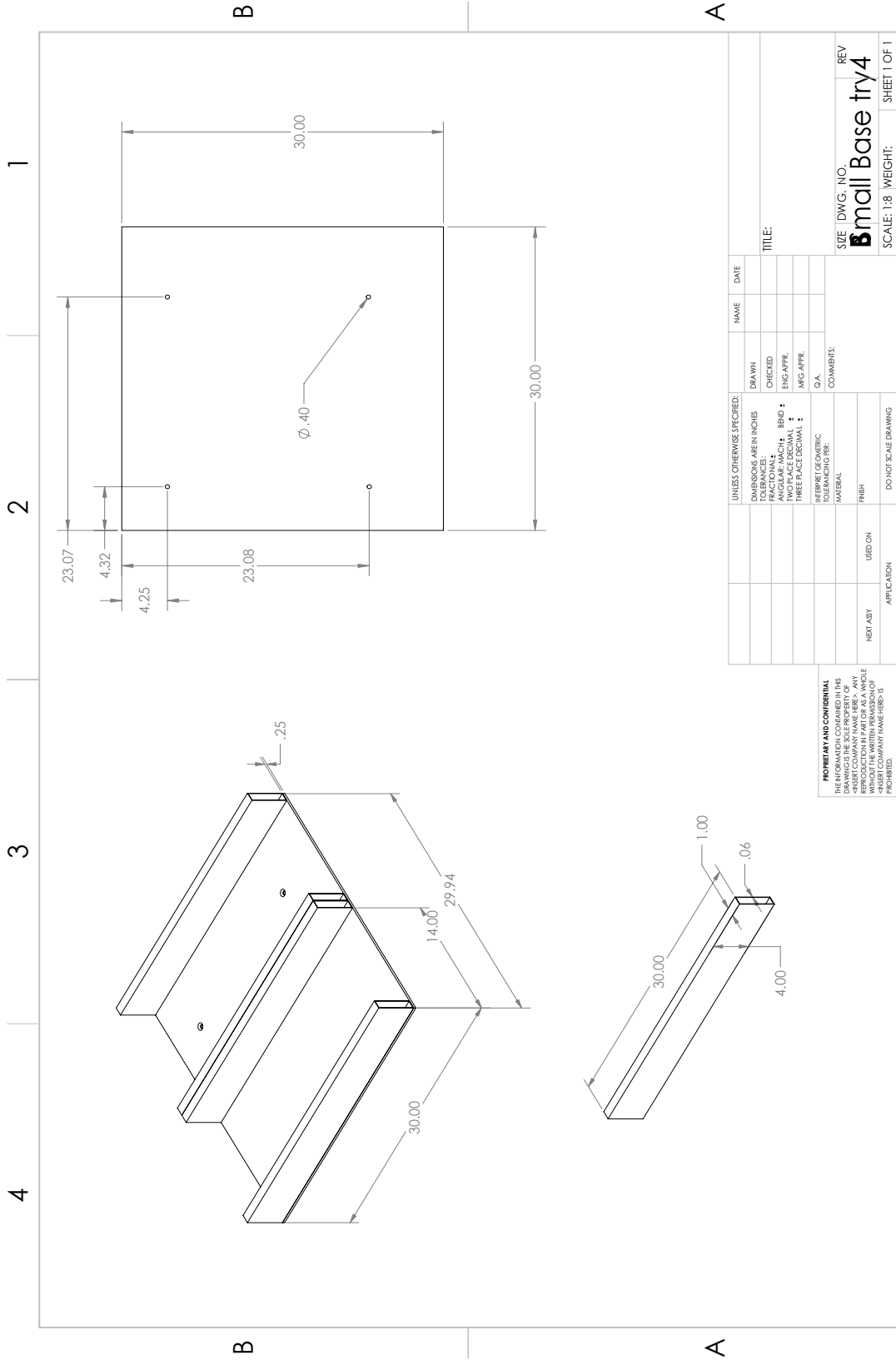
UNLESS OTHERWISE SPECIFIED:		NAME	DATE
DIMENSIONS ARE IN INCHES	DRAWN		
FRACTIONAL	CHECKED		
ANGULAR: MACH. BEND :	ENG APPR.		
THREE PLACE DECIMAL :	MFG APPR.		
	G.A.		
	COMMENTS:		
MATERIAL			
FINISH			
REVISIONS			
REVISION	USED ON		
DATE	APPLICATION		
	DO NOT SCALE DRAWING		

SIZE DWG. NO. REV  
**Shock Reflection Assembly**  
 SCALE: 1:24 WEIGHT: SHEET 1 OF 1

1 2 3 4

**APPENDIX C**

**MIRROR BASE DESIGN**



**PROPRIETARY AND CONFIDENTIAL**  
 THE INFORMATION CONTAINED IN THIS DRAWING IS THE SOLE PROPERTY OF Ball BEARING CO. REPRODUCTION IN PART OR AS A WHOLE WITHOUT THE WRITTEN PERMISSION OF Ball BEARING CO. IS PROHIBITED.

UNLESS OTHERWISE SPECIFIED:		NAME	DATE
DIMENSIONS ARE IN INCHES	DRAWN		
FRACTIONAL	CHECKED		
ANGULAR: MACH	ENG APPR.		
BEND	MFG APPR.		
THREE PLACE DECIMAL	G.A.		
UNLESS OTHERWISE SPECIFIED:	COMMENTS:		
MATERIAL			
FINISH			
HEAT TRT	USED ON		
APPLICATION	DO NOT SCALE DRAWING		

SIZE DWG. NO. REV  
**Small Base try4**  
 SCALE: 1:8 WEIGHT: SHEET 1 OF 1

# IRREGULAR REFLECTIONS OF UNSTEADY SHOCK WAVES

by

Kyle Oakley Winter

Permission to make digital or hard copies of all or part of this work for personal or classroom use is granted without fee provided that copies are not made or distributed for profit or commercial advantage and that copies bear this notice and the full citation on the last page. To copy otherwise, to republish, to post on servers or to redistribute to lists, requires prior specific permission and may require a fee.

